B7155

Lh 3028

LA-8114-PR
Progress Report

UC-21
Issued: June 1981

Inertial Fusion Program

January 1—June 30, 1979

MASTER

Roger B. Perkins and the
Inertial Fusion Program Staff

Compiled by
Frederick Skoberne

CONTENTS

INERTIAL FUSION PROGRAM
January 1—June 30, 1979

by

Roger B. Perkins and the Inertial Fusion Program Staff

Compiled by
Frederick Skoberne

ABSTRACT

Progress in the development of high-energy short-pulse carbon dioxide laser systems for fusion research is reported. Improvements are outlined for the Los Alamos National Laboratory's Gemini System, which permitted over 500 shots in support of 10 different target experiments; the transformation of our eight-beam system, Helios, from a developmental to an operational facility that is capable of irradiating targets on a routine basis is described; and progress made toward completion of Antares, our 100- to 200-TW target irradiation system, is detailed.

Investigations of phenomena such as phase conjugation by degenerate four-wave mixing and its applicability to laser fusion systems, and frequency multiplexing as a means toward multipulse energy extraction are summarized. Also discussed are experiments with targets designed for adiabatic compression, which reached the important milestone of compressing the fuel to a density 20 times that of liquid hydrogen. Results of opacity experiments, part of our modest military applications effort, are also given. Progress is reported in the development of accurate diagnostics, especially for the detection of expanding ions, of neutron yield, and of x-ray emission. Significant advances in our theoretical efforts are summarized, such as the adaptation of our target design codes for use with the CRAY-1 computer, and new results leading to a better understanding of implosion phenomena are reported, which will significantly affect the design of future targets. Improvements in the fabrication of complex targets are discussed and the development of cryogenics for the target retraction mechanism in Helios is described.

The results of various fusion reactor studies are summarized, including the development of an ICF reactor blanket that offers a promising alternative to the usual lithium blanket, and the formulation of a capital-cost data base for laser fusion reactors to permit meaningful comparisons with other technologies.

SUMMARY
(Laser Fusion Staff)

INTRODUCTION

The Los Alamos National Laboratory Inertial Fusion Program, in conjunction with the Department of Energy, is searching for a solution to the Nation's long-term energy problems and providing support for the nuclear weapons program. The first objective for both goals is to demonstrate that the fusion fuel contained in a target pellet can be ignited. To this end, our broadly based program involves the development of high-power drivers that can ignite the fuel, the design and fabrication of fuel pellets, experimental studies of target phenomenology to provide information for the design process, development of suitable diagnostics for such experiments, studies of weapons applications, and studies of concepts leading to the use of inertial fusion for power production.

Three medium sized CO_2 laser systems are being used for experiments, and the 100-kJ Antares CO_2 laser is being prepared for future tests.

CO_2 LASER PROGRAM

Helios Laser System

Since its first shot on target in July 1978, Helios has grown from a developmental facility to an operational facility capable of irradiating targets on a routine basis. During the first half of 1979, approximately two of every five work days were shooting days. During this time, 259 shots were fired—86 in support of the target program, and 173 in support of system development and/or maintenance. Important tasks accomplished during this period include

- installation and operation of the beam simultaneity system;
- measurements of the first optical multiplexing in a Helios power amplifier;
- installation and operation of the Data General S/230 computer system;
- installation of the first optical encoder system on the target mirrors of one of the eight beam lines; and
- optical isolation of the screen room that houses the Helios computer control system

Gemini Laser System

The Gemini laser system fired 513 shots in support of target experimentation. The desired output energy was produced in 423 shots with no measurable prelasing or prepulsing.

The following improvements were made in the Gemini system during the past 6 months.

- The internal saturable-absorber gas cell was tested hydrostatically and prepared for installation.
- The single-target insertion mechanism is ~90% complete.
- The deformable mirrors (Hughes Aircraft Company) are in the mirror-grinding stage.
- Ten target experiments were performed.
- The oscillator and preamplifier for the new front-end system are assembled and testing has begun.
- Antireflection-coated NaCl windows were installed on the Gemini target chamber.
- The control system upgrade was designed.

Gigawatt Test Facility

The Gigawatt Test Facility (GWTF) laser was upgraded in performance and reliability to provide more than 10 GW of output power for plasma physics and other studies. In addition, the components of the previous GWTF were reconfigured to produce a second beam line with line-selectable CO_2 pulses of 1 to 60 ns and up to 5 J energy. The associated experimental areas can now accommodate four simultaneous optical studies by means of a beam switchyard.

ANTARES

Antares comprises a six-beam, 100- to 200-TW CO_2 laser and associated target-irradiation facilities. Excellent progress was made in the design and procurement of the various components of the system, but inclement weather caused construction delays of some of the large buildings that will house the system.

The design and procurement of hardware was completed for the first of the six power amplifiers and for the optical test bed (a beam line devoted to optical work) and awaited delivery of large long-lead-time parts. The first power-amplifier parts to be delivered will be the vacuum envelope for the first electron gun, and support stands and pressure shells for the first two power amplifiers. Because the Laser Building will not be complete by July 1979, these large components will be located in temporary facilities.

The optical design of the Antares oscillator and preamplifier stages (optical front end) was completed. A one-beam prototype incorporating Antares hardware is being built in a laboratory set aside for front-end development. Preamplifiers were received, and a new, more efficient design of a multipass preamplifier was assembled and tested. Specifications for the system's output (driver) amplifiers were written, and a fixed-price contract for an initial unit, with options for five or more, was awarded.

A major development and procurement contract was awarded to Maxwell Laboratories, Inc., for the main Antares energy storage system. Antares requires 24 Marx generators, each storing 300 kJ at 1.2 MV. The performance specifications required that the units have less than 3-μH inductance and a jitter below 20-ns rms. However, because such stringent specifications were new to the pulse-power industry, we designed and tested a prototype unit. This work was successful and three contractors submitted fixed-price quotations in response to our requests for proposal.

We defined a tree-structured, hierarchical architecture for the controls system, and requested quotations based on detailed specifications for the controls computers and communications networks. In addition, specifications were written and released for shielded rooms, CAMAC crates, fiber-optic cable, and other standard Antares components.

Union Carbide Corporation's Oak Ridge Y-12 Plant made significant improvements in the quality of surface finish and figure of large single-point diamond-turned mirrors. At Harshaw Chemical Company, Solon, Ohio, 45.7-cm (18-in.) NaCl windows were forged, and the optical quality of their large salt windows was improved significantly.

Finally, the Los Alamos development program on large mirror positioners was completed. Their development was especially important because of the large number needed and because of the total cost. The Los Alamos positioners were designed around flexures (rather than gimbals) that hold the mirrors from behind, thereby accommodating the close-packed arrays characteristic of the Antares beams.

A two-phase contract was awarded to Pittsburgh-Des Moines Steel Company (PDM) at the beginning of FY-79 for target vacuum system design and procurement. The fixed-price ($4.5M) contract was awarded on the basis of cost and technical compliance with the specifications. The 1300-m^3 system requires that the vacuum pumping units be cryogenic, self-contained pods. On the basis of preliminary design reviews, PDM was allowed to procure long-lead-time materials and components before final design review by DOE, scheduled for mid-August 1979.

We were disappointed that the buildings will not be completed on schedule. The most recent projection for beneficial occupancy of the entire facility is November 15, 1979.

CO_2 LASER TECHNOLOGY

We successfully built and tested a retropulse isolator suitable for a CO_2 oscillator-amplifier system. The isolator is based on absorption of the retrodirected energy by a dense plasma created at the focus of a specially configured spatial filter. The plasma is initiated or "seeded" by the trailing portion of the forward-going pulse, and is driven to high density by the retropulse itself. Up to 33 dB attenuation was observed for the retropulse.

Our work with solid-state saturable absorbers based on substitutional dopants in alkali halide hosts continues to be encouraging.

For very short pulse laser fusion applications of phase conjugation by degenerate four-wave mixing, the response obtained for the conjugation device may differ considerably from steady-state predictions that have appeared in the literature. Accordingly, we have developed a transient theory for this process. Our results indicate that extreme pulse-shape distortions are possible in the transient response of degenerate four-wave mixers.

We continue to improve our understanding of gas-phase isolator systems, which, at present, are the most successful means of isolating CO_2 laser systems from parasitic oscillations. Particularly interesting are the effects of buffer gases, which are used to speed up absorption relaxation, and the effects of varying input

pulse duration on ultimate saturation that can be obtained with SF_6-based isolator mixtures.

We are studying angular and frequency multiplexing as a means to extract multipulse energy from CO_2 laser amplifiers, which would permit conversion of a significantly higher fraction of vibrational energy stored in the gas into laser light. With our conditions, the angular multiplex technique increases both the energy extracted and the efficiency by more than fivefold. Problems of parasitic oscillation can also be mitigated by the multiplex approach.

The suitability of copper and salt optical surfaces in a high gain laser facility has been assessed for two distances each from the centers of microexplosions of two pellet designs with and without gas protection by xenon or argon. Under these conditions, salt optics are unacceptable without gas protection, except for the weakest pellet effect at the longest distance, but copper mirrors appear to be acceptable under all conditions.

TARGET EXPERIMENTS

We have departed from exploding-pusher-type targets to adiabatically compressed targets because they are energy efficient and offer the best hope for scalability to ignition conditions. Using thick-walled spherical targets, we have shown that absorbed CO_2 laser light can be coupled efficiently to the fuel. Fuel densities of approximately 20 times that of liquid deuterium have been achieved, and simultaneous fusion yield and time-history measurements have matched those predicted, confirming the adiabatic behavior of the target.

We demonstrated that increased coupling of energy into the fuel is obtained by proper preparation of the target surface. Energy loss caused by fast ions and lateral transport is small, or at least manageable.

Initial experiments demonstrated that x-ray backlighting will be useful for examining hydrodynamic stability and breakup of pusher shells—essential information that could not be obtained previously.

MILITARY APPLICATIONS

Experiments with our Nd:glass laser system have confirmed that useful information can be obtained concerning equation-of-state parameters of unknown materials in the 10-Mbar pressure region. For known materials, the results of experiments agree well with calculations when the properties of the laser irradiation system are known and included. Useful opacity data can also be extracted from experiments.

TARGET DIAGNOSTICS

A development program for instruments essential to accurate diagnosis of laser-heated and imploded targets is producing equipment that incorporates significant advances over previous designs.

Because a large fraction of the absorbed laser energy produces an expanding region of ions, accurate detection can enhance our understanding of the energy partition within the heated region of a target. New developments in plastic ion-damage-track detectors are being incorporated into our diagnostics. Measurements of the total amount of laser light absorbed by a target are of continuing interest, as are the time dependence and target dependence of such absorption. We are developing accurate techniques for these studies at each CO_2 laser facility.

Because the most direct measure of fusion output is the neutron yield—which, in some target designs, may be kept low—accurate, sensitive neutron detection is essential. We have developed new integrated yield measurement techniques that increase dynamic range and sensibility, and new recording techniques for various instruments will lead to accurate and rapid data acquisition and retrieval.

X-ray imaging diagnostics are essential for the diagnosis of nearly every type of laser target. Pinhole cameras, x ray microscopes, and imaging spectrographs are all used in our experiments, and we have continued to extend their wavelength response and resolution. We have developed detailed deconvolution techniques to relate actual source distributions to observed images. We should soon have temporally resolved one-dimensional x-ray images of CO_2 laser-heated targets.

High-energy x-ray measurements typically suffer from large background contamination and have been notoriously poor sources from which to derive a suprathermal-electron temperature. A new K-edge system of detectors, recently developed, should remove much of the background problem and provide accurate spectral data in the 25- to 200-keV region.

As we advance to more complicated target geometries, radiochemical diagnostic materials within an implosion system will become increasingly important. Their use in diagnostics depends on retrieval of a significant fraction

of the disassembled target debris. Improved collectors have demonstrated 12% efficiency, which is adequate for our purposes.

THEORETICAL STUDIES—PROGRAM SUPPORT AND DIRECTION

Advances were made in all four sections of our theoretical group. Target design effort for Helios experiments included two-dimensional studies of effects of asymmetry on the 20-times-liquid-density experiment and parameter studies on exploding-pusher targets to test the physical model in our design code. Also, target design codes were converted to run on the much more efficient FTN compiler in preparation for their conversion to the CRAY-1 computer. In addition, a new ion beam deposition package was added to allow more reliable calculation of ion-beam driven targets.

We obtained important new results in supporting physics, which will affect future target designs. Because of a more detailed understanding of the hot electron generation mechanism, we have concluded that the source is, indeed, very close to a Maxwellian, which verifies the basic assumption used in our target designs. A clear understanding of the physics involved in the observed low level of stimulated Brillouin scattering for CO_2 laser light has also been achieved. Detailed modeling of the electron transport processes has shown that, in one dimension, either density structures are the only effective transport inhibiting mechanism or the fundamental transport equations of Braginskii are not valid. The degree of inhibition possible seems to be larger for lasers of shorter wavelength.

Theoretical support was also provided for investigations of saturable absorption optimization, multiple pulse extraction, and optimization of advanced CO_2 laser systems (discussed in detail in Sec. III).

LASER FUSION TARGET FABRICATION

Characterization of laser fusion targets has improved in several areas. We developed a simple method of determining the composition and pressure of gases inside glass microballoons (GMBs) and significantly improved the sensitivity of our microradiographic techniques. We developed methods of studying mechanical properties of GMBs at elevated temperature and found a higher strength retention than expected; we also produced extremely smooth (≤ 0.05 μm), transparent plastic coatings on GMBs. We are manufacturing x-ray diagnostic GMB targets filled with nonpermeable gases by a drill, fill, and plug (DFP) technique that uses a dye laser to drill 1- to 3-μm-diam holes in the glass shell. Development of the cryogenics for the target retraction mechanism in the Helios installation is essentially complete.

FEASIBILITY AND SYSTEMS STUDIES

Inertial confinement fusion (ICF) reactor design studies continued. Investigations of high Z gases as barriers for x rays in conjunction with magnetic protection of cylindrical reaction chamber walls led to the development of a numerical code that solves the governing differential equations and thus models cavity phenomena.

We have developed an ICF reactor blanket that offers a promising alternative to the lithium blanket. It is more compact, yet delivers a similar fraction of fusion reactor energy release at high temperature and achieves a similar tritium breeding ratio. The concept involves pressurizing the liquid lithium enough to prevent boiling, although 1 atm at 1600 K is sufficient, we selected a design pressure of 30 atm to match the blanket pressure and the process stream pressure of our most promising bismuth sulfate cycle for hydrogen production by water splitting. Our new high temperature concept also offers the possibility of more efficient electric power generation.

As part of our investigations of fusion fission applications of ICF, we performed an engineering feasibility study for a low power density fissile fuel factory. We demonstrated a structurally feasible, remotely refueled and maintained, lithium cooled, modular spherical cavity blanket system in which maximum fissile fuel is bred and sufficient tritium and electric power are produced to operate the plant.

Because the production cost of advanced technology electric power will be dominated by capital cost recovery and debt servicing, capital cost projections are essential for any cost estimation. In a joint project with an outside firm, we have developed a capital cost data base for laser fusion reactors so that comparisons with other technologies can be made.

In conclusion, steady progress toward our goals was made during the first half of 1979. The most significant demonstration was that of efficient coupling of CO_2 laser light to the fuel. We met on schedule the important milestone of compressing the fuel to a density 20 times that of liquid deuterium.

I. CO_2 LASER PROGRAM

(J. P. Carpenter, J. S. Ladish)

Research and development on high-energy short-pulse CO_2 lasers began at Los Alamos in 1969. The Single-Beam System, designed in 1971, began operating in 1973 and was phased out in November 1977. Two large systems now operating are Gemini and Helios. Gemini will ultimately generate pulses of 2 to 4 TW for target-irradiation experiments. Helios began operating in April 1978 and surpassed the design goal on June 21, 1978, with an output of 10 kJ at a power level of ~20 TW. In July 1978, we began target-irradiation experiments on Helios. Compression of fuel to a density more than 20 times that of liquid, the first important event in Helios, was achieved in June 1979. The third system, Antares, is in the design and prototype stage. This system, described in Sec. II, will generate laser pulses of 100 to 200 TW, with the objective of demonstrating scientific breakeven.

GEMINI LASER SYSTEM

Introduction (J. P. Carpenter)

The following target experiments were performed by the Gemini system during the past 6 months.

1. Neon spectra experiments to compare with Helios data
2. X ray emission efficiency tests
3. X ray shadowgraph experiment
4. Electron emission from needle target studies
5. Retropulse protection measurements
6. Target contamination studies
7. Target shots with target chamber backfilled with high Z gases
8. Calorimeter damage-threshold tests
9. Time resolved thermal transport experiments
10. Vega and Mira target studies

Of the 513 shots made for these experiments, 82% produced the desired energy with no measurable prelasing or prepulsing.

Laser Performance and Diagnostics (J. J. Hayden, J. McLeod, D. Hebron)

One of the two NaCl windows on the south-beam target chamber gas cell has been replaced with a wedged NaCl window because reflection from the wedged window permits measurements of the complete output pulse with no second-surface interference.

The internal saturable-absorber gas cell has been tested hydrostatically and will be installed during the first quarter of FY 80. This cell will house the deformable recollimating mirror and should allow the delivery of ~1 TW onto a target.

The small-signal gain diagnostic channel has been installed in the optical diagnostics shield room.

Oscillator-Preamplifier System (V. Romero, E. Coffelt)

The smoothing tube, switched-out oscillator, and two preamplifiers were assembled for use in the new front end, and initial testing has begun. This front end will replace the existing system with minimal downtime during early FY 80.

During the past 6 months, more than 5000 shots were fired by the existing front end for diagnostic trigger tests, system alignment, and target experimentation shots.

Computer and Control Systems (S. Hackenberry, P. Castine)

Design of the upgraded computerized control system is complete. This system will monitor the timing of 20

events during the firing of the entire Gemini system.

The hardware for a shot-number display system to be installed on the Gemini main floor nas been received. This computer-controlled system will automatically display the current shot number with 15.25-cm (6-in.)-high numerals.

A new radio-based public address system has been purchased for the Gemini building, which will also serve as a means of intercommunication between Gemini personnel.

The electronic network analysis program NET-2 was extensively used to simulate malfunctions in the pulse power capacitor banks. In one instance the technique located a malfunctioning spark gap before serious damage occurred.

HELIOS LASER SYSTEM

Introduction (J. S. Ladish)

During the first half of 1979, the primary objective of Helios was to maintain a target irradiation capability in the 3 to 5 kJ range, consistent with our overall plan to complete the facility.

As Helios operations become more routine, facility work is directed more toward improving reliability and systems operations. This is reflected in a separate subsection on Helios operations that summarizes system performance during this period.

Helios has achieved worldwide recognition as a unique fusion laboratory, as evidenced by the ever increasing number of requests for interviews, information, motion pictures, and tours. More important, however, is the wealth of *new* and significant data that have extended our understanding of laser plasma interactions.

In the next few years, the burden of proof that CO_2 is a viable laser fusion driver for energy use rests almost exclusively on the Helios system and its experimental program.

Operations (J. S. Ladish)

As Helios approaches full operational capability, overall system performance and operational parameters are becoming increasingly important. Although this transition is not fully complete, the operational aspects of the Helios system have developed sufficiently to deserve special note.

During the first half of 1979, the Helios system was fired 259 times: 86 times (≃33%) in support of the target experimental program, and 173 times in support of system development and/or maintenance. About two of every five workdays were shooting days with the remaining three days devoted to facility work directed toward completion of the system, modifications of system hardware and software to improve reliability and/or facilitate operations, and routine maintenance. A view of the target insertion mechanism inside the Helios chamber during diagnostics installation is shown in Fig. I.1.

The system can now routinely deliver a maximum energy of 5 kJ in an 0.8-ns pulse (FWHM) to a target at a system shot rate of about once per half hour. The limitation of on target energy is self imposed by our desire to minimize the electrical stress to which the power amplifier modules are subjected, and by target amplifier parasitics that require a saturable absorber, which results in a reduced energy output. These conditions have not been corrected because our highest priority is to conduct the target irradiation program without unnecessary delays.

During the next 6 months the primary *operational objectives* are to increase system reliability to reduce downtime between shots, to develop a realistic maintenance schedule, to provide a reasonable inventory of items essential to operation, and to develop an operational team (or teams) whose sole function will be the operation and maintenance of the Helios system at a defined operating point.

Fig. I.1.
Target insertion mechanism inside Helios Chamber during diagnostics installation.

Objectives such as increasing the energy on target or characterizing the beam intensity at the focal spot will be addressed by investigators who are not members of the operational team.

Front End (R. Carlson, R. Quicksilver, M. Weber)

During this period, priority was given to installation and checkout of the simultaneity system.

Initial measurements made with the beam simultaneity system indicate a round trip optical attenuation of ≃5 to 20×10^4, depending upon which beam line is used. These measurements have been performed with the triple-pass amplifiers (TPAs) evacuated to a few torr. The 40-MHz modulated signal received by the HgCdTe photovoltaic detector produced ~ 35 to 140 μV (rms). This signal is increased to ~ 5 to 20 mV (rms) by a low noise-tuned rf preamplifier. The signal-to-noise ratio under these conditions is greater than 500:1. The electrical noise of the system has been reduced to the thermal noise of the 50-Ω terminations in the system. The signal to glint ratio (glint: any ghost reflection in the system) of the system can be increased to greater than 500:1 by removing the SF2 spatial filter pinholes in the front end. The SF3 spatial filter pinholes and beamsplitters are the next predominant sources of glint in the system; careful alignment of these items improved the signal-to-glint ratio by another factor of 4. When trying to achieve stable phase readings with a jitter < ± 0.1 (< ± 2.5-ps resolution), we discovered that a stray reflection from the mode-matching telescope of the alignment laser system was causing a laser-modulator interaction, which produced erratic phase readings of several degrees. This condition has been resolved by tilting one of the mode-matching telescope lenses. Repeated measurements taken over a 3-day period gave path-length errors using beam line 4A as the reference as shown in column A, Table I-I. First-order path-length corrections to beam lines 1A, 2B, and 3B were made and results are shown in column B. All measurements contain a path-length error of ±0.5 cm. The effects of day-to-day beam alignment on the reproducibility and accuracy of the beam simultaneity system will be studied during the next 6 months. These preliminary results indicate that our goal of adjusting all eight beams to within ±1 cm can be met easily.

Improvements to the front-end system to achieve long-term reliability included the following.

- Dual trigger units and power supplies have been installed on preamplifiers 1 and 2.
- New controls have been installed for the oscillator (including an improved plasma-tube current regulator), for preamplifiers 1 and 2, and for the laser preamplifier gas-flow system.

TABLE I I

PATH LENGTH ERRORS FOR EIGHT HELIOS BEAMS

Beam Line	Path Length Error (cm) A Before Adjustment	B After Adjustment
1A	-3.5 ± 0.5 cm[a]	-1.0 ± 0.5 cm
1B	0.5	−0.5
2A	-0.5	−0.5
2B	+2.5[a]	-1.0
3A	1.5	−1.5
3B	-2.5	−1.0
4A (reference)	0	0
4B	−0.75	−0.75

[a]Path length is shorter than the reference; i.e., pulse arrives earlier.

- Covers have been installed around the oscillator, saturable-absorber cells, and periscope mirror stand to protect the optical elements from the environment.
- An improved switchout with mode-matching telescope and vacuum stations for the plasma tube and the gas cell of saturable absorber 1 have been designed.
- Pockels cells of wider bandwidth have been built for the improved triple-switchout assembly.

Laser Physics (G. T. Schappert, D. Casperson, R. Haglund, J. Busse)

To increase the energy on target in Helios, we have made parasitic threshold measurements with Hartmann aligned targets at the focal plane. When we saw that the reentrant beam tube at the entrance to the TPA was coupled to the target and was lowering the stability threshold, we removed all eight beam tubes from the power amplifiers. Although the threshold for the onset of parasitics was thus raised substantially, we discovered that the severe attenuation of the oscillator pulse passing through the full length of the saturable-absorber cell resulted in a degraded temporal pulse shape: both the rise and fall times of the pulse were increased, resulting in reduced peak power.

Our discovery that the output pulse from the Helios TPA had lengthened after removal of the beam tubes prompted us to investigate the transmission of Mix 907 at powers ranging from 10 to 200 MW/cm^2, using the nominal 780-ps pulse (FWHM) from the Helios front end. Measurements were made in a 120-cm-long cell, with calorimeters measuring the input and output energies. Results are shown in Fig. I-2. We concluded that the first-pass attenuation of the pulse in the TPA gas cell is severe enough to reduce the drive pulse below the saturation level on the first pass, thus contributing to a lengthened tail on the pulse after three passes through the gain medium.

We have not measured in detail the transmission of multiline pulses in the absorber or possible changes in pulse shape after the pulse traversed the gas cell.

As a result of the transmission measurements, we considered it important to establish a new operating point for the TPAs with beam tubes out. A series of parasitics studies showed that the saturable-absorber pressure in the TPA gas cell could be reduced to 12 torr at a pulse-forming network (PFN) change voltage of 50 kV without sacrificing machine stability. This change increased the energy output by 8-10% and reduced the pulse length from ~900-950 ps to 800-850 ps. A half-size beam tube has been designed and is being tested for the tradeoff between parasitics threshold and temporal pulse degradation.

TPA output-beam uniformity was also questioned and measurements were made in amplifier 4A with an array of seven 2.54-cm (1-in.) Scientech calorimeters sampling the 35-cm-diam aperture. The calorimeters were placed behind holes in photographic burn paper in an attempt to qualitatively calibrate the nonlinear response of the burn paper to the output pulse of the TPA. A photograph of a typical burn pattern showing the location of the calorimeter sampling holes is presented in Fig. I-3. The distribution of energies recorded for a typical shot is shown in Fig. I-4. The results indicate that the inherently low- and high-gain regions of the TPA yield output energies that differ by as much as a factor of 6; however, six of the seven sampled energies differed by only a factor of ~2. Detailed gain uniformity measurements are being planned.

The first experiments with optical multiplexing in a Helios TPA have been completed. Two oscillator pulses separated by 60 ns were injected into amplifier 4B. The 30 Gallery West diagnostics channels were adjusted and calibrated to measure the individual energy output for the two pulses. The results showed that the energy in the second pulse ranged from 30-40% of the energy in the first pulse. Note, however, that the (3:1:4:1) laser gas mix was not optimized for multiple-pulse energy extraction and that further increases could be obtained with longer pulse separation. These experiments were performed to advance understanding of gain recovery in

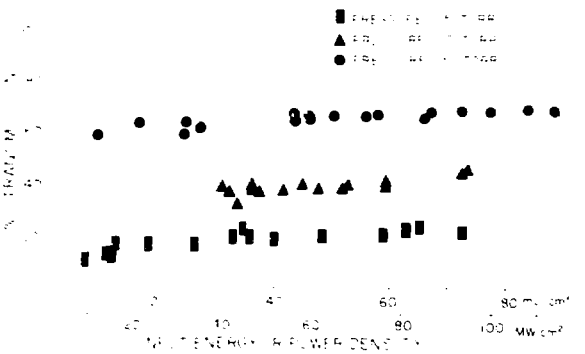

Fig. I-2.
Large signal transmission curves for saturable-absorber Mix 907 at several pressures.

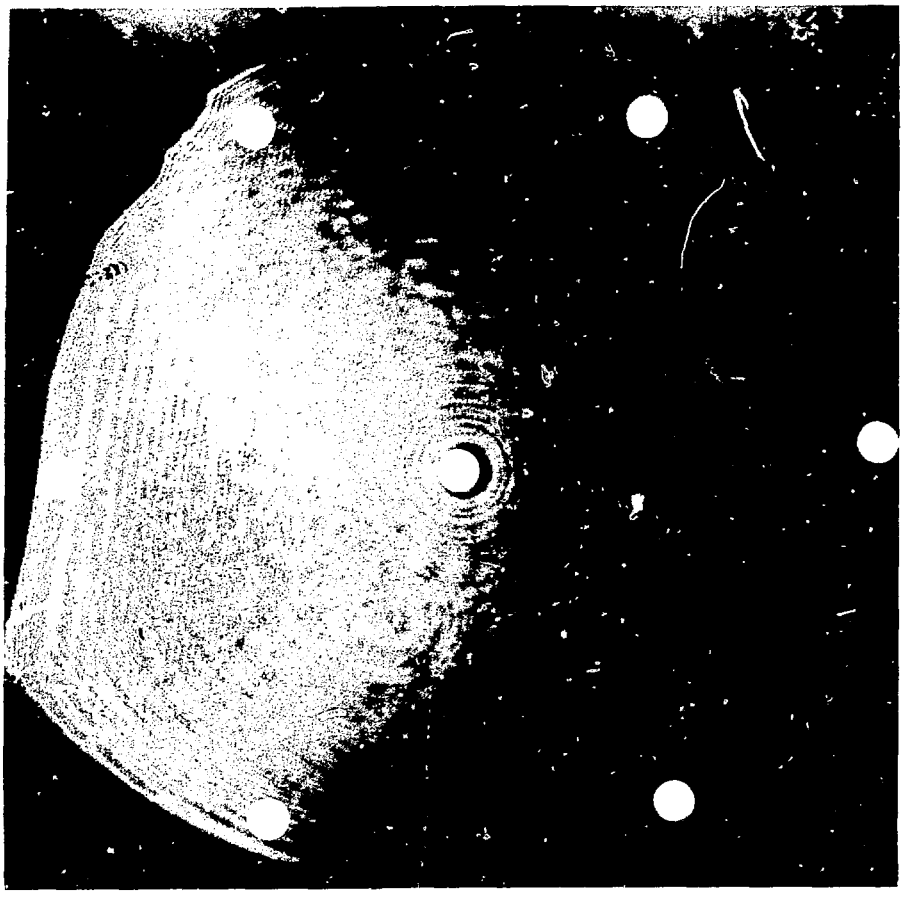

Fig. I-3.
Burn pattern of energy distribution on beam line 4A measured at the output of the TPA. The anode is to the right. Calorimeters were placed behind the seven holes shown in the photograph.

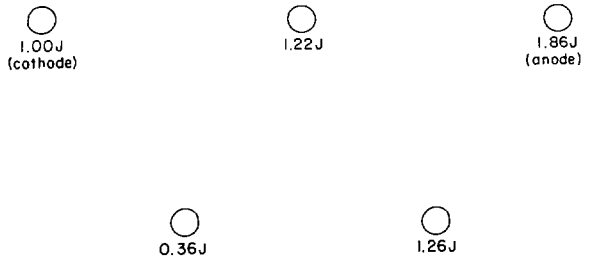

Fig. I-4.
Energies recorded by 1-in. Scientech calorimeters for the shot shown in Fig. I-3. Amplifier conditions were e-beam at 60 kV/stage; gas pressure at 1800 torr.

the amplifier, although measurements of the recovery time in the saturable-absorber cell will be required to obtain more quantitative results. Such measurements are being prepared.

An experimental plan was proposed and partially completed for measuring the parasitics threshold of copper-jacketed GMBs—the prototype targets for the radiochemical (Rad Chem) measurements. All tests were carried out at a PFN change voltage of 50 kV and an electron-beam change voltage of 55 kV. The following thresholds for the onset of parasitics were observed (expressed in terms of Mix 907 pressure required for TPA stability).

GMB Target	Stability Threshold (torr)
250-μm	10
250-μm with 1-μm Cu jacket	9
250-μm with 1-μm and 10-μm CH coating	11
250-μm with 1-μm Cu and 40-μm CH coating	10

These rather surprising results indicate that the copper-coated targets pose no TPA stability problems. This experiment should be completed in July.

The Perkin-Elmer chromatograph purchased for laser-gas analysis arrived in late May, and was installed and calibrated. The composition of the saturable absorber in Helios is being monitored by this chromatograph. Batch-to-batch composition of Mix 907 appears to be reproducible to within ~ ±5% of the specified partial pressure of individual components. Comparison of the chromatography results with spectrophotometer measurements indicates that such a small variation is not detectable in our ir-transmission measurements.

Controls (E. L. Jolly, M. D. Thomason, W. Kelly, J. Sutton, F. D. Wells, W. Hanna, K. M. Spencer)

The control tasks accomplished during this period fall into three broad categories of programming, computer hardware, and control hardware. Significant results are listed.

Programming.

- A BASIC language system was installed on the computer system. BASIC is a simple language and should be a helpful addition for the part-time or beginning programmer.
- Our short-pulse energy extraction code was converted to run on either the S/200 or the S/230 computer system. Major changes were required because of double-precision arithmetic in some key calculations and because of new plot routines.
- The front-end data-collection LINES program was rewritten so that histogram scanning and percent line strength calculations are performed automatically; a manual recalculation option is also available.
- The front-end line content and switchout timing measurements were placed into the HELIOS computer program. To accomplish this, a new overlay was created and added to the program.
- Several programs were written to develop the capability of data transmittal from Gallery West to the main computer. This included writing a routine for converting the CC-8085 floating-point format to a Data General floating-point number. We can now test Gallery West for readiness; determine the location of data in memory; and request transfer, receive, convert, and display data.
- The encoder counting algorithm for the mirror position display was investigated, and modifications in the encoder counting software resulted in an algorithm that correctly counts the stepping motions of the mirror mounts. Several minor modifications in the display-chassis software improved the operation of the system.
- Two operating systems for the dual processor system and two new macrocommands for initializing the computers were written. Documentation and diagnostic listings for the new S/230 computer were sorted and organized. Routines for control and testing of the input/output bus switch were written. One of these routines has been added to HELIOS to test the state of the input/output bus switch before a shot is fired.

Computer Hardware.

- The new S/230 computer was received and installed. The terminal interface boards were modified to allow the use of Tektronix 4000 series terminals.

- Some minor computer problems connected with the dual processors S/200 and S/300 were resolved.
- The dual processor system is now in routine use.
- The HELIOS operations code, run on both machines, demonstrated that useful work can be performed on one machine while the other is involved in Helios firing operations.

Control Hardware.

- Six optical encoders were installed on the two target-mirror mounts associated with beam line 4A. This equipment operates satisfactorily, and accurate counts are recorded for any motor stepping rate up to 400 steps per second. Additional encoders will be installed on the remaining 14 target mirror mounts at a convenient time. The encoder CPU chassis was mounted near the target chamber; however, the display chassis was installed in the control room. The fiber-optic cables that connect these two units were also installed.
- Installation of new bulkhead feedthrough connectors and cables for the mirror-mount drive motors of the power amplifiers was completed.
- Recurring switch problems in the keyboards of the Model 200 beam positioners caused us to replace both keyboards in the control room with more reliable units. Construction of a new chassis for the beam positioner equipment is ~50% complete. One beam positioner module was installed in this chassis and another is to be installed. The wire wrap boards and LED displays from the existing units were installed in this chassis, along with new keyboards. In addition, optical isolators were installed in the control-cable circuits to the experimental area to eliminate potential ground loops in the existing wiring. This work should be completed during the next 6 months.
- A complete review of the mirror-mount controller circuits caused several minor changes to be made, including the addition of circuits to clear all registers to 0 when power is turned on, and the incorporation of logic that allows only the entry of the target chamber-mount addresses. These modifications were installed and tested in the portable controller and will be installed in the control-room chassis during periods when the unit is not required for beam-alignment operations.
- An optical isolation unit was installed to reduce noise and ground-loop problems between the screen room and the control room. Isolation eliminated previous noise problems in the digitizers housed in the computer screen room.
- A shutter control system has been installed to facilitate alignment and beam simultaneity measurements. The system provides remote control of eight shutters to block the eight beam paths and two shutters to block the oscillator and CO_2 alignment laser. Information on shutter positions is displayed and monitored. One remote controller is located in the front-end room and the other in the control room. During firing of the laser, status and control information on the shutter system is relayed to the computer via CAMAC.
- A system was designed to control the oil flow among the four pulse-forming-network tanks, two storage tanks, an oil purifier, the main building, and an external tanker truck.
- To facilitate the mixing of gases for the saturable absorbers, an automatic controller was designed to mix 10 gases, each with a separate partial pressure set point. This automatic system will be fabricated and installed during the next 6 months.
- A fifth control chassis was added to the TPA side-arm pressure-control system. This chassis is located in the control room and permits manual or computer control.
- The front-end oscillator, preamplifier, and laser-gas controllers were redesigned, the appropriate modifications were made, and the improved versions were installed.
- The optical trigger receivers that trigger the electron-beam pulsed-power supplies were redesigned to reduce their susceptibility to EMI and to improve their maintainability. A prototype was constructed and is ready for testing.
- A new main control console was installed in the Helios control room. The new console is larger and was designed to improve the man-machine interface. The additional space provided by the new console will be used for the Helios television monitor system.

Mechanical Assembly and Engineering (E. L. Zimmerman, B. Maestas, D. Martinez, J. Valencia)

A major engineering effort in Helios was directed toward mechanical improvements that will increase system reliability and improve maintainability. Considerable work went into the redesign of various optical components and covers, and into upgrading the entire system. In addition, a new TPA saturable-absorber beam tube was designed and built, and various diagnostic platforms were fabricated.

Major mechanical tasks completed during this reporting period include

- installation and testing of the first composite foil window consisting of 0.05-mm thick aluminum bonded to 0.05-mm-thick kapton;
- installation of two pumping-chamber cable termination oil troughs modified to prevent oil spills;
- installation of metal work platforms at both input and output ends of all dual-beam modules;
- installation of a higher capacity target-chamber air blower and filter system;
- installation of rupture disk pressure-relief devices on all amplifiers;
- relocation of the helium, nitrogen, and carbon dioxide gas storage tanks; and
- installation of a remote-control shutter at the input of each TPA.

Helios Laser Beam Diagnostics (I. Bigio, S. Jackson, C. Smith, S. Caldwell, R. Ainsworth, H. Reisch)

Six of the eight channels for total energy detection were calibrated; calibration will be repeated every 6-12 months, or whenever new ar-coated salt windows are installed on the target chamber. Current calibration factors are shown below.

Channel	Target Chamber Salt Window Coated	Calibration Factor (J/mV)
1A	no	0.954
1B	yes	1.77
2A	yes	1.63
2B	yes	1.65 (estimated)
3A	yes	1.65 (estimated)
3B	no	0.958
4A	yes	1.57
4B	yes	1.72

Electrical problems encountered in the prepulse measurement were solved and four additional prepulse (3Q) channels were installed in the screen room. The following laser parameters can now be monitored.

- Total energy - all eight beams
- 3Q ratio (i.e., the ratio of energies in prepulse, main pulse, and postpulse) - five beams
- Temporal pulse shape - two beams
- Front end energies - all four beams
- Front end spectral content

A grating spectrometer was constructed to measure the spectral line content on one Helios main beam. Installation awaits mechanical redesign, already under way, and reassembly of the 3Q and pulse shape diagnostics into a modular system to provide space in the screen room for the spectrometer.

A retropulse channel was installed on beam line 2A to measure the amount of laser light reflected from the target. To date, only relative energy measurements have been performed; we expect to obtain absolute values for reflected energy after an energy calibration of the channel.

The Gallery West screen room was expanded by ~20% to make room for additional 3 GHz oscilloscopes needed for temporal pulse shape measurements.

Several programs were written for the Gallery West 8085 microcomputer substation to permit communication between the 8085 and the main Helios Eclipse computer. Data from Gallery West are being transmitted to an Eclipse background routine, which will soon be incorporated into the main Helios operating system.

Optical Systems (J. Hanlon, V. K. Viswanathan, P. Bolen, R. Parnell)

The optical systems tasks accomplished during this period include improvements, listed below, in the Helios optical transport and alignment system, continuation of the CO_2 adaptive-optics study, and changeover to coated salt windows and the infrared microscope.

- All Helios optical components from the first beamsplitters in the front end to the entrance to the TPAs were removed, checked as mounted in the Optical Evaluation Laboratory interferometer, cleaned, remounted using three-point support, rechecked in the interferometer, and then reinstalled and realigned. In most cases, we obtained a noticeable difference in the optical figure of the mirrors.

Of the 52 mirrors tested and remounted, 32 improved in optical figure, 6 became worse, and 14 remained unchanged. In general, the three-point mounting returned the mirrors to the free-standing state. A log containing interferograms of each component in each beam line has been started.

- A new automatic alignment parallel-sequencer controller was designed and installed. This system will increase the reliability of the automatic-alignment system and will allow greater flexibility in beam alignment.
- The orthogonal autocollimating telescopes were removed from the target chamber to determine ways to improve the image contrast. An optical evaluation of these systems showed that one telescope system was very good ($\sim \frac{1}{4}\ \lambda$ distortion after a double pass at 6328 Å); the other telescope system had to be replaced. Several illumination schemes for projecting the telescope reticle were tested and new autocollimator illuminators for the target autocollimators were installed. These changes permitted us to mount the autocollimator lamp outside the target chamber and to remove the beamsplitters that were being damaged.
- New masks for the autocollimating Hartmann target alignment scheme were installed on Helios and oriented to improve the return Hartmann pattern. The pyroelectric vidicon camera tubes were also oriented so that all the return patterns move in the same direction for similar target-chamber optical motions.
- Modifications to six of our nine pyroelectric vidicon cameras resulted in significant improvements; the modified cameras now cause very few problems during target shots. The remaining three cameras will be similarly modified at a convenient date.
- Eight single-sided coated salt windows 38-cm (15-in.) diam were installed on the Helios system. Fifteen windows (eight double-sided, seven single-sided) remain to be installed.
- The first adaptive-optics mirror system was received from Rocketdyne. Some initial testing of the system was performed, but final evaluation awaits an experimental determination of the Helios optical-beam quality to ascertain whether the Helios system aberrations can be corrected by this adaptive-optics scheme. In preparation for these tasks, a 110.6-μm Smartt interferometer plate was perfected to measure Helios beam quality and to evaluate the performance of the Rocketdyne adaptive optics.
- Final detailing of the mechanical parts for the infrared microscope is complete, and the system is ready for fabrication.

II. ANTARES—HIGH-ENERGY GAS LASER FACILITY

(T. F. Stratton, J. Jansen)

The High-Energy Gas Laser Facility (HEGLF) with its Antares CO_2 laser system is a Department of Energy line-item construction project aimed at building a 200-TW CO_2 gas laser for the investigation of inertial confinement fusion. We believe that scientific breakeven—a release of thermonuclear energy from D-T reactions equal to the laser energy incident on a target—is within reach of this machine.

INTRODUCTION (T. F. Stratton, J. Jansen)

Antares will be operational early in 1984. Antares experiments will address the wavelength scaling of pellet physics and the coupling efficiency of 10-μm radiation to targets at energy and power levels that are an order of magnitude higher than those available from Helios. We expect to achieve significant thermonuclear burn and to study laser matter interaction processes under physical conditions near ignition.

The delivery of long-lead-time laser hardware was on schedule, but building construction was significantly late (only 65% complete). Delivery of pressure shells for the first two power-amplifier modules and the first electron-gun vacuum vessel was expected in early July 1979. Because construction was so far behind schedule, we prepared a special experimental facility in another area to receive, assemble, and test electron guns as they arrive. Assembly of the power-amplifier pressure vessels was postponed until mid-October because the Laser Hall was not complete. We will occupy the building during construction on a joint-occupancy basis so that we can assemble the first power amplifier unit.

Maxwell Laboratories, Inc., was awarded the contract to design and build 24 Marx generators that will drive the power amplifiers. Design work started in January and assembly of the first unit began in June 1979.

Large optical components and mirror positioners were improved during the last 6 months. Union Carbide Corporation's Y-12 plant significantly improved the quality of surface finish and figure of large single-point diamond-turned mirrors. Harshaw Chemical Company began production of the forgings for the 46-cm-diam NaCl laser windows. We designed, built, and tested large mirror positioners that rely on flexures (rather than gimbals) to hold the mirror from behind, thereby accommodating close packed arrays. The design also reduces the total cost of fabrication of these components.

OPTICAL SYSTEM (A. Saxman, Q. Appert, W. Bauke, C. Bjork, R. Bjurstrom, D. Blevins, R. Cutler, J. Goldstein, W. Miller, J. Munroe, W. Reichelt, C. Silvernail, J. Sollid, T. Swann, W. Sweatt, P. Wolfe)

Introduction

The Antares optical system interfaces and subsystems for beam alignment and diagnostics are being designed. The preliminary analyses and designs of the prototype subsystems are complete, and final design details of subsystem components are being drawn. Many of the required hardware items are available locally or at Los Alamos.

To facilitate an organized integration of the optical subsystems into the Antares laser, much of the early prototyping and evaluation is being done in a beam detector evaluation laboratory and in a mockup of an Antares single-sector beam line.

Optical Systems Analysis

Tolerance Analysis. The integrated optical-system requirements for the power-amplifier assembly and optical-element placement tolerance have been established. By selecting tight tolerances for movable mirrors and fixed elements, we were able to increase the tolerances

for the power amplifier assembly and the placement of elements.

Error Budget and Component Quality. An improved equation for the surface of the target-system focus mirrors has reduced the reflected beam wave-front error from $\lambda/7$ to $\lambda/70$ rms (10 μm).

Beam Scattering by Mirror Microfinish Characteristics. A study to describe the beam scattering caused by microfinished surfaces predicts that a 2 μin. rms surface (6 μin. peak to peak) scatters 0.4% of a 10.6-μm beam, so that six single point diamond turned (SPDT) mirrors per beam line would scatter 2.4% of the energy. If the microfinished surface can be held to 1 μin. rms, the scatter at 10.6 μm would be 0.1% per mirror. A profilometer measurement of the surface of two 8 in. SPDT flats cut on the Moore machine at the Y-12 Plant showed the actual microfinish to be less than 0.7 μin. rms over 0.15 in. increments, although there were some 2 μin. rms regions over 0.5 in. sample lengths. Production mirrors will soon be available for evaluation.

Optical Code Development. Most of the interferometric data reduction code, FRINGE III, was installed on a computer. The basic interferogram digitization and data reduction parts are fully operational. The result is a very fast and usable method for evaluating optical components and subassemblies. Guidelines for Antares mirror interferogram reduction procedures are being determined and analyzed. Inaccuracies introduced by operator imprecision and digitization errors, automatic data reduction codes, and program shortcomings are being evaluated.

The Antares optical beam lines from the front-end amplifier drivers to the target are being modeled on the ACCOS ray tracing code. The optical characteristics of any of the 72 beam line sectors can be calculated by including the optical sensitivity to mirror tilts, beam decentrations, wave front quality, obscurations, incident compound angles, mirror figure, component transmission, reflections, and beam divergence.

Optical System Engineering

Power Amplifier and Target System. The power amplifier relay optics and the periscope mirrors were verified for position and function. The spatial coordinate positions, compound angle tilts, and exact geometric shape and dimensions of the target-system optical components were detailed.

Parasitics and Retropulse Protection.

Calculation of Target-Induced Parasitics in Antares. The absorption of energy by a fusion target due to the growth of parasitic oscillations between the target and an Antares power amplifier has been re-evaluated. The computations reflect anticipated values of operating parameters of the laser system as well as an improved calculational method. The results are shown in Fig. II-1.

The inset shows the time-dependence of the net gain length (at a frequency corresponding to the center of the P-20 line of the 10 μm transition) of one azimuthal segment of a power amplifier. The location of the static

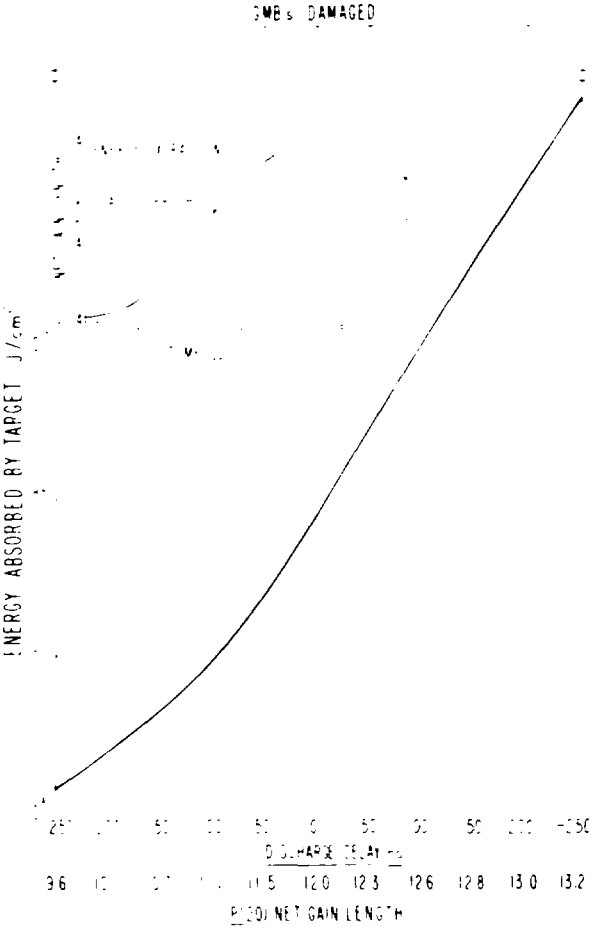

Fig. II-1.
Target absorption of parasitic oscillations.

parasitic-threshold gain-length product (g_oL) and the short-pulse energy-extraction g_oL (needed to yield 100 kJ in a multiline nanosecond pulse) are marked. The energy density at the target focus is shown in the larger graph. If the initiation of the amplifier discharge is on time (zero time delay), the energy density at the focus up to the time of arrival of the main pulse (when the amplifier's g_oL value is 12) is $\sim 6 \times 10^{-7}$ J cm^{-2}. If the discharge is initiated earlier (negative time delay) or later (positive time delay) than the nominal timing (due to statistical fluctuations of the high voltage switching system), the amplifier will reach a larger or smaller g_oL value, respectively, when the short pulse is injected into it (we assume a fixed short pulse injection time relative to the time the oscillator pulse is switched out). The resulting energy density at the focus will be correspondingly larger or smaller than for the nominal timing case.

As in previous calculations, the amplified spontaneous emission due to all high gain lines of the 10 μm transition (P 12 to P 24 and R 12 to R 20) are included (the 9 μm lines have lower gain and do not contribute significantly to the total absorbed energy); the finite linewidth of all lines is also included.

GMBs are known to damage at 0.1 J cm^{-2}. We conclude from our calculations that if the pulse energy extraction is late by no more than 250 ns, the prepulse energy density on target will be less than 0.001 J cm^{-2}, two orders of magnitude below the damage threshold. By meeting the established jitter specification of ± 100 ns about a predetermined pulse energy extraction point, we will ensure that the target is not damaged.

Gemini Retropulse Experiment. The Gemini retropulse experiment was completed. A discrepancy between computer model and experiment indicates that the model is conservative. Two possibilities being considered to explain the discrepancy are (1) the formation of a standing wave in the laser beam near the overlap mirror due to interference of the incoming and reflected laser beams and (2) the presence of particulates in the laser medium, which lower breakdown thresholds and increase absorption. Both mechanisms occur and reduce the retropulse transmission through the overlap region.

Mirror and Mirror Positioner Design and Assembly.

Mirrors. Production of periscopes and rear reflectors continued. The target-system focusing mirrors have been designed and drawn. Two different focusing mirrors (inner and outer) will be required. Each beam array will have eight outer and four inner mirrors.

Holes for alignment buttons have been added to Periscope 2 and to the back-reflector mirrors. Final drawings on periscope and back reflector mirrors were issued and the first lot of periscope substrates have been delivered to the plater.

Mirror Positioners. A new design of the drive nut for the actuator screw incorporates a Teflon lining to simplify manufacture and reduce friction between the nut and the screw. Fabrication is easy because lapping of the nut is eliminated and friction torque of the actuator is reduced to about one third of the available torque. This design will be used for the Optical Test Bed (OTB) positioners. The prototype that was built and tested is shown in Fig. II.2.

Switches that indicate tip and tilt travel limits were incorporated into the positioner design.

The design for the manually adjustable large mirror positioner uses the basic flexure mechanism in the standard tip tilt positioner and a new differential screw to actuate the face plate. Prototype parts are being made in our shops and production drawings have been prepared. Parts for motorizing the differential screw are being made. This motorized differential screw drive is being considered for an alternative lower cost drive for the motorized positioners.

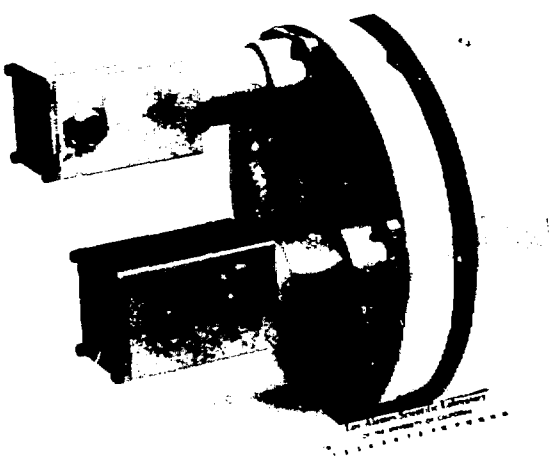

Fig. II.2.
Antares large mirror mount positioner.

Optical Component Evaluation

Optical Analysis. Thermal tests on the Antares prototype periscope mirrors (large 40.6 cm wide trapezoids) were completed. When the flat mirrors were cooled to the design temperature, they became convex; they became concave when heated above the design temperature. Measurements indicate that the mirror figure changed by $\lambda/3$ at 10 μm per kelvin for a few degrees about the design temperature.

Optical tests on these mirrors indicated that the three-post mount to be used throughout the power amplifier and target chamber introduced no measureable distortions. These test results indicate that the beam quality of Antares will be limited only by the optical figure attained in the fabricated parts.

Thermal Mechanical Analysis. Tests on the Antares standard large mirror positioner demonstrated a thermal drift of 0.9 arc s per Kelvin. These results were better than those obtained from small commercial mirror positioners.

Requirements of small mirror mounts for the power amplifier are met by the mechanical and thermal properties of the Oriel 17774 mount.

Beam Alignment

Manual Alignment. We have collected data on the stability and repeatability of our optical tooling instrumentation (scopes, supports, and mounts), and the expected tolerance range in which we can maintain the master data for the optical systems.

This work was performed under controlled conditions in our Optical Evaluation Laboratory (OEL). At present, we are refining the experimental setup to measure thermally induced movements (errors) in the manual alignment equipment.

Automatic Alignment. Work continued on the procurement of parts for the OEL full-size mockup of one sector of an Antares beam line. Design of various stands and mount assemblies for the installation of Antares hardware is complete. Fabrication of these items was begun and some components were delivered. Optical components procured included the alignment laser beam expander and the back reflector flip-in sensor. Designs for the periscope-carousel assembly, the polyhedron alignment sensor, and the front end alignment sensor were completed.

An analysis to establish the requirements of the telescope for an alternative imaging see-through alignment system is complete. The range of focus and resolution requirements for an alignment telescope were established; a telescope will be procured for test and evaluation with the OEL beam line.

Testing of various prospective detectors continued. Each centering detector being tested fulfills the centering sensitivity requirements determined for the Antares beam alignment system. The next phase of testing will establish the type of electronic interface that will fulfill the system control functions of sensors coupled to motor driven units through the local machine interface control units.

Beam Diagnostics

The beam diagnostic interface layout drawings for the power amplifier and target system are complete. The specific diagnostic hardware interfaces are the input beam calorimeter for the power amplifier; the sector input calorimeter; the diagnostic spool full power calorimeter, the low power, full beam sampling calorimeter and power detector; and the retropulse calorimeter.

Diagnostics

The first of three aluminum frame diffraction-grating prototypes was wound with 20-μm-diam gold-plated tungsten wire. The optical performance of the diffraction grating is affected by wire diameter, spacing, and stagger (flatness of the strung plane). To maintain control over this process we designed an alignment jig, which supports the aluminum frame and maintains the wrapped wire plane within 8 μm. Our goal was 25 μm maximum. The main source of error in wire spacing was eliminated by redesigning the fixture support bearings in the wire wrap machine. This improvement ensured that we will be within our prescribed limit of ±51 μm in axial spacing. Figure II-3 illustrates the diffraction grating, alignment jig setup, and wire-wrapping fixture.

The wire diffraction gratings will sample the output beams of Antares by diffracting a small fraction of the total output energy to calorimeters located in the turning-mirror chambers. A single properly designed calorimeter can record the energy of the 12 beams producing the output from a power amplifier. The diffraction gratings are inexpensive and relatively easy to

Fig. II 3.
Antares wire diffraction grating.

fabricate. Their principal flaw is the 6% energy penalty (3% geometric, 3% diffraction). This loss in the beam can be compensated for only if the output NaCl windows are antireflection (ar) coated.

Recent projections of the cost of ar coated salt windows for Antares led us to reconsider beam sampling by Fresnel reflections from wedged, uncoated output windows. Properly wedged (~18.89 arcmin) and oriented, the windows serve the same function as the transmission gratings by refracting a beam sample to the calorimeter in the turning-mirror chamber. Analysis showed that the wedge affects system performance only slightly in one-band operation and is easily compensated for by a wedge in the see through alignment system is ultimately selected for Antares. The system loss for grating sampling is 8%, compared to 6% for ar-coated output windows or 14% without coating. Consultation with Harshaw Chemical Company revealed that finishing the windows with a wedge to the required tolerances was relatively easy and that the finishing cost would be less than the fabrication cost of the gratings. Therefore, we intend to sample the output beams from Antares with wedged, uncoated output windows. Further development and testing of the wire diffraction gratings will be discontinued.

Outside Contracts

Single Point Diamond Turned Mirror Development at Y-12. Preproduction runs of spherical mirrors indicate a production figure of ~4 μm rms and a finish of ~2.0 μin. peak to valley (p-v). First time yields are 84%. Preliminary preproduction runs of large flat mirrors indicate a surface figure of ~5 μin. rms and a finish of 2.0 μin. p-v. Quality and cost data are summarized in Table II 1.

Hughes Research Laboratories. Hughes Research Laboratories completed Phase III of the target chamber alignment system study by evaluating the optical design and application of adaptive optics to the HPGSL system. The contractual tasks included a conceptual design of the target system beam alignment system, a

TABLE II 1

QUALITY AND COST
OF LARGE CO. OPTICS
(1000-cm² APERTURE)

Component	Surface Finish	Surface Figure	Cost ($k)
NaCl Window Unmounted, Uncoated	60-40 Dig-Scratch	1 Fringe Visible ($1/30\lambda_r$, 10μm)	27
Coated			35
Metal Optics (Copper)	≤2 μin. p-v ($1/20\lambda_{p-v}$, 10μm)	4-μin. rms ($1/10\lambda$rms 10μm)	3

ray trace and diffraction-sensitivity analysis of the Antares beam focus pattern on a target, a diffraction analysis of the Hartmann-mask beam pattern as used in the Helios system and projected possible uses in the Antares system, and verification of our calculations of the target system's 72 mirror position coordinates and corresponding beam directional and spatial coordinate parameters throughout the target system.

FRONT END SYSTEM (W. Leland, E. Foley, M. Kircher, C. Knapp, D. Swanson, G. York)

Prototype Front End

The one beam prototype activities consisted of procurement, installation, and checkout. The driver amplifier is complete, but a successful performance test must be made by the manufacturer before it is shipped. The final preamplifier (a Lumonics 602) was checked for gain, gain uniformity, and short-pulse amplification with triple pass on axis Cassegrain optics. Gain and gain uniformity met specifications. Parasitic oscillations occurred at the threshold that was predicted by diffraction feedback calculations. The parasitics have been suppressed completely with the saturable absorbers designed for that purpose. A multiline output of 4 J—twice the design-point value—in 1 ns was obtained. These tests used the complete beam-line optics up through the Lumonics output. The remaining beam line from the Lumonics preamplifier to the driver is in place but lacks a few optics in a spatial filter. Plans for fiber-optic links and computer controls were formulated and are being implemented. Equipment for beam diagnostics has been acquired to permit characterization of the one-beam front end.

Antares Front End

The Antares front end is a sixfold copy of the prototype front end, with a different oscillator. The Antares design calls for six cw oscillators tuned to desired lines. The six beams pass through a switch attenuator complex, allowing pulse shaping by individual amplitude and/or turn-on-time adjustment. After shaping, the six beams are combined and amplified to 1 mJ/ns and passed through a final switchout to control the total pulse length and to enhance the contrast ratio. Detailed design of the Antares oscillator is complete (Fig. II-4) and procurement was initiated.

POWER AMPLIFIER SYSTEM (R. Stine, G. Allen, J. Bickford, W. Gaskill, W. Miller, G. Ross, R. Scarlett, W. Turner, B. Weinstein, N. Wilson, E. Yavornik)

A model of the six Antares power amplifiers installed in the Laser Hall is shown in Fig. II-5. Each power amplifier is 16 m long and has a diameter of 3.7 m.

The primary achievement during this reporting period was the fabrication of hardware. The large support stand for the first power amplifiers is complete and ready for delivery. The second stand will follow in about 2 months.

Fabrication of two spacer spools and two pumping chambers was also completed. Six additional pumping chambers are being fabricated and will be delivered about 2 months after the first set. The large end domes are also being fabricated.

The electron gun vacuum shell was machined and welded. The completed unit is 1.5 m in diameter and 7.3 m long. The coaxial feed bushing (Fig. II-6) was tested electrically to 900 kV, 50% over the normal electron-gun operating voltage.

Pumping Chamber

Electrical Design and Testing. Life-testing of a solid anode bushing has been completed with satisfactory results at voltages up to 900 kV. We are studying the design to determine whether cost and complexity can be reduced. A model of a double tapered design has shown that it will remove all the air during insertion of the cable, which suggests that this may be an alternative to the more complex versions.

A prototype dielectric divider has been cast and will be tested in the prototype power amplifier.

Mechanical. Fabrication of the pumping chamber and spacer spool sections for the first power amplifier is proceeding well. Two of the four pumping chambers are completely machined, and the remaining two are nearly completed. The spacer spools required for the first two power amplifiers are complete. Figures II-7 and -8 show the units during fabrication.

Eleven electron-gun rail-support plates were ordered, and delivery of five units for the first power-amplifier assembly is expected by October 15, 1979. We have requested proposals for fabrication of our electron-gun support rails and we expect to place the order soon.

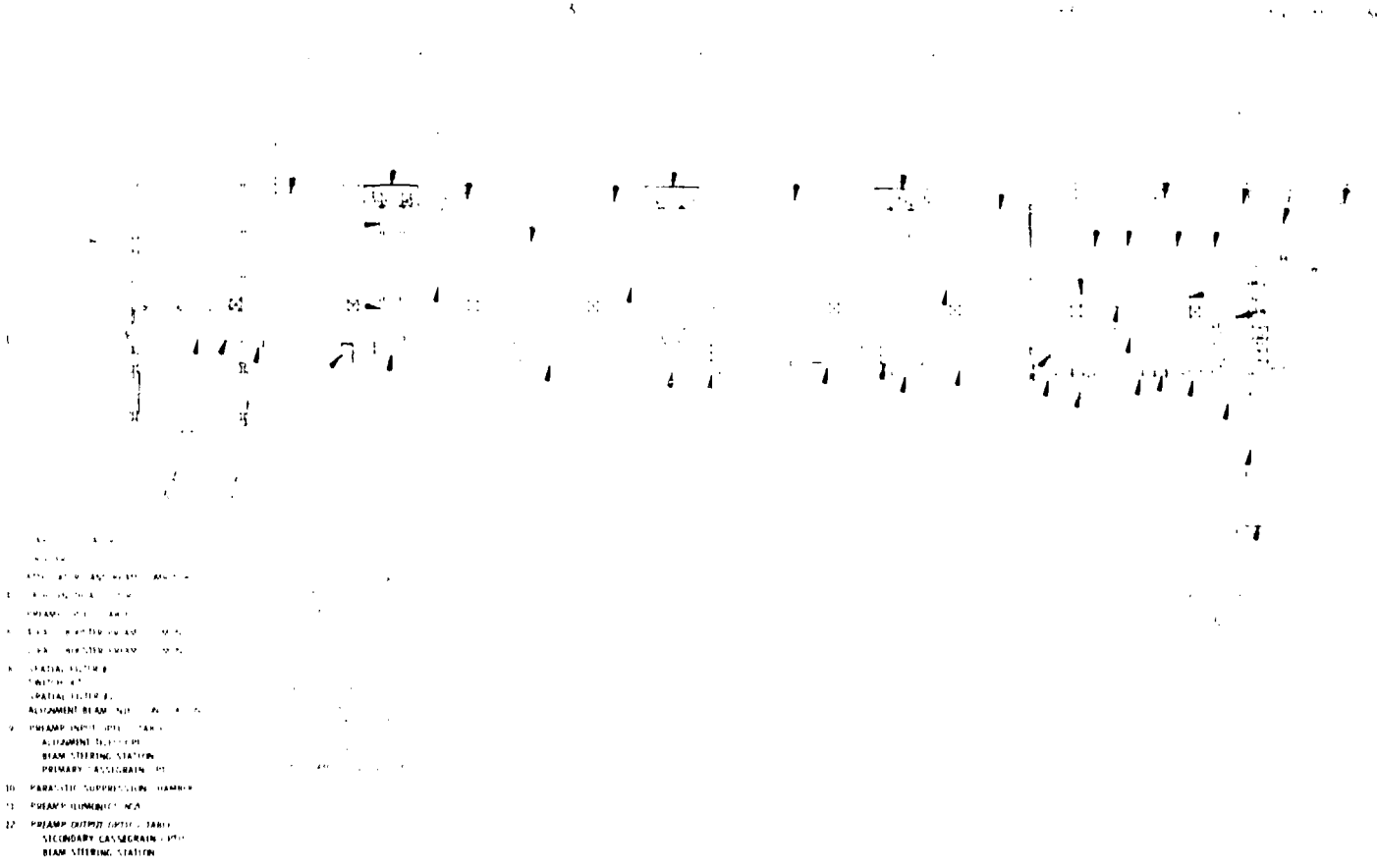

Fig. II.4.
Antares front end room floor plan.

Fig. II 5.
Model of the Antares Laser Hall

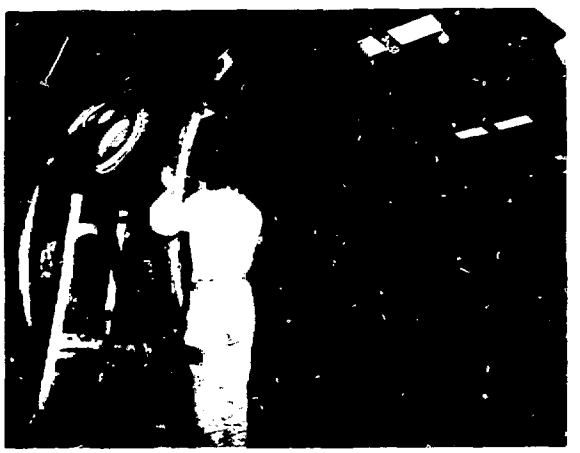

Fig. II 7.
Pumping chamber in fabrication.

Fig. II 6.
Electron gun coaxial feed bushing.

Fig. II 8.
Spacer spool being fabricated.

Fabrication of the redesigned salt window domes and of the back reflector dome and shell combination is ~50% complete. We expect delivery of the first units by November 1, 1979.

Design of the remaining optical shell sections is complete. Fabrication drawings for the In Out optics access, shell, dome, and diagnostics sections are being released for procurement.

Electron Gun

Electrical Design and Testing. The required building modifications to the Electron Gun Test Facility (TSL 85) are complete. A computer system for electron gun testing was received and is being checked out.

Prototype electron gun testing has continued. We tested a spark cathode developed by Systems, Science and Software (S^3). Data evaluation is not complete, but the spark cathode performs at least as well as the conventional tantalum blade cathodes.

Mechanical. Four machined electron-gun vacuum vessel sections were welded successfully by using a pulsed-arc, tungsten, gas-shielded method. Figure II 9 shows three sections set up in the pulse-arc welding jig. The completed assembly after welding was straight

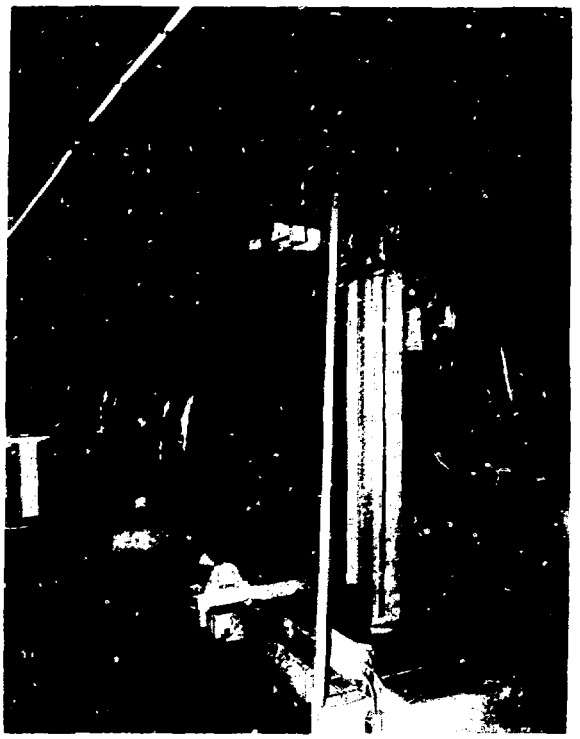

Fig. II 9.
Electron gun vacuum vessel in the welding jig.

within 0.81 mm over its 7.32 m length. Welding of the machined sections into one completed assembly was a critical achievement in fabricating the electron gun vacuum vessel.

Three electron gun vacuum spools were fabricated and are being machined. Our first coaxial feed bushing was received and vacuum tested. We also received two electron gun support bushings for the first electron gun assembly.

We have obtained well bonded joints with polyurethane and epoxy resin, and are using both materials in the fabrication of titanium foil electron gun windows.

Hardware for the cathode grid assembly is ~35% complete. Tooling for perforating the 1.22 m long stainless steel sheet is complete. All cathode components made by spinning are complete, and the copper plating process for the aluminum detail pieces was developed.

Gas and Vacuum Subsystem

The control requirements for electron-gun vacuum system tests were defined. A prototype for Antares was designed, fabricated, and checked out. The prototype consists of several commercial machine-control units and read-out devices integrated into a unit subsystem by a hard-wired relay controller. The controller was designed for maximum operational flexibility to facilitate checkout of the electron-gun vacuum system and allows manual control of each vacuum pump and valve in the subsystem, with adequate interlocking and sequential logic to prevent operator-initiated faults. The controller design also has provisions for future computer-control attachments so that the electron-gun vacuum system can be used as a test and debugging facility for computer hardware and software. The first-generation electron gun vacuum system control software has been written but not debugged.

An LSI 11 microcomputer with two floppy disks, an RT 11 operating system, and the OMSI-Pascal compiler were acquired for use with this system. Fiber-optic links and interface modules are being designed and will be used during the electron-gun checkout.

Evacuation of the electron gun will be accomplished by a 3500 ℓ/s turbomolecular high-vacuum pump assembly backed by two 26-ℓ/s dedicated rotary vane mechanical pumps. This apparatus, arranged in two modules is assembled and ready for testing. All high vacuum components to be mounted on the electron gun are assembled in a two-section frame, one section of which is adjustable in height to permit installation in the bottom of the electron-gun vacuum spool. The mechanical pumps are assembled with required manifolds on a relocatable base plate for ultimate installation on the north wall of the Laser Hall in the area set aside for vibrating machinery.

We completed a control console for electron gun testing, which permits remote manual or computer-interfaced operation. All required functional system controls and monitoring are provided. Insofar as possible, all components are those that are to be integrated into the Antares systems.

Design layout of the power-amplifier roughing manifold and the laser gas-fill and pressure-relief systems is in process. This equipment, which will be integrated into the Laser Hall vacuum system, is being arranged so that piping will be mounted on the power-amplifier support

stands at locations that do not interfere with cables or other systems. Where possible, manifolding will be modularized to permit preassembly and testing at other locations before being installed on a power amplifier. The Laser Hall vacuum system, composed of a 1200-ℓ/s ROOTS blower and 250-ℓ/s mechanical vacuum pump, is fabricated and ready for preshipment testing.

A Vacuum System Evaluation and Test Laboratory is now equipped with a high-vacuum, dynamic, outgassing-rate test chamber. This chamber, large enough to accommodate individual assembled mirror-mount drives, is being used to measure the outgassing rate of electrical connectors and stepper motors, as well as of anodized and bare metal surfaces. Painted metals and nonmetallic components, wires, and small assemblies will be tested as they are identified. Initial measurements show that outgassing rates as small as 5×10^{-7} torr/ℓ/s can be determined. Measurements performed on electrical connectors show that connectors containing plastics and rubbers are 50 to 500 times higher in outgassing rate than connectors of metal-glass/ceramic construction. Three connector manufacturers have submitted sample connectors, typical of those necessary for Antares, that exhibit acceptable unit outgassing rates of $\leq 3 \times 10^{-6}$ torr-ℓ/s.

Handling Equipment

Electron-gun handling equipment designs are nearly complete. An off-loading cradle for the electron-gun grid was designed and fabrication drawings are ready for release. Design modifications were made to the low-boy fixture and fabrication is under way.

A fabrication order for the cathode carrier fixture was placed. We received the electron-gun vacuum vessel off-loading cradle. This unit is critical to the handling of the extremely long vacuum-vessel weldment.

Air compressors for the Electron-Gun Test Facility have been selected and will be used to operate the air casters on the electron-gun handling fixtures.

Optical Support Structures

All mirror mounts contained within the Antares power amplifier are supported on three basic frameworks; back reflector, relay, and In/Out support structures. Our designs are complete and manufacturing proposals are being obtained. The large aluminum plates for these items were ordered.

In conjunction with the optical support frame design, we prepared detailed designs for the small optical mounts that interface with these structures. Kinematic mirror mounting methods used in these optical components were prototyped and tested for their effects on distortion. No measurable mirror distortion due to mirror mounting could be discerned by standard interferometry.

Support Stand

Fabrication of the first Antares power-amplifier support stand was completed in June 1979. Figure II-10 shows the completed assembly undergoing Los Alamos optical inspection at the manufacturing site. Weldments of the second stand (Fig. II-11) are complete and being readied for stress relieving.

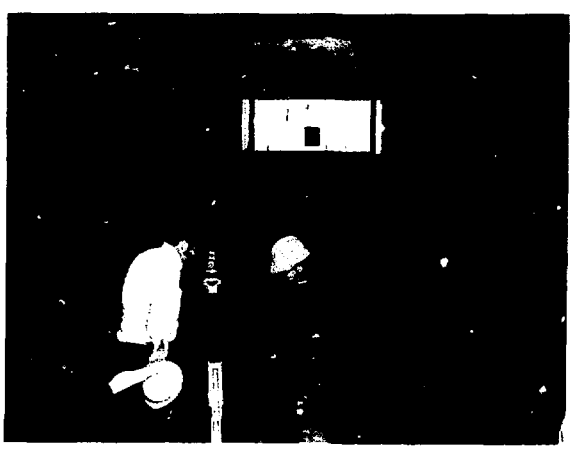

Fig. II-10.
Support stand inspection.

Fig. II 11.
Support stand weldment.

ENERGY STORAGE SYSTEM (K. B. Riepe, G. Allen)

Gas Pulsers

A firm fixed-price contract was awarded to Maxwell Laboratories to deliver 25 Marx generators, storing 300 kJ each at 1.2 MV. Design work was begun in January 1979. The first milestone is a 2000-shot performance test that will determine whether the design will meet specifications on inductance, jitter, and prefire rate, and will determine design changes that will improve reliability.

Testing of the Los Alamos prototype gas pulser continued. Jitter was measured by using a fiber-optic-coupled single-turn magnetic loop and a digital time counter. Jitter was ~15 ns, with either liquid or solid Carborundum charge and trigger coupling resistors, and a 160-kV trigger Marx. Prefire rate was ~0.01 when the gaps were operated with a safety factor of 2. When air filters with 10-μm mesh screens were installed on each spark gap, the prefire rate decreased to 0.002 (1 prefire in 550 shots)—a significant improvement. Internal tracking of the spark-gap insulators after ~200 shots was evident. Equalizing the flushing-air flow by connecting the spark gaps in series increased the life to ~500 shots, which is still not adequate. The air system was changed again so that a separate air line leads to each spark gap from a manifold outside the tank. The gaps are flushed for 0.5 min at ~4 ℓ/s per gap, which gives about five gas changes. This system has performed in 500 shots without problems.

Electron-Gun Pulser

The specification for the electron-gun pulser was set at 600 kV with 72 kJ stored. This requires 4 μF at 60 kV for a stage. The largest qualified capacitors are rated at 2.8 μF, 60 kV. We asked Aerovox Corp. and Maxwell Laboratories to fabricate and test two capacitors each and to qualify them for use in the gun pulsers. The tests were made and the results are being evaluated.

Power Supplies

A letter of agreement was signed with Universal Voltronics Corp. for the dc charging supplies for the Antares energy storage systems. Delivery of the first units is expected in September 1979.

TARGET SYSTEM (P. Wolfe, J. Allen, W. Sweatt, N. Wilson, V. Zeigner, C. Cummings, R. Day)

Highlights

The target vacuum system (TVS) design was completed by Pittsburgh-Des Moines Steel Co. (PDM) and approved by Los Alamos. Components are being procured and structures fabricated in preparation for installation this fall. Basic design of the target-chamber space frame was also completed and DOE approval was obtained for final design and fabrication by PDM as part of their target-vacuum-system contract. This arrangement simplifies the specification of the space frame and yet ensures attention to important, subtle TVS interfaces.

Optical Train

All turning, folding, and focusing mirrors have been defined as to size and shape (and focal length, in the case of the parabolas), and final drawings are complete. The configuration now incorporates a slight (0.16°) outward radial tilt of each focusing mirror, to minimize astigmatism on target due to convergence of the incident beams at the parabolic arrays. Diffraction calculations on the new short-focal-length system show that the Antares specification of 80% of energy in a 400-μm-diam circle will be easily met.

Target Positioner

This device, also called the target-insertion mechanism, performs all the functions connected with the introduction and handling of fusion targets in the target chamber. Design constraints are now sufficiently determined to permit detailed layout work to proceed. Key constraints and requirements are listed below.

- To establish a point in space that is routinely relocatable to ±5 μm. This is the primary reference point for the Antares beams, the target, and all alignment devices.
- To position secondary laser alignment devices to within 5 μm of the primary reference location.
- To translate the target in three orthogonal directions within 1 mm of the primary reference location in steps of 1.5 to 2.8 μm.
- To operate at a pressure of 10^{-7} torr without introducing particulates or condensible contaminants.
- To remain usable after single shot yields of 4.5×10^{14} neutrons originating at the target, on a schedule of 2 shots per week.
- To change a target (through an air vacuum lock) in 20 min.

The target positioner is being designed and developed in two stages: (1) a prototype device, patterned after the Helios positioner, is to be completed for use with the first full single beam tests of Antares; (2) the prototype will subsequently be upgraded to a final version for use in routine fusion experiments. The upgrading will correct any deficiencies that appear in the prototype, add features for processing cryogenic targets *in situ*, allow targets to be filled with helium, and make it possible to change targets remotely (from the control room).

A completed design layout of the structure that supports the target positioner in the target-chamber space frame is being analyzed for vibrational stability. An earlier design had a natural frequency of ~50 Hz, which implied adequate stiffness for the application, but several changes in the space frame and in the manner the support structure will be attached require that the analysis be repeated. We expect the stability of the new design to be comparable.

Space Frame

The basic space-frame design selected in late 1978 has been carried through several cycles of analysis and modification. Evaluations were made of the static deflections and natural frequencies of the system, and structural members were added where necessary to increase the system stiffness; unnecessary members were removed.

The modified design, with mirrors and mirror-support structures installed, has a natural frequency of 14 to 15 Hz and maximum member deflections under gravity loads of ~1.0 mm. Installation of the space frame into the target chamber will require the firm attachment of the space frame to the chamber. Coupling these two components dynamically will lower the natural frequency of the system to ~12 to 13 Hz. This result should be adequate because the major sources of vibration in the target building operate in the 30- to 60-Hz range with only a few parts providing 15-Hz excitation; natural subseismic vibration, on the other hand, is most energetic in the 4- to 10 Hz range.

PDM will develop the detailed manufacturing design and will fabricate the space frame by an addendum to their contract for the target vacuum system. We supplied the space frame definition package in June 1979 to allow PDM to commence detailed design work. A part of this package is the 1:20 scale model of the space frame shown in Fig. II-12. The model provides insurance against design errors that might arise from the essential irregularity and complexity of the structure.

We continue to analyze in detail the geometry of the system to ensure against the existence of interferences between structural members and optical beams. We are ready to start the detailed design of the supplementary frames that will support the 12 mirror arrays in the space frame.

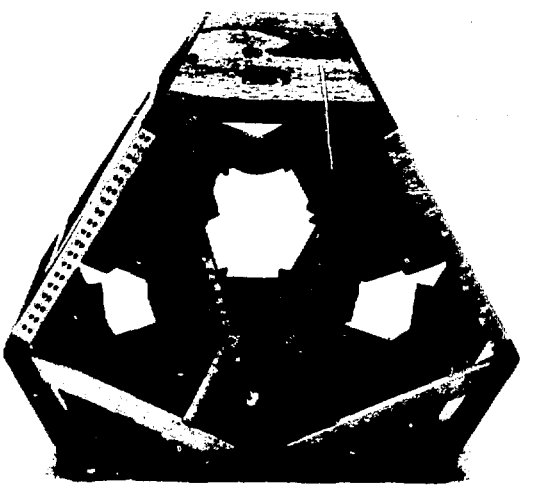

Fig. II-12.
Antares target chamber space frame model.

Target Vacuum System

The structural steel components of the vacuum system have been designed and are in various stages of fabrication at PDM Plants in Provo, Utah, and Des Moines, Iowa. Most of the system design has been approved, and vacuum-pumping-equipment valves and gauges are being obtained by PDM. Detailed engineering of the electrical system is nearly complete and is expected to be approved at the final design review in mid-August 1979. Throughout the project, we held daily discussions with PDM engineers, and attended several two-day interim reviews on selected design areas.

Antares construction was scheduled so that the Target Building and Laser Hall would be ready for PDM to begin field erection of the target vacuum system on August 1, 1979, however, building construction has been delayed. It is now planned to give PDM joint occupancy beginning October 1, 1979, which will still permit the target vacuum system to be completed by late spring of 1980.

CONTROL SYSTEM (M. Thuot, D. Call, D. Carstensen, D. Gutscher, P. Johnson, R. Kirk, A. Kozubal, R. Lindberg, F. Maestas, F. McGirt, S. White)

Control-System Architecture

The control system for Antares is based on a computer network. At the lowest level (controlling valves and relays and collecting data) are numerous microprocessors (LSI-11); PDP 11/34 and PDP 11/60 minicomputers supervise the microprocessors and allow the laser subsystems to be separately installed, tested, and maintained. The entire Antares laser is operated through the top-level computer, a PDP 11/70. The levels of control are shown in Fig. II.13.

Front-End Controls Project

Most of the requirements for the front end control system were determined and specifications are being

Fig. II.13.
Antares control system implementation.

written. Operating sequences have been identified for normal operation. The details of subsystem operation within each sequence have been defined for most sequences. Data definitions and data flow requirements are also being reviewed so that control software can be specified for the front end.

The front end shielded room will be larger than originally planned and will have a plenum floor. A tentative layout of equipment racks and of the control console was used as the basis for determining the overall size and shape of the shielded room.

Laser Hall Controls Project

Beam Line 1 Controls. Antares computer network software will not be completed in time for use on early operations of beam line 1. The control requirements will be met by using several isolated LSI-11 computer systems with software based on that developed by the early support team. Work for Laser Hall controls is now directed toward developing the systems for beam line 1.

Energy Storage Controls. A Marx bank simulator is again in use for software development. The first control of a high voltage system will occur in the Electron Gun Test Facility (EGTF), where the electron gun pulser will be controlled.

Power Amplifier Controls. An LSI-11 computer system will be used to control the electron gun vacuum in the EGTF. Design and assembly of that system are nearly complete. Simulators will be used for development of other vacuum and gas systems.

Timing System Project

The Antares laser requires two timing systems. The central timing system will control all events that occur before the firing of the switchout in the front end and will provide 10-ns accuracy with respect to the beam initiation. The other timing system will be driven by the switchout spark gap and will provide an accuracy of ≥ 1 ns with respect to beam initiation. The second system can only be used to control events that occur after the firing of the switchout.

Antares Controls Hardware Team

EMI Protection. The central control room specification is complete, procurement has begun, and a vendor has been chosen. Other shielded rooms are in the planning stage.

Requirements have been defined for fiber optics and development of the major components is nearly complete.

Machine Interface (MI) Computer Design. System requirements, specifications, and development are all in process. Our design for downline loading of the system and for applications task software over DECnet to an LSI-11 computer is nearly complete.

A test program for LSI-11 components is nearly designed. Component testing will be used for vendors, acceptance-testing of new items, troubleshooting, identification of suspected failures, and confirmation of repairs.

CAMAC Development. The process of specifying requirements for CAMAC modules and equipment is essentially complete. Detailed specifications were written for most items and limited quantities of each item were purchased after competitive bidding. Antares "standards" were established for the CAMAC crate and power supply, the crate controller, and the waveform digitizer.

LSI-11 System Assembly. About 15 LSI-11, RT-11 computer systems will be used in various Antares laboratories outside the control network. The hardware team bought hardware and has assembled seven systems. Others are in process.

Miscellaneous. Requirements for external interfaces to control stepping motors and for analog/digital conversion were documented and design has started. Standard equipment rack requirements and specifications are complete. A console device multiplexer for the Antares computer network was documented and is being built.

HEGLF SITE AND STRUCTURES (J. Allen)

Construction Package 1

As of June 30, 1979, the job was 62% complete (excluding stored material). This is a net gain of 25% for

this report period. The 48% cited in the last report included stored material. Completion is scheduled for February 1980. A joint-occupancy arrangement between Los Alamos and the Contractor will allow power-amplifier installation to start October 1, 1979, in the Laser Hall and will provide warehouse area by August 15.

Laser Building. The structural parts of the walls, roof, and floor are complete. The interior walls are being erected. All crane rails have been installed. The delivery of the overhead cranes may affect the date of joint occupancy by Los Alamos.

Piping and ducting installation is well under way except in the Laser Hall. Lighting and conduit installation has started. Some mechanical equipment and the primary transformers have been installed.

Modifications are being made to add piping, vacuum equipment, and partitions with doors and windows in the front-end room.

Mechanical Building and Passageway. Piping and electrical installation are nearing completion. The roofing is being installed. A room is being added for the target vacuum system control console.

Office Building. The primary structure is complete, and interior walls and ceilings are nearing completion. Ducting and electrical work is nearly complete. Completed roofing was rejected because of moisture content and delamination of the test specimens.

Warehouse. The structure and its fire protection system are complete and painted. A few odd items such as louvers, dampers, unit heater, floor sealer, lights, and electrical connection to the main transformer remain to be installed. Beneficial occupancy is expected by August 15.

Package II

The Target Building walls and roof are complete. Interior walls and equipment piers are being formed and poured. The line of sight instrumentation stations are being erected. Package II is 66% complete.

Building completion is scheduled for December 1979. Part of this schedule delay is caused by dependence of Package II on Package I for its electrical power and its air conditioning system. The target vacuum system contractor will move in October 1, 1979, on a joint occupancy basis.

III. CO_2 LASER TECHNOLOGY

(J. F. Figueira)

Each CO_2 laser system described earlier represents a significant advance in reliable CO_2 laser subsystems, components, and diagnostics. Such advance in the design, construction, and improvements of the systems requires basic support of CO_2 technology. This support has been valuable in the development of subsystems for suppressing excessive prepulse energy, system self-oscillation (involving the study of relaxation mechanisms in bleachable gases), and damaging amplified retropulses; in the identification of passive means to enhance laser beam quality and simultaneously providing automatic target alignment through phase conjugation.

INTRODUCTION

Our work in CO_2 laser technology is directed toward improving the isolation methods available for use on our laser fusion drivers, developing improved means for characterizing and controlling the evolution of CO_2 laser beam parameters during propagation, and developing reliable, moderate scale drivers to facilitate plasma physics and other studies.

Our Gigawatt Test Facility (GWTF) has been used for saturable absorber studies and for some plasma work. To provide suitable facilities for rapid turnaround moderate scale plasma experiments, we expanded the GWTF performance to include a factor of increase in peak power and greater versatility in selecting wavelength and pulse duration.

We are studying infrared phase conjugation because it may substantially improve the quality of our laser beams, and it may provide automatic beam pointing in some applications. It is also being studied by the optical fusion community.

Another area of investigation concerns isolator development, which encompasses several disparate areas of materials study. For example, we study ways to improve existing *saturable* absorbers, including complex gas mixtures and substitutional dopants in alkali halides. These materials provide more efficient operation of our lasers by becoming transparent at high optical intensity, but otherwise remaining opaque to prevent self oscillation. At the other extreme, we introduce in this report the characterization of an *inducible* absorber, which becomes more opaque with increasing optical intensity. This device, based on plasma formation, will be used to prevent intense, amplified retroreflections from damaging sensitive laser components.

We are also continuing our efforts to obtain new laser systems and to improve existing ones. We have gained a better understanding of saturable absorbers and have performed calculations for target induced parasitics in Antares.

Finally, we are addressing the key driver performance criteria (for example, cost, efficiency, reliability, life, and maintenance requirements) of inertial confinement fusion.

GIGAWATT TEST FACILITY (J. F. Figueira, S. J. Czuchlewski, E. J. McClellan, T. S. Kaffenberger, A. V. Nowak)

The CO_2 laser system of the GWTF was substantially upgraded in both performance and flexibility. Two independent beam lines now exist. The components of the previous GWTF were redesigned into a compact multipass amplifier configuration that can produce 1- to 60 ns pulses of line-selectable CO_2 radiation at energies up to 5 J.

To provide subnanosecond operation for plasma physics studies, a second laser system has been added to the facility. This system consists of a high-pressure, multipass, reinjection oscillator (RIO) driving a 3-pass commercial amplifier. The RIO, shown in Fig. III-1, was described in Ref. 1. The beam from the oscillator portion of the RIO is sent to a conventional 3-stage Pockels cell, where a pulse of the desired duration is selected. This pulse is returned to the RIO for four additional passes of

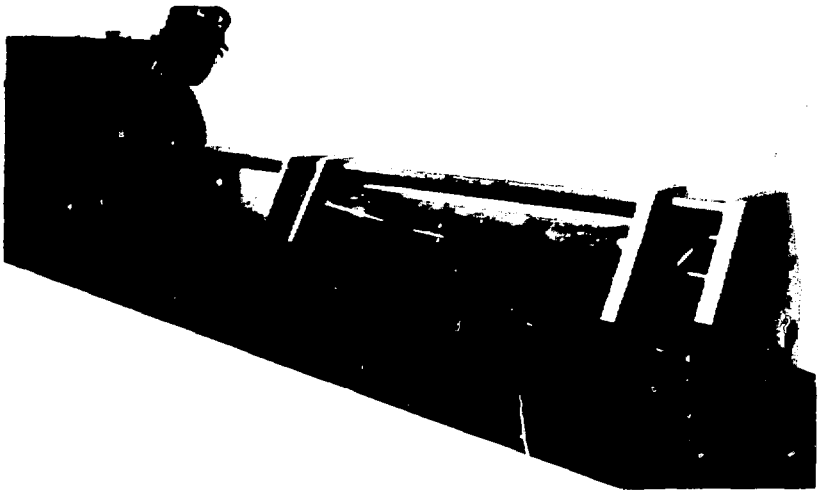

Fig. III 1.
The reinjection oscillator (RIO) consisting of a high pressure oscillator and multipassed preamplifier in a single package. Output power is 0.5 GW. This system is a central part of the upgraded GWTF.

amplification, producing a 1 ns, 0.5 GW, multiline output signal. After three additional passes through the Lumonics 601 amplifier, powers in excess of 10 GW are obtained.

A layout of the entire facility is shown in Fig. III 2. The smaller screen room shown is dedicated to laser system control, whereas the larger screen room provides an experimental environment with a low level of electrical interference. This low level is achieved by good system design techniques, for example, by using fiber-optic links to interconnect the screen rooms.

The experimental area is arranged to handle four simultaneous investigations. An optical bench adjacent to the experimental screen room serves as a switchyard for both laser systems and contains the laser diagnostics for the RIO-Lumonics system. In addition to the areas shown, a vacuum target chamber and screen room are available for plasma diagnostics studies.

System 1 is fully functional and is being used in laser development experiments. The RIO-Lumonics system is being interfaced to the target facility.

RETROPULSE ISOLATION STUDIES (C. R. Phipps, J. F. Figueira, S. J. Czuchlewski, S. J. Thomas)

Introduction

Intense, backward propagating pulses arising from amplified reflections can cause unacceptable damage in high power fusion lasers unless the system is isolated in this respect. Although devices capable of blocking retropulses are well known,[1-11] the situation at CO_2 wavelengths is made more difficult by the lack of such components as Faraday rotators[1] or Stark effect modulators[2] with adequate aperture, damage resistance, figure of merit, and cost effectiveness. For this reason, practical solutions to the CO_2 retropulse problem involve absorption of the undesired signal in an optically dense plasma.

These plasma isolators fall into two categories – those that are essentially passive, where the plasma is created by a portion of the forward going laser beam,[3-8,10,11] and those in which the plasma is created or initiated by an

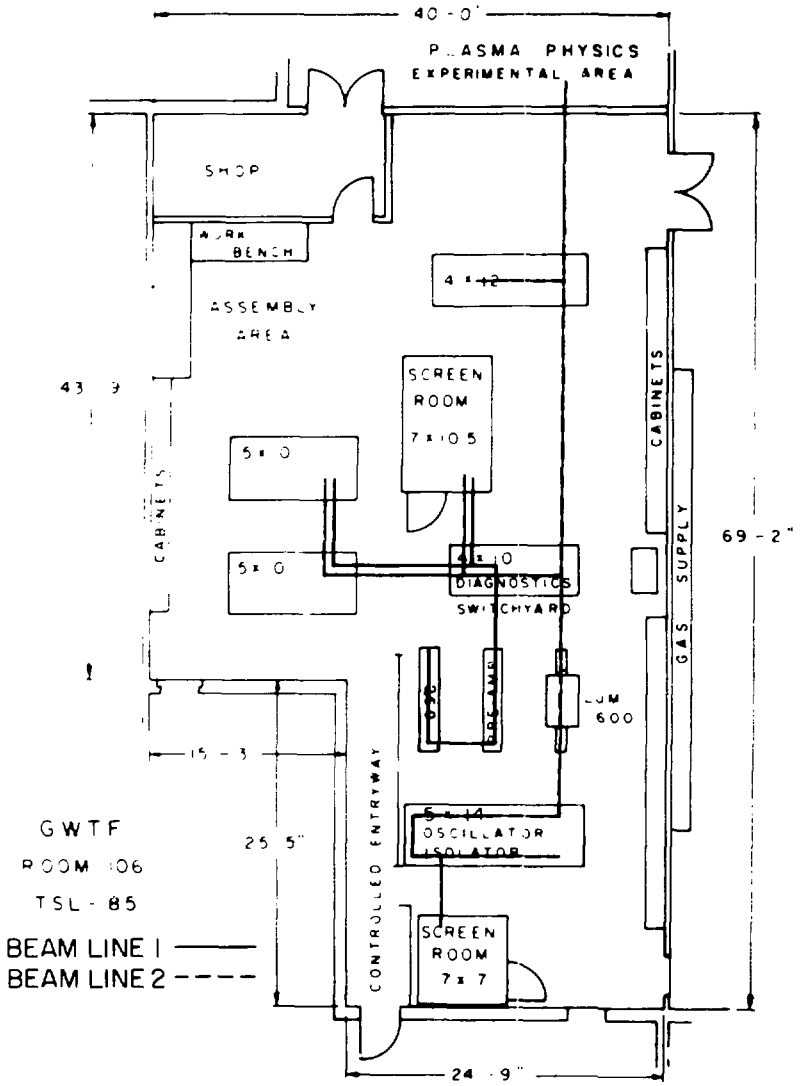

Fig. III-2.
Plan of the upgraded GWTF System 1 (dashed line) and the new RIO/Lumonics laser system (solid line). The experimental areas can accommodate four simultaneous studies.

auxiliary laser or electrical device.[5,6,9] In the former case, the interval between passage of the forward-going pulse and incidence of the retropulse must exceed the plasma decay time. Very specialized isolation methods, such as "blitz" mirrors[4] are not considered here.

Unfortunately, plans to adapt plasma isolators used on Gemini and Helios to other laser systems are hampered by the lack of quantitative performance measurements needed for accurate design scaling. In the references cited, only Ref. 6 presents an attenuation measurement with error bars, or a corresponding incident infrared fluence, and this study considered laser pulses 50 times longer than those of interest to us. For our purposes, the difference between 20 and 40 dB attenuation can be of crucial importance, as are measurements of closure time, operating fluence, operating lifetime, and transmitted beam quality. These measurements will also provide an effective retropulse-isolation scheme for the GWTF.

Because there is no evidence in favor of the active devices, and because operational reliability is required for retropulse isolation, we chose to study only passive devices. For attenuation levels in the desirable range above 30 dB, it was clear from previous work[5,6] that electrical or optical preinitiation is essential. That is, a seed plasma must be present in the region traversed by the retropulse at its time of arrival. In addition, it was obviously important to restrict the optical path in such a way that refraction around the plasma was prevented.

These considerations led us to study the performance of a standard laser beam spatial filter as a retropulse isolator, operating either in vacuum or with a dry nitrogen backfill at pressures up to 590 torr, but with abnormally high focal fluences sufficient to cause plasma initiation at the filter iris perimeter during passage of the forward going pulse.

For such a concept to be useful, an operating point is necessary at which the forward fluence will initiate the plasma reliably without causing undue sacrifice of forward transmission; at the same time, the plasma thus formed must provide substantial attenuation that decays slowly for ~100 ns. We found that these conditions could be satisfied in a highly reliable arrangement, which should be capable of scaling to much higher laser energies than those used in our tests. Typically, we obtained 33 dB reverse attenuation for 2 ns simulated retropulses occurring 120 ns after plasma initiation in a 590 torr background gas, and a figure of merit (the ratio of forward to reverse attenuation) of 22 to 29 dB. This represents adequate performance for many CO_2 system applications.

In this section, we will present the results of a systematic investigation of the interaction of several parameters in the plasma isolator problem, and describe the performance obtained in detail.

Focusing optics that illuminated irises in this study used f numbers from ~10 to ~50. Molybdenum and stainless steel irises ranging from 120 to 800 μm in diameter were used. Calibrated attenuators adjusted incident fluence, and detection systems with bandwidths up to 3 GHz were used as required to study the structure of incident and transmitted signals.

Throughout the studies we will report, the gas fill used in the isolator focal region was dry filtered nitrogen. Reproducible plasma initiation could not be obtained without special attention to the removal of water vapor and suspended particulates down to 5 μm.

Plasma Decay Measurements

To obtain an idea of the plasma residence time in the focal region, we measured the decay of visible plasma luminosity vs incident 10.6 μm fluence for 2 ns pulses and background pressures from 0 to 590 torr.

The volumetric source density of bremsstrahlung radiation by a plasma is proportional to the second power of the plasma density[12] n_e, and, if we consider an expanding plasma ball that has become optically thin for its own thermal (hard uv) radiation, the total luminosity observed in the present case is due to bremsstrahlung and is proportional to the product of the total number N_e ($n_e V$) and the number density of electrons ($L \propto N n_e$). If the plasma remains too hot for significant recombination to occur, total luminosity would be proportional to the plasma density.

As shown in Fig. III 3, luminosity decay time constants up to 4 μs are easily obtained at 590 torr, and up to 1 μs in vacuum, indicating that the available isolation time should greatly exceed our requirements. However, for similar residence times, almost 100 times higher fluence is required at the iris edge in vacuum compared to that required at 590 torr. This difference is related to the greater difficulty of obtaining closure, and thus total

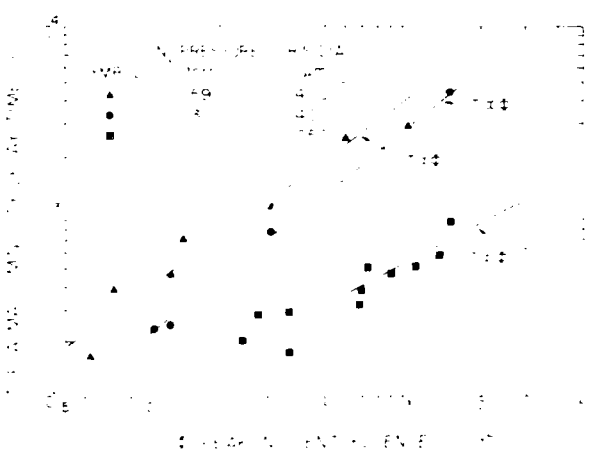

Fig. III 3

Decay time constant of plasma luminosity vs peak incident fluence in the focal plane for 2 ns, 10.6 μm pulses incident in vacuum and 590 torr N_2. For the 590 torr data, 3.3% of this peak fluence was incident on the iris perimeter, whereas in the vacuum case, 13% of the peak fluence struck the iris. The iris diameters used were 400 to 250 μm, respectively. A fluence of $10\ \mathrm{J\,cm^{-2}}$ corresponds to a total energy of 210 mJ.

absorption of the incident laser energy when closure is initiated from the iris edge as in vacuum, rather than throughout the focal volume as with gas fill. The data indicate that, once the plasma is formed, its decay time follows a similar trend vs incident fluence, whether it is initiated in gaseous or metal vapor plasma. However, the metal vapor plasma decay time increases less rapidly with fluence above threshold.

Closure Time and Time Resolved Forward Transmission

Wide bandwidth measurements with 2 ns pulses showed a similar evolution of aperture closure by the plasma for both gas and vacuum backgrounds.

Figure III 4a shows the features of the typical input and output signals we observed, with the 400 μm iris and a 590 torr N_2 background, using identical absolute intensity scaling for both signals. Figure III 4b shows the computed transmission vs time during the input pulse, obtained by careful calibration of the proper time interval between the two signals.

Similar measurements for a 250 μm iris in vacuum are presented in Fig. III 5. Breakdown for 2 ns pulses occurred with a peak fluence of 20 ± 4 Jcm^{-2} incident on the iris perimeter, corresponding to 150 ± 30 Jcm^{-2} peak focal fluence. With 590 torr dry N_2 in the focal region, the corresponding values for 2 ns pulses were 1 ± 0.2 and 30 ± 5 Jcm^{-2}, with this iris.

Figure III 6 shows the pressure dependence of the observed breakdown fluence for 2 ns laser signals with a 400 μm iris in dry nitrogen, compared to the predicted behavior for air without the iris.[13] Also plotted is the vacuum threshold for the 400-μm iris. Even when it is large enough to intercept only 3.3% of the peak on-axis fluence, the iris plays a determining role in the breakdown. This is especially true at lower pressures at which the threshold for the gas has substantially increased.

Qualitatively similar results were obtained for smoothed 60-ns pulses at the same pressure, except that the breakdown fluence in this instance was much smaller than that obtained without the iris because 48% of the peak focal fluence was incident on the iris perimeter. As illustrated in Fig. III 7, for a pulse with a peak spatial input fluence of 63 Jcm^{-2}, well above the breakdown threshold for this configuration, the leading edge of the output pulse follows the input until plasma formation begins. Transmission then terminates abruptly, presumably with a speed greater than that of the detection system used.

Transmission as a function of time is shown in Fig. III 8 for a series of pulses of similar duration but with a much broader fluence range than was possible with 2-ns pulses. As expected, pulses with higher peak energy initiate a breakdown earlier than those with lower peak energy.

In fact, if we compute transmission as a function of the instantaneous time integral of incident intensity for

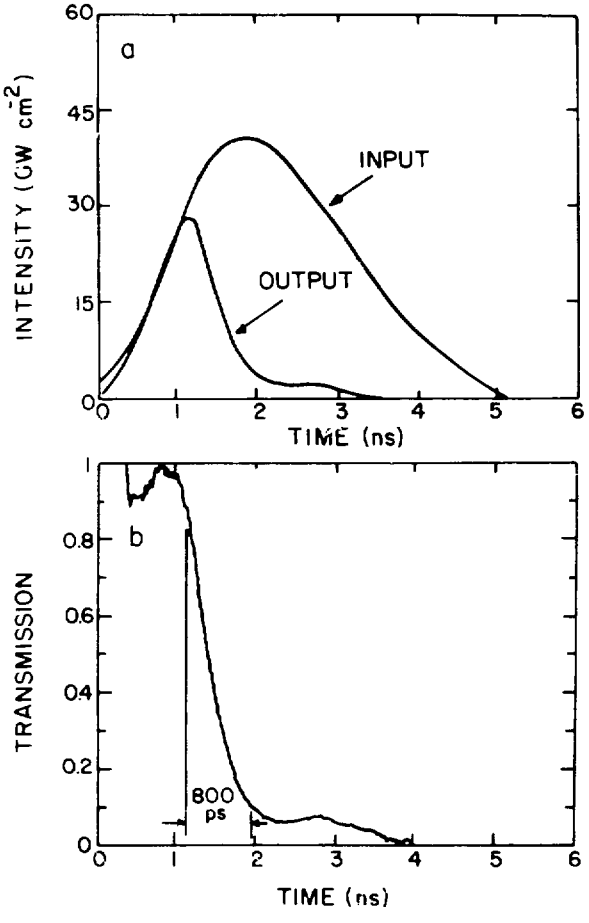

Fig. III 4.

High speed oscilloscope traces showing truncation of a 2 ns, 10.6 μm, forward going laser pulse during formation of the seed plasma in 590 torr N_2.

(a) Typical input and output signals scaled to the same absolute intensities via calibration procedures.

(b) Computed transmission vs time for the pulse pair shown in (a). Essentially perfect transmission is maintained until plasma initiation, after which forward transmission drops to a low value of ~3% in ~800 ps. At much later times, when some expansion of the plasma has occurred, transmission is much lower yet.

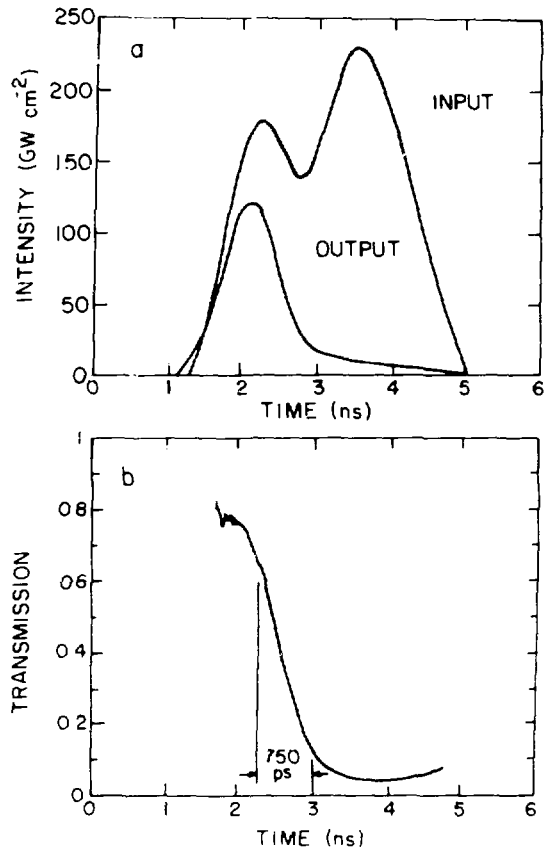

Fig. III 5.
Traces photographed under conditions similar to those of Fig. III 4 during initiation of the plasma in vacuum.
(a) Input and output signals with the appropriate absolute intensity scale.
(b) Computed transmission vs time, showing 750 ps closure time.

these same pulses, as in Fig. III 9, the plasma evolution after breakdown depends mainly on the accumulated incident energy. Figure III-9 also shows that the peak focal-plane fluence at breakdown for this configuration and 60-ns pulses is 6 ± 1 Jcm^{-2}. Because the iris interception fraction was 48% in this experiment, the corresponding fluence on the iris perimeter was 3 ± 0.5 Jcm^{-2}. This value is only three times higher than the fluence on the iris reported in the 2-ns work described above, where the interception fraction was only 3.3%, further emphasizing the controlling influence of the fluence intercepted by the iris in breakdown initiation. As might be expected, these thresholds are significantly below the breakdown fluence that is obtained in the absence of adjacent solid surfaces.[13,16]

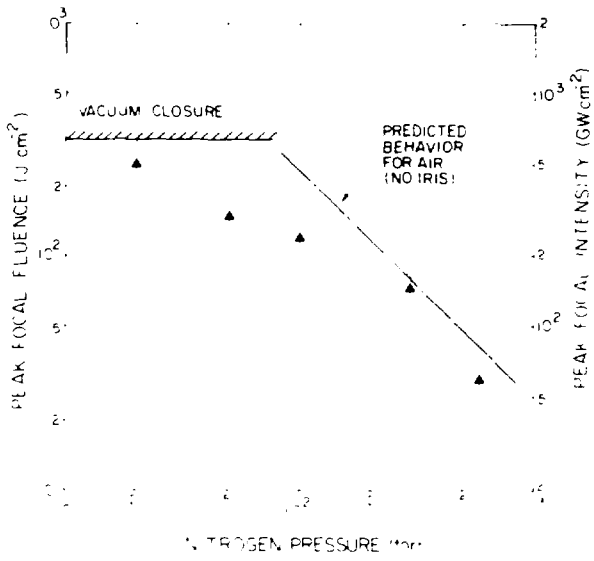

Fig. III 6.
Focal plane fluence required for breakdown vs nitrogen pressure with 2 ns pulses. In this case, the iris intercepted 3.3% of the ordinate fluence value. The breakdown predictions for air are those of Ref. 13 in the high intensity limit, with no iris, for comparison with observed behavior.

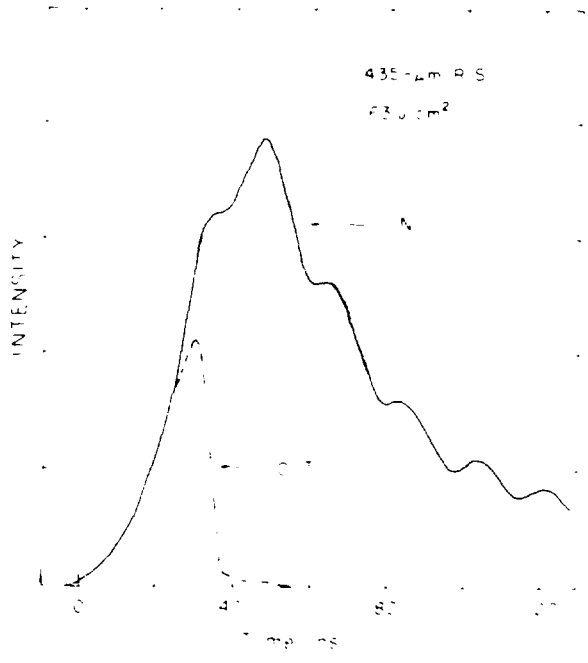

Fig. III 7.
Input and output temporal pulse shapes, for 60 ns incident 10.6 μm pulses, 590 torr N_2, and a 400 μm diam iris. In this case, the iris perimeter intercepted 48% of the peak focal plane fluence, which was 6.3 Jcm^{-2}. Plasma formation is evident at ~30 ns.

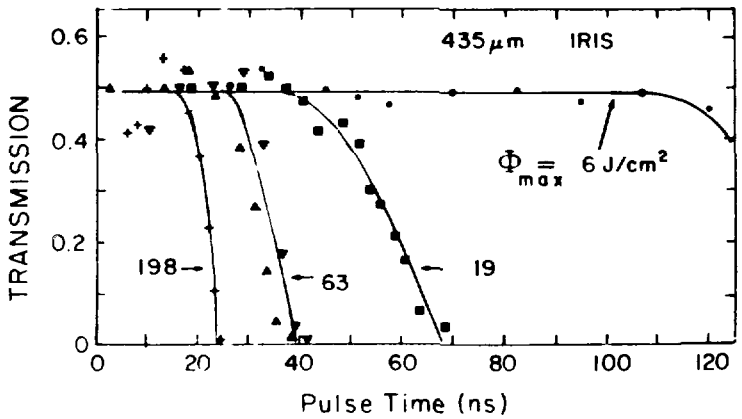

Fig. III 8.
Time resolved transmission for laser pulses with a wide range of peak fluence in the Fig. III 7 configuration. Here, as in Fig. III 7, time begins at the point where the input signal first exceeds 1% of maximum.

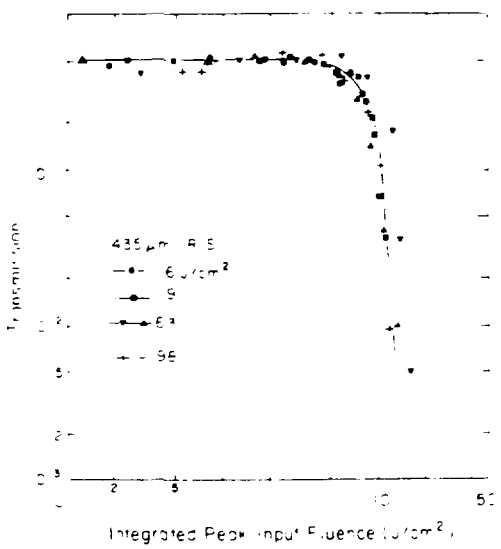

Fig. III 9.
Time resolved transmission vs the time integral of incident intensity for laser pulses with a wide range of peak fluence and intensity. The configuration and pulse durations are the same for Figs. III 7 through III 10.

We have shown that, for pressures from 0 to 590 torr and pulse durations from 2 to 60 ns, the correct model for the time-resolved forward optical transmission function in the plasma spatial filter consists of very rapid extinction at a threshold determined mainly by the iris-interception fraction. These results are summarized in Table III-I. The role of the iris is discussed in more detail below.

Time-Averaged Forward Transmission Behavior

An equally important characterization of forward-transmission behavior in the plasma spatial filter is provided by a study of time-averaged, rather than time-resolved, incident and transmitted quantities. Figure III-10 shows the measured dependence of time-averaged transmission on peak incident fluence at the focal plane for 60-ns incident pulses. The experimental configuration is unchanged. It is seen that the chief characteristic of the time-averaged transmission is the imposition of an output flux limit. This "clamping flux" is ~7 Jcm^{-2} for 60-ns pulse inputs ranging from 20 Jcm^{-2} to nearly 600 Jcm^{-2} in the present experimental configuration.

This behavior is not obvious from the time-resolved data. However, the types of behavior are consistent, given an energy or fluence-dependent component in the breakdown process. Also, very similar flux-limiting behavior is predicted by an instantaneous model in which transmission is extinguished at the point where incident intensity, rather than the integral, first exceeds a critical value. Figure III-11 shows the replotted transmission data of Fig. III-10 for comparison of the two models.

It is clear from the previous discussions and from Fig. III-11 that the plasma formation threshold for 60-ns duration depends strongly on the total laser *energy* incident on the focal volume, and that the common feature among different configurations in this study is the energy incident on the iris perimeter.

Hard-uv radiation arising in the first spots to break down in the focal volume may lower the threshold elsewhere sufficiently to make the ensuing breakdown

TABLE III-I

TYPICAL TIME-RESOLVED FORWARD TRANSMISSION PARAMETERS

Configuration	Min Transmission ($t \leq 5$ ns) (%)	Measured Closure Time (ps)[a]	Corresponding Closure Velocity ($cm\ s^{-1}$)[a]	Iris Intercept Fraction (%)	Iris Fluence at Breakdown (Jcm^{-2})	Corresponding Focal Plane Fluence (Jcm^{-2})
2 ns pulse 590 torr N_2 400 μm iris	3[a]	800	2.5×10^7	3.3	1	30
60 ns pulse 590 torr N_2 435 μm iris	5	~3000		48	3	6
2 ns pulse vacuum 200 μm iris	4[a]	750	1.4×10^7	13	20	150

[a]Risetime of the detection system used in the 2-ns-pulse measurements was ~130 ps. Closure velocity was computed from the ratio of aperture radius to closure time, and is not necessarily a physical velocity. Closure time is the measured time required for transmission to fall from 90% of its maximum value to within 10% of its final value at breakdown.

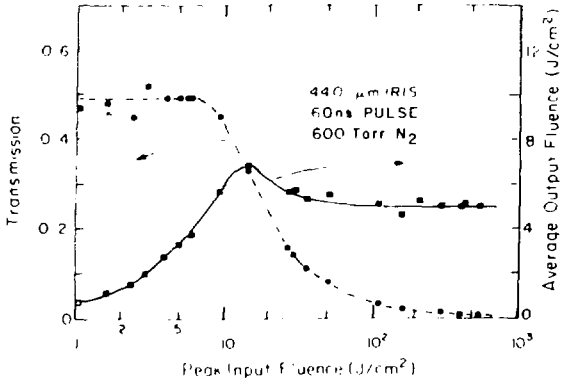

Fig. III-10.
Time averaged transmission (the ratio of output to input energy) and space averaged output fluence vs peak incident fluence at the focal plane, with 435 μm-diam iris in 600 torr N_2.

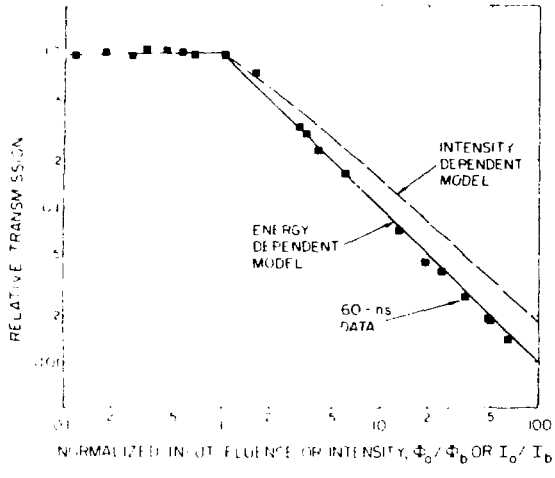

Fig. III-11.
Transmission data of Fig. III-9 replotted for comparison with theoretical model predictions. Solid curves: predicted transmission with fluence-dependent threshold; dashed curve: predicted transmission with intensity-dependent threshold.

process appear to be energy-dependent. No cases were found, however, in which breakdown occurred after the peak of the input pulse. Iris spallation may also explain this result.

Effect of Varying Iris Interception Fraction

If the focal-plane iris is removed completely from a gas-filled isolator, the most noticeable effect is a dramatic increase in the postpulse transmission as shown in Fig. III-12. By comparing, for example, Fig. III-4a, where the postpulse transmission with an iris is 3%, we can clearly see that the iris is essential in causing extinction of the laser signal, presumably by preventing refraction around the highly absorptive core region of the plasma.

As shown in Fig. III-13, subtle changes also occur in the time-averaged transmission characteristics with the

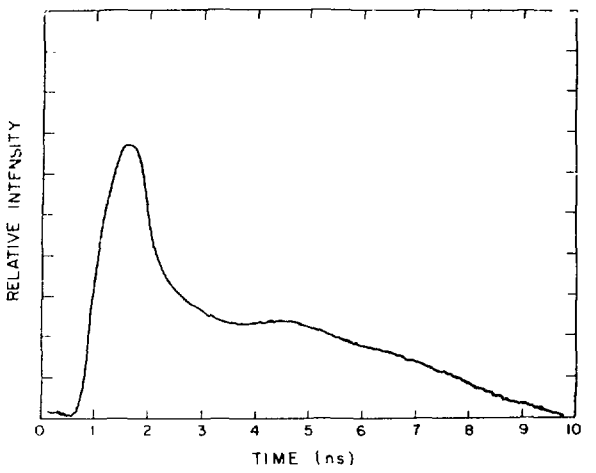

Fig. III-12.
Transmission vs time for 2-ns pulses in 590 torr N_2 with spatial filter iris removed, showing increased postbreakdown transmission.

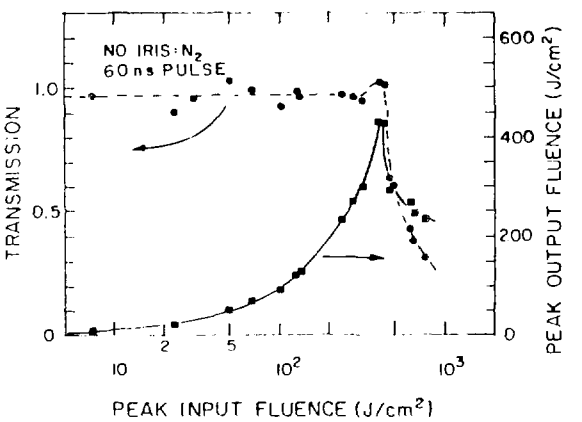

Fig. III-13.
Time-averaged transmission and space-average output fluence vs peak incident fluence at the focal plane with filter iris removed.

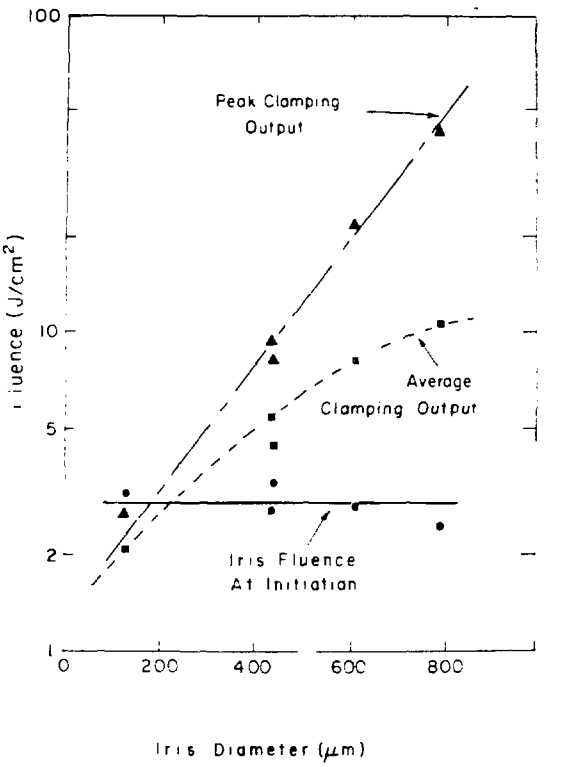

Fig. III-14.
Effect of varying iris size on breakdown threshold in 590 torr N_2 with 60-ns pulses. Points labeled "initiation at iris" represent the fluence incident on the iris perimeter under breakdown conditions at the indicated iris diameter. Total peak and spatially averaged output are indicated, respectively, by triangles and squares.

iris removed (compare Fig. III-10). This configuration is less easy to model because, in the absence of an iris, measurements of transmitted light are more subject to refractive effects before breakdown. We believe these effects led to the exaggerated peak seen in the transmission characteristic near threshold.

Figure III-14 shows the effect of intermediate iris sizes on the breakdown fluence for the 60-ns, 590-torr configuration. Note that a plasma was initiated whenever the fluence incident on the iris perimeter reached 2.9 Jcm^{-2}. This shows that the iris plays a dominant role in the breakdown process for interception ratios ranging from ~6% to near unity with 60-ns pulses. Table III-II summarizes the transmission and the limit of transmitted fluence observed with the various iris diameters The last entry gives transmitted energy with no iris. No significant difference was noted in the behavior of irises that were thin or thick with respect to their diameter.

Power Required to Sustain the Plasma

Additional work is needed to establish accurate scaling relationships for plasma sizes much larger than those in this study. However, determination of the specific plasma dissipation for our conditions provides a baseline for such future studies as well as valuable design

TABLE III-II

MAXIMUM TRANSMITTED FLUENCE AT THE IRIS PLANE DETERMINED BY PLASMA FORMATION, THE CORRESPONDING TRANSMITTED ENERGY, AND THE GEOMETRICAL TRANSPARENCY OF THE IRIS BELOW PLASMA THRESHOLD OBSERVED FOR IRISES OF SEVERAL DIAMETERS

Iris Diam (μm)	Max. Transmitted Fluence (Jcm^{-2})	Transmitted Energy (mJ)	Transparency of Iris Below Plasma Threshold (%)
130	2.11	0.28	6
435	5.38	8.0	49
440	4.41	6.7	50
608	8.27	24.0	65
792	10.8	53.0	75
∞	...	$\lesssim$380.0	100

information at ~1 mm diameter. Plasma dissipation was determined by measuring the transmission of a train of 2-ns pulses with 12.5-ns intervals and gradually decreasing intensity as shown in Fig. III-15. The average input intensity at the point where transmission reaches a minimum and begins to increase can be used as a measure of plasma dissipation, because, as we separately determined, reflectivity is quite small for 2-ns pulses at these intensities. Transmission at the minimum shown was less than 1% and the dissipation level in this case (0 torr) was 2.6 $GWcm^{-2}$.

As might be expected, measurements of sustaining intensity up to pressures of 590 torr N_2 showed little variation. We measured 1.5 $GWcm^{-2}$ at 50 torr and 1.2 $GWcm^{-2}$ at 590 torr when peak attenuation was in the same range. Dissipation also did not vary strongly with attenuation.

In the case shown in Fig. III-15, the ratio between the intensity required to initiate breakdown and that required to maintain it is nearly two orders of magnitude, in agreement with Raizer.[17]

The magnitude of this ratio suggests the possibility of economically maintaining the plasma for times much longer than the natural decay time with an auxiliary low-power laser signal.

Isolator Performance vs Pressure

A standard spatial filter with f-15 ZnSe optics was used to test overall retropulse isolation performance for 2-ns pulses. The experimental setup we used is illustrated in Fig. III-16. A small portion of the available 10.6-μm single-line laser signal was used to provide plasma initiation 105 ns before arrival of the delayed simulated retropulse, which was more than 10 times as intense as the initiation pulse (Fig. III-16). This arrangement provided the most realistic simulation of the intended application of such an isolator, where the reverse fluence will ordinarily exceed the forward fluence by a large margin.

As shown in Fig. III-17, a peak power isolation figure of merit ranging from 22 to 29 dB was obtained for nitrogen fill pressures between 50 and 600 torr, consistent plasma initiation being doubtful for lower pressures at the forward fluence used. Time-average isolation figure of merit was about 3 dB less, in general, but never less than 20 dB in the same pressure range. Note that, compared to the 3% transmission recorded at the end of the pulse in Fig. III-4b, two-orders-of-magnitude greater attenuation is achieved during the retropulse, primarily because of its greater fluence.

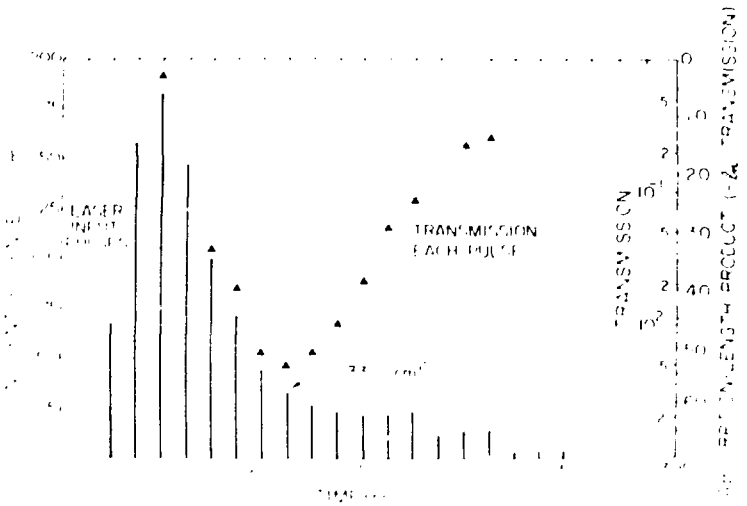

Fig. III 15.
Transmission vs incident fluence in a train of pulses with 12.5 ns interval and 2 ns duration. The turning point for the absorption gives an approximate sustaining power for the plasma of 2.6 GWcm . 62 ns after initiation.

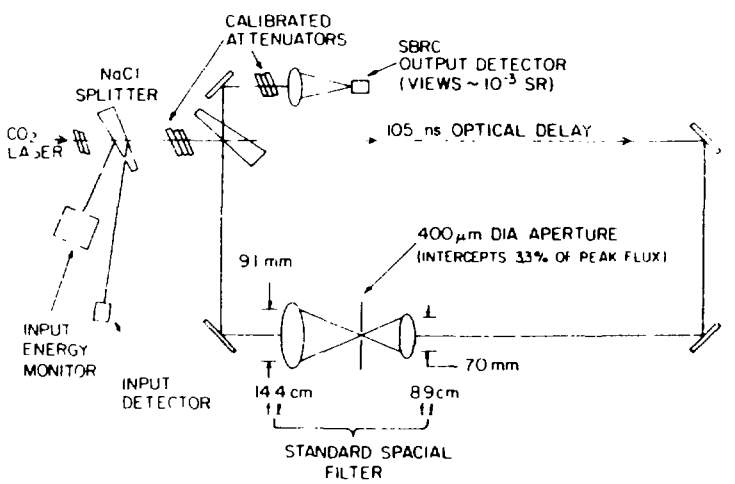

Fig. III 16.
Experimental setup for retropulse isolation measurements shown in Figs. III 17 and 18. The transmitted retropulse detector subtended 10 ⁻¹ sterad (full angle about 2 degrees).

At 590 torr, Fig. III 18 shows the corresponding transmitted retrofluence at the focal plane to be ~5 Jcm ⁻², 40 times less than the fluence used to initiate the plasma. Over the 50- to 600-torr range, and with the specific parameters used here, transmitted fluence varies inversely with pressure until initiation ceases to be a factor and the vacuum threshold for the iris limits further transmission.

Similar data for the metallic plasma in vacuum are not yet available. However, the fact that similar luminosity decay times are easily obtained (Fig. III-3), combined with the similarities in instantaneous transmission during breakdown, indicates that similar performance will be seen in an evacuated vs a gas-filled spatial filter, but at correspondingly higher fluence levels.

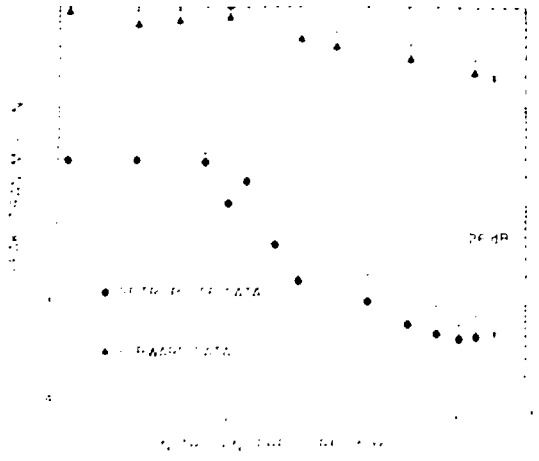

Fig. III 17.
Overall isolation performance of the plasma spatial filter vs nitrogen pressure for 2 ns, 10.6 μm forward and retropulses separated by a 105 ns delay. The focal plane fluence of the forward pulse was typically 230 J cm⁻², whereas the retropulse fluence was typically 2900 J cm⁻². Iris diameter was 400 μm, and iris interception fraction was 3.3%. Other measurements show this forward fluence to be sufficient to provide reliable plasma initiation down to 50 torr. The data show the isolation figure of merit ranging from 22 to 29 dB, with a typical value of 26 dB at 500 torr.

Fig. III 18.
Transmitted fluence vs pressure for conditions similar to those of Fig. III 16. Here, forward fluence ranged from 140 to 280 J cm⁻² and retrofluence from 1800 to 3600 J cm⁻². The trend for the data obeys P ∝ , constant for pressures down to 50 torr N , where other data indicate that initiation probably did not occur at the forward fluences used.

Conclusions

We have shown that a retropulse isolator with nearly 33 dB attenuation for retropulses occurring up to 105 ns later than the forward traveling pulse and operating at focal intensities up to 1.5 TW cm⁻² can be constructed from a simple spatial filter. The spatial filter iris is a critical part of the isolator's successful operation. In vacuum, it provides the metallic plasma that attenuates the retrosignal; in a neutral gas background, it controls plasma initiation when as little as 3.3% of the peak on-axis illumination is incident on the iris perimeter, and adds greatly to isolator performance by preventing refraction of undesired light around the focal plasma.

The forward transmission characteristic can be described as flux limiting; transmission vs flux above threshold appears to be determined by the integrated power incident on the iris, even though a Gaussian radial distribution was used. This indicates that hard-uv photons originating in the breakdown or iris spallation play an important part in energy transport within the focal volume for times short compared to 1 ns for focal diameters ~1 mm such as we studied. We have shown that we can model the observed transmission above the plasma formation threshold. Because up to 100 times less laser power is needed to sustain the plasma than is required to form it, reliable isolation for times much longer than the natural plasma decay time can be maintained economically. However, luminosity decay measurements suggest that this will not be necessary for most applications.

SOLID STATE SATURABLE ABSORBER (J. F. Figueira, C. R. Phipps)

Introduction

Previous investigations[18] demonstrated the potential utility of a new class of solid state saturable absorbers based on the nonlinear optical properties of impurity dopants in alkali halide host materials. Possible applications of this concept range from their use as saturable absorbers for gain isolation in large CO_2 lasers to use as an optical storage medium for uv excimer lasers.

In this section, we discuss the continuing work on absorber materials applicable to CO_2 laser work. We will describe the results of pulse-propagation experiments in KCl host material doped with $KReO_4$, and, in addition, will discuss the results of the material fabrication program at Harshaw Chemical Company.

Pulse Propagation

The ReO_4^- ion has an ir active vibrational mode (the ν_3 mode) that occurs in the gas phase at 920 cm^{-1}. When the ion is doped into an alkali halide host lattice, the resonant frequency increases as the lattice spacing decreases. For the KCl lattice with a 3.3 Å spacing, Fig. III-19 shows the room temperature absorption spectrum obtained from a fast Fourier transform spectrometer with 0.1 cm^{-1} resolution. The line center is 936.5 cm^{-1} and the linewidth (FWHM) is 1.4 cm^{-1}. As the sample is cooled, the lattice contracts and the resonance frequency shifts to higher values. Figure III-20 shows a typical absorption spectrum at 100 K with a spectrometer resolution of 0.05 cm^{-1}. In contrast to earlier published data,[17] two bands are now resolved, corresponding to the two dominant isotopic masses of the rhenium atom. The lines are centered at 938.83 and 939.38 cm^{-1}, with measured linewidths of 0.09 and 0.12 cm^{-1}, respectively.

At high powers the lines were shown previously[18] to saturate as a homogeneously (phonon) broadened, two-level system, with saturation parameters of 1.45 MW/cm^2 at room temperature, decreasing to 0.21 MW/cm^2 at 100 K.

To understand and characterize the transient response of the $KCl:ReO_4$ material, a series of pulse compression experiments were conducted and the results were compared to the prediction of a computer calculation. A conventional CO_2 oscillator and double pass amplifier were used to generate 75 ns, 40 MW pulses of CO_2 radiation at the P(28) line of the 10 μm band. The output pulse from this system was temporally smoothed by a low pressure discharge in the oscillator. Pyroelectric calorimeters and photon drag detectors were used to measure energy and power as required. Samples were single crystal KCl doped with 1000 ppm by weight of $KReO_4$ and grown by Harshaw Chemical Company. Samples 8 cm in length were cut and polished. Each sample had a measured small-signal transmission at the P(28) line of the 10 μm band of 0.82%, and was of excellent optical quality, with no residual strains.

The output from the oscillator/amplifier system was mildly focused through the sample, and input and output power and energy were measured. Figure III-21 shows a typical input output pair of time histories. Compressions of 40% are easily obtained with powers in the range of 3 to 5 MW/cm^2 for the 75-ns input pulses. By taking a series of these measurements, the compression history of this material can be constructed as shown in Fig. III-22.

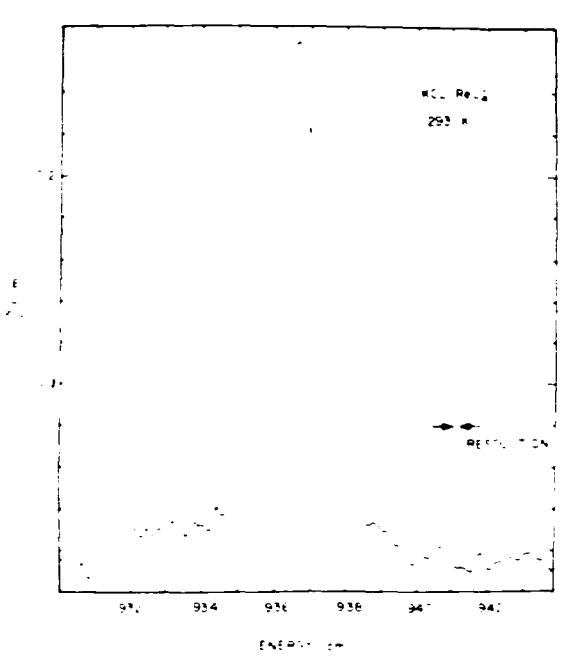

Fig. III-19.
Room temperature absorption spectrum of $KCl:KReO_4$ absorber, obtained with a fast Fourier transform spectrometer. The spectral resolution is 0.1 cm^{-1}.

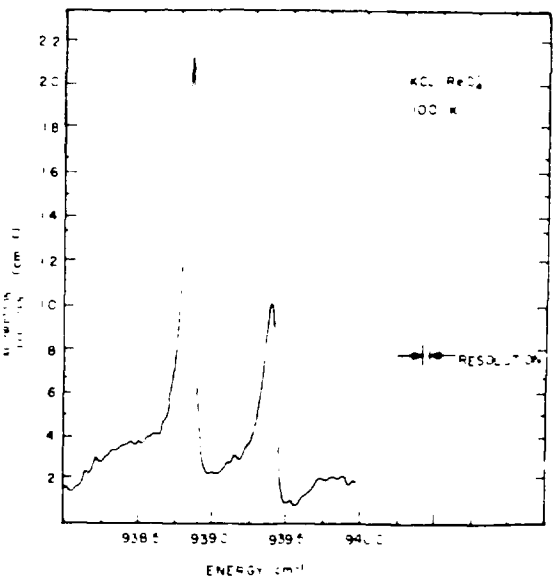

Fig. III-20.
Absorption spectrum of $KCl:KReO_4$ absorber at 100 K obtained as in Fig. III-19. The spectrum center has shifted toward the blue due to contraction of the host lattice at low temperature.

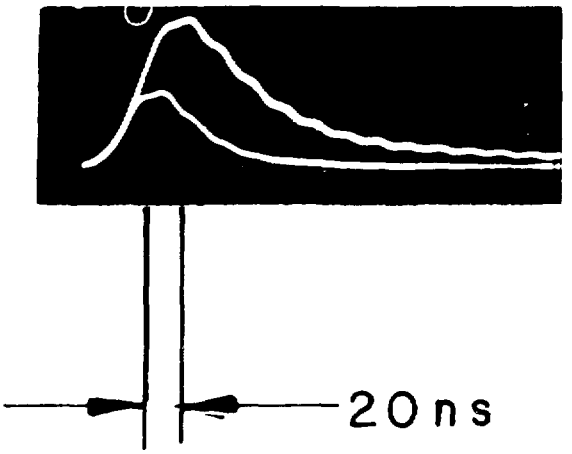

Fig. III 21
Typical pair of input output signals in KCl:KReO$_4$ absorber showing 40% passive pulse compression.

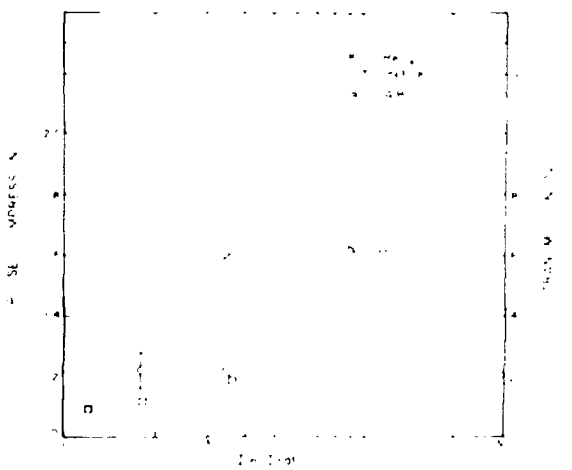

Fig. III 22.
Pulse compression and transmission in KCl:KReO$_4$ absorber vs input intensity. Input signals are 75 ns duration at the P 28 (10 μm) wavelength.

The compression ratio rises as input power is initially increased. However, as the maximum slope of the saturation curve is reached, the compression ratio reaches a maximum value (~1.75 in the present case) and then decreases with further increase in input power. These effects can be calculated by a straightforward adaptation of the basic Rigrod[19] formulation for the saturation behavior of a two-level absorber. The solid curve shows the results of these calculations for plane wave irradiation using the measured parameters of this experiment and our earlier results.[18] The calculation is in qualitative agreement with the experiment. However, the value of the saturation flux required for an optimal fit to the data is ~2 MWcm^{-2}, somewhat larger than previously measured. Related experiments indicate this effect may be due to a reduction in the optical cross section of the ReO_4 caused by different growth techniques for the KCl host. It is also noted that the measured compression curve is slightly narrower than the calculated curve. This difference is due to nonuniform illumination and to spatial hot spots in the input beam that tend to compress in time more dramatically than the plane waves assumed in the calculation.

The above experiments have addressed the time regime where the pulse duration τ_p is much longer than the characteristic relaxation time of the absorber. T_1 is ~70 ps at room temperature for the KCl:ReO_4 as compared to τ_p ~ 70 ns in the above experiments. Future experiments will address the region where $\tau_p \sim T_1$ to test our modeling capability.

Alkali Halide Fabrication

In conjunction with Harshaw Chemical Company, we are investigating the relevant technology issues and looking for possible limitations in the scalability of this technology for the fabrication of impurity doped alkali halides. This program has three immediate goals. First, *using existing and conventional growth techniques*, Harshaw is to produce high quality single crystal samples of KCl:ReO_4. Second, if the first goal is achieved, Harshaw will continue this work with the aim of producing a large (15 to 25 cm (6 to 10 in.) diam boule of hot forged polycrystalline KCl:ReO_4. The third goal is to apply the knowledge accumulated in the first two phases to NaCl in an attempt to produce samples of single crystal as well as hot forged polycrystal NaCl:ReO_4. In all aspects of this program, emphasis is on the material fabrication technology, rather than on attempting to produce an isolator for a specific CO_2 laser system.

The previous crystal growth work at Cornell University pointed to several problem areas that required further systematic study. First, the Cornell samples, grown by the Czochralski method, showed large residual strains, making them unsuited for applications involving

good optical properties in transmission. Second, the Cornell work suggested the existence of a solubility limit for the ReO_4 ion in the KCl lattice that could limit the attainable optical density to an impractically small value.

To investigate these problems, Harshaw produced a series of single crystal KCl samples doped with various concentrations of $KReO_4$. These were typically 6 cm in diameter and 25 cm long. By use of the modified Stockbarger technique for crystal growth, where the material is continuously zone refined as it is grown, Harshaw was able to produce single crystal KCl:ReO_4 material that is free of visible strains.

To investigate the possibility of achieving a controlled doping density of the ReO_4 ion in the KCl lattice, samples were made with a systematic variation of the $KReO_4$ concentration in the starting melt. We determined the actual ReO_4 ion concentration in the crystal by neutron activation analysis of the rhenium atom concentration in the resulting KCl matrix. We also determined, by the use of high resolution, fast Fourier transform spectroscopy, the absorption coefficient and cross section of the ReO_4 at 935 cm^{-1}. The optical cross section of the Harshaw material was measured to be $0.46 \pm 0.3 \times 10^{-16}$ cm^2 as compared to earlier measurements on the Cornell samples of $0.76 \pm 0.02 \times 10^{-16}$ cm. The observed difference in the optical cross section of the ReO_4 ion produced by the two growth methods is not yet understood and is being investigated.

The starting $KReO_4$ concentrations and the resulting ReO_4 ion concentrations can be used to construct a solubility plot, as shown in Fig. III 23. At a low starting concentration of $KReO_4$ (10^2 ppm) the resulting ReO_4 concentration is less than 10^{14} cm^{-3}, which is the smallest concentration we can measure. However, for concentrations in excess of 10^2 ppm by weight of $KReO_4$, a measurable concentration of the ReO_4 ion is produced. At the highest levels produced to date, the concentration of ReO_4 was 4×10^{16} cm^{-3}. Because the measured cross section is 0.46×10^{-16} cm^2 this concentration implies an absorption coefficient of 1.84 cm^{-1}.

In summary, it has been demonstrated that the KCl:ReO_4 solid state saturable absorber can be produced in single crystal form by conventional growth techniques. High dopant concentrations have been achieved in strain-free material. Work will continue on hot-forging KCl:ReO_4 material. In addition, applications of these growth techniques to other impurity-doped alkali halides will be studied.

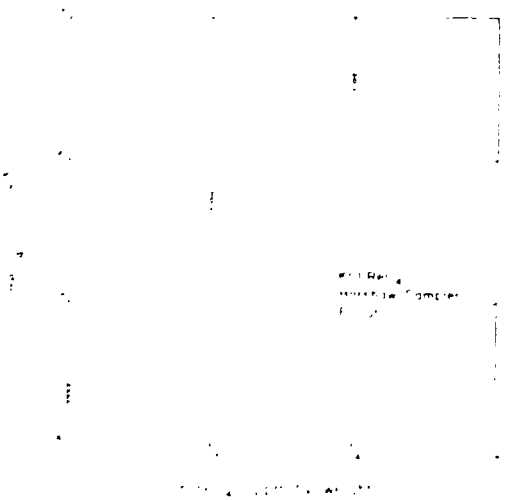

Fig. III 23.
Solubility plot for actual ReO_4 ion concentration obtained in KCl lattice vs starting $KReO_4$ concentration.

TRANSIENT RESPONSE OF PHASE CONJUGATION BY DEGENERATE FOUR-WAVE MIXING

(B. J. Feldman, R. A. Fisher)

Previously, we reported experimental demonstration of degenerate four wave mixing in germanium leading to phase conjugate reflectivities as high as 20% in a 15-cm long sample. Our results were in agreement with simple steady-state theory,[20] which predicts that the reflectivity from the degenerate four-wave mixing process is given by

$$R = \tan^2(\beta L),$$

where

$\beta = 12\pi\omega\chi_{n\nu}^{(3)} E_1 E_2 / nc$

and

ω = angular frequency of applied fields,
$\chi_{n\nu}^{(3)}$ = third-order nonlinear coefficient,
$E_{1,2}$ = field strengths of oppositely directed pumps,
n = refractive index of material, and
c = velocity of light.

The 100-ns pulses used in these experiments were substantially longer than the optical transit time for the germanium samples used, which justifies the use of steady-state theory. However, for laser fusion applications where shorter pulses are desired, the response may differ from steady-state predictions. Therefore, we have developed a transient theory that is valid for optical

pulses shorter than the optical transit time of the material. The theory, which solves the coupled nonlinear Maxwell equations governing the response of a third order nonlinear material such as germanium, follows closely the earlier Fourier and Laplace transform techniques used by Bobroff and Haus[21] to solve backward oscillator interactions in traveling-wave tubes. The resulting solutions for the reflected pulse subjected to a delta function input probe field, in the absence of pump depletion, may be written analytically in the form

$$E_r(0,t) = \frac{-i\gamma c}{2n} F(T_1)$$

where

$$F(T_1) = [I_0(T_1) - I_2(T_1)] e^{-T_1/2}$$

$$+ \sum_{r=1}^{\infty} \left(\frac{T - nT_1}{T + nT_1}\right)^{n-1} \left\{ I_{n-1}\left(\frac{T^2 - (nT_1)^2}{2}\right) \right.$$

$$-2\left(\frac{T - nT_1}{T + nT_1}\right) I_{n+1}\left(\frac{T^2 - (nT_1)^2}{2}\right) +$$

$$\left.\left(\frac{T - nT_1}{T + nT_1}\right) I_{n+3}\left(\frac{T^2 - (nT_1)^2}{2}\right)\right\} e^{-T - nT_1}$$

where $T = \beta$ct n, $T_1 = 2\beta L$, n = refractive index, and $I_n(z)$ = modified Bessel function of order n, argument z. The response is plotted numerically for certain characteristic cases in Fig. III 24. For $\beta L < \pi/2$, the response starts at a finite value and slowly rises until the delta function input strikes the exit plane, at which time the signal falls off sharply. For $\beta L = \pi/2$, the response of the system rapidly approaches steady state. For $\beta L > 4$, the response grows exponentially, indicating the onset of backward parametric lasing, and will continue to grow until pump depletion reduces the coupling coefficient.

Fig. III 24
Calculated transient reflectivity for an input pulse delta function of the form $E_{in} = E_0\delta(t)$. The normalized output intensity $(E_r/E_0)^2$ is plotted vs time. The case chosen is a 6.6 cm long CS$_2$ conjugator with pumpwave intensities adjusted for the interaction strength $\beta L = 1$.

These results indicate that extreme pulse shape distortions are possible in the transient response of degenerate four wave mixers. Additional studies describing the response of the system to finite input pulses are in progress and will be reported together with a comparison of experimental results upon completion of the work.

THALLIUM DOPED KCl STORAGE LASER (R. A. Fisher, B. J. Feldman)

Experiments are in progress to investigate the possibility of thallium-doped KCl as an optical storage material for the KrF laser at 2500 Å. Thallium doped KCl has a strong absorption band centered at 2500 Å. When optically pumped in this band, the crystal luminesces strongly at 3000Å with a characteristic lifetime of 300 ns. Luminescense efficiency is ~50%. Attempts are under way to measure the gain of the 3000 Å transition

when the crystal is pumped by a 50 MW cm^{-2}, 20 ns KrF laser pulse at 2480 Å. Estimates are that the gain at 3000 Å should be ~0.03 cm^{-1}, assuming the absence of multiple photon ionization at 2500 Å and possible existence of laser-induced color center absorption at 3000 Å.

GASEOUS SATURABLE ABSORBERS (A. V. Nowak)

Introduction

[illegible] continuing work on improved understanding of [illegible]able gas-phase isolator systems for the 10 μm [illegible]s directed toward obtaining better saturability, as [illegible] as more rapid relaxation. Improved saturation characteristics would offer the same protection against parasitics with improved forward pulse transmission, and faster relaxation would offer protection against retropulses as well as provide isolation for multiplexed CO_2 systems.

In a previous report,[22] our discussion of double resonance measurements showed that an effective way to increase the relaxation rate of SF_6 based absorber mixes is to buffer the mix with hydrogen. These results showed, for example, that the 10.6 μm, small signal absorption of a 10 torr partial pressure of Mix 804* buffered by 800 torr of H_2 relaxed exponentially to thermal equilibrium with a ~7 ns time constant, offering hope of achieving the above goals.

In this report, we discuss the concomitant question of the effects of the hydrogen buffer on the degree of saturation of the isolator mixture for nanosecond duration CO_2 signals. In addition, we describe the effects of varying pulse duration in the 1 to 70 ns range, and of using single vs multiple pulses, on the saturability of several gas mixtures.

*Mix 804 composition

SF_6	1.51%
cyclo-C_4F_8	4.04%
CF_2ClCF_2Cl (FC-114)	12.2%
$CF_2ClCFCl_2$ (FC-113)	19.85%
CF_2Cl_2 (FC-12)	62.4%

Short Pulse Transmission Through Mix 804 with Added Buffer Gas

Reference 22 showed that a hydrogen buffer greatly improves the relaxation rate of absorption in Mix 804. Now, we describe measurements of the effects of this buffer on transmission saturation with nanosecond duration 10.6 μm signals.

Figure III 25 shows the transmission of a 1.1 ns, 10.6 μm, CO_2 laser pulse through an 18.9 cm long cell containing 15.0 torr of Mix 804 buffered by four partial pressures of H_2. The incident pulse characteristics are listed in the left column of Table III III.

As expected, increasing amounts of H_2 will reduce the degree of saturation at a fixed fluence, but note that linear extrapolations in the direction of increasing pulse fluence show an apparent common point of convergence for all five data sets. This point lies near 1.7 Jcm^{-2} with a corresponding transmission of ~83%. However, it is unlikely that a linear extrapolation accurately predicts pulse transmission above 1 Jcm^{-2}. The curves probably bend and become parallel.

These results suggest that for 15 torr of Mix 804 in a 19 cm long cell, the preferred operating point is above 1 Jcm^{-2}, where the transmission is near its maximum and is reasonably independent of H_2 pressure. At this fluence level, the experimenter can adjust the H_2 pressure to select the recovery time of his choice (within limits) without paying a saturated transmission penalty.

Figure III 26 shows data sets in which N_2 replaced H_2 as the buffer. It is remarkable that the N_2 curves almost duplicate the H_2 curves, although the H_2 molecule collides with SF_6 about three times as frequently as does N_2. A difference in the two figures is noticeable above 200 mJcm^{-2}, where the transmission in the N_2 buffered mix is slightly greater. The apparent point of convergence is located at an incident fluence of ~1 Jcm^{-2} and a transmission of ~81%.

This result suggests that many other buffer molecules may have transmission curves similar to those in Figs. III 25 and and 26. If such gases exist, the experimenter could select that which is most effective for vibration to translation (V T) relaxation in a particular situation without concern that the transmission curve would be seriously degraded. Examples of gases that are known

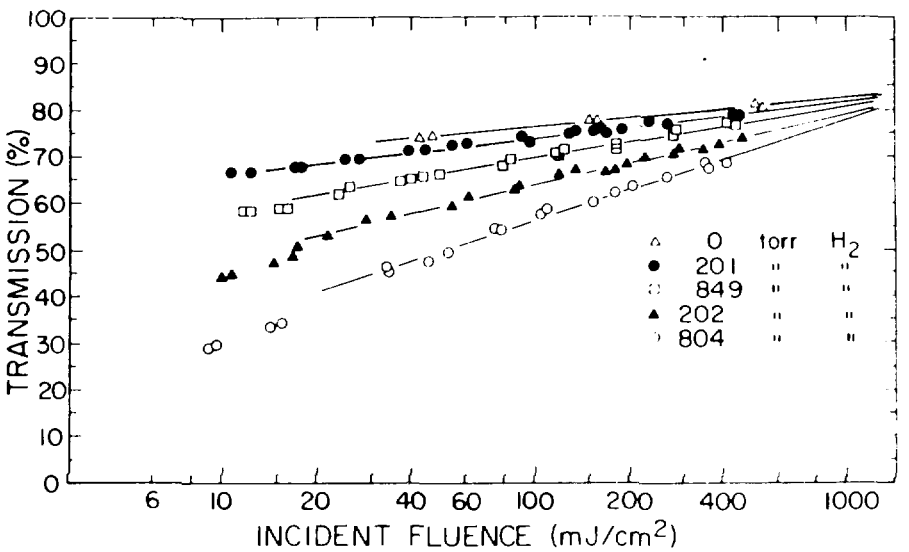

Fig. III 25.
Pulse transmission through Mix 804 buffered by H2. P(804) = 5.07 torr, pulse duration is 1.1 ns, and beam area at e⁻¹ intensity is 0.62 cm²; λ = 10 μm P(20), L = 18.9 cm.

TABLE III-III

CHARACTERISTICS OF LASER SIGNALS USED TO OBTAIN RESULTS PLOTTED IN FIGURES III 25 - III 29

	1 ns Pulse	2.5 ns Pulse
Method of Pulse Formation	Pulse chopped from smooth 70 ns gain-switched output of a TEA oscillator by means of a CdTe electro-optic switch.	Pulse selected from a train of modelocked pulses by means of a CdTe electro-optic switch.
Pulse Transverse Spatial Character	Gaussian, slightly elliptical. Area = 0.62 cm² at e⁻¹ intensity contour.	Gaussian, slightly elliptical. Area was 0.22 cm² at e⁻¹ intensity contour.
Pulse Temporal Background	Low-intensity duplicate of temporally smooth 70-ns gain-switched pulse. Energy ~4% of total output. FWHM = 70 ns; risetime = 20 ns; fall time = 100 ns.	Low intensity train of 2.5 ns pulses, 12.5 ns interval. Energy about 5% of total output. Spike envelope had FWHM of 50 ns with 25 ns risetime and 50 ns fall time.
Temporal Shape	FWHM = 1.1 ±0.1 ns; risetime = 0.6 ns; fall time = 0.8 ns.	Pulses changed shape from shot to shot. Many were closely spaced double pulses. Pulse duration ranged from 1.6 to 3.5 ns, but typical duration was 2.5-ns FWHM.

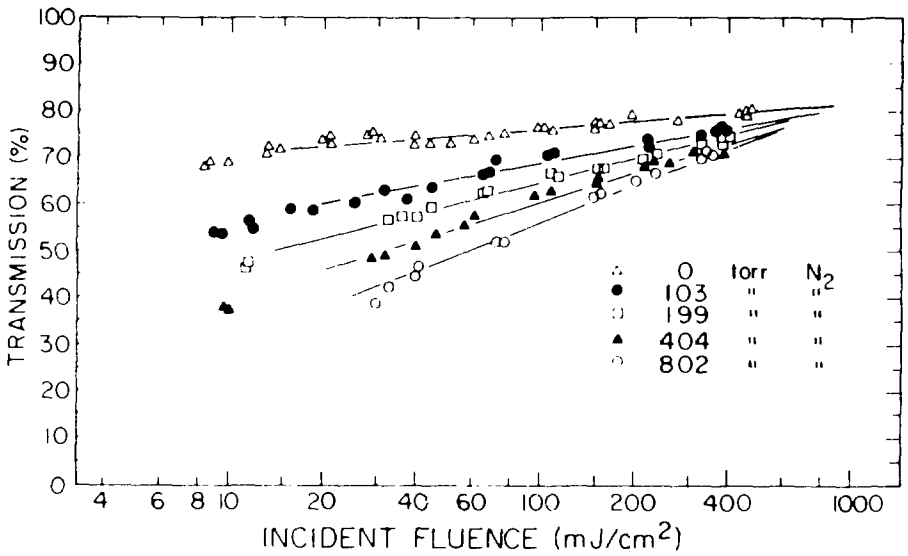

Fig. III 26.
Pulse transmission through Mix 804 buffered by N₂. P(804) = 15.07 torr, pulse duration is 1.1 ns, beam area at e⁻¹ intensity is 0.62 cm²; λ = 10 μm P(20), L = 18.9 cm.

to be more effective V-T relaxers of SF_6 than hydrogen are ethane and dimethyl ether.[23] Experiments to test this hypothesis are under way.

It is not unreasonable to expect that all saturable absorber mixes that use SF_6 as the saturable component will show pulse transmission behavior similar to that of Mix 804, as shown in Figs. III 25 and 26. On the other hand, the same may not be true of mixes based on the saturable absorber CH_3CHF_2 (FC 152a). Data taken by Kung and Friedman[24] show that the risetime of the double resonance signal for FC 152a is exponential with a time constant of 4.6 μs torr for H_2 and 11.7 μs torr for N_2. This result is quite different from that of double resonance experiments we conducted on SF_6 in which the risetime of the signal in all cases was faster than the detector response time of 3 ns. Experiments will be initiated to study the effects of buffering FC 152a.

Short-Pulse Transmission Through Mix 907

We have measured the transmission of 2.5-ns duration pulses through the seven-component saturable absorber Mix 907.* This mix was formulated at our Helios facility to improve the efficiency of suppressing the parasitics over that of Mix 804.

Figure III 27 shows the transmission of 2.5 ns 10.6-μm signals through 8.0, 12.0, and 16.0 torr of Mix 907 in a 109-cm long cell. The properties of the 2.5 ns signal we used in these studies are found in Table III III. Helios data for transmission of 0.75 ns pulses through 10 torr of Mix 907 with the same wavelengths and optical path are summarized in Fig. III 27 by the dashed line. Note that the transmission is considerably higher than that using 2.5-ns pulses.

An effort was made to correlate the transmission of nanosecond-duration pulses through Mix 907 with naturally occurring changes in their duration. Close examination of the data in Fig. III-27 reveals no systematic

*Mix 907 composition

SF_6	= 0.8%
Cyclo C_4F_8	= 2.3%
CF_3CF_2CL (FC 115)	= 6.6%
CH_3CHF_2 (FC 152a)	= 9.1%
CF_2CCl_2 (FC 1112a)	= 13.6%
CF_2Cl_2 (FC 12)	= 25%
CF_2CFCl (FC 1113)	= 42.6%

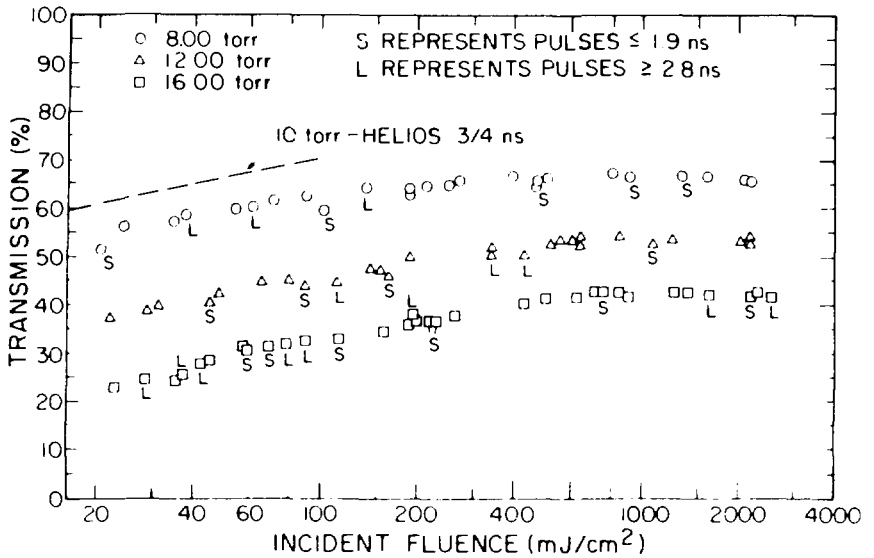

Fig. III 27.
Pulse transmission through Mix 907. Pulse duration (measured) is 2.2 ± 0.5 ns, beam area at e⁻¹ intensity is 0.22 cm², 10 μm P(20), L = 109 cm. Dashed line represents data taken with Helios front end pulse; S represents pulses < 1.9 ns, L represents pulses > 2.8 ns.

difference in the absorption of pulses shorter than 2 ns from that for pulses longer than 2.9 ns. However, the results do not have a clear interpretation because the longer pulses were usually double pulses with separation about equal to pulse width.

We will not attempt to explain these differences until we have a more extensive data base for transmission as a function of pulse duration.

Behavior of Saturated Transmission in Mixes 705 and 804 Under Single and Multiple Pulse Illumination.

The modelocked laser described in Table III III was used to compare the transmission of a train of pulses with that for a single pulse in saturable absorbers Mix 705* and Mix 804. Mix 705, like Mix 907, is a hybrid in that both SF_6 and FC 152a are saturable components at 10.6 μm.

The three data sets indicated by the open symbols in Fig. III 28 represent the transmission of a single switched out, modelocked pulse through a 109-cm long cell containing 2.46, 6.00, and 9.05 torr of Mix 705.

Also shown in the figure are the data points for the transmission of 1.1 ns pulses through 3.46 torr of Mix 705 in a 27.5 cm long cell, which has the same pressure length product as 2.46 torr in a 109 cm long cell. The solid squares in Fig. III 28 represent pulse transmission through 3.46 torr of Mix 705 with the plasma tube in the oscillator turned off. The net effect is to obtain pulses of randomly varying duration in the range 0.8 to 1.5 ns, with shorter pulses predominating. Note the slightly higher attenuation of these pulses. The same effect was observed for 9.7 torr of Mix 804 in a 10.1 cm cell (not shown).

The bottom most data points show the transmission of a train of 2 ns pulses through 9.05 torr of Mix 705. These data points lie well below the single pulse data.

About 90% of the energy of the train of pulses is contained in the central eight spikes, so that we estimate an average energy per pulse of ~10% of the total train energy E. If the gas were fully relaxed in the interval between pulses, the transmission for the pulse train would correspond to the transmission of a single pulse at 0.1E. This is not the case, as shown in Fig. III 28, which shows the transmission of the train at 300 mJcm⁻² to be 35% of that for a single pulse at 30 mJcm⁻².

Because Mix 705 at 9 torr has a V-T recovery time of several hundred nanoseconds, it is quite possible that

*Mix 705 composition

SF_6	1.47%
CF_3CF_2Cl (FC 115)	20.5%
CF_2CFCl (FC 1113)	33.2%
CH_2CHF_2 (FC 152a)	44.8%

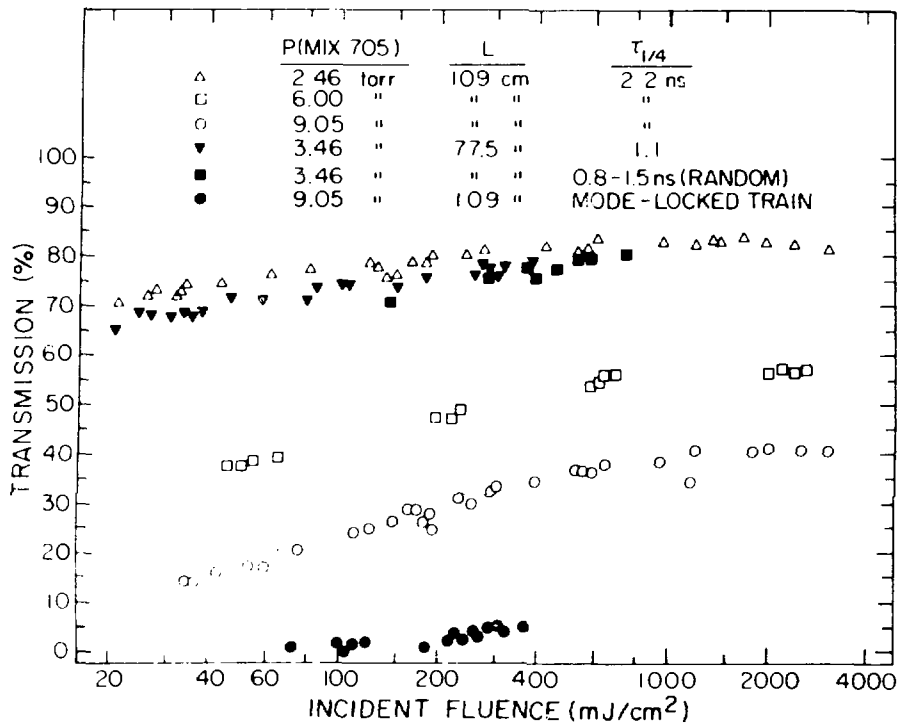

Fig. III 28.

Pulse transmission through Mix 705. See Table III III for properties of 1.1- and 2.5-ns lasers. The 0.8- to 1.5-ns pulses were obtained from the 1.1-ns laser by turning off the oscillator plasma tube. The modelocked train was derived from the 2.5-ns laser by turning off the E.O. switch; λ 10 μm P(20).

the faster V-V energy transfer processes are redistributing molecules throughout the vibrational ladder into an ensemble with a different vibrational temperature and higher net absorption cross section for light at 10.6 μm. The process is analogous to thermal heating of SF_6 from room temperature to 400 K, in which range the net cross section for absorption of 10.6-μm photons increases.[25]

Figure III 29 shows a similar comparison of single- and multiple-pulse transmission for Mix 804. The upper part of the figure shows measurements of transmission of both 2.5- and 1.1-ns pulses through 2.67 and 9.07 torr of Mix 804 in a 109-cm-long cell. There is good agreement at 2.67 torr, but at 9.09 torr the transmission of 1.1-ns pulses is slightly lower.

The points in the lowest part of the figure show the transmission of the train of modelocked pulses through 9.07 torr of Mix 804 in a 109-cm path. By the same arguments as for Mix 705, we estimate that if the mix recovers fully before arrival of the next pulse, the transmission of the train should correspond roughly to the transmission of a single pulse at one-tenth the energy. This condition is only slightly better fulfilled in this case.

Because Mix 804 at 9 torr requires several hundred *nanoseconds to recover, V-V energy transfer processes* are probably also causing increased absorption in the same way as discussed for Mix 705 above.

Absorption of Temporally Smooth 1.6- and 70-ns Pulses in Mix 804

Recent results obtained in the upgraded GWTF show how transmission through 70 and 111 torr of Mix 804 in a 3.95-cm cell depends upon pulse duration. The results are plotted in Fig. III-30. The short pulse had a FWHM of 1.6 ns, a risetime of 0.5 ns, and a fall time of 2 ns. The long pulse was characterized by a smooth intensity profile with a FWHM of 70 ns and with rise and fall times of 20 and 100 ns, respectively. The beam had a uniform radial profile with an area of ~5 cm^2. A ratio of

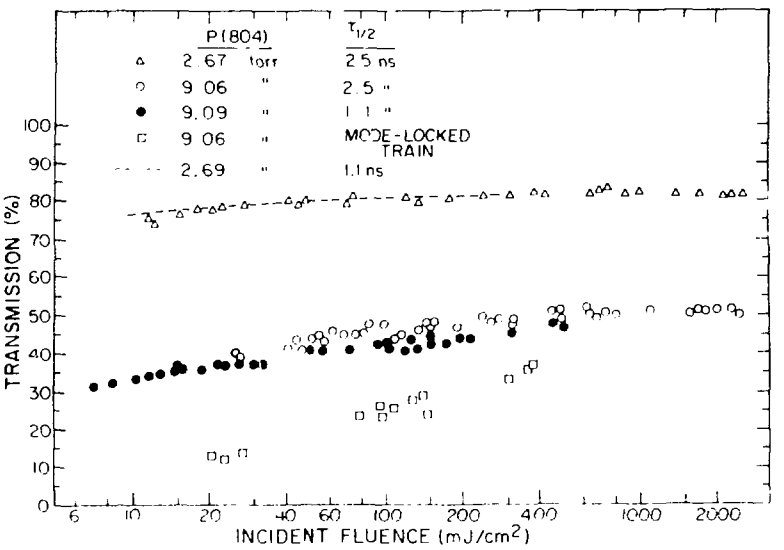

Fig. III-29.
Pulse transmission through Mix 804. See Table III-III for properties of 2.5 and 1.1 ns pulses. Cell length is 109 cm; λ = 10 μm P(20).

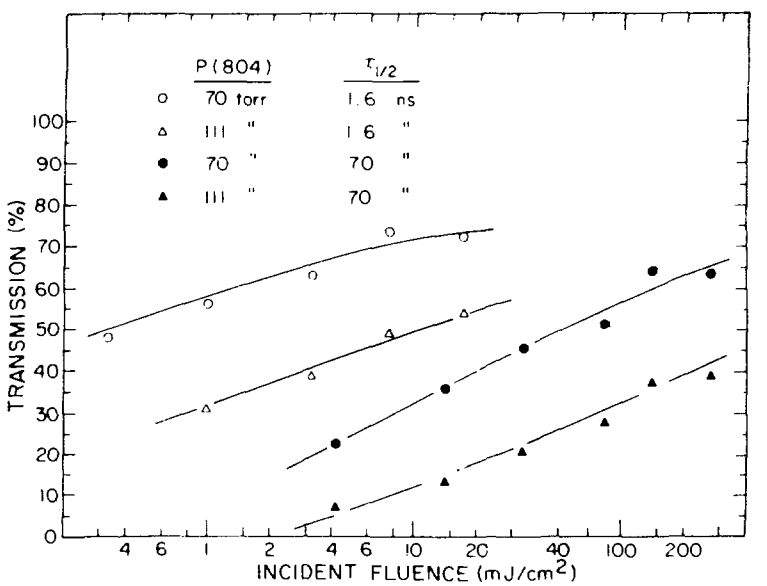

Fig. III-30.
Pulse transmission through Mix 804. Cell length is 109 cm; beam area is 5 cm ^{2}, "top-hat" distribution: λ = 10 μm P(20).

~40:1 in peak powers existed between the short and long pulses. On both a fluence and a peak-power scale the long pulse is much more attenuated than the short pulse.

From the results of double-resonance experiments at 5, 10, and 20 torr of Mix 804, we estimate that the V-T relaxation times of the mix at 70 and 111 torr are ~40 and 25 ns, indicating that the gas relaxes significantly during the long pulse. In this case, V-T relaxation may indeed explain the differences in transmission.

Modeling of Saturable-Absorber Performance (C. J. Elliott)

We suppress parasitic oscillations in Helios and Gemini by the use of gaseous saturable absorbers.[26] At low signal levels a saturable absorber acts like an ordinary linear absorber. If sufficient signal is passed through the absorber, it bleaches and becomes more transparent. The residual absorption in the bleached or saturated state ideally vanishes. Any remaining absorption decreases the usefulness of the saturable absorber, but initial small-signal absorption suppresses parasitic oscillations. Such oscillations must be suppressed not only on the laser wavelengths used to extract energy, but on all other wavelengths that have gain. Oscillations of these other wavelengths could be suppressed by a wavelength-selective absorber, which would have low transmission on the wavelength to be suppressed and would be nearly transparent at the extraction wavelengths. Because perfect saturable absorbers and perfect wavelength-selective absorbers do not exist, we have constructed a mathematical model to treat realistic compromises.

Although the model is idealized in many ways, the result is a prediction of the optimal mixture of gases, which takes into account the residual saturable absorption and the residual wavelength-selective absorption on the extraction lines. These residuals limit the amount of each type of gas that can be added, because too much gas will reduce the transmission on the extraction line. The model requires a known small-signal gain profile on the lines to be suppressed, a model for the small-signal transmission, and a model for the large-signal or saturated transmission. The small-signal gain profile is calculated by the technique described by Goldstein.[27] The small-signal transmission is described by a Beer's law, and the bleached transmission is described by a Beer's law with intensity-independent coefficients. The model, then, maximizes the transmission for the extraction lines while suppressing parasitic oscillations on all lines with gain.

The small-signal transmission on the jth line is given by

$$T_j^{ss} = \exp(-\Sigma_i \alpha_{ij}^{ss} P_i L) \quad . \tag{III-1}$$

where α_{ij}^{ss} is the small-signal absorption on the *j*th line at wavelength λ_j, where P_i is the partial pressure of fill of this ith gas and L is the length of the absorption cell. If any of the gases reacts with another, Eq. (III-1) will not hold. Also, if pressure-broadening and pressure shifts were large compared to the absorption structure, the model would need modification.

The bleached state is modeled similarly, subject to the same stipulations. In addition, we assume that the bleached-state absorption is appropriate for the energy-extracting pulse, regardless of its intensity or energy history; that is, the part of the energy-extracting pulse required to bleach the absorber must be negligible, and once the bleached state is reached, the absorption coefficients become constants. If we extract on a number of lines denoted by subscript k, the bleached transmission on the kth line T_k^b is given by

$$T_k^b = \exp(-\Sigma_i \alpha_{ik}^b P_i L) \quad , \tag{III-2}$$

where α_{ik}^b is the bleached absorption coefficient on the kth line for gas i. In practice, for 1-ns CO_2 pulses, efficient pulse extraction requires four extraction lines; and for each saturable-absorber gas component, four measurements are required in the bleached state to describe the bleached transmission. Suppose the energy fluence on the kth line is ϕ_k going into the absorber cell and $\bar{\phi}_k$ coming out: then the total energy fluence $\bar{\phi}$ emerging from the cell is given by

$$\bar{\phi} = \Sigma \bar{\phi}_k = \Sigma T_k^b \phi_k \quad . \tag{III-3}$$

We may define an average, bleached, saturated-absorption coefficient $\bar{\alpha}_i^b$ for gas i by

$$\frac{1}{\bar{\phi}} \frac{\partial \bar{\phi}}{\partial P_i} = \bar{\alpha}_i^b L \quad , \tag{III-4}$$

where

$$\bar{\alpha}_i^b = \Sigma \bar{\phi}_k \alpha_{ik} / \Sigma \bar{\phi}_k \quad . \tag{III-5}$$

We are expanding ϕ in the neighborhood of the case where the partial pressures are P_i. For small excursions in P_i, Eq. (III-4) may also be obtained by the bleached transmission T^b given by

$$T^b = \exp(-\Sigma\, \bar{\alpha}_i^b\, P_i L) \quad , \tag{III-6}$$

and Eq. (III-6) is the same as that for a single extraction line on which the bleached absorption coefficients are $\bar{\alpha}_i^b$ for gas i; that is, Eq (III-6) has the same form as Eq. (III-2).

If we know the ratio of the emerging fluences ϕ_k from the saturable-absorber cell, then we average the bleached-absorption coefficient over each extraction line, weighted by the extraction fluence. In a design where all the relative $\bar{\phi}_k$ are specified (they might all be equal), the optimum saturable-absorber mix will determine T_i^b and, in turn, the input fluences ϕ_k to the absorber cell.

If the design problem consisted of giving ϕ_k, the $\bar{\phi}_k$ would have to be found by iteration. Initially we would guess at the mix of output fluences ϕ_k and then we would form $\bar{\alpha}_i^b$. The optimization procedure gives a new mix of ϕ_k, and we iterate until the solution converges.

Thus, the general problem of extraction on many lines has been reduced to solving one or more single line-extraction problems. Below, we will assume that the mix of output fluences is known so that we will be solving only one linear programming problem.

We have not described a model for parasitic oscillations. Parasitic oscillations involve the coupling of stray light between two diffuse surfaces separated by a gain region. The optical system permits a solid angle $\Delta\Omega_1$ of light leaving the center of surface 1 to arrive at surface 2; likewise, a solid angle $\Delta\Omega_2$ from the center of surface 2 arrives at surface 1. If ρ_1 and ρ_2 are the respective reflection coefficients per unit solid angle, then, in the presence of a gain-length product of $g_0\ell$ between surfaces 1 and 2, the net round-trip amplification of a photon at wavelength λ_j is

$$(T^{ss})^2 F\ \rho_1\ \Delta\Omega_1\ \rho_2\ \Delta\Omega_2\ \exp(2g_{0j}\ell) \quad ,$$

where F is of order unity and where T^{ss} is the transmission of a single pass in the unbleached state. Writing the definition of g_{th} as

$$F\rho_1\ \Delta\Omega_1\rho_2\Delta\Omega_2 = \exp(-2g_{th}\ell) \quad , \tag{III-7}$$

the condition for net amplification of a photon at wavelength λ_j is given by

$$T_j^{ss}\ \exp(g_{0j} - g_{th})\ell \geq 1 \quad . \tag{III-8}$$

The quantity g_{th} is the raw threshold gain for parasitics and is usually assumed to be independent of wavelength. In the absence of a saturable absorber ($T_j^{ss} = 1$), the laser is stable for all g_{0j} up to g_{th}. When the small-signal transmission is less than unity, more loss is introduced into the system and the threshold increases above the raw threshold to

$$g_0 = \mathrm{Min}_j\left(g_{th} + \frac{1}{\ell}\ln\frac{1}{T_j^{ss}}\right) \quad .$$

The optimum saturable absorber may be found by maximizing T_b given by Eq. (III-6), subject to meeting the parasitic constraints

$$T_j^{ss}\ \exp[(g_{0j} - g_{th})\ell] \leq 1 \quad , \tag{III-9}$$

for all j. This is the same as minimizing Λ where

$$\Lambda = \Sigma\, \bar{\alpha}_i^b\, P_i L \quad , \tag{III-10}$$

subject to

$$g_{0j} \geq g_{th} - \frac{1}{\ell}\ln T_j^{ss} \quad , \tag{III-11}$$

and

$$P_i \geq 0 \quad . \tag{III-12}$$

Cast in the form of Eqs. (III-10)-(III-12), we have a standard linear programming problem[28] to find the P_i.

The relative gain distribution depends primarily on the rotational temperature T_R, whereas the overall magnitude of the gain coefficients depends primarily on the vibrational temperature T_A of the upper laser level (the asymmetric stretch mode). The gain coefficients can be written as

$$g_{0j} = g_0 f_j \quad , \tag{III-13}$$

where g_0 is the maximum gain coefficient [usually that for the 10-μm P(18) or P(20) lines].

Written in this form, the optimum mix only depends on f_j and on g_{th}/g_o. This result can be obtained by dividing Eqs. (III-10) and (III-11) by $g_o\ell$ and multiplying Eq. (III-12) by $L/g_o\ell$; then we conclude that at the optimum mix

$$\frac{F_i L}{g_o \ell} = F_i\left(\frac{g_{th}}{g_o}, f_K, \alpha_{K,i}^{ss}, \alpha_{K,c}^{ss}, \bar{\alpha}_K^b\right) . \quad \text{(III-14)}$$

Linear programming theory or further manipulation of Eqs. (III-10)-(III-12) yields the result that the set F_i is piecewise linear in g_{th}/g_o.

We may arrive at a concept of a figure of merit for a mixture of absorber gases. The optimum value of Λ defined in Eq. (III-10) is obtained by substituting Eq. (III-14) in Eq. (III-10), giving

$$\Lambda_{min} = g_o \ell - \bar{\alpha}_c^b \ell F_i\left(\frac{g_{th}}{g_o}\right) , \quad \text{(III-15)}$$

where only the g_{th}/g_o argument of F_i is shown. The figure of merit (FOM) will be shown to have the required property and is defined by

$$FOM = \frac{(g_o - g_{th})\ell}{\Lambda_{min}} . \quad \text{(III-16)}$$

This FOM is finite at the limit $g_o = g_{th}$. (Under this condition, no suppression of parasitics is required so that $T^b = 1$ and $\Lambda_{min} = 0$.) Using Eqs. (III-6), (III-10), and (III-16), we demonstrate a more important property by interpretation of

$$T^b = \exp - \frac{(g_o - g_{th})\ell}{FOM} , \quad \text{(III-17)}$$

which manifests the desired property of a FOM. The numerator of the argument of the exponential depends only on properties of the laser and not on those of the absorber cell. To reach $g_o\ell = 8$ in a design problem where $g_{th} = 4.5$, we would examine various gas mixtures to find that mixture with the largest bleached transmission T_b. Equation (III-17) shows that this procedure is equivalent to that of finding a mixture with the highest FOM.

The additional optimization problem, that is, of deciding at what g_o to operate the laser system, depends on energy-extraction calculations and is beyond the scope of the present treatment. The required input for such a calculation with an optimum absorber mix is just the FOM curve plotted against g_{th}/g_o combined with Eq. (III-17) along with a pulse-propagation code. Optimizing the relative fluences on the extraction lines and choosing the extraction lines themselves are even more complex problems that require as inputs the results of our model along with detailed modeling of rotational relaxation in the pulse-propagation codes.

The results of the FOM calculation of our model are shown in Fig. III-31. The shaded regions represent uncertainties due to two possible small-signal absorption coefficients for SF_6. The gain curve was computed by using 1800 torr of a 3:1/4:1::He:N_2:CO_2 laser mixture filled at 300 K, a symmetric and bending-mode temperature of 370 K, and an asymmetric stretch-mode temperature of 1310 K. In addition to the optimal mix computed by the linear programming approach (the optimal mix varies with g_{th}/g_o), we also show the FOM for two fixed mixes. The optimal curve is the envelope of all such possible mixes.

Detailed examination of the results of the linear programming procedure suggested a simple experimental means of choosing a gas to create a mixture that is closer to the optimum. Figure III-32 shows the basis for obtaining the criterion for choosing between two gases. We must be able to detect which parasitic wavelength is oscillating, and, as shown in the figure, suppression is desired at the oscillation at wavelength λ_c. The extraction wavelengths are all assumed to be near λ_{ex}. The pressures of gases A and B are separately adjusted to give the required $\alpha^{sat}P$ to suppress the oscillation. We then look at the impact at the extraction region. Although gas B saturates at all wavelengths, it is not a very good wavelength selective absorber. Gas A, on the other hand, does not bleach at all but is a very good wavelength selective absorber. This figure shows that the suppression ratio $\alpha^{sat}(\lambda_c)/\alpha^b(\lambda_{ex})$ is the correct criterion for decision.

In practice, the gas to be added is correctly chosen by the suppression-ratio criterion even when several lines are oscillating at once. Each oscillating line has an associated gas given by the best suppression ratio for that individual line. A gas chosen to suppress a particular line also helps to suppress another line, and this has been important in determining the amounts of the gases to add, but not in the choice itself.

Future Work

Much yet remains to be learned about the dependence of transmission on pulse shape and duration in gaseous absorbers for the 10-μm region.

A program is under way to obtain a data base that will permit construction of an appropriate model. The im-

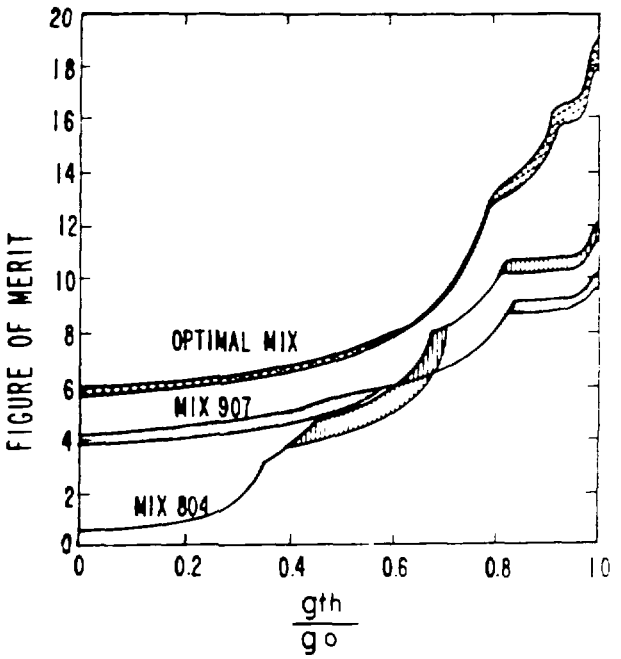

Fig. III-31.
Figure of merit curves for several gas mixtures as a function of maximum stable gain on the 10 μm P(20) line.

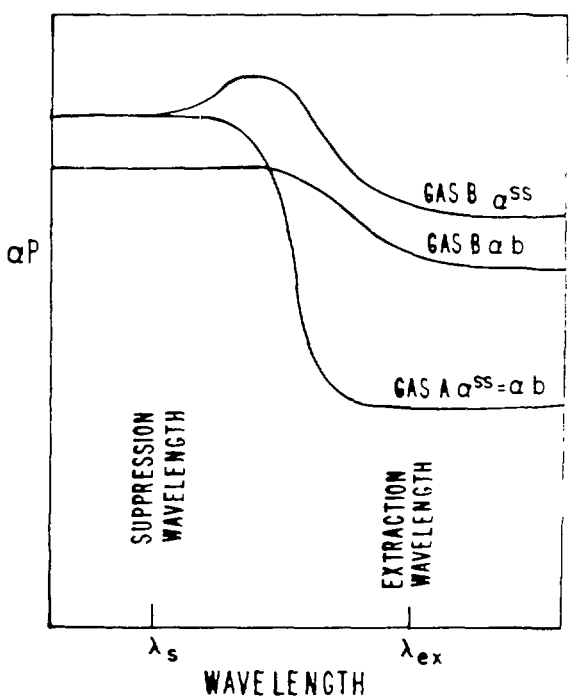

Fig. III-32.
Illustration of the rule for deciding between absorber gases A and B, with differing loss coefficients αP. The wavelength to be suppressed is λ_s, while energy is extracted at λ_{ex}.

portance of this program is underscored by noting that the transmission for 0.75 ns pulses through Mix 907 is considerably greater than for 2.5 ns pulses, as shown in Fig. III-27.

CO_2 LASER PHYSICS

Introduction

We are continuing to design new laser systems and to improve existing systems. We have gained a better understanding of saturable absorbers, of hot band contributions to gain, and of nonlinear phase distortion in NaCl. Current calculations for target induced parasitics in Antares show that the latest design changes have *relieved the problem substantially*.

Calculation of Small-Signal Gain Coefficients in CO_2 (J. C. Goldstein)

The code CO2GAIN was constructed to predict small-signal gain coefficients for the P- and R-lines of the 10.6- and 9.4-μm bands of CO_2. The code evaluates the gain coefficient at a particular frequency by summing

over contributions (at that frequency) from several hundred individual transitions in four sequence bands, two hot bands, and the main bands. The results of the code compared well with laser gain data[22] but a more stringent test of the code's validity is a comparison with thermal equilibrium absorption coefficient data where the gas temperature in an experimental cell is well known and controlled.

Figure III 33 compares measured[20] and calculated line center absorption coefficients of three of the 10.6 μm lines in pure CO_2 at 200 torr as a function of temperature. Agreement for the P(20) and P(14) lines is rather good. The curves suggest that a near coincidence from some other transition, not in the calculation, may become significant for the P(24) absorption at higher temperatures. A scan of the Air Force Geophysical Laboratory line listing for CO_2 does reveal a near coincidence of the P(24) line of the 00°1 10°0 transition with the R(34) line of the 20°0 10°1 transition, a transition not in the code.

Under conditions tested to date, CO2GAIN performs well in calculating CO_2 line center gain coefficients. However, as more extreme conditions are checked, it may be necessary to add more transitions to the calculation to accurately obtain gain coefficients.

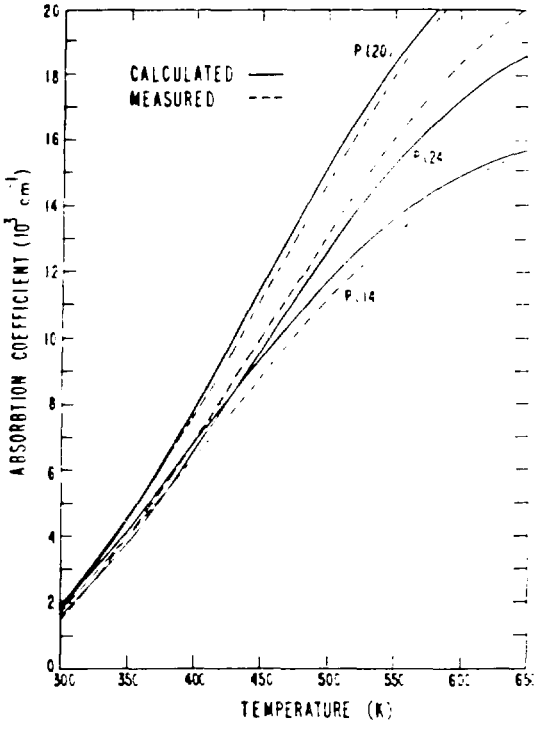

Fig. III 33.
Comparison of calculated and measured line-center absorption coefficients in pure CO_2 at 200 torr at various temperatures for three lines of the 10.6 μm branch.

Calculation of Target Induced Parasitics in Antares (J. C. Goldstein)

The statistical fluctuations in switching high voltage to the four longitudinal sections of an Antares amplifier cause discharge initiation timing errors in each section. The SPON8 code was created to study the effects of these errors on target induced parasitics in Antares. If each section initiates the pumping discharge on time, the gain of the amplifier when the short pulse arrives will be just enough to yield a 100-kJ pulse on the output. If some sections fire early, the gain rises sooner and more time is given for parasitics to grow.

Table III IV lists the computed results for the energy density absorbed by the target, $E_{ABS}(t_0)$, in J/cm^2 up to the time of arrival (t_0) of the main pulse, and the maximum intensity on the surface in W/cm^2, for various time delays (in ns; negative delay means early initiation) of the four longitudinal pumping sections of one of the six power amplifiers. The calculations show that a 200-ns early initiation of the entire amplifier is roughly equivalent to zero timing error, but to a 15% higher gain coefficient in all sections.

Figure III 34 shows $E_{ABS}(t_0)$ for various timing errors, assuming the same timing error for each of the four pumping sections. The inset shows the corresponding gain curve. Note that, due to modified system parameters and improved computational methods, target induced parasitics in Antares are calculated to be well below the GMB damage threshold of ~0.5 J/cm^2.

Nonlinear Optical Phase Distortion in NaCl (C. J. Elliott)

In our CO_2 laser fusion program, we have consistently used NaCl windows because of their high damage threshold, availability in large diameters (currently, 45 cm), and adequate material strength.[30] Because salt, a solid-state material, is irradiated at high intensities, self focusing and phase distortion are natural concerns. We require good beam quality for fusion experiments, and therefore seek phase distortions less than $\lambda/10$—one-tenth of the wavelength; achieving this goal

TABLE III-IV

ENERGY DENSITY AND MAXIMUM INTENSITY ABSORBED BY A FUSION TARGET FROM PARASITICS IN ONE ANTARES AMPLIFIER FOR VARIOUS DISCHARGE INITIATION TIMING ERRORS IN EACH OF THE FOUR LONGITUDINAL PUMPING SECTIONS.
GMB DAMAGE, >0.5 J/cm²

Type	$E_{ABS}(t_0)$ (J/cm²)	$I(t_0)$ (W/cm²)
0.0.0.0	9.107×10^{-1}	7.385×10^{3}
100.0.0.0	1.669×10^{0}	1.405×10^{4}
200.0.0.0	2.924×10^{0}	2.441×10^{4}
200, 100.0.0	5.606×10^{0}	4.716×10^{4}
200, 200.0.0	1.012×10^{1}	8.271×10^{4}
200, 200, 100.0	1.983×10^{1}	1.610×10^{5}
200, 200, 200.0	3.631×10^{1}	2.839×10^{5}
200, 200, 200, 100	7.194×10^{1}	5.555×10^{5}
200, 200, 200, 200	1.330×10^{2}	9.860×10^{5}

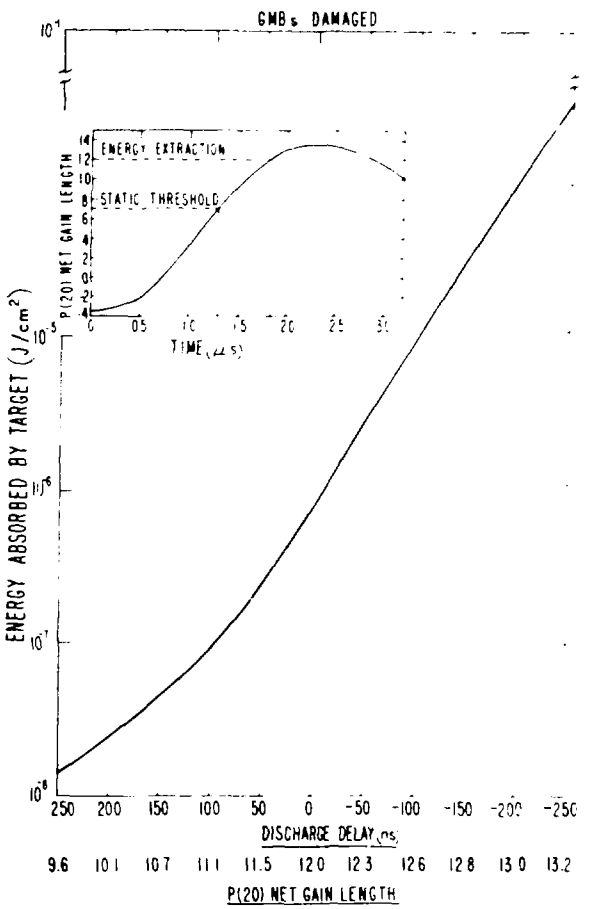

Fig. III 34.
Energy density absorbed by the target due to the growth of parasitics in one Antares amplifier for various discharge initiation timing errors.

automatically guarantees that self focusing cannot occur. Appreciable self focusing does not set in until phase distortion of λ or greater occurs. It appears that a distortion of $\lambda/10$ is easily obtained for 10 μm fusion applications.

The phasor of the electric field in traveling a distance l in a medium of index of refraction n at wavelength λ is $\exp(2\pi i n l/\lambda)$. The optical path length P measured in wavelengths is just nl/λ. For salt we expect

$$n = n_0 + n_2 \langle E^2 \rangle ,$$

where n_2 is the nonlinear index of refraction; E is the optical electric field expressed in statvolts, and is averaged over a period of the wave, indicated by $\langle \cdots \rangle$. The change in optical path δP due to the field E is just

$$\delta P = n_2 \langle E^2 \rangle 2l/\lambda .$$

The Poynting vector in Gaussian units is related to the intensity I in W/cm² and E in cm/s by

$$10^7 I = \frac{c}{4\pi} \langle E \times B \rangle = \frac{cE^2}{4\pi} \langle E^2 \rangle ,$$

so that

$$\delta P = \frac{4\pi \cdot 10^7}{cE^2} I \frac{2l}{\lambda} n_2 .$$

The above expressions assume antireflection coatings on the salt windows.

The optical path change δP is not the phase distortion of the beam. The distortion introduced into the beam is related to the transverse gradient of δP across the beam. A measure of the distortion is then ΔP, which is the change in δP across the beam, and

$$\Delta P = \frac{\Delta x}{x} \frac{4\pi \cdot 10^7}{cE^2} I \frac{2l}{\lambda} n_2 .$$

The factor $\Delta I/I$ is a measure of the beam spatial nonuniformity. A conservative estimate for $\Delta I/I$ is unity, which would be used when there is concern that the energy in the spatial edge of the beam goes with the rest of the beam. For our estimate, we take $\Delta I/I = 1/2$; it is conceivable that if we are concerned with only 85% of the energy, $\Delta I/I$ could be as small as 1/5.

The peak intensity can be determined on the basis of a triangular temporal profile. In this case, the energy pulse width (the illuminance in J/cm² divided by the peak intensity) is the same as the FWHM intensity. Thus, we use $I = 3 \times 10^9$ W/cm² for this calculation. If we consider FWHM 0.5-ns pulses rather than FWHM 1 ns pulses, the phase distortion doubles.

Another approach to beam focus for Gaussian beams described by Goldstein[11] and Suydam[12] gives the ratio of the square of the best rms spot size of a focused Gaussian beam to that of a focused beam that first went through a thin nonlinear medium. In terms of our notation, this ratio is

$$R_1 = \frac{1}{1 + \frac{7}{9}(\delta P)^2} ,$$

and may be compared to the Strehl ratio. If we do not refocus the system to compensate for the nonlinearity, but stay at the point of best focus for a purely Gaussian beam, this ratio becomes worse as

$$R_2 = \frac{1}{1 + \frac{16}{9}(\delta P)^2} .$$

The peak intensity ratio (Strehl) of a Gaussian beam traveling through a thin nonlinear medium to that of a pure Gaussian is given by

$$R_3 = \frac{C^2(\sqrt{4\delta P}) + S^2(\sqrt{4\delta P})}{4\delta P} = 1 - \frac{16}{45}(\delta P)^2 + \frac{1024}{1890}(\delta P)^4 + O(\delta P)^6 ,$$

where C and S are the usual Fresnel integrals.[13] This latter result is at the plane of the best focus for the purely Gaussian beam.

Each ratio suggests a different wavelength criterion. At our $\lambda/10$ criterion, we compute $R_1 = 93\%$, $R_2 = 85\%$, $R_3 = 97\%$. The Strehl ratio R_3 indicates that the beam is quite acceptable; however, the R_2 criterion indicates that it is marginal.

The first determination of n_2 at 1.06 μm was made by Smith, Bechtel, and Bloembergen[14] by examination of optical breakdown in NaCl. They obtained different intensities in the focal spot by using different focal-length lenses. Then they plotted the reciprocal beam power at breakdown vs the reciprocal beam waist in the absence of self focusing, and they obtained a straight line whose intercept is a measure of n_2. A problem with this experiment is that it is invalid if the breakdown intensity depends on the focal-spot size. The interpretation also depends on the model for self-focusing. At 1.06 μm, they obtained $n_2 = (6.5 \pm 3.2) \times 10^{-13}$ esu.

The second determination, by Weber, Milam, and Smith,[15] used time-resolved interferometry. It is a direct measurement of the nonlinear phase shift, independent of

the mechanism. They report $n_2 = (1.2 \pm 0.2) \times 10^{-13}$ esu.

Our measurement[36] was not sensitive enough to detect any ellipse rotation, implying a value of χ_3^{1221} of less than 3×10^{-14} esu. The quantity n_2 is given as

$$n_2 = \frac{12\pi}{n}\chi_3^{1111} ,$$

and we measured χ_3^{1221}. When the electronic mechanism dominates for an isotropic substance[37]

$$\chi_3^{1111} = 3\chi_3^{1221} .$$

The upper bound for n_2 is, thus, estimated to be

$$n_2 < 23 \times 10^{-13} \text{ esu}.$$

This value is in doubt due to the possibility of nuclear contributions and anisotropic effects.

Several ways of estimating n_2 from the linear index of refraction have evolved, the simplest[38] of which is $X_1 |X_1|^4 \times 10^{-10}$ esu, which gives $n_2 = 2 \times 10^{-13}$ esu. Wang's rule[39] was used by Goldstein[34] to compute $n_2 = 4.8 \times 10^{-13}$ at 10 μm, however this type of estimate is of uncertain validity. Boling, Glass, and Owyoung[40] show a free parameter in the theory, which depends on the nature of the important resonances. If the resonances change as we go from 1 to 10 μm, the formula would change. If the resonances do not change in going from 1 to 10 μm, we would expect the 1 μm value of n_2 to be a good measure of the 10 μm value. However, the 1 μm value was for crystalline salt, not the polycrystalline salt used in our windows.

The various determinations of n_2, summarized in Table III V, suggest a conservative estimate of $n_2 \approx 5 \times 10^{-13}$ esu at 10 μm. At this value and using $I = 3 \times 10^9$ W cm^{-2}, $\Delta I / I = 0.5$, $L = 14$ cm, and $n = 1.5$; $\Delta P = 0.028$, a distortion of only $\lambda/36$.

CO_2 LASER SYSTEMS STUDIES

Introduction (E. E. Stark)

The CO_2 Laser Systems Studies were begun to define the key driver performance criteria influencing the feasibility of inertial confinement fusion. These criteria are cost, efficiency, reliability, life, and maintenance requirements. The technical studies addressing these issues include development of systems concepts, analysis of advanced technology impacts, and specific subsystem optimization studies. New baseline designs that have extended the technology of single-pulse amplifiers will serve as a standard against which multipulse schemes will be judged.

Emphasis has been placed recently on scoping the CO_2 laser's short pulse amplification efficiency, one of its major advantages as an inertial confinement fusion driver.

Design of CO_2 Laser Amplifier for Future Systems (J. C. Comly, C. J. Elliott, K. B. Riepe)

Introduction. We have begun a long range study of the performance of high energy CO_2 amplifiers that can be used in future systems in the laser fusion program. The goals are

(1) to determine constraints on the module design imposed by cost, efficiency, beam quality, parasitics suppression, and material limitations;
(2) to model the many tradeoffs involved with minor module design variations and with radically different approaches; and
(3) to interface numerous existing Los Alamos codes for use in module optimization and, eventually, for systems design.

Our initial calculations were limited to simply scaling amplifier configurations and extraction schemes that have been demonstrated in our working systems. We intend to use a laser system designed in this conservative manner as a reliable yardstick for comparing alternative concepts. Therefore, the examples shown below apply to the following conceptual module: a rectangular discharge cavity with salt windows, amplifying a single 1 ns pulse with 4 lines in the 10.6 μm band. Figure III 35 shows curves[41] of constant output energy fluence E_{out} vs the gain length product $g_0 L$ and pressure. Potential operating points are shown for the following constraints: $g_0 L = 7.5$ (due to internal parasitics), $E_{out} = 2.5$ J cm^{-2} (due to salt damage), and minimum pressure. In such an amplifier concept, the size of the aperture will be limited by high voltage and salt window technology.

Power Supply Cost Minimization. Given the desired characteristics of the output pulse, we can design the amplifier module and its power supply. In a full systems study, a complete optimization would include many tradeoffs involving all the components of the laser and its

TABLE III-V

VARIOUS DETERMINATIONS OF n_2 FOR NaCl

Investigators	Wavelength (μm)	n_2(10^{-11} esu)
Smith, Bechtel, Bloembergen[14]	1.06	6.5 ± 3.2
Weber, Milam, Smith[15]	1.06	1.2 ± 0.2
Watkins, Phipps, Thomas[16]	10.6	~ 23
Simple rule	1.06 10.6	2
Wang's rule (Goldstein)[15, 16]	10.6	4.8

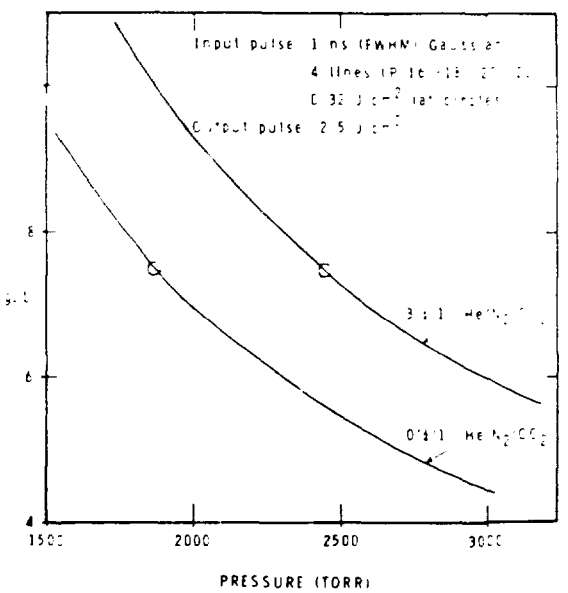

Fig. III 35.
Possible operating conditions for two CO_2 laser gas mixes, holding the output energy fluence constant at 2.5 J/cm²; the circles indicate operating points (pressures) where g_0L equals 7.5.

operating costs; however, an efficient and inexpensive module power supply package would still be our goal.

Figure III-36 shows the model used to optimize the performance of a Helios-type amplifier driven by an Antares type power supply. Because cost savings are often associated with large power supplies, we have allowed for driving N amplifier modules with one power supply; integer values for N are of most interest due to [illegible] mode and operational considerations.

The power supply model contains a capacitor C_s charged to a voltage V_s in series with an inductor L_s and a resistor R_s; the resistor represents the N amplifier module discharges, each with a length L in the optical path direction, a width W and a height D in the discharge direction. Conceptually, this is equivalent to pumping one discharge of length NL, and then subdividing it into pieces with the desired value of g_0L. Other simplifications made in the calculations were assumed to be constant (rather than dependent on the discharge voltage V_1), and L_s was specified at a value consistent with the largest V_s expected.

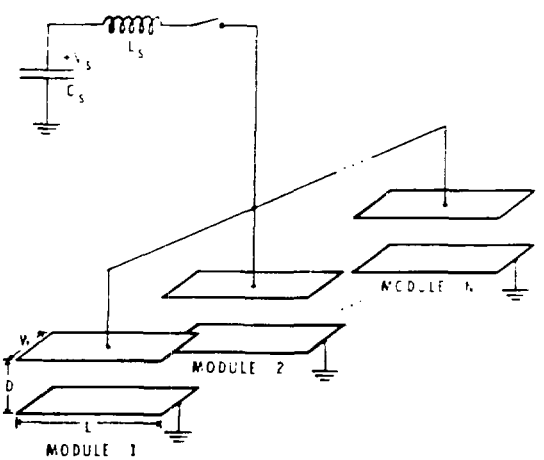

Fig. III-36.
Model of idealized single-mesh Marx bank driving N discharges, as used in the system optimization studies.

Results of a typical optimization run are shown in Fig. III 37: here the power supply energy is fixed at 225 kJ, and the number of attached amplifiers N is plotted as a function of the variables Q and NL, where Q is the usual circuit quality parameter related to the risetime of the voltage pulse, and NL scales the current density. The other parameters shown in the figure correspond to Helios dimensions and Antares power-supply components. As shown in Fig. III 36, the output fluence is 2.5 J/cm^2; thus, each module produces ~3060 J over its square aperture, or 2400 J over a 35 cm-diam circular aperture, giving an efficiency of EFF (%) 1.07 N (circular aperture). Figure III 38 shows, for this case, the peak current density J_{max}, the time to peak gain t_{gain}, and the module length L.

The kinetics portion of the code as used was developed by Lockett[42] and modified by W. Leland of Los Alamos. The general causes for the peaked behavior of the efficiency (N) are explained as follows. At low Q, the gain peaks before the input power pulse has risen very far; at high Q, the current rings, with decreasing energy in the first cycle; at very large NL, the current density is too low to pump to a positive gain; and at very low NL, efficiency drops because there is a limited g_0 that can be attained for any pumping.

The code also includes a model for the cost of the power supply, based on state-of-the-art components as used in Antares; Table III-VI shows that, in this model, there is a fixed cost of $59k per Marx bank, along with a marginal cost of $0.29 J. In most cases, these costs were obtained by matching data at Marx energies of 40 and 300 kJ; the switch costs, however, are based upon current and charge transfer, which relates to stored energy. The oil cost is based on $1 gal.; "Miscellaneous" includes relays, resistors, hanging hardware, trigger systems, and other. Overhead and profit were assumed to be 30% of the other costs; cable costs were not included.

This cost model cannot determine the optimum amplifier design, because, for example, all points along the N = 4 curve in Fig. III 37 have the same supply cost per module (or per joule of output). However, operating and construction costs may suggest using the minimum module length, leading to the design point labeled L_{min} on Fig. III 38; in other cases, this point may be moved to reduce t_{gain} (reducing parasitics) or J_{max} (improving

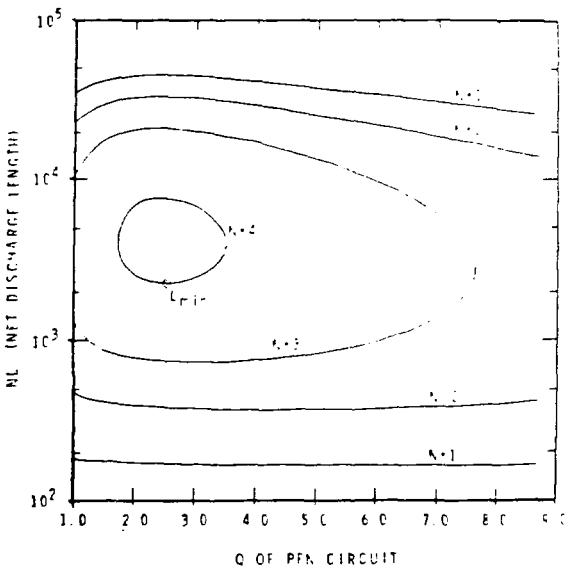

Fig. III 37.
Number of discharge modules N that can be driven by a single-stage PFN vs the circuit Q-value and the net gain-length NL. The supply energy is held fixed at 225 kJ, the inductance at 2.5 μH, and the peak voltage across the discharge at 500 kV; the discharge cross section is 23 by 35 cm, the gas is 2438 torr of a 3:0.25:1 mix, and each module has a g_0L = 7.5. The point L_{min} indicates the shortest N = 4 configuration.

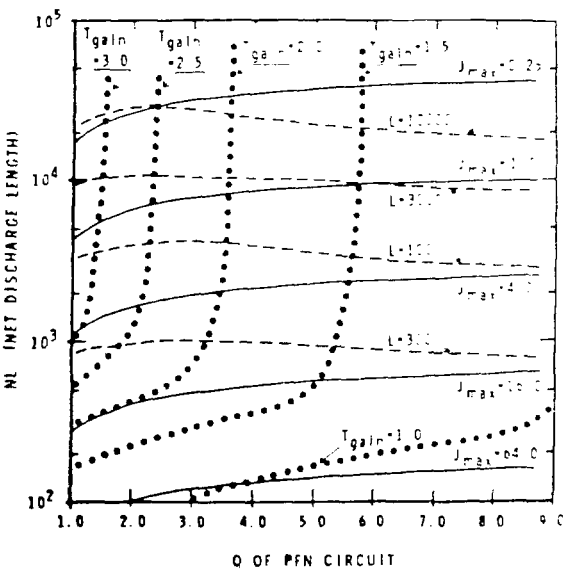

Fig. III 38.
Contours of constant peak current density J_{max} (A/cm^2), time to peak gain t_{gain} (μs), and module length L(cm) for the parameters of Fig. III 37.

TABLE III-VI

COSTS OF POWER SUPPLY COMPONENTS[a]

Cost Item	Fixed Cost (10^3 $)	Marginal Cost/Joule (¢)
Capacitor	$ 8.5	3.8
Switches	0.4	1.5
Tank	8.5	3.8
Oil	3.0	1.3
Assembly	8.5	3.8
Miscellaneous	16.9	7.7
Overhead & Profit	13.7	6.6
Total	$59.	29.

[a] The model assumes a single stage PFN. A linear relationship between the supply energy and the cost has been used.

uniformity). Using the minimum length criterion and varying E_s, the curves in Fig. III-39 were obtained. Values of E_s up to 300 kJ were used, but there is little marginal gain in driving more than four modules. A system design point can be obtained from this figure when the incremental costs of increasing L are known.

Some general conclusions can be drawn from this study.

1. The results confirm our previous analyses, which showed that good laser efficiencies are possible with a single stage PFN (pulse forming network) power supply (the N = 4 curve in Fig. III-37 implies over 5% onto a square aperture); the field-dependent resistivity will further improve the efficiency.
2. Low gain modules with low current densities appear to yield good efficiencies while alleviating nonuniformities from magnetic pinching; the point L_{min} in Fig. III-37 is for a 569-cm long module, with a peak g_0 of 0.0132 cm^{-1}, and a peak current density of 2.99 A cm^2 (for which the gain uniformity should be quite good).

Uniformity in Large Aperture CO_2 Amplifiers. To produce more energy per amplifier, future CO_2 systems will probably use larger apertures. We have examined the possibility of scaling our present design philosophies to such systems. Figure III-40 shows the electron-beam deposition density, as calculated with a Monte-Carlo electron transport code, for a module with a 66-cm-diam aperture. For this example, the gas mix (0.5:0.25:1::He:N_2:CO_2 at 1875 torr) was taken from Fig. III-35 to yield an output energy E_{out} of 2.5 J/cm^2 at a g_0L value of 7.5. The current density of 5.833 A/cm^2 is the same as the Antares design point, scaled with pressure. The 66-cm-diam salt window and megavolt cables are consistent with present technology.

Figure III-41 shows the corresponding distribution of discharge power for this module. The uniformity in this contour plot compares favorably with similar calculations for Helios and other Los Alamos systems, suggesting that the module's output would be acceptable. To a good approximation, the intensity in the beam is expected to follow the discharge power distribution; quantitatively, this leads to a value of 0.772 for the ratio of average to peak intensity. This result implies a peak fluence of 3.2 J cm^2 with an output energy of 8553 J in a circular beam.

Several techniques are available for improving the uniformity of such a discharge; for example, the anode and or the cathode can be shaped or the e-beam can be selectively masked. Also, we discussed in the preceding section the benefits to efficiency and uniformity with a device of lower current density. Finally, a magnetic guide field could be applied, although this does not appear essential. Thus, we can conclude that present CO_2 discharge systems can be scaled successfully to larger apertures without degradation of uniformity.

Multipulse Energy Extraction in CO_2 Laser Amplifiers (H. C. Volkin)

The specific pumping kinetics of the electric discharge-excited CO_2 laser make efficient energy storage in this laser possible. With multipulse energy extraction in CO_2 laser amplifiers, we can convert a significantly higher fraction of the vibrational energy stored in the gas by the discharge into laser light. The time scale for efficient energy extractions is determined by the collisional transfer rates for the flow of vibrational energy into and among the various vibrational modes of the gas molecules. Figure III-42 shows typical collisional transfer times of the following V-V processes that transfer vibrational energy:

1. intermolecular V-V transfer from N_2 into the antisymmetric stretch-(A) mode,
2. intramode vibrational relaxation within the A-mode,
3. intramolecular V-V transfer from the symmetric stretch-(S) mode into the bending (B) mode through the strongly coupled Fermi-resonance levels,

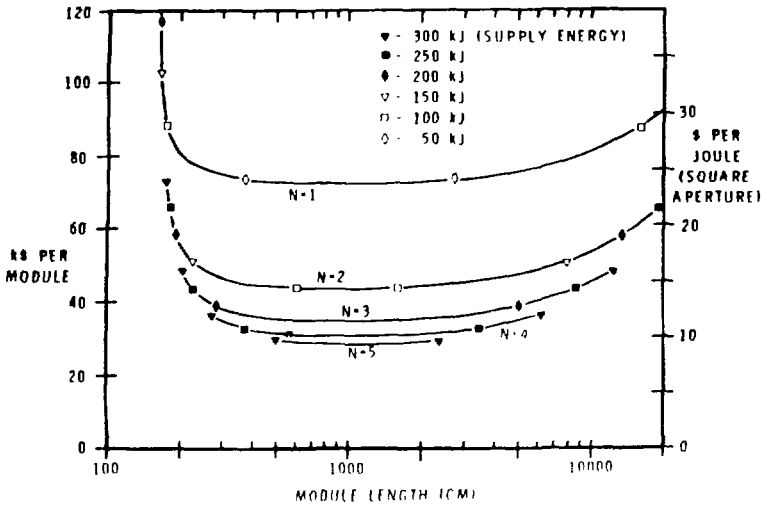

Fig. III 39.
Power supply cost vs module length. N is the number of modules driven with one power supply, and the circled point corresponds to the point L_{min} of Fig. III 37. The required power supply energies are shown at some points.

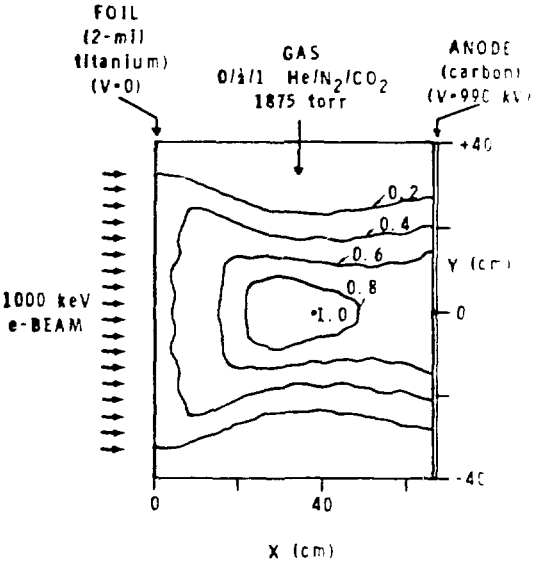

Fig. III 40.
Distribution of energy deposited by an electron beam at 1 MeV entering (through the foil) into a 66- by 66-cm discharge; the contours have been normalized to the peak. The discharge voltage is 990 kV and the current is 5.83 A/cm^2.

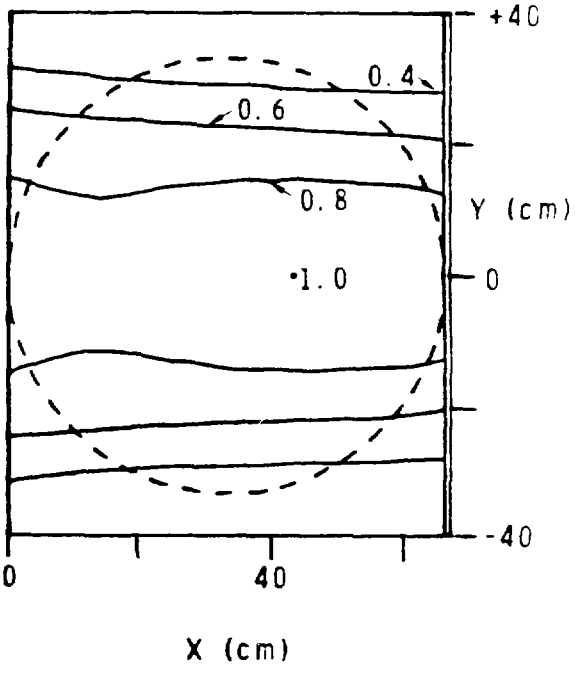

Fig. III 41.
Distribution of discharge power (pumping power) for the case shown in Fig. III 40; the contour values are relative. The laser aperture position is shown by the dotted lines.

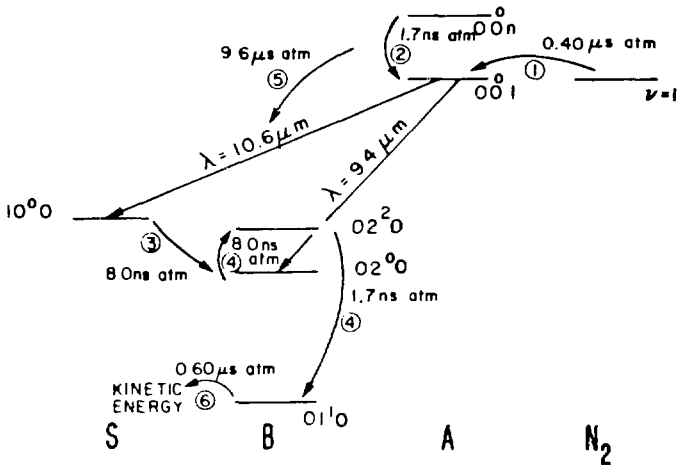

Fig. III-42.
Molecular kinetics of CO_2 laser. S, B, A refer to the symmetric stretch, bending, and asymmetric stretch vibrational modes of the CO_2 molecule. Processes 1 through 6, explained in the text, have relaxation times that scale inversely with pressure. The energy transfer times for the processes shown apply to $He:N_2::CO_2::3:1:1$ gas mix at 300 K.

4. intramode vibrational relaxation in the B mode,
5. decay of vibrational energy stored in the A mode by the intramolecular V-V transfer into the S and B modes, and
6. vibrational energy into kinetic energy of the gas molecules by V-T energy transfer from the B mode (V-T conversion occurs also to some extent in the V-V transfer processes because the initial and final vibrational energies of the collision partners are not precisely equal).

After energy is extracted by a short optical pulse passing through an amplifier, processes 1 and 2 replenish the population of the upper lasing level ($0.0^0,1$), and processes 3 and 4 empty the lower level. Process 5 determines the inversion lifetime. Process 6 relieves the "bottleneck" at the ($0,1^1,0$) level in the relaxation of the lower lasing level but raises the gas kinetic temperature. The V-V transfer times given in Fig. III-42 apply to a $3:1:1::He:N_2:CO_2$ gas mixture at 300 K.

Population inversion on the 10.6- and 9.4-μm bands is produced in the electric discharge by electron collisions with CO_2 and N_2 molecules, which vibrationally excite these molecules. In the multiple-pulse (multiplex) energy extraction technique, a timed sequence of two or more light pulses is sent, one at a time, through the power amplifier during and after each electrical discharge.[43,44] When a nanosecond optical pulse propagates through the amplifier, vibrational energy stored in the nitrogen molecules and in the higher levels of the A-mode is unavailable for energy extraction because of the time scale of vibrational relaxation. However, the stored energy continually flows into the upper lasing level ($00^0 1$). After a suitable time interval, vibrational relaxation and (during the discharge) electronic excitation restore the population inversion sufficiently to permit energy extraction by another optical pulse. In the limit of very short time intervals between the optical pulses, the efficiency approaches a quasi-cw value. For a $3:1:1::He:N_2:CO_2$ gas mixture, the quasi-cw efficiency is 28%.

To use the train of optical pulses in laser fusion, it must be possible to separate them spatially so that they can be directed along different paths. By choosing the path lengths carefully, time delays can be introduced that enable all the pulses to arrive simultaneously on a single target or allow various groups of pulses to irradiate different targets. Figure III-43 shows schematic optical techniques by which the required spatial separation can be realized.

- In angular multiplexing (AM), each pulse traverses the amplifier at a slightly different angle and the pulse paths diverge after leaving the amplifier.
- In frequency multiplexing (FM), all the pulses travel collinearly through the amplifier, but each pulse has a different frequency, that is, corresponds to a different line in the 10.6- or 9.4-μm vibration-rotation band. After leaving the amplifier, the pulses strike a large diffraction grating from which their paths separate.

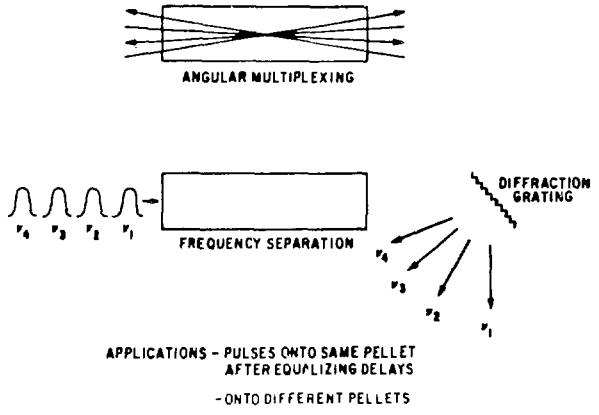

Fig. III 43.
Multipulse amplification schemes.

The FM approach uses the volume of gain medium more completely than that of the AM, whose volume use decreases with increasing number of pulses. Another advantage of the FM method is that all the pulses may be combined into a single short pulse by introducing suitable time delays, then reflecting the pulses simultaneously from a second grating into a collinear path. But FM requires further grating development, whereas AM uses current technology.

The performance attainable with multiplex energy extraction is calculated with our discharge kinetics computer code. Some results are given in Figs. III-44 through III-47. The cumulative electrical-to-optical efficiency reached with each optical pulse is indicated by an X, and the curves show the gain evolution with time between pulses.

The results shown are for a 3:1:1::He:N^2:CO_2 gas mixture, which has been found to give good efficiency. (Somewhat lower efficiencies are obtained with a helium-free mix of, for example, 0:1:2.) The following conditions are used:

Gas mix, 3:1:1

Fill pressure and temperature, 1800 torr and 300 K

Electric field, optimum for the mix

Discharge time duration, 2 μs.

With no discharge excitation, the gain following an energy extraction recovers to a maximum value in ~250 ns at 350 K. The total energy deposition by the discharge is 260 $J\ell^{-1}$. Each optical pulse is assumed to extract all the available energy in the 10.6-μm band at pulse time.

Figure III-44 shows six pulses during the discharge, the first at 0.7 μs after the start and the rest spaced at intervals of 260 ns. The pulses after the discharge are timed to occur at maximum gain recovery, which is ~260 ns. The next case illustrates how, during the discharge, the peak gain can be kept fixed and the pulse energies equalized. In Fig. III-45, each of the six pulses in the discharge occurs just as the gain coefficient reaches the value $g_0 = 2.5\%\ cm^{-1}$. In the third case, the gain peaks in the discharge are kept at $g_0 = 2\%\ cm^{-1}$, as shown in Fig. III-46. Figure III-47 shows a typical result with three pulses in the discharge, which gives larger energies for these pulses.

Following a 2-μs discharge without energy extraction, the gain coefficient reaches 3.9% cm^{-1} and does not increase significantly thereafter by vibrational relaxation. A single energy extraction at the end of the discharge gives a pulse energy of 9.48 $J\ell^{-1}$ and an efficiency of 3.65%. Under the conditions selected, the multiplex energy technique has increased the energy extracted and the efficiency by more than fivefold. Also, problems of parasitic oscillation can be mitigated by the multiplex approach because the peak and average gains in the amplifier can be kept to desired values by appropriate timing of the pulse sequence. The results illustrate the high electrical-to-optical efficiencies, attractive for future commercial applications, that can be achieved with CO_2 lasers.

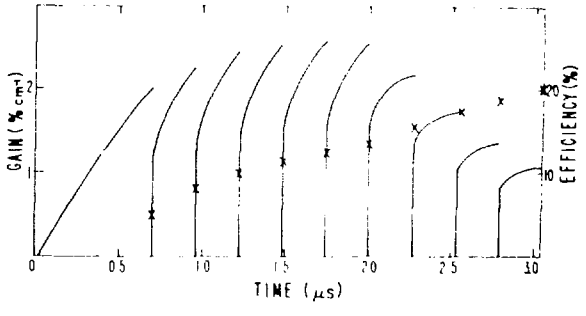

Fig. III 44.
Six pulses amplified during the discharge at 260-ns intervals. Gain histories and cumulative efficiencies (X) are shown.

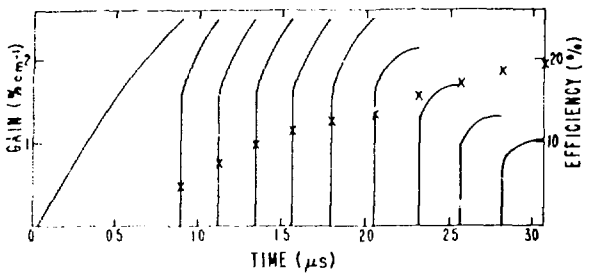

Fig. III-45.
Six equal energy pulses can be extracted during the discharge by timing them to occur at g_o 2% cm^{-1}.

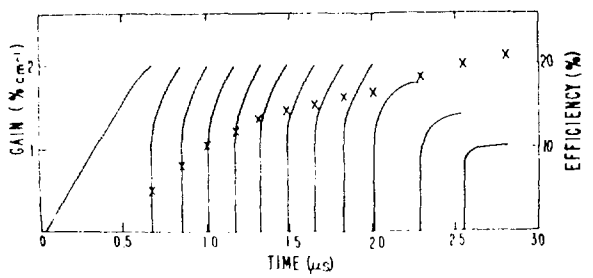

Fig. III-46.
Nine equal-energy pulses during the discharge, timed to occur at g_o 2% cm^{-1}.

Multipass Irradiation of a Flowing-Gas Reaction Chamber (J. J. Devaney)

We have addressed two specific problems in the multipass illumination of a gas reaction chamber. The first question is whether hot spots of higher-than-average light intensity exist. Higher intensity as well as lower intensity (along surfaces parallel to mirrors and spaced one-half wavelength divided by the sine of the angle of incidence) is an inevitable concomitant of the quasi-standing wave formed by mirror boundary conditions on the light wave. Second, the net effect of mirror irregularities upon irradiation was considered, and a ray-tracing algorithm for determining the effect of irregularities whose scale is significantly greater than a wavelength was derived. For most efficient use of the available laser light, the chamber mirrors should be very slightly canted to prevent escape of the laser beam at the far end rather than using an external mirror at that end.

High-Gain Facility Definition (J. J. Devaney)

Extrapolation of our first-wall erosion studies on carbon to copper and to salt (NaCl) permitted preliminary assessment of the suitability of these two materials for last optical surfaces in a high-gain laser facility (1 or more MJ in gains of 100 or more). Erosion of these surfaces occurs from x rays, ion heating, and sputtering. The studies were made at two radii, 8.5 and 10 m, for two pellet outputs typical of early 300-MJ-yield pellets and later for outputs of 120 to 170 MJ. The chamber atmospheres considered ranged from vacuum to 10^{17} Ar/cm^3, as well as to 10^{17} Xe/cm^3 (3.1 torr at 300 K). Assuming that uniform erosion *per se* of an optical surface is not damaging, we used erosions of 3 μm ($\sim\lambda/3$) as our criterion for unacceptable damage. Because it is not clear whether this assumption is realistic, we have recommended that the appropriate criterion be determined experimentally. Note that alterations of optics visible to the eye do not determine the

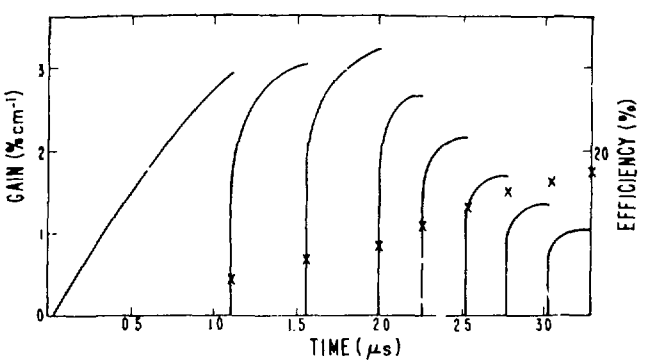

Fig. III-47.
Three pulses amplified during the discharge.

operational damage of optics to functional use by the much higher CO_2 wavelength (10.6 vs 0.55 μm). However, using the 3-μm erosion criterion, we have calculated erosion rates shown in Tables III-VII and -VIII. The data show that, without gas protection, salt optics are unacceptable except for the weakest pellet effects at a distance of 10 m. On the other hand, copper mirrors appear acceptable at distances of 8.5 and 10 m for both pellet types without gas protection.

Gas protection begins to be effective at 10^{13}/cm^3 (xenon) and at 10^{14}/cm^3 (argon). The ions are stopped in the chamber at densities of 10^{15}/cm^3 and above. At 8.5 m, salt is not sufficiently protected against all effects by an atmosphere of 10^{16} Ar/cm^3, although it is protected for that density of xenon. However, the higher densities studied for surface protection are unlikely to permit accurate laser beam focusing or efficient transmission onto a small pellet. This matter is extremely uncertain theoretically; however, a preliminary experiment of this type does rule out densities greater than 10^{16} Xe.cm^3 (Ref. 45). Consequently, we have determined that the final optical surface for the high-gain facility can be copper placed at a distance of at least 10 m from the microexplosion. We reserve the options of adding a small amount of chamber gas uniformly or of using a higher density (differentially) close to the mirrors if needed.

For flexibility and uniformity of pellet illumination we recommend that eight laser beams bundled into beam groups be focused symmetrically along the apexes of a cube, the upper half (4 bundles) being rotated relative to the lower by 45° about a vertical axis.

Based on Monte Carlo calculations[46,47] for the Antares 100-kJ laser facility, we have calculated dose rates expected within and outside the target chamber, outside the facility, and down the laser pipes. For a facility yield of 100 full-scale shots of 100 MJ of thermonuclear yield per year (i.e., 10 GJ yield per annum) in a conventional Helios-like design, we estimate the total dose in the laser hall through the light pipes to be 0.3 mrem/yr with the dose from the direct shine down the laser pipes into the laser hall being only 13 prem/shot or less. Thus, the total dose is primarily derived from neutrons that have followed a multiple scattering and absorption path. Good, conservative working levels (84 mrem/yr) in the target building can be achieved with 2.67-m-thick concrete or equivalent shielding. Close-in shielding is advantageous because it is less massive, less expensive, and allows beneficial use of the remainder of the target building external to the shield even during full-scale shots. However, shielding of the light pipe some distance beyond the chamber shielding is required.

Total dose per year to the public outside the grounds is 0.42 mrem yr, a very low value (the natural dose at high altitudes is ~170 mrem yr). The maximum direct dose in the laser hall from the microexplosions is 0.9 mrem yr, without laser hall shielding. The unshielded laser electron guns impart a much higher dose from x rays (one dual module operating at 200 pulses week in typical Helios experience of gas present gas absent gives a mean dose of ~100 rem yr). A shield of only 0.45 cm thick lead, or 32 cm thick standard concrete, drops this dose to 100 mrem yr. For the same parameters except voltage, a 1 MV gun needs 7.2 cm of lead or 48 cm of concrete to reduce the dose the same amount.

Target chamber residual radioactivity is only a problem within the target concrete shield. Outside that shield the doses are negligible, ranging from 0.05 μrem h immediately after 100 full scale shots to 2 prem h after 1 month of cooldown. The highest induced activity within the shield and just outside the target chamber vacuum vessel is 815 rem h (100 shots, immediately after the last shot), and 0.05 rem h after one week of cooldown. These radioactivity fields are far in excess of maximum permissible yearly working fields (0.25 mrem h or 5 rem yr). It is possible with the use of exotic structural materials such as quartz or Kevlar composites to reduce postshot doses to acceptable working levels after 0.5 to 7.0 days of cooldown if pellet debris is removed or debris is not radioactively limiting, and if the integrated dose from copper mirrors can also be kept low. For prompt postshot access, aluminum is not a suitable structural material because it is worse than iron up to 8 days after the last shot. However, it is a tentative choice for construction because its long term activity is low (~1 mrem h within the target chamber 1 month following 100 shots at 100 MJ over a year) and its use in construction is well understood.

Unfortunately, copper, although resistant to pellet and laser damage, provides isotopes with long lived activities (12.9 h, 5 yr, 92 yr) leading to high activities near a copper-coated mirror. For a 70 cm diam (that is, f 15 and f = 10 m) 40-mil-thick copper-coated mirror on a substrate of 9.0 cm (3.5 in.) of 6061 aluminum with a 15.25-cm (6.0 in.) solid 6061 aluminum space frame equivalent to the same area as the mirror, we estimate a dose of 0.79 mrem/h after one week following one shot (100 MJ), and a 1.6 mrem/h after one week following 100 shots over 1 year (100 MJ each). This dose is for only one mirror along the centerline at a distance of

TABLE III-VII

EROSION OF COPPER SURFACE—ABRIDGED RESULTS[a]

Chamber Atom Density (cm^{-3})	Erosion from, or Lifetime	Argon				Xenon				
		Case I		Case II		Case I		Case II		
		r=8.5 m	r=10 m	r=8.5 m	r=10 m	r=8.5 m	r 10 m	r=8.5 m	r=10 m	
0	Total erosion	3.5(−6)	3(−8)	1(−6)	5.2(−7)	3.5(−6)	3(−8)	1(−6)	5.2(−7)	
	lifetime	86.	1.(4)	294	581	86	1.(4)	294	581	
10^{13}	Total erosion	3.5(−6)	3.(−8)	9.6(−7)	4.8(−7)	3.4(−6)	3(−8)	8.7(−7)	4.3(−7)	
(0.3 mtorr)	lifetime	86	1(4)	314	627	88	1.(4)	347	702	
10^{14}	Total erosion	3.4(−6)	2.9(−8)	4.3(−7)	1.8(−7)	2.9(−6)	1.6(−8)	8.7(−13)	1.7(−17)	
(3.1 mtorr)	lifetime	89	1.1(4)	690	1693	103	1.9(4)	3.4(8)	1.7(13)	
10^{15}	Total	2.5(−6)	7.3(−10)	6.7(−13)	1.3(−20)	6.3(−7)	1.4(−10)	1.(−32)	6.1(−41)	Ions fail
(31 mtorr)	lifetime	120	4.1(5)	4.5(8)	2.4(16)	478	2.1(6)	3(28)	4.9(36)	to reach
10^{16}	Total	1.4(−7)	2.5(−11)	7.3(−34)	2.8(−42)	1.4(−13)	2.2(−18)	0	0	surface
(0.31 torr)	lifetime	2134	1.2(7)	4.1(29)	1.1(38)	2.1(9)	1.4(14)			
10^{17}	Total	4.5(−20)	5(−26)	0	0	5.1(−80)	1.5(−96)	0	0	
(3.1 torr)	lifetime	8.7(15)	8(21)			5.9(75)	2(92)			

[a]Erosion is in cm/shot; lifetimes in number of shots to erode 3 μm.

TABLE III VIII

EROSION OF SODIUM CHLORIDE SURFACE - ABRIDGED RESULTS[a]

Chamber Atom Density (cm^{-3})	Erosion or Lifetime	Argon				Xenon				
		Case I		Case II		Case I		Case II		
		r 8.5 m	r 10 m	r 8.5 m	r 10 m	r 8.5 m	r 10 m	r 8.5 m	r 10 m	
0	Total erosion	2.8(4)	9.7(8)	9.4(5)	4.7(5)	2.8(4)	9.7(8)	9.4(5)	4.7(5)	
	lifetime	1.07	3.1(3)	3.2	6.4	1.07	3.1(3)	3.2	6.4	
10^{13}	Total erosion	2.8(4)	9.7(8)	8.8(5)	4.2(5)	2.8(4)	9.5(8)	7.9(5)	3.6(5)	
(0.31 mtorr)	lifetime	1.07	3.1(3)	3.4	7.2	1.09	3.1(3)	3.8	8.2	
10^{14}	Total erosion	2.7(4)	9.4(8)	3.7(5)	1.3(5)	2.4(4)	7.7(8)	1.4(10)	2.8(15)	
(3.1 mtorr)	lifetime	1.10	3.2(3)	8.1	23.4	1.27	3.9(3)	2.2(6)	1.1(11)	
10^{15}	Total	2(4)	6(8)	1.1(10)	2(18)	5.1(5)	1.2(8)	1.6(30)	9.65(39)	ions fail
(31 mtorr)	lifetime	1.47	5.(3)	2.8(6)	1.5(14)	5.9	2.6(4)	1.9(26)	3.1(34)	to reach
10^{16}	Total	1.1(5)	2.(9)	1.2(31)	4.4(40)	1.2(11)	1.8(16)	0	0	surface
(0.31 torr)	lifetime	26.2	1.5(5)	2.6(27)	6.9(35)	2.6(7)	1.7(12)			
10^{17}	Total	3.7(18)	4.1(24)	0	0	4.1(78)	1.2(94)	0	0	
(3.1 torr)	lifetime	8.2(13)	7.4(19)			7.3(73)	2.5(90)			

[a]Erosion is in cm/shot; lifetimes in number of shots to erode 3 μm.

1.0 m in front of it. Off centerline the dose falls off. In an actual facility, additional doses will be derived from the other mirrors and from other structures. If the substrate and space frame could be made of quartz, the resulting Cu SiO structure could have the following doses 1.0 m in front of the mirror after one week of cooldown: 0.0011 mrem/h for one shot and 0.045 mrem/h after 100 shots over a year (all at 100 MJ yield each).

The greatest care in limiting the radioactive afterheat of chamber, mirrors, and structure will be to no avail if equal care is not expended in control of pellet debris radioactivity. Pellet debris is exposed to the most intense high-energy neutron flux, and, if activated, can dominate afterheats. For such a case, we recommend placing sacrificial liners or entrapping materials within the vacuum vessel, as well as chamber flush-out provision. Further, to avoid excessive downtime to allow for activity cooldown to levels permitting human entry, remote target chamber operation where possible is also recommended.

REFERENCES

1. J. Skoberne, Comp., "Inertial Fusion Program, July–December 1978," Los Alamos National Laboratory report LA-7587-PR (May 1980).

2. A. R. Johnston and R. D. S. Melville, Jr., Appl. Phys. Lett. **19**, 503 (1971).

3. C. R. Phipps, Jr., and S. J. Thomas, Appl. Phys. Lett. **25**, 313 (1974).

4. P. J. Mallozzi et al., Proc. Esfahan Symp. 167 (Wiley Interscience, New York, 1973).

5. N. H. Burnett and M. C. Richardson, Rev. Sci. Instrum. **47**, 241 (1976).

6. P. Weiss, Appl. Phys. Lett. **30**, 261 (1977).

7. J. A. Glaze, Opt. Eng. **15**, 136 (1976).

8. R. F. Benjamin, D. B. Henderson, K. B. Mitchell, and M. A. Stroscio, Appl. Phys. Lett. **31**, 511 (1977).

9. L. P. Bradley, W. L. Gagnon, and B. M. Carder, Proc. 7th Symp. on Engineering Problems of Fusion Research, Knoxville, October 25–28, 1977.

10. C. E. Max, W. C. Mead, and J. J. Thomson, Appl. Phys. Lett. **29**, 783 (1976).

11. Y. Kawamura, H. Takeda, M. Matoba, S. Nakai, and C. Yamanaka, Appl. Phys. Lett. **33**, 10 (1978).

12. S. Glasstone and R. H. Lovberg, *Controlled Thermonuclear Reactions* (van Nostrand, Princeton, 1960).

13. S. D. Rockwood, Proc. VIII Intern. Quantum Electronics Conf., San Francisco, 1974.

14. P. J. Berger and D. C. Smith, Appl. Phys. Lett. **21**, 167 (1972).

15. G. A. Hill, D. J. James, and S. A. Ramsden, J. Phys. D. (Great Britain) **5**, L97 (1972).

16. G. H. Canavan, W. A. Proctor, P. E. Nielsen, and S. D. Rockwood, IEEE J. Quant. Electron. QE-**8**, 564 (1972).

17. Yu P. Raizer, Sov. Phys. Uspekhi **8**, 650 (1966).

18. R. K. Ahrenkiel, J. F. Figueira, C. R. Phipps, Jr., D. J. Dunlavy, S. J. Thomas, and A. J. Sievers, Appl. Phys. Lett. **33**, 705 (1978).

19. W. W. Rigrod, J. Appl. Phys. **34**, 2602 (1963).

20. R. Hellwarth, J. Opt. Soc. Am. **67**, 1 (1977).

21. D. L. Bobroff and H. A. Haus, "Impulse Response of Active Coupled Wave Systems," J. Appl. Phys. **38**, 309–403 (1967).

22. R. B. Perkins and the Laser Fusion Program Staff, "Inertial Fusion Program, July–December, 1978," Los Alamos National Laboratory report LA-7755-PR (September 1980).

23. J. I. Steinfeld, I. Burak, D. G. Sutton, and A. V. Nowak, J. Chem. Phys. **52**, 5421 (1970).

24. R. T. V. Kung and H. W. Friedman, J. Chem. Phys., to be published (1979).

25. A. V. Nowak and J. L. Lyman, J. Quant. Spectrosc. Radiat. Transf. 15, 945 (1975).

26. R. F. Haglund, D. E. Casperson, S. J. Czuchlewski, C. J. Elliott, J. C. Goldstein, J. S. Ladish, and A. V. Nowak, "Optimization of a Multicomponent Gaseous Saturable Absorber for the Helios CO_2 Laser System," paper 21 12, Los Alamos National Laboratory Conference on Optics '79, Los Alamos, New Mexico, May 23 25, 1979.

27. J. C. Goldstein, "Calculation of Small Signal Gain," Los Alamos National Laboratory Conference on Optics '79, Los Alamos, New Mexico, May 23 25, 1979.

28. H. F. Doyle, "LINPR A Code to Solve Linear Programming Problems and Two Person Zero Sum Games," Air Force Weapons Laboratory report AFWL TR 74 35 (May 1974).

29. A. M. Robinson and N. Sutton, Appl. Optics 18, 378 (1 Feb. 1979).

30. W. H. Reichelt, J. C. Munroe, K. C. Jones, A. C. Saxman, and J. C. Sollid, "Antares Optical Design and Analysis," paper TUC9 1, topical meeting on Inertial Confinement Fusion, February 7 9, 1978, San Diego, California.

31. J. C. Goldstein, "Focal Spot Degradation for CO_2 Laser Due To Intensity Dependent Index of Refraction in NaCl Window," Los Alamos National Laboratory T-Division memorandum T 6(12 75)23 (1975). Several values in this memorandum have been revised. We use the latest values.

32. B. R. Suydam, IEEE J. Quant. Electron. QE 11, 225 (1975).

33. C. R. Phipps, Jr., S. G. Thomas, and D. E. Watkins, "Effect of Nonlinear Refraction on Beam Brightness in Laser Fusion Applications," Proc. Int. Conf. on Lasers 1979 (STS Press, McLean, Virginia, 1980), pp. 78-89.

34. W. L. Smith, J. H. Bechtel, and N. Bloembergen, Phys. Rev. B 12, 706 (1975).

35. M. J. Weber, D. Milam, and W. L. Smith, Opt. Eng. 17, 463 (1978).

36. D. F. Watkins, C. R. Phipps, Jr., and S. J. Thomas, "Ellipse Rotation in Germanium," CLEA Conf., Washington, DC, May 30 June 1, 1979, Los Alamos National Laboratory paper LA UR 78 3326.

37. Adelbert Owyoung, "The Origins of the Nonlinear Refractive Indices of Liquids and Glasses," thesis, California Institute of Technology (December 1971).

38. C. C. Wang, Phys. Rev. B 2, 2045 (1970).

39. J. C. Goldstein, Los Alamos National Laboratory Group T 6 internal memorandum, August 23, 1974.

40. N. L. Boling, A. J. Glass, and A. Owyoung, IEEE J. Quant. Electron. QE 14, 601 (1978).

41. H. C. Volkin, "Calculations of g, L vs Pressure for AFT," Los Alamos National Laboratory L Division internal report L5 79:36, February 23, 1979.

42. A. M. Lockett, III, 26th Annual Gaseous Electronics Conf., Madison, Wisconsin, 1973.

43. E. F. Stark, Jr., W. T. Leland, and H. C. Volkin, "Nanosecond Pulse Amplification in CO_2 at Efficiencies Exceeding 20%," Topical Meeting on Inertial Confinement Fusion, San Diego, California, February 7 9, 1978.

44. E. F. Stark, Jr., "Lasers and Power Systems for Inertial Confinement Fusion Reactors," Am. Nucl. Soc. Third Topical Meeting on the Technology of Controlled Nuclear Fusion, Santa Fe, New Mexico, May 9 11, 1978.

45. J. J. Devaney, "Multipass Irradiation of a Flowing Gas Reaction Chamber," Los Alamos National Laboratory L Division memorandum L5 79:110 (May 24, 1979); J. J. Devaney and D. E. Jackson, "Optical Design of a Reaction Chamber for Weakly

Absorbed Light. I. Canted and Parallel Mirrors." Los Alamos National Laboratory report LA 5986 MS, Vol. I (June 1975); J. J. Devaney and E. T. Finch, "Optical Design of a Reaction Chamber for Weakly Absorbed Light. II. Parallel Mirrors, Multitravel." Los Alamos National Laboratory report LA 5986 MS, Vol. II (June 1975); J. J. Devaney, "Optical Design of a Reaction Chamber for Weakly Absorbed Light. III Asymmetric Confocal Resonator." Los Alamos National Laboratory report LA 5986 MS, Vol. III (August 1975).

46. W. L. Thompson, "A Neutron Photon Electron Shielding Study for a Laser Fusion Facility," 5th Int. Conf. React. Shielding, Knoxville, Tennessee (April 1977).

47. M. E. Battat and D. J. Dudziak, "Shield Analyses for Intense 14 MeV Neutron Sources," 5th Int. Conf. React. Shielding, Knoxville, Tennessee (April 1977); and M. Singh in T. J. Gilmartin et al., "Shiva Upgrade Nova CPGD Preliminary Report, Lawrence Livermore National Laboratory report LLL Misc 2242 (September 1976).

IV. TARGET EXPERIMENTS AND MILITARY APPLICATIONS
(R. P. Godwin, T. H. McNally)

In an integrated program of target experiments, theory, and target design, we are establishing a fundamental understanding of laser target interactions, particularly of the relevant plasma physics and hydrodynamics. Experimental and theoretical efforts have addressed the scaling of consistent models to higher laser intensities. Emphasis has been placed on the development and demonstration of experimental techniques needed to determine conclusively the performance of present and future targets. A modest experimental effort is directed toward military applications.

TARGET EXPERIMENTS

Introduction (R. Godwin)

Previous experiments using thin shelled, exploding pusher targets that were nearly isothermal during their implosion history verified that the energy absorption, transport in thin systems, hydrodynamics, and fusion yield calculations were being done correctly in the large computer design codes. Such targets, however, are inherently wasteful of the limited available laser energy, and do not scale to ignition conditions at reasonable laser inputs. Thus, our attention has turned to adiabatically compressed targets, which make efficient use of the laser input. These targets make use of the reaction force from material ejected from the outer edge of a spherical system to compress the inner portion, or pusher material, and the fusible fuel.

Target preparation methods were investigated to maximize the momentum transfer between the outer, ablated material and the inner part of the target. We found that removal of hydrogen from the surface of a higher mass target material could significantly increase momentum transfer while reducing the energy loss to fast ion expansion. Lateral energy loss to electron return currents was also confirmed as being small.

The first adiabatic compressions were achieved by using thick walled microspheres whose outer edge was ablated, driving the pusher and fuel inward. Densities of about 20 times that of liquid deuterium were achieved in the fuel. A systematic approach of increasing ablator thickness was adopted to track the behavior of targets, moving away from the exploding pusher toward the adiabatic implosion regime. Simultaneous measurements of fusion yield, peak fuel ion temperature, pusher run in time to peak compression, and peak fuel density confirmed the calculated predictions. All these measurements first required significant diagnostics development. Fuel densities, for example, were determined from reconstruction of x ray images of the imploded glass pushers and from spectral and spatial resolution of characteristic x ray line emissions from argon impurities mixed with the fuel.

A real concern in future targets having large spherical convergence ratios will be the stability of the imploding pusher shell. This shell must not become hydrodynamically unstable and break up before peak compression and fuel burn are achieved. To image the imploding pusher during the time of outward acceleration is difficult. One technique proposed for this purpose uses an x ray backlighting flash radiograph. The first experiments designed to verify production of an adequate x ray source and an imaging technique have been completed and verify that the approach is feasible.

Effect of Target Purity on Laser Produced Ion Blowoff (W. Ehler, F. Begay, T. H. Tan, J. Hayden, J. McLeod)

One beam of our Gemini CO_2 laser system was used to irradiate extensive massive targets of various materials. The laser energy on target varied from ~100 to 200 J

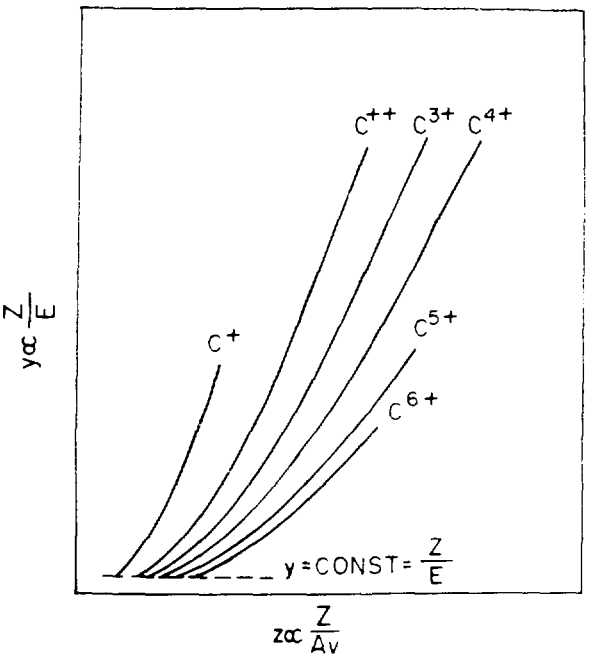

Fig. IV-2.
Thomson spectrogram of heated carbon rod shows a C^{+} ion energy E/z const. as though all the carbon ions were accelerated through the same potential.

spectrograph was visible. These data seem to suggest that plasma transport around the wire is present only when hydrogen contamination is present.

At the end of the laser pulse, the plasma edge expanded isothermally to a distance of ~1 cm. The plasma then expanded adiabatically out to the various ion detectors. The peak ion speed measured was ~3% higher than the ion speed at the end of the laser pulse.

A tentative chart of the clean-target results is shown in Fig. IV-3. Target cleanliness may reduce target preheat and increase shock impulse into the target. This could have significant effects on laser fusion target performance.

Optical Measurements of Lateral Energy Flow (R. F. Benjamin, J. Riffle)

We used visible-light streak photography to improve the measurement of lateral energy flow in a target support structure. Previous studies[6] of GMBs mounted on a long, tortuous support fiber involved time-integrated telephotography and a voltage probe. The earlier results suggested that return current heating is largely responsible for the heating of the target support fiber at a distance of many focal radii from the GMB. The present measurements make this explanation more credible. We found that the luminous front propagates along the fiber away from the GMB at a velocity in excess of 10^{9} cm s. We also observed a plasma from the GMB cross the vacuum gap on the side opposite the support fiber, where it struck a probe fiber causing a visible flash. The flash occurred several nanoseconds after the GMB began emitting visible light. Because these energy transport mechanisms appear to be prompt, modification of the target support structure may influence the hot electron spectrum. Further measurements are planned with higher spatial and temporal measurements.

High Density Experiments (T. H. Tan)

The Helios laser produces enough energy on target to allow the design of targets that we can compress to densities higher than that of solid DT and produce adiabatic conditions in the fuel. In our first sequence of high density experiments, GMB targets were coated with different thicknesses of parylene (0-100 μm). The targets were designed for systematic investigation of high density pellet compression and to demonstrate the transition from the exploding pusher mode to the adiabatic mode of implosion. Low density parylene ablators were used to shield the target interior efficiently against electron preheat. The ablator also allows maximum outer target radius for a given mass, hence, lower laser intensity, thus minimizing the hot electron temperature. Each GMB was 300 μm in diameter with a wall thickness of 1 μm and was filled with 30 atm of DT gas. The yield, implosion time, ion temperature, and fuel density were estimated theoretically and were compared with measured values for each thickness of parylene coating and laser energy.

Ultrafast time resolved neutron detectors[7,8] were used to properly characterize some of the crucial nuclear burn parameters. Each detector was assembled by coupling an ultrafast, quenched scintillator of optimum size to a high gain ITT microchannel plate photomultiplier (MCP PMT). With a 5 GHz oscilloscope as recorder, it is possible to obtain a resolution of better than 100 ps in time shift and pulse broadening. In our experiments, a 2%-quenched scintillator 5 cm in diameter by 2.5 cm thick was coupled directly to the face of the MCP. A 1 GHz Tektronix 7104 oscilloscope was used as a recorder, with a low-loss, ultrafast coaxial cable for

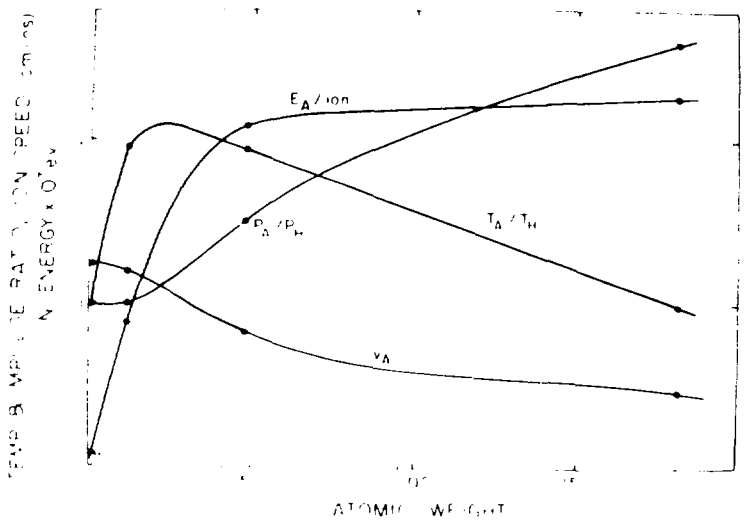

Fig. IV-3.
Tentative chart of clean target results.

signal transmission. This system provided a neutron response time of 800 ps (FWHM) and achieved a gain $\sim 10^7$. This detector system was designed primarily for speed at the expense of high detection efficiency. At yields $< 10^7$ we generally use the more conventional fast NE 111 plastic scintillator XP 2020 photomultiplier assembly to measure yields and longer implosion times. We also found that, in our laser energy regime, time-of-flight measurement provides the most reliable yield value.

Figure IV-4a shows an oscilloscope trace of a neutron time-of-flight measurement from a DT filled GMB target shot. The arrival time of the neutron pulse with respect to the x-ray fiducial can be measured to an accuracy of 200 ps at a writing speed of 5 ns per division. When the x-ray fiducial is delayed to allow 2-ns writing speed, we can measure 100 ps time shifts. The implosion time is measured as a delay in excess of the expected prompt neutron arrival time. A 22-μm parylene-coated GMB target emits a neutron pulse (Fig. IV-4b) that is delayed by an additional 0.6 ± 0.2 ns. This clearly illustrates a departure from the exploding-pusher mode of target implosion.

Figure IV-5 shows two traces comparing an 88-μm-coated target shot at 3.9 kJ with a bare GMB exploding-pusher target. Additional delay > 2.8 ± 0.5 ns in neutron arrival time for the coated target is clearly visible. Such time delay, which is significantly longer than the 1-ns laser pulse, is clear evidence of adiabatic implosion. It must be emphasized that this condition must be achieved before high pellet compression is possible.

Figure IV-6 shows a neutron time spectrum from a 25 μm coated target. The apparent width of 1.28 ns can be deconvolved into an intrinsic neutron pulse width of 1

A. 3[illegible] μm d.a. glass microballoon (GMB)
[illegible] μm wall, 30 atm DT

B. Target A GMB + 22 μm parylene coating

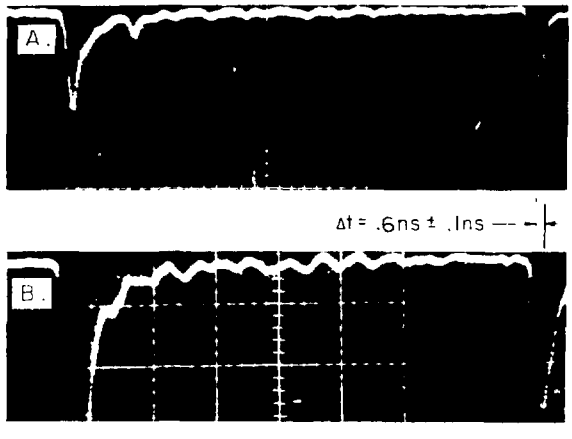

Fig. IV-4.
Oscilloscope trace showing neutron time-of-flight spectrum from (A) bare GMB target, and (B) 22-μm parylene-coated target.

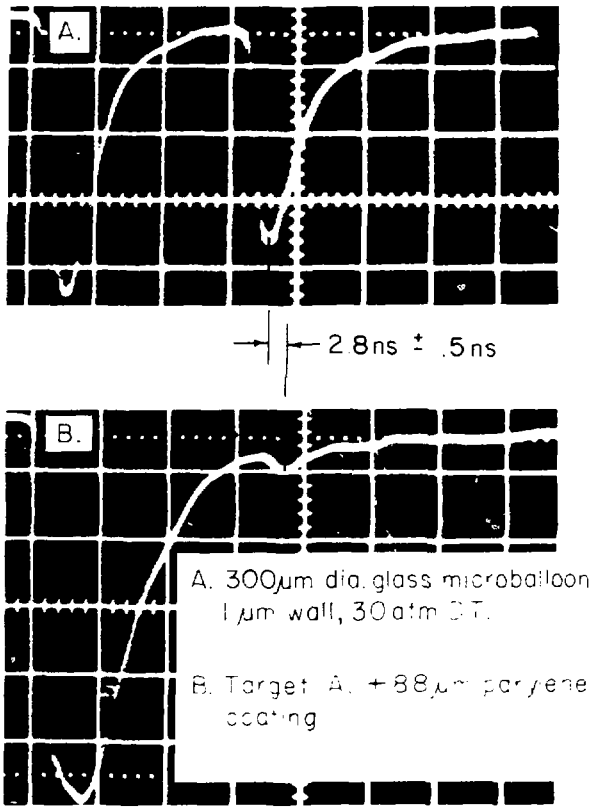

Fig. IV-5.
Oscilloscope trace showing neutron time of flight spectrum from (A) bare GMB target, and (B) 88 μm parylene coated target.

ns. At a flight distance of 970 cm, this corresponds to a fuel ion temperature of 0.7 keV.

In the present generation of laser energy and target design, the yield at high compression is generally low, $\leq 10^6$, and the burn duration is typically < 100 ps. Hence, it is not now possible to deduce the fuel density directly from neutron time of flight. Fortunately for our present investigations, x rays emitted from the pusher during the burn can still be detected and have been used to provide the density information. Figure IV-7 shows a 55-μm-coated target with an estimated fuel density of $3.8^{+1.2}_{-1.5}$ g/cm^3.

Figure IV-8 shows a composite display of yield, implosion time, ion temperature, and fuel density as functions of parylene ablator thickness. The measured quantities and the theoretical predictions are compared. Note that the yields are generally lower than predicted. The implosion times agree reasonably well with calculated values. Because of low detection efficiency, the counting statistics for fuel temperature determinations are very poor at yields $< 10^8$. However, at one point (20 μm) where statistics are good, the measured value agrees quite well with prediction. Measured densities for coatings ~60 μm appear to be at least equal to or higher than predicted. The lower measured yields and possibly higher measured densities can be attributed in part to our inadequate knowledge of the details of the hot electron energy distribution and energy transport.

This is the first series of high density experiments. We expect to improve the accuracy of our measurements by optimizing our instruments and by introducing supplemental techniques such as radiochemistry, fuel seeding, and back lighting. We may have achieved our near term goal of 20 times liquid density compression. The important points, however, are that we have measured adiabatic implosion and that target performance of these higher density targets by 1 ns CO_2 laser beams is within the expected range of design predictions.

Reconstruction of the X Ray Emission Profiles of Imploded Cores from Pinhole Photographs (M. M. Mueller)

One method for determining the diameter of an imploded target at or near the turnaround time is to unfold the pinhole image irradiance distribution to obtain the spherical source x ray emission function. With a DT filled GMB target as an example, if no mixing occurs, a spherical shell of emission due largely to the silicon in the compressed shell can be expected to be the dominant feature. The effective diameter of this region of silicon emission is an upper bound to the minimum core diameter and a lower bound to the maximum compressed density.

Differential methods for performing the inversion of image data to reconstruct the radial source emission profile exist[7,10] and have the advantage of speed and uniqueness. However, in practice, data noise along with aperture constraints make differential methods nearly useless. Iterative integral methods, by contrast, have not been described in the literature, but are capable of source reconstruction from noisy image data taken with relatively wide apertures. The only drawback, in principle, is that the solution cannot be guaranteed to be unique. In practice, however, because of the additional constraint that the reconstruction be physically reasonable, uniqueness does not appear to be a problem of much concern.

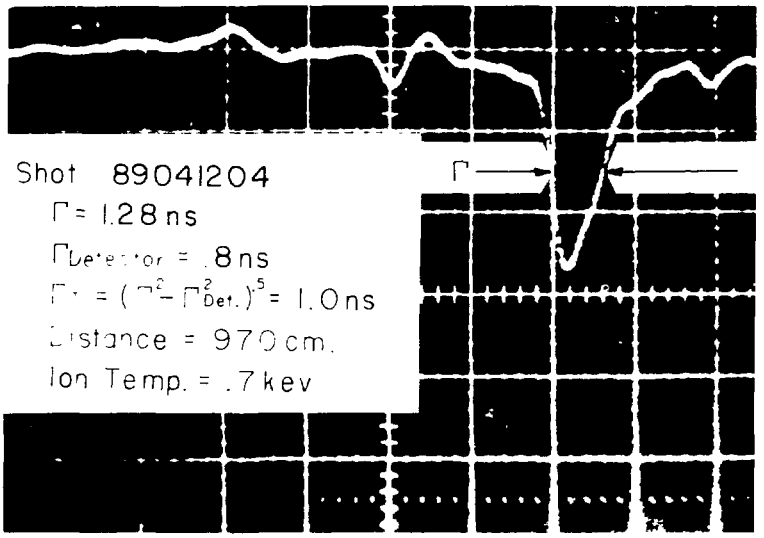

Fig. IV 6.
Neutron time spectrum illustrating fuel ion temperature measurement.

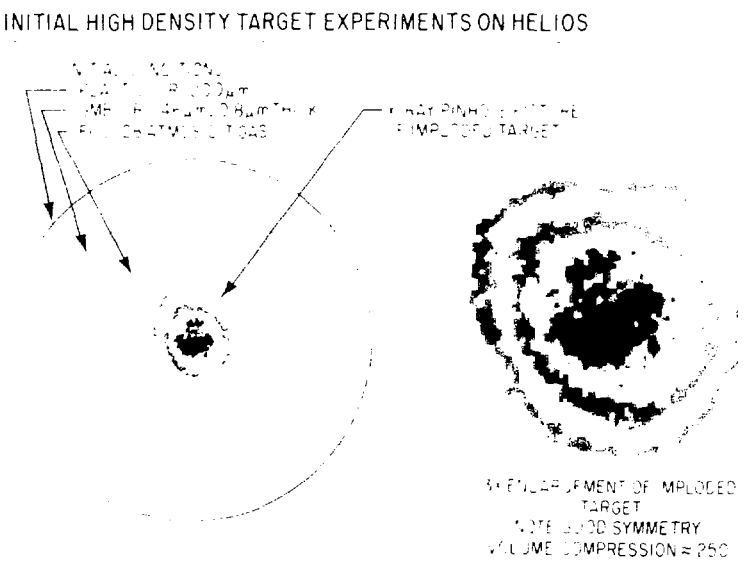

Fig. IV 7.
X ray pinhole picture showing pellet compression for a 55 μm parylene coated target.

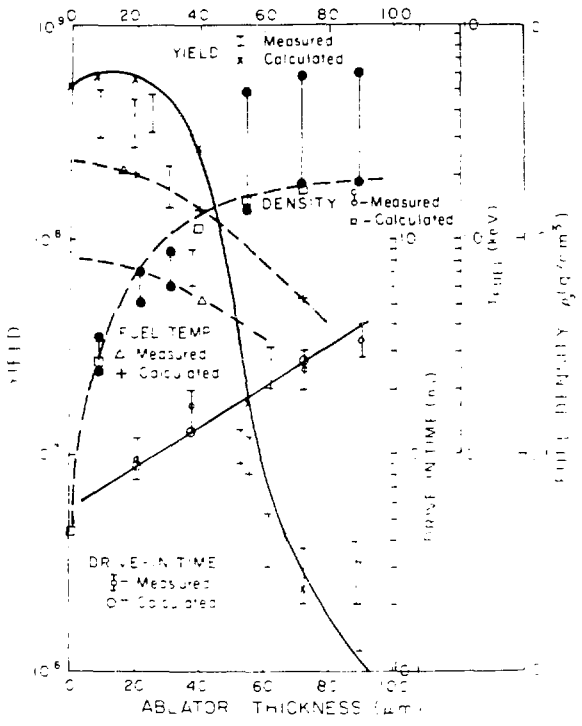

Fig. IV-8.
Summarized experimental results showing a composite display of yield, implosion time, ion temperature, and fuel density as a function of parylene ablator thickness.

Our method uses an image-simulation computer code. The initial input source emission function, which must have radial symmetry in the present circumstances, is integrated to give the radiance distribution over a disk perpendicular to the line of sight. Then this disk of radiance is convolved with the projected aperture function to simulate the image without diffraction. The source function is modified iteratively until the simulated image irradiance distribution agrees with the discrete data points obtained from microdensitometer scans of the actual pinhole image. One difficulty, shared with all other methods based on x-ray images, is that self-absorption within the compressed target may not be negligible. In the small GMB targets used earlier, the plasmas are expected to be optically thin under the conditions of peak emission; however, in the larger targets now being used with the Helios system, self-absorption could be important. The problem of plasma opacity to x rays is very difficult, and proper accounting for self-absorption would also require detailed knowledge of the distribution of temperature, composition, and density within the imploded target. Here, we have neglected the effects of self-absorption.

The first source reconstruction attempted was for Helios shot 88110707, which used a GMB target with an outer CH plastic coating 55 μm thick covering a 300-μm-diam, 1-μm glass wall filled with 6.9 mg·cm^{-3} of DT fuel. Six beams delivered a total of 2230 J onto the target. The intensity data from a reduced microdensitometer scan through the center of the image (averaged over the two sides) are shown in Fig. IV-9 with 1σ error bars in the ordinate; the abscissal bars represent the bin widths used in the data reduction. The image was formed by a roughly circular pinhole with a diameter of 11 μm; camera magnification was 8.86. Under these conditions, diffraction effects are nearly negligible at photon energies that transmit through the 8-μm-thick beryllium window.

The dominant feature of the image irradiance profile is a somewhat dimmer central region. This central dimness depends on only one data point, and may thus be questioned. However, barring a gross nonstatistical error, some central dimness is highly probable, as supported by the observations of similar central dimness in two other Helios shots. This central dimness of the image leads to the important inference that the x-ray emission from the imploded core is hollow—or at least greatly reduced at the center. Even if the first data point were to be shifted upward over 2σ, where it has the same intensity as the second point, the core would still be

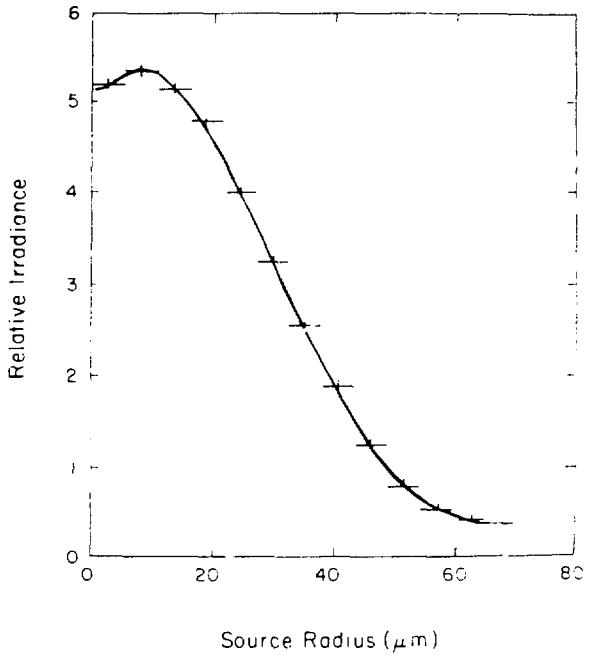

Fig. IV 9.
Irradiance data from Helios shot 88110707 as fitted by means of a two dimensional convolution calculation using an 11 μm diam pinhole and a magnification of 8.86. The source emission function that generated the smooth curve in the histogram is shown in Fig. IV 10.

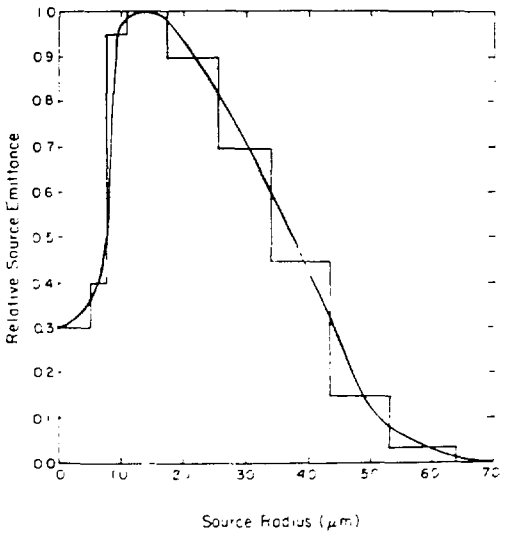

Fig. IV 10.
Source emission profile that gives the smooth curve of Fig. IV 9. The smooth curve here is a hand-sketched interpolation of the histogram.

hollow. Indeed, it can be shown[11] that some degree of core hollowness can be inferred (for a pinhole in the narrow-aperture regime) unless the irradiance distribution falls off monotonically (no flat central region) from the center outward.

Figure IV-9 also shows the simulated irradiance distribution that is a result of the final stage of an iterative source model-adjusting process. Note that this curve passes by the data points rather closely. The source model that produced this curve is displayed as a histogram in Fig. IV-10. The smooth curve in Fig. IV-10 is a hand-sketched interpolation of the histogrammic input function. The histogrammic source model was chosen to facilitate iterative adjustments relative to those of a smooth analytical function. Note that no trace of histogrammic abruptness remains in the simulated image.

Hence, the imploded target is significantly hollow in terms of x-ray emission. The fact that the emission at the center is not nearly zero may be indicative of pusher-fuel mixing. This, along with the neglect of self-absorption, makes the interpretation of the emission model hazardous in terms of fuel radius at turnaround. Nevertheless, if one were to assume that only DT fuel filled the volume to the radius of the peak emission, one would infer a compressed fuel density of 8 g/cm^3.

The second source to be reconstructed was Helios shot 89041208, which used a GMB target 300 μm in diameter with a wall 0.84 μm thick, covered with 72 μm of CH ablator and filled with 6.4 mg/cm^3 of DT fuel. Seven beams delivered a total of 3490 J onto the target. For this shot, two pinhole cameras with viewing directions 52° apart were used. The pinholes, used in place for several previous shots, were removed for examination and measurement after this shot. They had become rather large apertures, roughly 27 and 48 μm in diameter, which makes the unfolding process more difficult.

The computer code was reconstructed and expanded to allow the use of smooth analytical source emission functions instead of histograms. However, histogrammic model-adjusting is faster and easier than using three-parameter analytical functions.

Under the initial assumption that the two camera views of the source are intrinsically identical, we were faced with the novel situation of performing simultaneous fittings of two data sets using different pinholes. Hence, while the fitting effort rose markedly, the results should be correspondingly more reliable. The two data sets to be fitted by adjusting a common source model are

shown in Figs. IV-11 and -12 for the smaller and larger pinholes, respectively. Note that the irradiance pattern of the larger pinhole does not give any indication of source hollowness. The most successful common-source model displayed in Fig. IV-13 shows the respective irradiance curves of Figs. IV-11 and -12. The analytical source-emission function of Fig. IV-13 is the three parameter relationship $E(r) = r^P e^{-Qr^A}$, in which Q is chosen so that E(r) is 1/300 of its peak value when r equals some trial "overall core radius" value. Note that the shape of the emission function resembles a skewed Gaussian. The best fit obtained so far is for P = 9.5, Q = 0.00137, and A = 2.1, with r in micrometers. While this cannot be established until all possible physically reasonable emission functions have been tried, we suspect that the two data sets shown in Figs. IV-11 and -12 are slightly inconsistent and, therefore, cannot be exactly fitted by a common source-emission function. Two of several possible causes for such inconsistency are that the source could appear different from two views 52° apart, or that the actual pinhole shapes (which are appreciably noncircular with unknown azimuthal orientations) could cause different image distortions.

Nevertheless, when one considers that these apertures are relatively large compared with the effective radius of the compressed core, it is surely noteworthy that the two data sets, using markedly different pinholes, can be fairly well fitted by a common source-emission function. Also noteworthy is the fact that this integral-fitting process is rather sensitive to fairly small changes in the trial emission mode. Using the 27-μm pinholes, for example, if the whole model is shifted 7 μm to the left (so that the peak now occurs at ~17 μm), all apparent trace of hollowness disappears and the simulated irradiance curve becomes monotonic. While a thorough error analysis has not been carried out, experience indicates that the uncertainty in the location of the emission peak caused by random data error, aperture determination error, and fitting model error is probably no greater than about ± 20%. Thus, the inferred lower limit to the compressed fuel density could be in error from these causes by a factor of somewhat less than 2.

A comforting consistency check is provided by comparing the FWHM of the emission model (13.2 μm) with the shell thickness expected simply on the basis of the

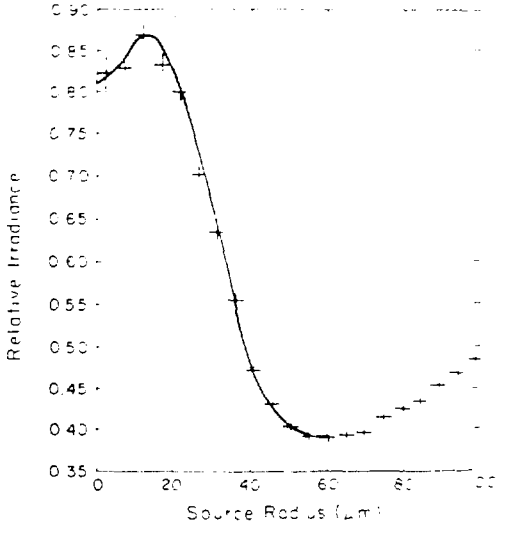

Fig. IV-11.
Irradiance data from Helios shot 89041208 as fitted (simultaneously with the data of Fig. IV-12) by means of a two-dimensional convolution calculation using a 27-μm-diam pinhole and a magnification of 8.7. The source emission function that generated the smooth curve is displayed in Fig. IV-13.

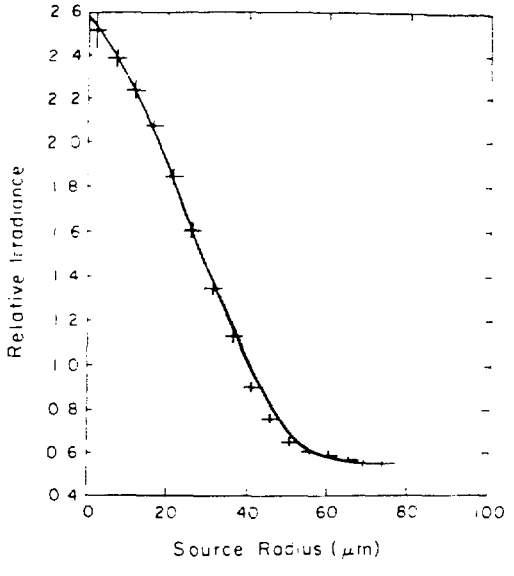

Fig. IV-12.
Irradiance data from Helios shot 89041208 as fitted (simultaneously with the data of Fig. IV-11) by means of a two-dimensional convolution calculation using a 48-μm-diam pinhole and a magnification of 8.7. The source emission function that generated the smooth curve is displayed in Fig. IV-13.

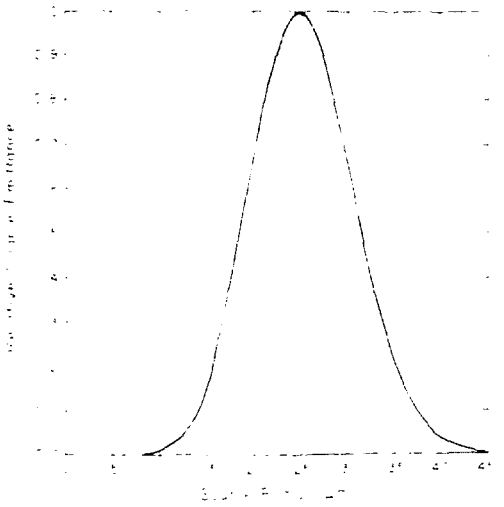

Fig. IV 13.
Source emission profile that gives the smooth curves of Figs. IV 11 and 12.

conservation of the mass of glass during compression to a mean radius (24.6 μm) given by the emission peak in the model. This compressed shell thickness is obtained by solving a cubic equation to get 14.4 μm. (The model-fitting was carried out completely independently of this congruence.)

If one assumes that the effective radius of the DT fuel at turnaround is given by the location of the peak emission, then the radial compression is 152/24.6 = 6.2, and the inferred fuel density is 1.5 g/cm^3. If the inferred emission profile of the model is indeed mainly due to the silicon, then the effective fuel radius would be smaller than 24.6 μm, and could be as small as 18 μm if there were little mixing. Thus, in the absence of appreciable mixing and self-absorption, the inferred fuel density using the emission peak is a lower limit.

High-Density Experiments with Gas-Filled Ablative Targets (K. Mitchell, D. vanHulsteyn, A. Hauer, F. Ameduri)

We conducted experiments to demonstrate the feasibility of determining the fuel density in ablatively driven targets from spectrographic measurements of a seed gas mixed with D_2 and DT. Also, we made qualitative determinations of the electron temperature in the fuel from bremsstrahlung continuum and intensities of argon lines.

The first experiment was performed with neon as the seed gas in DT filled GMB targets, both coated and uncoated. Neon lines were not observed in the spectrum when these targets were irradiated with 2.5 TW of 10-μm laser light in Helios. Targets from the same batch were also irradiated with 0.5 TW of laser power in Gemini, and did produce a neon line. The electron temperature T_e of the plasma produced by 2.5 TW was determined as 550 eV from the x ray continuum. We, therefore, concluded that the neon atoms were totally stripped of electrons.

We then conducted experiments using pure argon and argon D_2 as a fill gas in both GMBs (exploding-pusher targets) and plastic coated GMBs (ablative targets). The targets were filled with gas by a new drill-fill-plug method. Spectra were obtained with a convex PET crystal spectrograph and a parabolic PET crystal spectrograph. The latter was used to obtain space-resolved spectra of argon lines over a limited wavelength range from 3.3 to 4.2 Å. The parabolic crystal spectrograph had two slits 20 and 40 μm wide oriented 90° with respect to the dispersion direction giving a fourfold spatial magnification on film.

The spectrum from the compressed core of a laser-irradiated, argon-filled GMB target is shown in Fig. IV 14. The argon fill pressure was ~1 atm and the target was irradiated with 2.8 kJ of 10-μm laser energy. The spectrum shown consists predominantly of helium-like ($1s^2$-1snp) lines of argon. The hydrogen-like (1s-2p) line is weakly developed in this spectrum and its intensity is very weak with the plastic-coated GMB targets. Potassium lines that originate in the glass are also observed. The spatial extent of the potassium lines is equivalent to the size of the GMB, whereas the spatial extent of the argon lines shows that the argon radiation is originating from the compressed core. Note also that all argon lines are broad relative to the potassium (1s-2p) line. The major line-broadening (8 eV) is due to the Stark effect resulting from high density in the fuel region.

We then conducted experiments using Ar/D_2 mixtures in GMBs (exploding-pusher targets) and plastic-coated GMBs (ablative targets). Densities were determined chiefly from the spatial extent of the argon line ($1s^2$-1s3p) on spatially resolved spectrograms. The targets were filled with 0.2 atm of argon and 20 atm of D_2. The target fabrication technique was developmental and some targets leaked gas. Nevertheless, it is instructive to determine fuel densities from spectroscopic measurements of the argon lines. In Fig. IV-15, spatial profiles of the argon ($1s^2$-1s3p) line are shown from shot 8905030

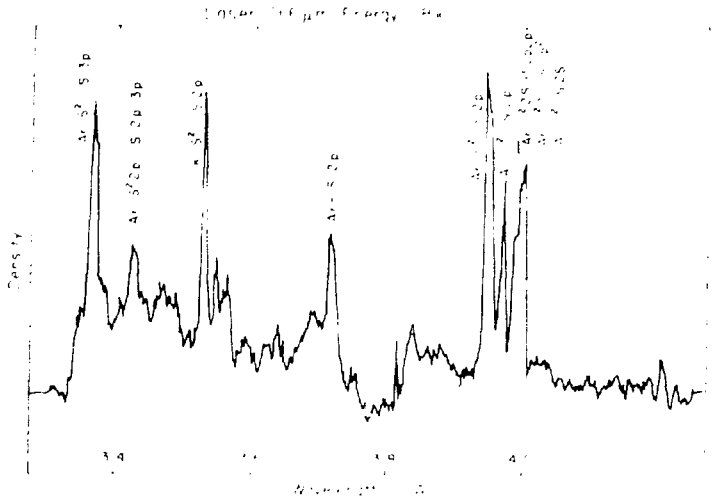

Fig. IV 14.
Spectrum from compressed core of laser irradiated, argon filled GMB targets.

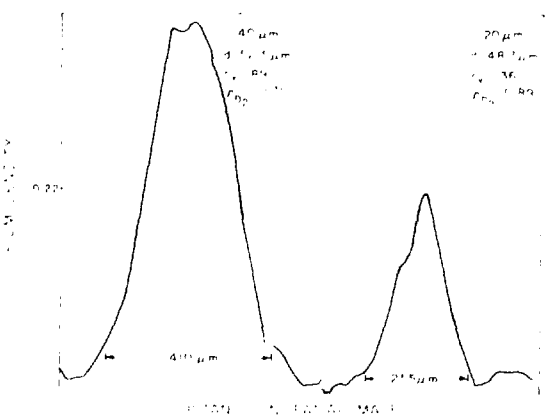

Fig. IV 15.
Spatial profiles of the argon line ($1s^2 1s3p$) from a 301 μm GMB coated with 33.3 μm of plastic and irradiated with a pulse of 3265 J.

receiving 3265 J onto a 301-μm-diam GMB coated with 33.3 μm of plastic. A comparison of spatial profiles was made for spectrograph slit widths of 40 and 20 μm. The equivalent D_2 densities derived from these profiles for 0.2 atm Ar/20 atm D_2 was 0.71 and 0.89 g/cm^3, respectively. These densities compare favorably with calculated values for ablative targets presented elsewhere in this report.

In Fig. IV-16 we compare the compressed core diameters from the ablative compression to those achieved from an exploding-pusher target. The compressed diameters were 73 μm (200 μm GMB) and 48.7 μm (301 μm GMB, 33.3 μm of plastic). This corresponds to a density gain of 10 for the ablator target.

The use of Stark broadening for density determination was limited in these experiments due to an absorption line blended with the $1s^2 1s3p$ argon line. The absorption line is probably from some species in the plastic ablator. In future experiments, the $1s^2 1s4p$ argon line will be included on the spectrograms.

Pinhole photographs were also taken during these Ar D_2 shots. Because the argon x ray lines lie in the 3 to 4 keV region, as we note from Fig. IV-15, a

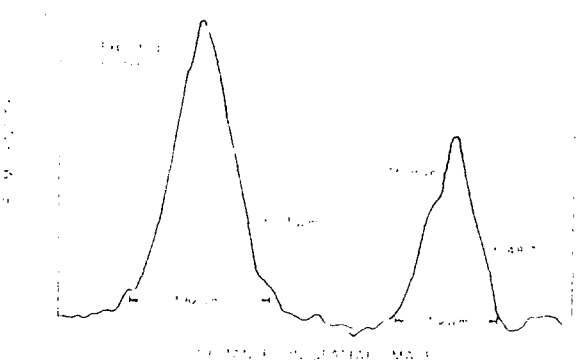

Fig. IV 16.
Comparison of compressed core diameters of an ablator and an exploding-pusher target.

2.75 μm thick tin filter was placed over a portion of the film in one of the two pinhole cameras. The transmission characteristics of this particular L edge filter are shown in Fig. IV 17: the peak efficiency of 0.5 occurs just above the strongly radiating lines. The filter also passes radiation above 5 keV, but this flux is reduced because of the exponential falloff of the continuum intensity and the reduced sensitivity of the Kodak RAR 2490 film.

Pinhole images of shot 89050305 are shown in Fig. IV 18. The first photograph (Fig. IV 18a) was taken through a broadband beryllium filter. The second (Fig. IV 18b) was taken through the tin filter and shows a much smaller radiating region. Note that the stalk radiation, which is visible through the beryllium, is blocked by the tin.

Densitometer traces of the image shown in Fig. IV 18b indicate compression diameters comparable with, but slightly larger than, the values obtained from the spectrographic data. This indicates that, while the filter discriminates in favor of the argon radiation, there is probably significant continuum flux from the imploded glass wall.

Similar photographs of an exploding pusher shot (89042409) are shown in Figs. IV 19a and b. Here it is much more difficult to measure an imploded core of the tin filtered image. This indicates that the silicon is heated earlier in the compression process if the GMB is not coated.

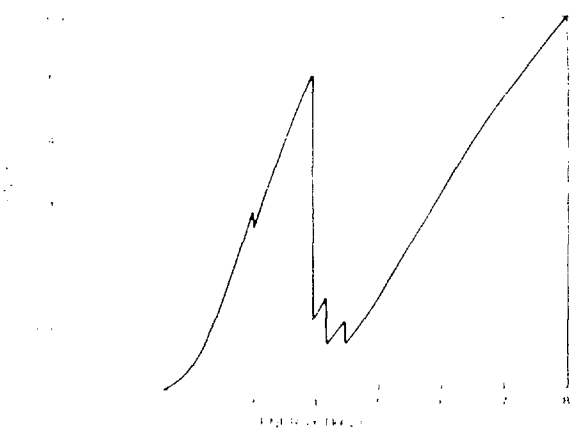

Fig. IV 17.
Transmission characteristics of a 2.75 μm-thick, L-edge, tin filter.

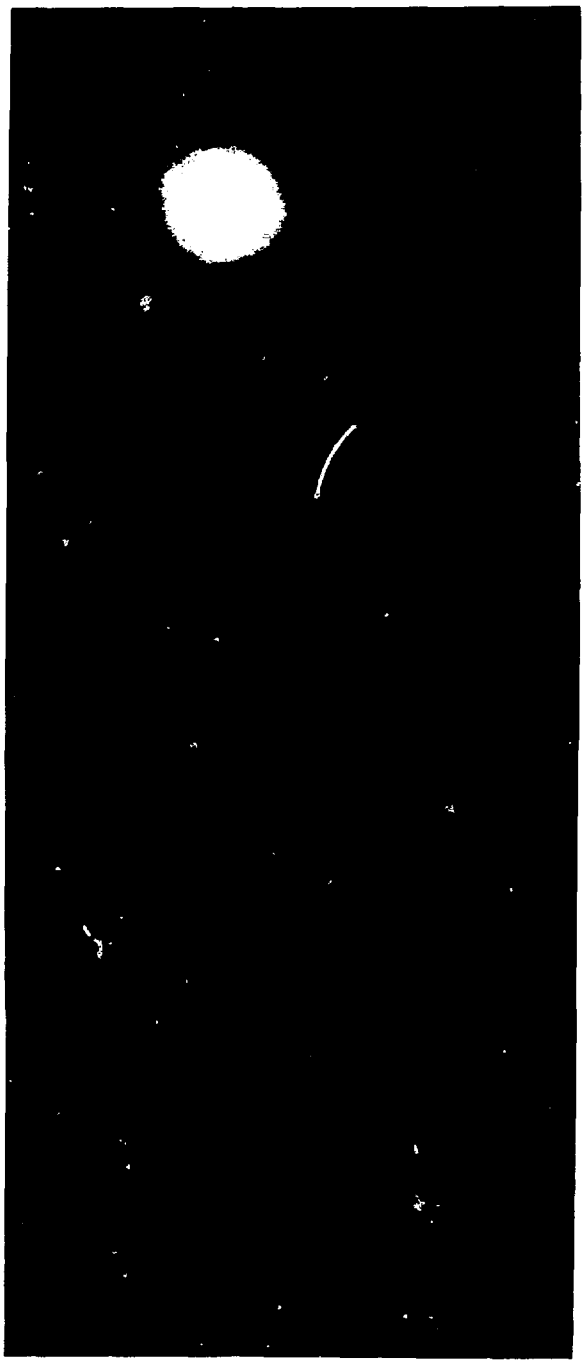

Fig. IV-18a.
Pinhole image of a plastic-coated GMB exposed through a broadband beryllium filter

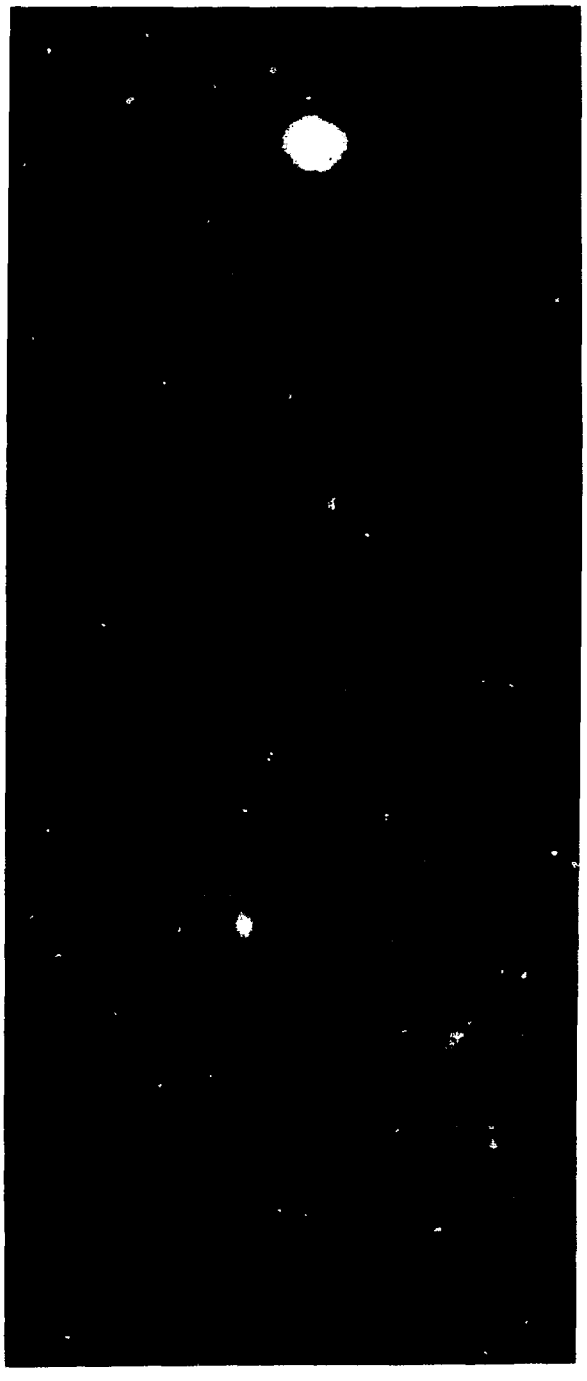

Fig. IV-18b.
Pinhole image of the event shown in Fig. IV-18a exposed through a tin filter.

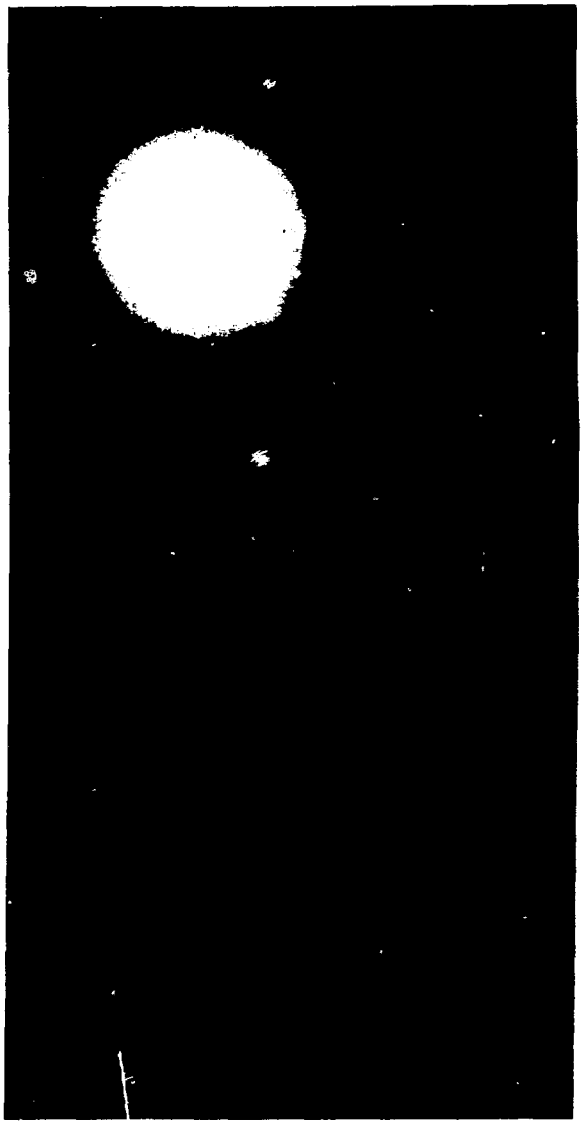

Fig. IV-19a.
Pinhole image of an exploding pusher target exposed through a broadband beryllium filter.

Experiments with X-Ray Backlighting (A. Hauer, D. vanHulsteyn)

Our present studies have included two basic objectives: (1) investigation of several methods for producing high-energy x rays as potential backlighting sources, and (2) investigation of practical backlighting camera configurations.

Fig. IV 19b.
Pinhole image of an exploding pusher target exposed through a tin filter.

Backlighting Source Development. We investigated the production of high-energy line radiation for monochromatic backlighting. We found, for laser energies of ~250 J and pulse widths on the order of 1.2 ns, that inner-shell radiation is the most practical line-generating mechanism. We observed strong inner-shell emission (K_α and K_β) from targets of Ca, Ti, Ni, Sc, Cr, and Fe. A typical spectrum obtained in these experiments is shown in Fig. IV-20; K_α emission is accompanied by K_α shifted by ionization. The shifted emission can be eliminated by coating the desired emitter with a thin layer of almost any material. Thus, K_α or inner-shell emission is potentially a spectrally pure source.

We investigated the production efficiency of K_α radiation as a function of laser energy and target Z. For ~50 J on target, the fast-electron spectrum is a roughly fixed quantity. With this given parameter, K_α production will vary with target Z. We find that for the given laser parameters, titanium is about the best K_α producer.

We investigated point sources using slab targets of about 20 μm diam. These experiments were performed to study radiation above 1 keV (filtered by 1 mil Be). These sources were bright enough to be practical for backlighting. In the point projection mode we demonstrated at least 50 μm resolution.

Experiments were performed with laser-driven current x ray sources. Needle targets, illustrated in Fig. IV 21, were irradiated with CO_2 lasers. Results suggest that these targets may be a good source of high energy continuum. Pinhole photographs and wire shadowing indicate that the source size was less than ~25 μm. Further measurements of the spectral distribution of these sources are needed. The nonlinearity of field emission makes a short-duration x-ray source possible.

Development of Backlighting Camera. We also investigated practical backlighting camera configurations. One of the objectives in these studies was the development of repeatable alignment techniques.

Two backlighting camera configurations, shown in Fig. IV 22, are under investigation. Both use a relatively large, spatially distributed probe source.

With one technique, a pinhole camera is used to image the shadowed source. The pinhole camera can be filtered to pass primarily line radiation.

The pinhole backlighting configuration has been used in several experiments to shadow both cold and imploded targets. Figure IV 23 shows a cold nickel shell shadowed

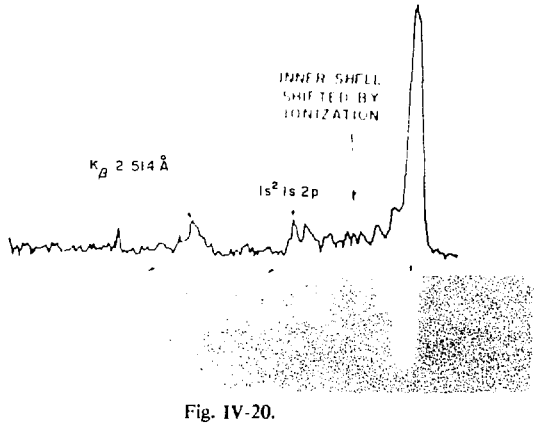

Fig. IV-20.
Spectrum of inner-shell (K_α and K_β) emission from titanium.

Fig. IV-21.
Needle target used to generate high energy continuum.

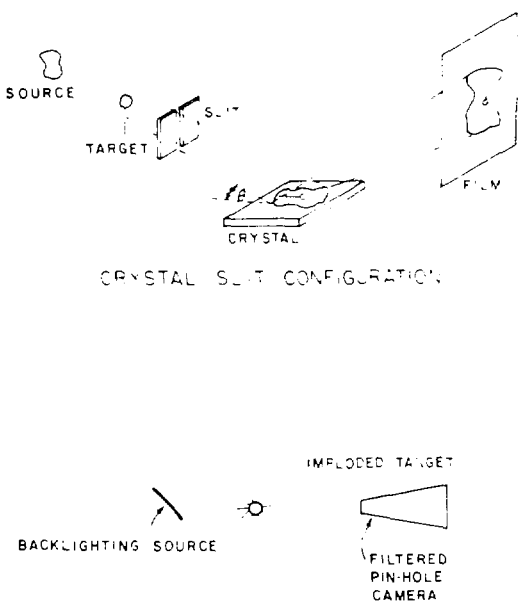

Fig. IV-22.
Backlighting camera configurations now being investigated.

by radiation from a titanium slab (about twice the size of the nickel shell). Figure IV-24 illustrates backlighting of an imploded target. In this experiment, one beam of the Gemini laser is used to implode a plastic coated nickel shell. The other beam produces the radiation from the titanium backlighting source. There is a definite distortion of the nickel sphere indicating that shadowing took place during the initial phases of implosion.

These tests were performed with a 25-μm beryllium filter so that relatively broadband radiation from the titanium source was used. Subsequent tests will use primarily monochromatic K_{α} radiation.

A special technique was devised for aligning the backlighting source and the target. Two Hartmann balls corresponding to the positions of backlighting source and target were mounted on the target holder. Two autocollimating alignment telescopes could then be used to establish the source and target positions. A third telescope was used to establish the line between targets and to position the pinhole camera.

Tests were also performed with the slit-crystal/camera configuration. In these tests a silicon backlighting source was used. The camera used a PET crystal and 50-μm slits. The alignment was set to image the $1s^2$-1s2p line

Fig. IV 23.
Pinhole photograph of cold nickel shell shadowed by radiation from a titanium slab.

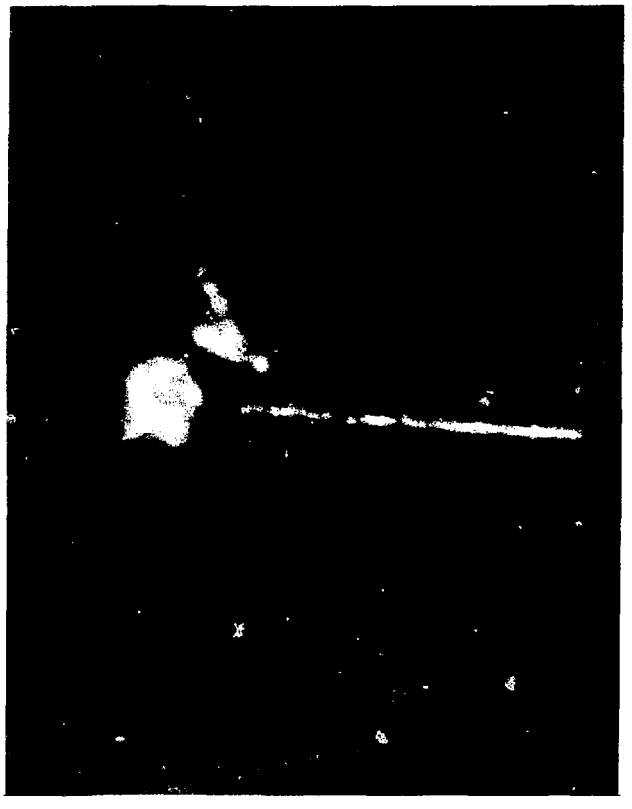

Fig. IV-24.
Pinhole photograph of an imploded plastic-coated nickel shell backlighted by radiation from a titanium source.

from the silicon backlighting source. Very weak images were obtained with this configuration indicating that the magnification (6X) used was too high. Subsequent experiments will be performed to investigate this type of imaging either with higher laser energy on target or lower camera magnification.

MILITARY APPLICATIONS

Introduction

Experiments with our Nd:glass laser system have confirmed that useful information can be obtained con cerning equation-of-state parameters of unknown materi als in the 10-Mbar pressure region. For known materials, the results of experiments agree well with calculations when the properties of the laser irradiation system are known and included. Useful opacity data can also be extracted from well conceived experiments.

Shock-Wave Experiments (P. D. Goldstone, C. Woods, P-1)

The primary objective of these experiments was to study shock wave formation and attenuation by measur ing shock velocities in laser-irradiated thin-foil target materials of low, medium, and high Z (Al, Ag, Au). These measurements will provide information on the coupling of laser light into hydrodynamic shocks. Meas ured shock attenuation can be compared with theoretical calculations to determine whether the calculated (trian gular) shock is a good physical approximation. To make these measurements, we used a technique developed at Los Alamos for determining shock breakout time in stepped targets.

These experiments were not conclusive. Some ques tions of beam quality and target quality must be resolved. Operation of our primary diagnostic (a vis ible-light streak camera) must be better characterized with respect to sweep speed and linearity. However, we did obtain useful information about laser-produced shocks in solids.

These experiments showed that the luminosity of shocks in aluminum, silver, gold, and molybdenum at the instant of breakout agrees qualitatively with the lumi nosities derived from shock temperatures predicted by theoretical calculations. We do not see anything unusual about the strength of shocks produced in high-Z materi als. We now believe, however, that new and more reliable diagnostics for the rear-surface behavior, and improved characterization and performance of the Nd:glass laser system, are required to do these experiments satisfac torily.

Shock-Wave and Equation-of-State Studies (L. Veeser, A. Lieber, J. Solem, D. Eckhart, P-3)

We spent six weeks with the Nd:glass laser and a new streak camera learning to make high-pressure equa tion-of-state (EOS) measurements. We also improved system optics and recording techniques so that we can now measure more than one target step.

In efforts to make impedance match measurements we observed a few good streaks, but did not obtain enough data to prove the reliability of the technique. Figure IV-25 shows a streak record for a shot with an intensity of $\sim 4 \times 10^{13}$ W/cm^2. Pressures were $\sim$ 0.3 TPa (3 Mbar) in the aluminum and 0.6 TPa in the gold. Although the space between the steps was partly filled with gold and aluminum, the streak record shows that good results can be obtained with better focal-spot

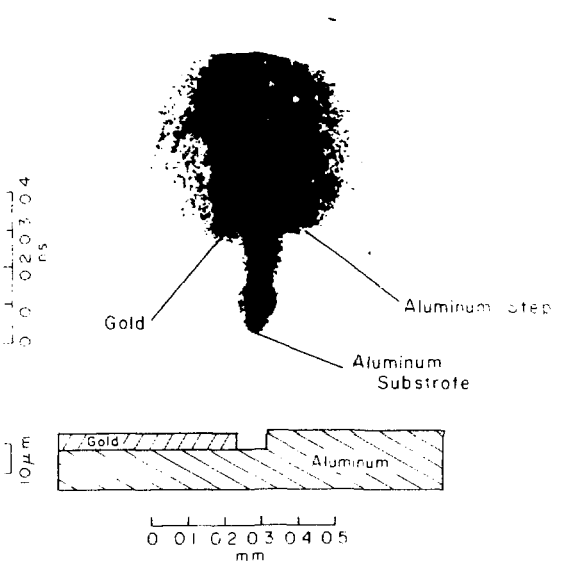

Fig. IV 25.
Streak camera record for shot with intensity of $\sim 4 \times 10^{13}$ W/cm^2. Pressures were $\sim$ 0.3 TPa (3 Mbar) in aluminum, 0.6 TPa in gold.

uniformity (which also produces flatter, more uniform shock breakthrough from the steps).

During this reporting period, we also developed other diagnostics, including a backup streak camera, a set of four x ray diodes, a new fast ion detector, and the repair of an S-1 streak camera to measure the laser-pulse time dependence. We have been unable to improve the focal spot uniformity significantly. A uniform spot is crucial to accurate EOS measurements, but the high cost of obtaining such uniformity has not been included in budgets for the immediate future. We may have to postpone the EOS work and concentrate on shock risetime measurements or other work that does not require a laser focal spot of such high quality.

Computer Calculations of Equation of State (EOS) (R. B. Schultz, TD 9)

Our continuing efforts to model EOS experiments numerically yielded much better results during the first half of 1979 than previously. Previous calculations indicated that the experimentally observed shock velocity in 13 μm thick aluminum foil targets could be matched only when the observed energy was ~ 4% of the total in the laser pulse. Our recent calculations indicate that new experimental data are consistent with 40% absorption and that earlier problems may have been due to difficulties in characterizing the spatial profile of the laser focal spot.

In a recent impedance-matching experiment, a target with a 13-μm-thick aluminum substrate and steps of 4.4 μm aluminum and 3.0 μm gold was illuminated with a Nd:glass laser pulse that focused 12.5 J in a laser focal spot with an equivalent radius of 160 μm. The shock velocity measured across the aluminum step was 1.60 cm/μs, whereas the shock velocity across the gold was 1.05 cm/μs. In our one-dimensional calculation with 40% absorption, we computed shock velocities in the aluminum and gold of 1.55 and 0.85 cm/μs, respectively. The calculated pressures averaged 3.8 Mbar in the aluminum and 6.3 Mbar in the gold.

Because of interest in shock-structure experiments, we attempted to improve on calculations of the intensity profile as viewed by the streak camera. Figure IV-26 is a plot of the detected power vs time in the optical (1- to 3-eV) band of a detector viewing the back surface of the gold. The detector was assumed to have an infinitely fast time response. The time resolution of the calculation is ~1 ps. The risetime of the optical pulse is a function of

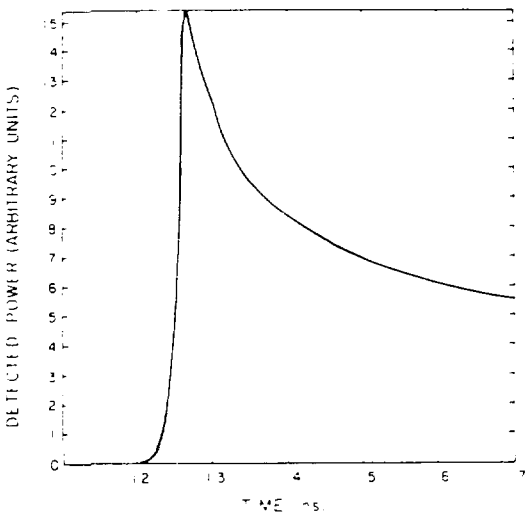

Fig. IV 26.
Plot of detected power vs time in the optical (1 to 3 eV) band of a detector viewing the back surface of gold step.

artificial viscosity in the numerical hydrodynamics, mesh sizes, opacities at low temperatures, and other factors that suggest caution when comparing the calculated results to experimental data.

Laser Opacity Experiment (N. M. Hoffman, L. W. Miller, J. M. Mack, J-15; H. W. Kruse, J-14)

The data obtained with the Nd:glass laser in March 1979 are still being studied. Most of these data were an attempt to observe limb darkening in red light, using a filter that cut off wavelengths < 6500 Å folded with an S-20 response. For these wavelengths, the limb darkening is expected to be less than it is in the blue region of the spectrum. The data tend to verify this, but a great deal of scatter and other unexplained anomalies in the data make it necessary to repeat these measurements before conclusions are drawn.

The previously observed limb brightening at early gating times discussed in the last progress report has been tentatively attributed to nonsimultaneous gating of different portions of the channel-plate intensifier (CPI).[12,13] We demonstrated reproducibility of this effect by placing the two images at unequal distances from the center of the CPI photocathode, and then eliminating the effect by centering the images on the photocathode.

We will attempt to reproduce the limb-darkening results obtained earlier with white light and to understand the problems that remain in the March 1979 data.

We performed further theoretical work on optical limb darkening with the temperature of the radiating material less than hν/k, where ν is the frequency of the observed radiation and k is the Boltzmann constant.[12,13] Using the Kramers-Unsöld formula[14] for the opacity as a function of temperature, a simple analytic expression is obtained that, in conjunction with a model temperature profile, gives the limb-darkening function. This theory, discussed in more detail in Ref. 12, forms the basis for the design of the present experiment.

A small postprocessor program called IRAY2 has been written to calculate emergent intensities along various lines of sight through a planar laser-heated plasma. Such calculations can help predict the magnitude of the limb-darkening effect at x-ray photon energies in such a plasma.[15] The IRAY2 program takes into account the emission and absorption opacities, and thereby allows for the effects of nonlocalized thermodynamic equilibrium (LTE).

An example of the use of IRAY2 is shown in Figs. IV-27 through -29. A computer calculation was performed to simulate the behavior of an aluminum foil 12.7 μm thick, irradiated by a pulse of 10.6-μm laser light containing 500 J of energy. The FWHM of the pulse was 1.1 ns and the focal spot diameter was 200 μm.

Figure IV-27 shows the mass density and electron-temperature structure of the planar target 0.446 ns after the start of the laser pulse. (The beam is incident from the left.) The limb-darkening functions computed by IRAY2 for five photon groups are shown in Fig.

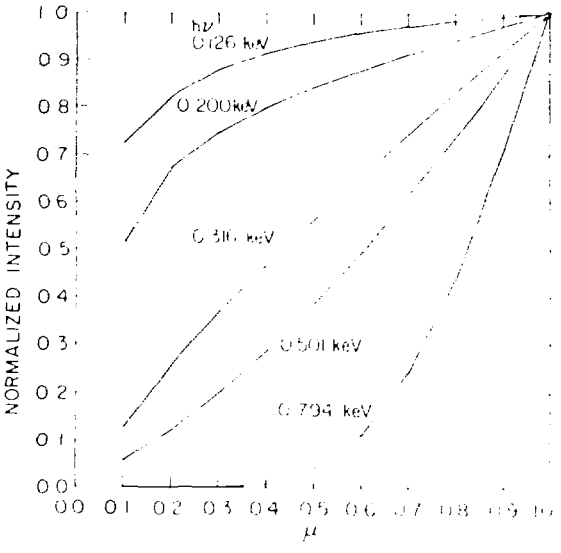

Fig. IV-28.
Limb darkening functions computed for five photon groups 0.446 ns after start of laser pulse.

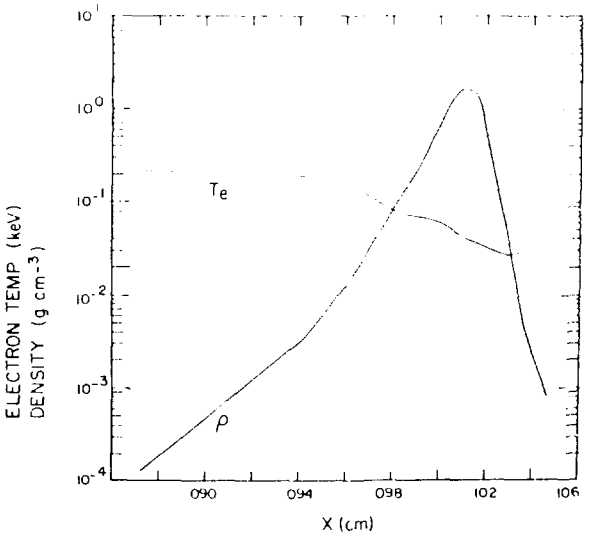

Fig. IV-27.
Mass density and electron temperature of planar target 0.446 ns after start of laser pulse.

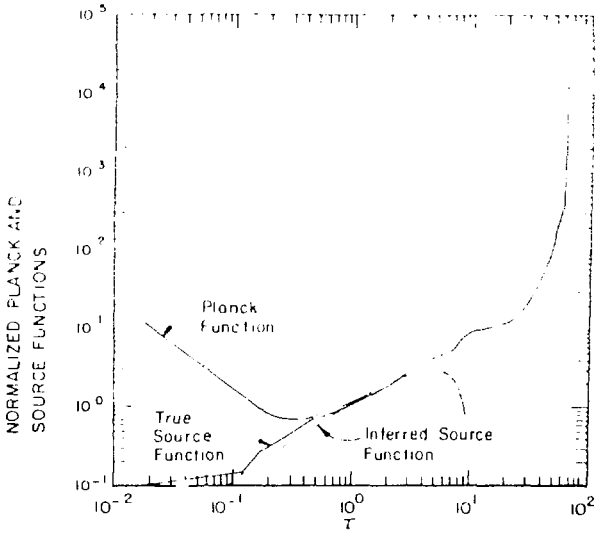

Fig. IV-29.
Planck and source functions vs optical depth at hν = 0.316 keV.

IV-28 for this instant of time. Here $\mu = \cos\theta$ is the viewing angle with respect to the plasma normal. The limb darkening effect is reasonably strong above a photon energy of ~0.300 keV. Figure IV-29 shows the Planck function and source function at $h\nu = 0.316$ keV (normalized by the emergent intensity at $\mu = 1$) plotted vs optical depth at 0.316 keV. They are equal for $\tau \gtrsim 1$, but depart from equality at small τ due to non-LTE effects. The dashed line shows the source function inferred from the limb darkening function at 0.316 keV, by a process similar to taking the inverse Laplace transform of the limb darkening function. As we expect, the inferred source function is a good match to the true source function for $\tau \sim 1$. Such calculations will allow us to simulate many aspects of the limb-darkening opacity experiment, including error propagation, the importance of non-LTE, and instrumental limitations.

Studies Using the Two Beam Nd:Glass Laser Facility (A. G. Engelhardt, R. H. Robertson, I. V. Johnson)

In addition to furnishing almost 900 on-target shots to the various user groups in the first 6 months of 1979, we began a major effort to redesign and upgrade the glass laser. Upgrading is concerned primarily with

- mounting a "frame-grabber" system to look at the beam footprint along the beam line,
- improving the enclosed-energy measurements, and
- automating the monitoring and adjusting of the dye concentration in the oscillator dye cell.

Only the B-beam was used for on-target shots; the pulse width was 300 ns FWHM and typical energies were 20 to 25 J/pulse.

During this reporting period, we moved the single-beam glass laser into the facility, built an enclosure for it and covered the optics of the two-beam laser to prevent dust damage from sawing, welding, burning, and other construction operations. The two-beam laser system was shut down for 3 weeks. On restart, we made corrections to alignment, changed the mirror supports, and began the improvements noted above.

User investigations can be categorized as follows.

- Equation-of-state experiments - 505 shots (L. Veeser, A. Lieber, J. Solem, D. Eckhart, P-3).
- Computer calculations of equations of state (R. Schultz, TD-9).
- Opacity experiments -195 shots (N. Hoffman, L. Miller, J. Mack, J-15; H. Kruse, J-14).
- Shock-wave experiments - 75 shots (P. Goldstone, C. Wood, P-1).
- Multiburst simulation and blast-wave interactions - 52 shots (M. Wilke, S. Stone, G. Barasch, J-10)
- Calibration, x-ray streak camera - 38 shots (P. Rockett, P. Lee, L-4).

REFERENCES

1. W. Ehler and W. I. Linbor, J. Appl. Phys. **44**, 4229 (1973).

2. E. Stark and F. Skoberne, "Laser Fusion Program at LASL, January 1-June 30, 1977," Los Alamos National Laboratory report LA-6982-PR (April 1978), Sec. IV, p. 79.

3. T. H. Tan, A. H. Williams, and G. H. McCall, Nucl. Instrum. Method **131**, 425 (1975).

4. V. S. Nikolaev et al., Sov. Phys. JETP **13**, 695 (1961).

5. R. R. Goforth and P. Hammerling, J. Appl. Phys. **47**, 3918 (1976).

6. R. F. Benjamin, G. H. McCall, and A. W. Ehler, Phys. Rev. Lett. **42**, 890 (1979).

7. T. H. Tan and A. H. Williams in "Inertial Fusion Program, July 1-December 31, 1978," Los Alamos National Laboratory report LA-7755-PR (November 1980).

8. P. Lyons, T. H. Tan, and A. H. Williams, "Ultra-Fast Particle Detectors for Laser Fusion Diagnostics," to be published.

9. M. M. Mueller, "Geometrical Single-Aperture Imaging and Wide-Aperture Deconvolution," Los Alamos National Laboratory paper LA-UR-78-2698 (1978).

10. M. M. Mueller, "Reconstruction of Spherically Symmetric Objects from Slit-Imaged Emission: Limitations Due to Finite Slit Width," Los Alamos National Laboratory paper LA-UR-79-1292 (1979).

11. M. M. Mueller, "Numerical Simulations of X-Ray Pinhole Images of Imploded Microballoons: Development of Narrow-Aperture Methods for Determining the Size and the Emission Structure of Imploded Cores." Los Alamos National Laboratory paper LA UR-79-1178 (1979).

12. L. W. Miller, H. W. Kruse, P. J. Kruse, D. E. Bartram, N. M. Hoffman, and J. M. Mack, "Design and Operation of a Time-Gated Optical System for Measuring the Angular Distribution of Light Emitted from Laser Targets." Los Alamos National Laboratory Conference on Optics 1979, Los Alamos, New Mexico, May 23-25, 1979 (to be published).

13. L. W. Miller, N. M. Hoffman, J. M. Mack, and H. W. Kruse, "The Limb-Darkening Opacity Experiment: Anisotropy of Optical Emission from the Back Side of Aluminum Foil Laser Targets," JOWOG 13 Test Diagnostics Conference, Lawrence Livermore National Laboratory, Livermore, California, May 15-17, 1979.

14. Ya. B. Zel'dovich and Yu. P. Raizer, *Physics of Shock Waves and High-Temperature Hydrodynamic Phenomena* (Academic Press, New York, San Francisco, London, 1966) Vol. 1, pp. 269-276.

15. N. M. Hoffman, L. W. Miller, and J. M. Mack, "Limb-Darkening Observations of Plasmas," JOWOG 13 Test Diagnostics Conference, Lawrence Livermore National Laboratory, Livermore, California, May 15-17, 1979.

V. DIAGNOSTICS
(D. Giovanielli)

The laser fusion process calls for new diagnostic techniques having spatial and temporal resolutions in the submicrometer and 1- to 100-ps regime. These needs are being met with a vigorous diagnostics program in such areas as laser calorimetry, charged-particle and neutron detection, x-ray spectrometry, and subnanosecond streak camera development.

TARGET DIAGNOSTICS

Introduction (D. Giovanielli)

We are continuing to improve and design instruments essential for accurate diagnosis of laser-heated and imploded targets. Many of these developments have produced significant advances over previous techniques.

Because a large fraction of the absorbed laser energy appears, eventually, as expansion of ions, proper detection of these particles can lead to an understanding of the energy partition within the heated region of a target. Plastic damage-track detectors have been used to advantage in the past and new developments in this area are being incorporated into our diagnostics. Measurements of the total amount of laser light absorbed by a target are of continuing interest, as are the time-dependence and target-dependence of such absorption. We are developing accurate techniques for these studies at each of the CO_2 laser facilities.

The most direct measure of fusion output is the neutron yield, which, in some target designs, may be kept low; accurate, sensitive neutron detection is therefore essential. New integrated yield measurement techniques have been developed, which increase dynamic range and sensibility, and new recording techniques for various instruments will lead to accurate and rapid data acquisition and retrieval.

Specifications for the Antares target facility require information from those who are building target diagnostics. Such information includes the estimate of maximum air pressure allowable in an ion and neutron drift tube. With approximate expressions for the scattering of ions from air molecules, a maximum pressure of 10^{-5} torr was found adequate for the drift tube to be used in the detection of ions with energies as low as 30 keV/Z.

X-ray imaging diagnostics are still essential for the diagnosis of nearly every type of laser target. Pinhole cameras, x-ray microscopes, and imaging spectrographs are all used in our experiments and continued development is extending their wavelength response and resolution. Detailed deconvolution techniques have been developed to relate actual source distributions to observed images. We hope soon to have temporally resolved one-dimensional x-ray images of CO_2 laser-heated targets.

High-energy x-ray measurements typically suffer from large background contamination and have been notoriously poor sources from which to derive a suprathermal-electron temperature. A recently developed K-edge system of detectors should remove much of the background problem and provide accurate spectral data in the 25- to 200-keV region.

Radiochemical diagnosis of materials rendered radioactive within an implosion system will become increasingly important as we advance to more complicated target geometries. Essential to the use of such techniques is the ability to capture a significant fraction of the disassembled target debris. Recent collector designs have demonstrated a collection efficiency of ~12%, adequate for our purposes.

Particle-Track Detectors (J. Kephart)

In the past we have used cellulose nitrate film on a polyester base as a particle-track detector. When etched in a NaOH solution, this material can record ion tracks, including the tracks of protons with energy less than 200 keV and α particles of energy less than ~4 MeV. However, it is difficult to record the very short tracks made by particles of very low energy; their surface

tracks interfere with the tracks produced by degraded higher energy particles.

A careful search for alternative materials disclosed another plastic material, CR-39, which should be superior to cellulose nitrate as a nuclear track detector.[1,2] Because this material is not commercially available in thin sheets, we are developing the capability to fabricate thin sheets and films. We expect CR-39 to be superior to cellulose nitrate because it can detect particles of higher energy (for example, protons of higher energy than 1 MeV) because it has a lower damage threshold for etchable tracks; because its superior optical properties should enable us to observe tracks of lower energy (very short tracks); and, because we hope to produce very thin films (with thicknesses <10 μm), it should be feasible to stack the film sheets so that the deeper layers are filtered by the first layers. This should make interpretation easier than in the case of the thick cellulose-nitrate films. Finally, self-supporting thin films provide the opportunity to observe tracks on both sides of the medium, in contrast to the backed cellulose-nitrate material.

We anticipate that this material will have wide application in imaging ions from the corona as well as α particles from D-T burn. It should also be superior to cellulose nitrate for ion spectrometry applications.

Diagnostics Development for Reflectance Measurements (R. Kristal)

Several projects focusing on the plasma reflectance problem are in various stages of design. We are building a simple infrared receiver to measure the time-dependence of diffuse-scattered CO_2 light at some arbitrary angle. The device consists of a single lens focusing its collected light onto a small pyroelectric detector. We hope to obtain ~100-ps response time by using high-speed cable and a 5-GHz oscilloscope near the target chamber. Initial use is planned for Gemini, viewing from outside the chamber through a salt window.

A 4π diffuse scatter measurement using an integrating sphere is also planned. A device has been ordered for this purpose, with a diameter of 12 in. (30.5 cm) and an inside surface of diffuse reflecting gold. This measurement will ultimately be used on Helios, with Gemini as a proving ground where it can be compared with the double-ellipsoid measurement.

The integrating sphere gives neither temporal nor spatial resolution. To obtain angular distributions, we are considering the use of specular optics. Clam-shell variations, arrays of small elements, and even holographic mirrors are being studied. The basic problem with a single optic is the large size needed to avoid damage, and the attendant fabrication difficulties with nonspherical surfaces. A pyroelectric vidicon (PEV) is appropriate for imaging the angular distribution. At this time, the PEV is still our only 10-μm two-dimensional imaging detector with serial readout (so that only one data channel is needed).

There are some longer range applications in which the PEV may also be useful. One of these is photography of the target imaged in scattered CO_2 light. Initially, these photographs would be time-integrated, although we hope to achieve time resolution via optical gating eventually. Gating should identify the origin of the scattered light. A natural extension of this effort is imaging in harmonic emission. Another scheme is photography in external light, which should provide information about cratering or rippling of the plasma surface. This measurement would also give information useful to another diagnostic: tracking a critical surface interferometrically by fringe-counting.

In the fringe-counting technique, a small portion of the target surface is used as a retroreflector in the scene arm of an interferometer (for example, a heterodyne interferometer). The interference beats between the scene and reference arms are then detected optically, giving information on the motion of the reflecting surface (and the preceding plasma) during the measurement interval. By using a low-energy laser pulse, nonlinear effects can be avoided, and purely geometrical properties of the expanding plasma should be observable. Fractional wavelength resolution is frequently obtainable with fringe-counting. This would be very useful in the present application. Multiple wavelengths might also be used to help reveal profile details. Of course, the reflecting surface must be somewhat cooperative in limiting the excursions in reflectivity that the probe beam sees. Also, a sufficient level of phase coherence must be maintained. Alternatively, the level of coherence may be an indicator of surface roughness.

Scintillation-Based Neutron Activation Counts (V. Cottles, A. Williams T. H. Tan)

The Lanther-Bannerman silver activation counter is a world standard for pulsed neutron measurements, but its dynamic range is only 5×10^3. We needed a counter

based on the same intrinsic principles, but with a higher dynamic range and, if possible, a higher sensitivity that would be suitable for the laser fusion program. A system of activation foils and scintillator viewed by a photomultiplier provided a measure of the enhanced performance sought.

Figure V-1 shows the geometry of the three heterogeneous activation foil/scintillator systems assembled to test the proposed higher performance systems. The geometrically identical units were constructed to mount (without optimizing light pipes) to a 6342A photomultiplier tube with an integral high-voltage and line driver system powered by a 35-V supply. These units were used in a direct comparison of silver and rhodium as activation foils. Because the scintillation systems have a higher background noise than the Geiger-Mueller-based L-B counter, the figure of merit used for sensitivity comparison is $\eta_{neutron} = \sigma_{Bkg}\, n_{n\ count}$. This measure of resolution gives minimum neutrons per standard deviation of monitored (i.e., gross) counts. The figure of merit $\xi = (1/\tau_{dead})N$ is used to compare dynamic ranges in which the scintillation systems excel. Both figures of merit are minimal for best performance of the detector.

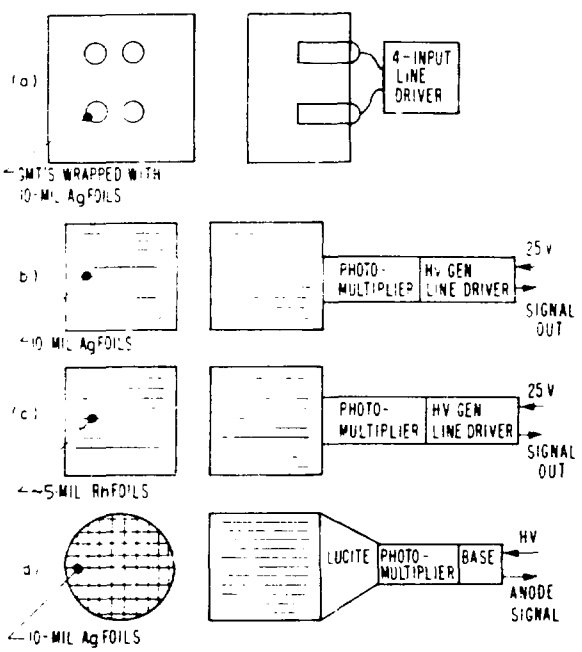

Fig. V-1.
Comparison of three heterogeneous activation foil/scintillator systems (b), (c), (d) with the Lanther-Bannerman silver activation counter (a).

When comparing the performance of the units described in Fig. V-1 for the two figures of merit, the new systems do not markedly increase intrinsic sensitivity, but they greatly increase the linear dynamic range. These units are usable for especially high-yield, single-pulse neutron sources.

Digital Pen Recorder for Slow Low-Level Signals (V. M. Cottles, L. Sprouse)

Laser fusion diagnostics require a large number of calorimeters that produce voltages of ~100 μV. In a given experiment a calorimeter may produce signals that vary by a factor of 100 on a shot-to-shot basis. The two methods presently used to monitor these calorimeters have several shortcomings:

1. Hewlett Packard series 7404A pen recorders have high sensitivity (1-μV resolution), but they are costly ($3.5k/channel), they must be manually digitized, they have too small a dynamic range, and they are bulky.
2. LeCroy series 2956 transient digitizers are inexpensive ($300/channel), they have a wide dynamic range and direct computer connection, but their sensitivity is low (250 μV), which requires outboard amplifiers, they have excessive zero-time uncertainty, requirements for external clocks and memory, and a lack of configuration encoding.

We have developed a recorder optimized for calorimeter work that incorporates all the features needed for precision calorimetric monitoring. It has the following characteristics.

- Size - triple width NIM
- Channels - 4 per module at $1k/channel;
- Resolution - 2, 5, 10, 20, 50, and 100 μV, selectable;
- Dynamic Range - 14 bits (1 part in 16 000);
- Encoded - All switch positions controlling, for example, sensitivity, sample rate, data saved before trigger, trigger time relative to sampling times (to 1 part per 1000th of sample period), current mode, module serial number.
- Can be used with a manual readout display unit independent of a computer system and chart recorder in case of a computer system failure.
- CAMAC interface for complete computer control and readout.

Figure V-2 compares a trace taken with Channel 1 of our pen recorder and that taken with Channel 1 of a HP 7404A recorder. The signal source is a Scientech Model 200 calorimeter given a 3-J electrical calibration pulse. It

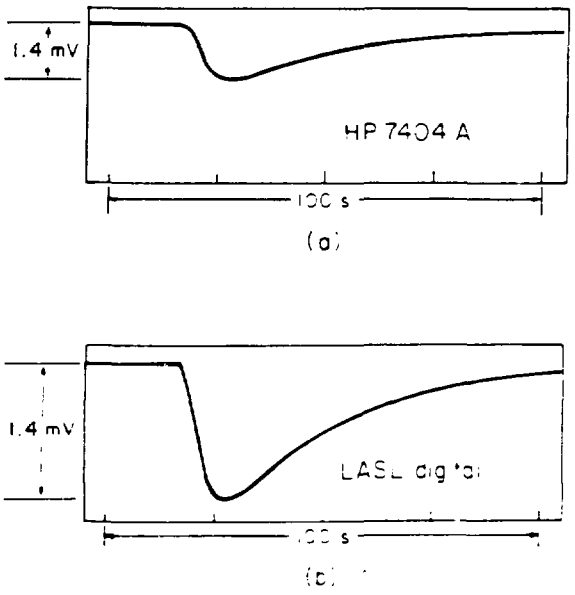

Fig. V 2.
Trace made with Hewlett Packard 7404A pen recorder (1a) compared with trace made by digital pen recorder developed for use with calorimeter (1b).

is expected that these units will offer a low-cost, highly flexible capability for the development of diagnostic calorimeters, will provide easy stand-alone development, and will be compatible with computerized data acquisition and analysis.

Calculation of Multiple Ion Scattering in Drift Tubes (M. M. Mueller)

The study concerned the multiple scattering of ions by the residual gas in a long evacuated tube of circular cross section. The 100-m-long time-of-flight drift tube will be used on the Antares system for neutron and ion diagnostics.

The drift tube is 30 cm in diameter and starts at the target-chamber wall 360 cm from the target. Our main concern is with an ion diagnostics station ~30 m from the target; another station at ~10 m is of secondary interest. Also of some interest is the possibility of using a small-diameter tube emerging from the target chamber and terminating within the target room. We will only be concerned with a small detector on the tube axis, which passes through the imploded-target source. Because there is no significant loss of ion particles or energy, even at 100 m and any gas pressure contemplated for the evacuated tube, the problem is essentially one of estimating the effect on detector response of multiple-angle scattering in a bounded medium. This problem is inherently complicated, and we have had to resort to drastic oversimplifications to obtain a timely useful solution.

We reviewed a multiple-scattering theory in search of a simplification that might lend itself to analytical treatment. We were successful in our small-angle regime: each ray of ions from the imploded target is scattered into a Gaussian angular distribution as it travels down the tube:

$$H(\theta) = e^{-\theta^2/\theta_e^2}$$

where θ is the scattering angle and

$$\theta_e = 1.1\epsilon \cdot \frac{Z}{A} \cdot (Z+1) \cdot \frac{s}{E^2}$$

in which Z and A are the atomic number and atomic weight of the scattering substance, E and z are the energy and charge of the projectile ion, and s is the path length traversed by the ion for $\theta = 0$. The angle θ_e is in angular degrees when E is in MeV and s is in mg/cm^2.

To distill such simplicity from the tedious complexity of multiple scattering seems too good to be true—and indeed it is. Essentially, we have a geometrically thick target, and θ is only poorly defined. This introduces about a factor-of-2 uncertainty in the calculated detector response.

Another problem is that multiple-scattering theories must start with knowledge of single-scattering cross sections, and these are not particularly accurate at low ion energies. We have simply assumed that the scattering theories remain valid down to 0.03 MeV/z. This approach probably overestimates the magnitude of the scattering at energies below ~ 0.1 MeV/z; our calculated results will therefore be conservative. Air pressure needed to reduce the detector response significantly is probably higher than calculated.

Another effect ignored in our treatment is the reflection and sputtering of ions at the tube wall. The very small grazing angles may make reflection especially troublesome, although the installation of baffling might help.

Because the geometry of multiple scattering is complicated, we do not present the calculations here. Details

are available in an internal memorandum.[3] The calculations are numerical evaluations of analytically expressed integrals.

The computed relative detector response (which approaches unity under all conditions as the tube diameter increases without bound) is plotted in Figs. V 3 through 5 under varying conditions, which we might expect to occur in the Antares system. The parameter in these plots is the reduced projectile ion energy E/z in MeV. Figures V 3 and 4 are concerned with detector response at two locations within the existing Antares drift tube, and Fig. V 5 gives the response using a smaller tube.

Uncertainties as great as a factor of 3 can be expected in our estimates of the air pressure required to cause a specified degradation of detector response. However, the accuracy obtained should be helpful in assessing the vacuum requirements within the drift tube. For example, we have imposed a 10^{-6} torr requirement for the 30 m detector station in the Antares drift tube.

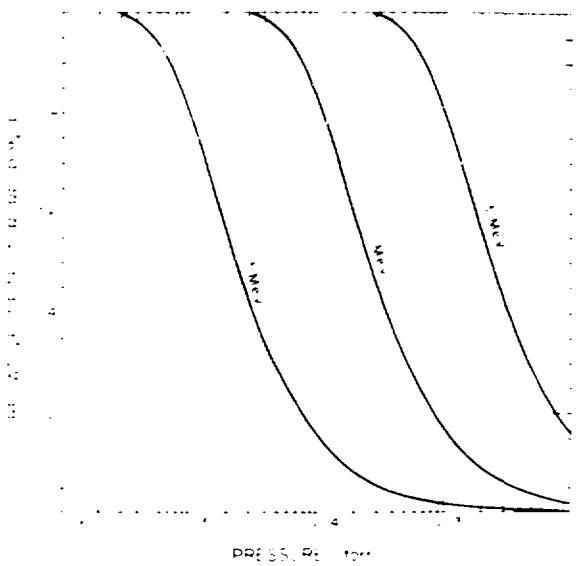

Fig. V 3.
Calculated detector response as a function of residual air pressure due to multiple ion scattering in a long drift tube with a 30 cm diam and a detector positioned at 30 m. The parameter is the reduced projectile energy E/z.

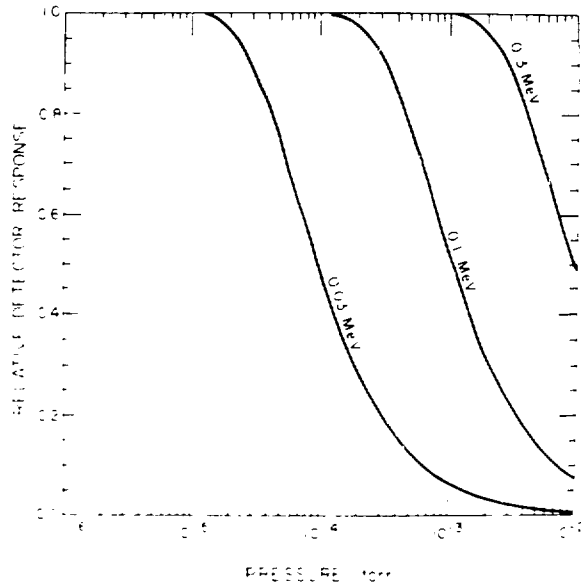

Fig. V 4.
Calculated detector response as a function of residual air pressure due to multiple ion scattering in a long drift tube with a 30 cm diam and a detector positioned at 10 m. The parameter is the reduced projectile energy E/z.

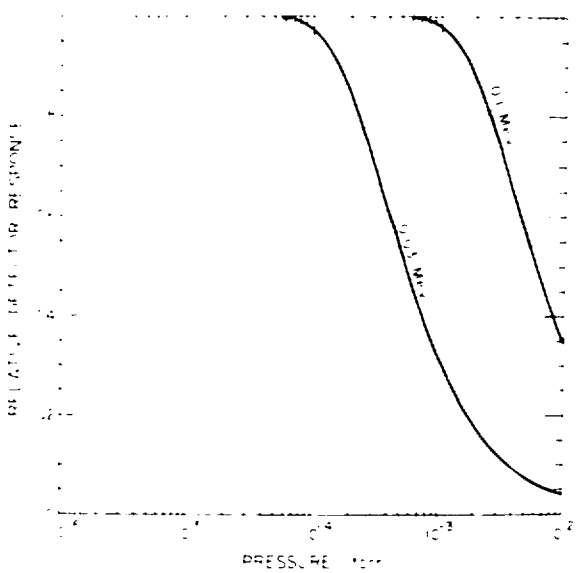

Fig. V 5.
Calculated detector response as a function of residual air pressure due to multiple ion scattering in a long drift tube with a 7.5 cm diam and a detector positioned at 7.5 m. The parameter is the reduced projectile energy E/z.

Reconstruction of Spherically Symmetric Source Emission Structure from Slit Images by Differential Methods (M. M. Mueller)

Preliminary work on this subject was discussed in the last progress report,[4] which should be consulted for context and background information. We report here the extension and conclusion of this investigation.

The final conclusions are similar to the preliminary ones. While the Vest and Steel method[5] is valid for infinitesimal slit widths and practically noise-free irradiance data, its validity does not extend to slits of practical width in the laser fusion program. However, we have developed a method for reducing the Vest-Steel plots with practical slit widths to obtain information on core diameter, shell diameter, and shell thickness. Thus, with our new reduction method, the Vest Steel method applied to low noise data taken with practical slits could be useful in the fusion program. At the least, it could serve as an adjunct method to check on the theoretical problem of uniqueness associated with the iterative integral method being used.

An example of the use of this differential method is the three shell source model shown in Fig. V 6. The thickness of each shell is 0.05 of the outermost radius b. The simulated irradiance distribution in the image of this source is shown in Fig. V 7. It is formed by a slit of half width a = 0.05 b with a camera magnification of 3. The flat regions are due to the little known fact that a slit images a spherical shell as a plateau. This slit width is approximately the practical lower limit for apertures used in our experimental program. The Vest Steel differential method applied to the simulated irradiance distribution gives the results shown in Fig. V 8. (The noise in the curve, especially evident near r = 0, is due to the use of finite zoning in the numerical convolution.) Distortion due to the finite slit width is evident in the ordinate scale, but is particularly pronounced in the abscissal scale.

However, the simple methods we have developed allow the *exact* recovery of the three outer radii of the source model (ignoring experimental data noise), as well as the approximate recovery of the shell thicknesses. The best accuracy achieved in reconstructing the shell thicknesses was better than ± 10%, although ± 20% may be more typical. The methods used are extensions of the simple geometrical relationships within the image that have been discussed previously.[6]

Figure V 9 illustrates the method applied to a larger aperture typical of those used in practice. Here a = 0.1 b.

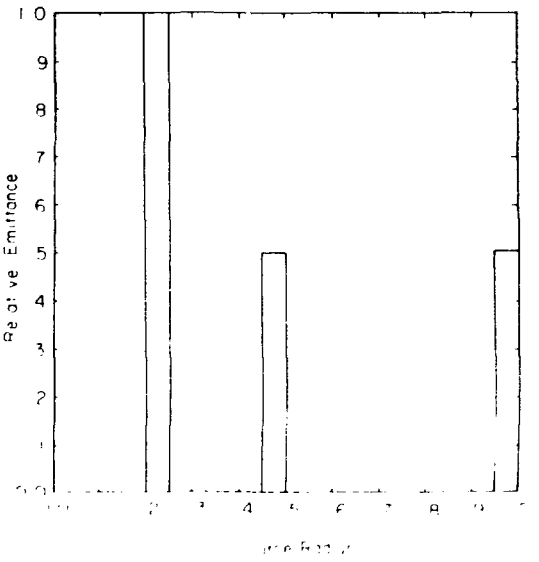

Fig. V 6.
Three shell model of a spherically symmetric source of emission. The thickness of each shell is 0.05 of the outermost radius b.

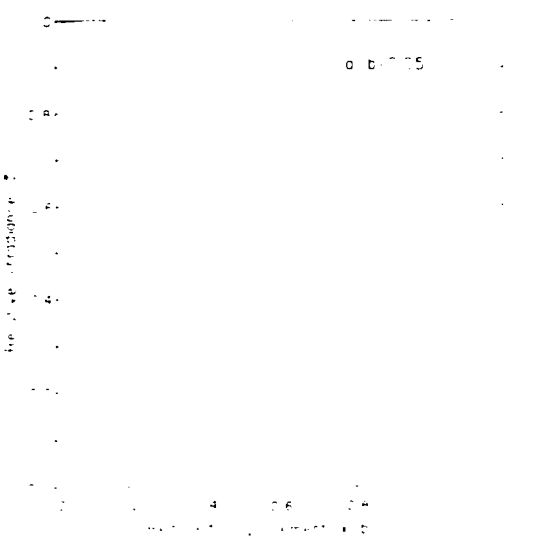

Fig. V 7
Vest Steel method applied to the irradiance distribution for a/b = 0.10 and M = 3

and the gross distortion is evident. The large spike at about r = 0.35 b is an artifact due to overlapping images of the two innermost shells, but could easily be misconstrued as real. Although the two innermost shells are

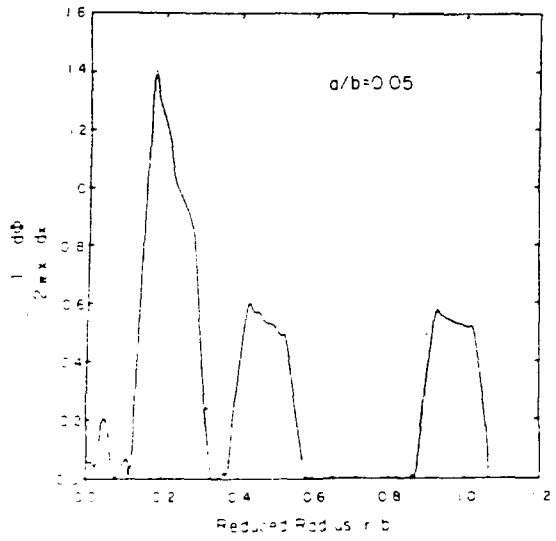

Fig. V.8.
Vest Steel method applied to the irradiance distribution for a/b = 0.05 and M = 3.

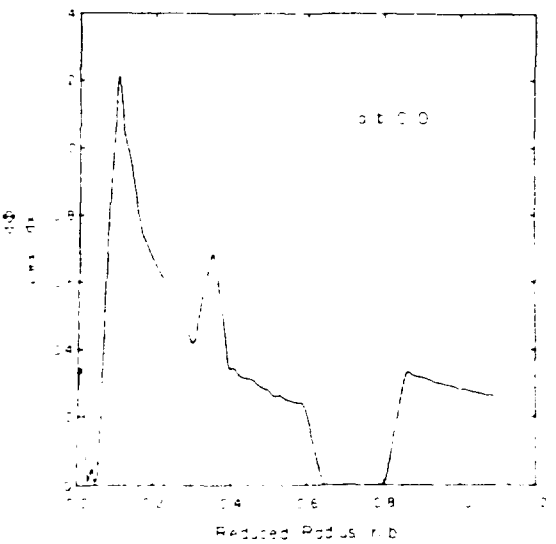

Fig. V.9.
Vest Steel method applied to the irradiance distribution for a/b = 0.10 and M = 3.

not resolved, the outer radii of the two outermost shells can still be reconstructed exactly. However, the thickness of only the most isolated shell can be recovered, but with about the same accuracy as with the smaller slit.

Extensions and Modifications to the Two-Dimensional Convolution Code (M. M. Mueller)

Three major modifications were made to enhance the versatility and efficiency of the image-simulation code previously developed.

- Previously, only apertures with the high symmetry of such functions as circles, generalized circles, or squares could be accommodated in the code. Because some pinhole apertures have an oval or elongated shape, we have modified the code to handle apertures of lower symmetry such as ellipses, generalized ellipses, or rectangles.
- Previously, the radiance integral was computed internally in the code only at grid points of the convolution. To increase the efficiency and versatility, the radiance is now computed at an arbitrary point by a subroutine.
- Although the code can handle any radiance distribution, much of our work uses radial source models. Thus, the code was unnecessarily cumbersome for much of our use with circular apertures. For this reason, a fully restructured, more efficient new version of the code was produced to handle cases having source and aperture radial symmetry. The augmented efficiency is nearly ten times higher for small pinholes, but only two times higher for large pinholes. This improvement is of particular value when the code is used iteratively to fit image data.

Optimization of Kirkpatrick-Baez X-Ray Microscopes for Helios (W. Priedhorsky)

Routine x ray target imaging at the Gemini and Helios laser facilities is performed by pinhole camera systems. Though pinhole systems offer ease of operation and acceptable throughput and resolution for routing broad band imaging, there may be some advantages in imaging with grazing-incidence x ray optical systems. Such optical systems include Wolter microscopes and Kirkpatrick Baez crossed cylinder microscopes. Wolter microscopes offer very large collection efficiency, but are difficult to construct and align; Kirkpatrick-Baez systems are less efficient, but are relatively easy to construct and align. We are developing a Wolter microscope for experiments requiring large collection efficiency.[7,8] In this report, however, we will describe the design of a Kirkpatrick Baez microscope system for routine use on the Helios system.

Kirkpatrick-Baez (KB) microscopes offer several operational advantages over pinhole cameras. A KB microscope can operate at distances >30 cm from the target, as compared to 3.5 cm for a pinhole camera. Because both pinholes and KB microscopes act like simple lenses for a constant magnification, the distance between film plane and target increases proportionately. Film background from penetrating radiation should be less at the film plane for a KB microscope because of the larger distance from the target; KB microscopes can achieve a resolution of 3.5 μm (full width), slightly better than a pinhole camera, while for energies less than ~2.5 keV, they offer significantly greater collection efficiency. Though x-ray grazing incidence systems lose efficiency rapidly as the design energy exceeds ~5 keV, they offer the complementary advantage that the grazing angle of any system defines the high energy cutoff quite well.

KB microscope systems reflect x rays from two successive cylindrical mirrors to form a point image (Fig. V-10a). Reflection from a single cylindrical surface at grazing incidence will form a line focus (Fig. V-10b); reflection from two perpendicular cylinders thus forces rays to a focal point at the intersection of the two line images. Four cylindrical surfaces can be combined in a system to produce four images.[7] The square symmetry of this system helps in optical alignment. For small grazing angles ($\theta_r \lesssim 2°$), the perpendicular reflections are independent, and microscope performance can be evaluated by analysis of the one dimensional systems. We designed two KB microscope systems for Helios using a one dimensional analysis that optimizes microscope efficiency and resolution.

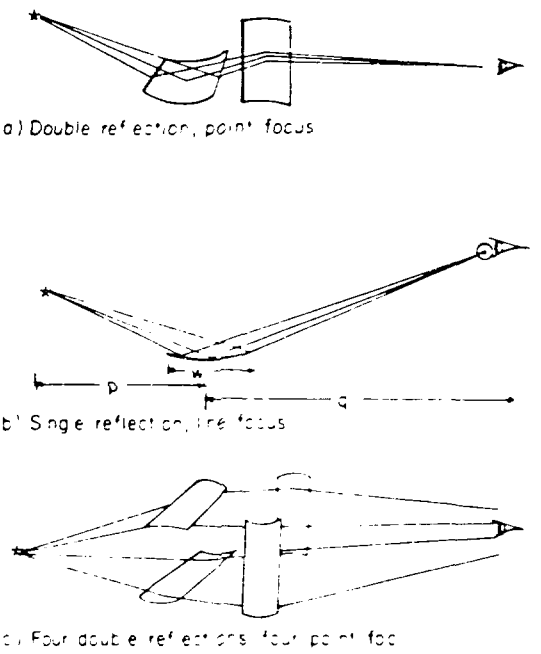

Fig. V-10.
KB microscope system: (a) reflection from two perpendicular cylindrical surfaces gives a point focus; (b) reflection from a single cylindrical surface gives a line focus; (c) reflection from four cylindrical surfaces combined to produce four images.

Each microscope is designed for maximum x-ray photon energy. Because x-ray intensity falls with increasing energy in the kilovolt band, the optimization scheme is to maximize collection efficiency at the maximum design energy, where the x-ray flux is weakest and efficiency is thus most important. For a given mirror length and target distance, the collection efficiency $\Omega_{eff} \sim \theta_r^2 R^2$, where θ_r is the reflection angle and R is the reflection efficiency. Both terms enter as the square because of the two reflections in the microscope. The reflection efficiency $R(\theta_r)$ is calculated at a given photon energy E and reflector material via the formulas of Giacconi et al.[8] The product $\theta_r^2 R^2$ can be calculated as a function of θ_r, allowing the determination of the maximum throughput $(\theta_r^2 R^2)_{max}$ and the optimum angle θ_{opt} for each point. Figure V-11 shows $(\theta_r^2 R^2)_{max}$ (E) for a number of potential reflector materials. The optimum mirror material and reflection angle for the design photon energy can thus be chosen. For a design energy of 4.0 keV, for example, we choose a nickel reflector. The optimum grazing angle for this case is 0.72°. Although reflectivity generally increases with increasing electron density and critical angle, nickel is preferred to elements of higher Z, such as gold, in the 2 to 6 keV range because of (a) the suppression of reflectivity in that band for the elements around gold due to M edges and (b) the relatively low x-ray absorption of nickel in that band, which yields a flat R vs θ_r curve up to the critical angle and sets θ_{opt} near the critical angle.

Three aberrations are significant in determining the resolution of a one dimensional grazing incidence focusing system: spherical aberration, coma, and diffraction. For a cylindrical reflector of magnification $M = p/q = 1$, where p is the object mirror distance and q is the mirror image distance, the proper focusing surface is a section of an ellipse rather than a circle. Use of a circle introduces an aberration (expressed in terms of full width at the object):

$$S_{sa} = \frac{3}{16} \frac{(M+1)}{(M-1)} \frac{(M+1)}{q^2} \theta_r^3 \qquad \text{(V-1)}$$

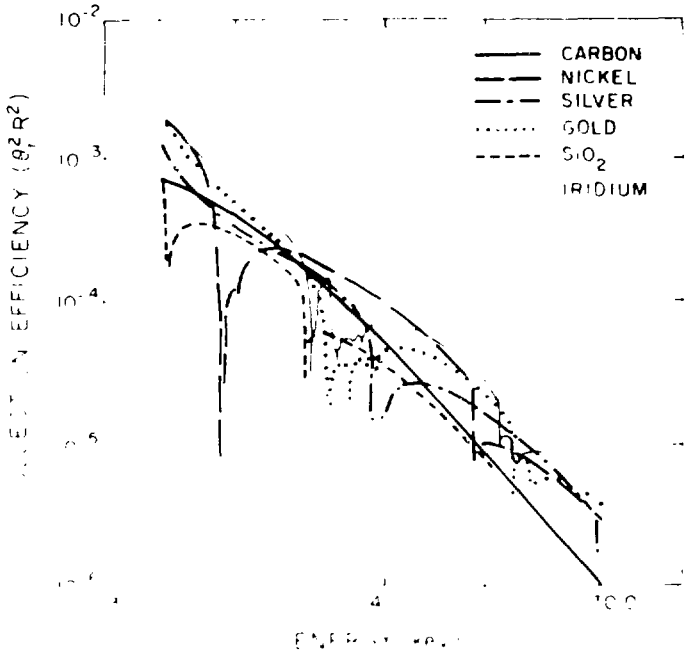

Fig. V.11
Comparison of collection efficiency for a number of potential reflector materials.

where γ = w/p, and w = mirror width. The fact that the effective magnification varies over the length of a finite mirror yields a comatic aberration:

$$S_c = \left(\frac{M+1}{M}\right)\gamma b, \qquad (V.2)$$

where S_c is again expressed as the full width of the aberration and b is the distance of a point off axis. The focusing surface acts like a slit of aperture $w\theta_g$ and thus produces a diffraction aberration of "full width" (first minimum to first minimum)

$$S_d = \frac{2\lambda}{\gamma\theta_g}. \qquad (V.3)$$

For the design case λ = 3.1 Å, θ_g = 0.72°, p = 50 cm, and M = 3.5. We find that S_c = S_d dominate for this case. The total resolution at the edge of the field of view is minimized by setting S_c = S_d:

$$\gamma = \left[\frac{2\lambda}{\theta_g b}\left(\frac{M}{M+1}\right)\right]^{1/2}. \qquad (V.4)$$

For a field of view b = ± 100 μm, we find an optimum γ of 0.02, corresponding to S_c = S_d = 2.5 μm. Spherical aberration is indeed not important: S_s = 0.4 μm. The second microscope, designed with θ_g = 1.2° for E_{max} = 2.3 keV, has w = 1.0 cm and p = 30 cm for γ = 0.033, slightly higher than optimum, to increase the efficiency for low flux experiments.

A fourth aberration can occur from crosstalk between the two reflectors. Because it scales as θ_g^3, S_x is not important for the systems described above. Its significance for higher angle systems is being investigated via ray traces.

In a "four banger" system the reflection angle is the same for the four channels. Channel responses are defined by K and L edge filters and by the choice of reflector material for each channel. Possible channel response functions are shown in Figs. V.12a and b for the 0.72° and 1.2° microscope systems. The four channel KB microscope allows the definition of several distinct response channels from a single instrument. These multiple responses may be useful in estimating temperature as a function of position on an image. We expect to field these devices on Helios during the next reporting period.

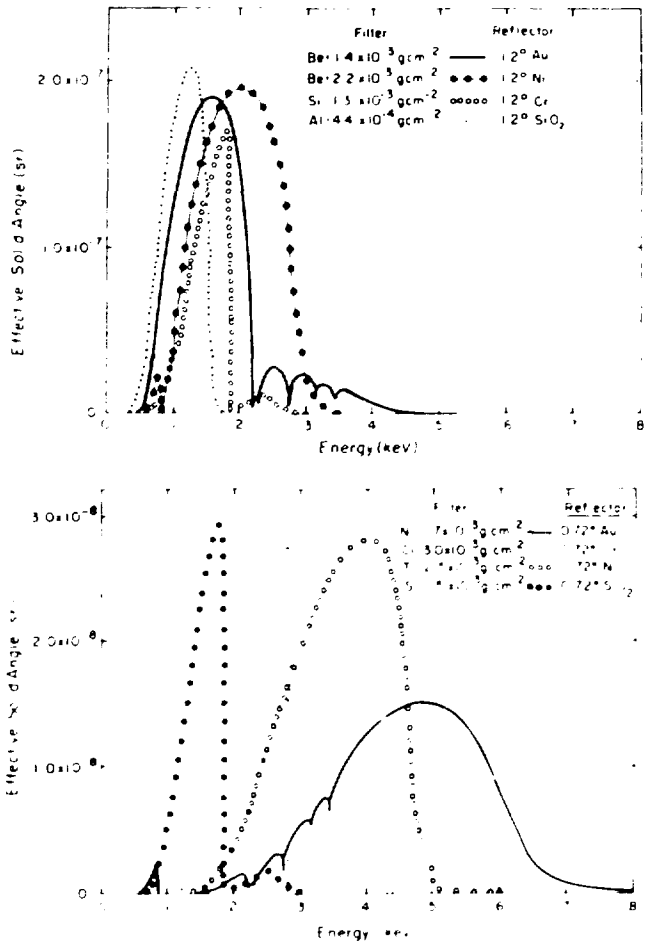

Fig. V 12
Possible channel response functions for microscope reflection angles of (a) 0.72° and (b) 1.2°

K Edge Filtered High Energy X Ray Detectors (Ping Lee)

A 10 channel system of K edge filter fluor photomultiplier tubes for x ray spectrometry, shown schematically in Fig. V 13, will be used at the Helios laser facility. Magnets, together with polyethylene drift tubes, prevent electrons from entering the spectrometer. Collimation of the detectors is provided by a 9.5 mm diam hole in 53 cm of aluminum plus 10 cm of lead. All the PM tubes are encased in at least 1.3 cm of lead.

The filter CsF fluor responses for six of the channels are shown in Fig. V 14. For a given filter, for example, silver, we used another filter to match the transmission beyond the K edge of the first filter. Here we used lead plus nickel. This allowed us to examine the importance of the secondary peak. The thickness and nominal peak energy response of the three paired channels are

Channel	Filter	Nominal Energy (keV)
1	25 μm Ag · 0.5 mm CsF	25 and 38
2	2 μm Pb · 0.1 mm Ni · 0.5 mm CsF	38
3	65 μm Au 2.5 mm CsF	57 and 87
4	0.15 mm Mo · 0.046 Su · 2.5 mm CsF	87
5	250 μm U · 6.4 mm CsF	132 and 200
6	25 μm Au · 1.8 mm Ag · 6.4 mm CsF	200

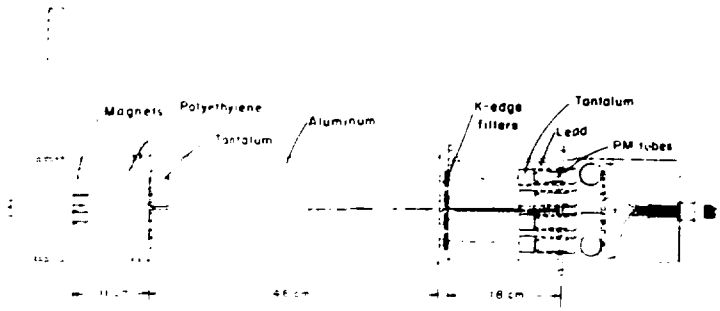

Fig. V 13.
Ten channel system of K edge filter fluor PM tubes for x ray spectrometry.

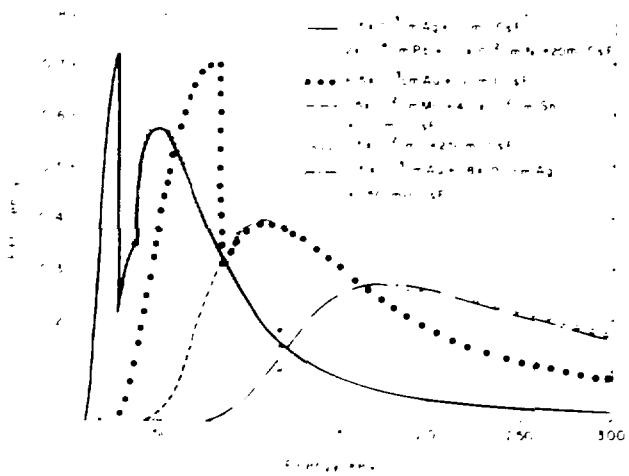

Fig. V 14.
Responses for six channels of the spectrometer system shown in Fig. V 13.

The signal will be integrated on a CAMAC integrator and stored in the PDP 11 70 computer. The integration window will be 20 ns

The ability of the system to determine the suprathermal electron temperature T_H is shown in Table V I. Here, we assumed the idealized case of a pure bremsstrahlung spectrum without noise or background. The signals in each channel are normalized to channel 1. The signal in channel 6 increases by nearly a factor of 2 in the 60- to 100-keV temperature range, with respect to channel 1. In this ideal case, T_H can be determined rather accurately. If the system has 20% noise and or back ground, then the measurement of T_H can be expected to be accurate to 20%.

X Ray Streak Camera Development (P. D. Rockett, J. S. McGurn)

Operating Parameters. The GEAR, Inc. Pico X x ray streak camera was successfully operated by using an all avalanche transistor string for triggering. The measured streak rate was ~59 ps/mm with a minimum temporal resolution of 21 ps. This produced a writing record of 1.06 ns across the 18-mm microchannel plate (MCP) intensifier output. The slit dimensions were 9 by 0.5 mm, resulting in a minimum spatial resolution of 166 μm at the camera. Triggering jitter was ~ ± 300 ps with a 10 V square-wave, fast rising (4-ns) trigger. This jitter was reduced to ± 100 ps by increasing the trigger

TABLE V-I

SUPRATHERMAL ELECTRON TEMPERATURES
FROM DATA TAKEN WITH X-RAY SPECTROMETER

Channel	Nominal Energy of Detector (keV)	Detected Signal Relative to Channel 1 X Ray Temperature (keV)				
		20	40	60	80	100
1	25	1.00	1.00	1.00	1.00	1.00
2	38	0.50	0.68	0.74	0.78	0.80
3	57	0.27	0.55	0.72	0.83	0.91
4	87	0.48	1.95	3.26	4.53	5.10
5	132	0.42	1.72	2.92	3.92	4.71
6	200	0.049	0.55	1.22	1.93	2.56

amplitude to 35 V and decreasing the trigger rise time to 1.5 ns.

Timing measurements were made by viewing the x ray pulses from laser irradiated gold coated microballoons. The two beam glass laser was used to illuminate 200 μm GMBs coated with ~1 μm of gold. Incident energies varied from 5 to 20 J in a 300 ps pulse. (Laser pulse width and structure were characterized with a 5 GHz oscilloscope.) The Pico X streak camera was oriented at 90° to the opposing, incoming laser beams (Fig. V-15). The photocathode was placed 15.25 cm (6 in.) from the target and no pinhole was used. (No filter was used during the shots discussed in this report.) Triggering began with an optical pick off into a fast photodiode. This signal was delayed and sent to a low jitter discriminator pulser, producing a constant 10 V square pulse which, in turn, triggered the camera avalanche transistor string. Camera triggering was monitored every shot by viewing the leakage current returning from the base of the input avalanche transistor.

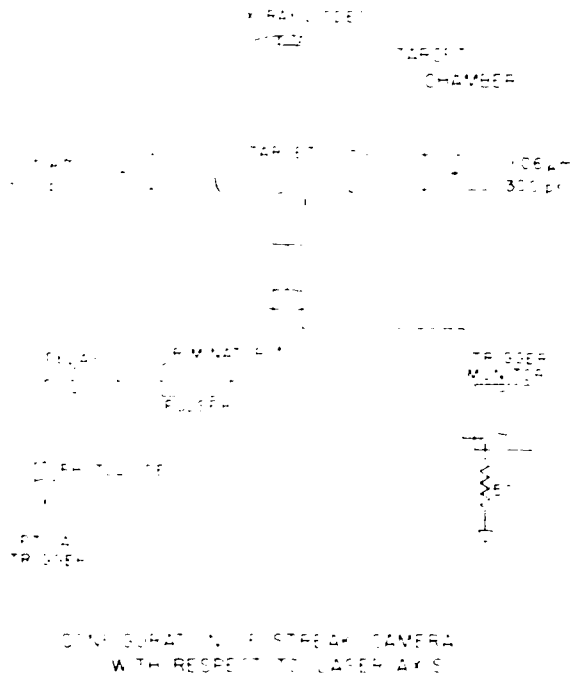

Fig. V-15.
Arrangement for x ray streak camera timing measurements.

Sweep speed of the streak camera was determined by offsetting the two incident laser beams in time and observing the x ray pulse time difference. The sweep rate was 59 ps/mm with a full streak window of 1.06 ns. Much structure in the x ray pulses was not visible on a fast x ray diode (XRD) that was also used in this experiment. The XRD sensitivity peaked at 1.25 keV with a 0.5 keV bandwidth. Streak camera sensitivity is plotted in Fig. V-16. Streak photographs revealed an x ray pulse half width of only 150 ps, possibly due to the high energy spectral region being observed. At low incident laser energies a clear step in the emitted flux was observed preceding the x ray pulse—a step not seen on the fast XRD. One example of a pulse recorded on the streak camera is shown in Fig. V-17.

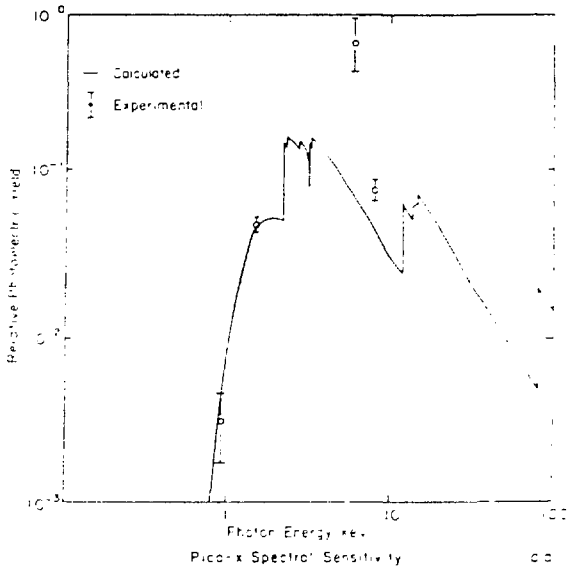

Fig. V-16.
Measured streak camera sensitivity compared with calculated values.

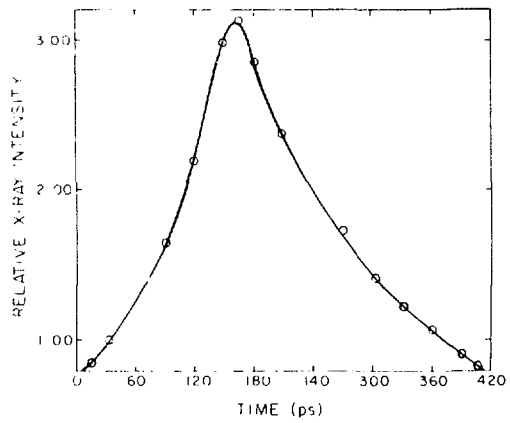

Fig. V-17.
Example of a pulse recorded on the Pico-X streak camera.

Streak-camera sensitivity was compared to dc measurements made earlier on a Henke tube source. Using the data in Fig. V-16, a comparison was made to the XRD data whose sensitivity peaked at 1.25 keV. The pulsed sensitivity of the camera was measured to be about five times that measured in a dc mode. This result was consistent with prior concern that space-charge build-up in the the streak tube collimator microchannel plate would increase the required input signal. The sensitivity would thus appear lower than it actually was. How much lower was not known.

Noise Sensitivity. A null test was run on the Pico-X streak camera in the Helios laser chamber. The camera was run in a dc mode with all voltages on and the slit imaged onto the lower portion of the phosphor. A 1.3-cm-thick, 10-cm-diam lead disk shielded the camera from direct x-ray radiation. A 0.6-cm-thick polyethylene disk covered the lead to minimize the effect of fast electrons; 0.6-cm-thick lead covered the camera on three sides; the bottom was protected by 5 cm of aluminum. The rear of the camera was unshielded. The entire streak camera and all controls were isolated from electrical contact with the vacuum chamber, and the camera photocathode was placed 1 m from the target.

The resulting film was examined for evidence of a noise signal. Initially, the entire laser was fired without allowing light to strike a target. This failed to produce any detectable signal on the film. The irradiation of targets, however, produced a noticeable background fog. With 3.5 to 4.0 kJ of CO_2 laser energy focused onto 400-μm-diam GMBs, the background density rose from 0.24 to 0.42 on bare GMBs and to 0.68 on plastic-coated GMBs. The direct, hard x-ray shine-through was very small, but noticeable, resulting in a further increase in density of ~0.10.

The source of the noise was not identified; however, the plastic-coated shots provided a strong hint. The lack of a strong direct-shine signal plus failure to expose medical no-screen film within the camera gave evidence that hard x rays were not the primary culprit. Plastic-coated targets produce a copious number of fast ions and, in turn, fast electrons, while their primary x-ray flux is low. Fast ions are efficient producers of characteristic x radiation, which would not penetrate the camera and shielding. Fast electrons, however, could penetrate the shielding and interact with the phosphor and intensifier within the camera. They could also generate x rays in the shielding and camera body via Compton scattering and bremsstrahlung. High-energy (>100-keV) electrons are difficult to shield against. A new shield incorporates 5 cm of Teflon in an attempt to decrease the electron flux striking the camera. Magnetic fields required to deflect electrons >1 MeV would also disturb the swept electrons within the streak tube. Thus, they are not used in this application. Even with the present noise background, signals from irradiated targets will be

readable. Further efforts are under way to understand the noise generation mechanism and to minimize it.

Absorption Apparatus for Gemini (V. M. Cottles, A. H. Williams)

A series of absorption experiments using the single-beam system (SBS) resulted in the development of the "egg" collection optics to monitor the scattered light for various targets. These experiments yielded the first 4π measurements of CO_2 laser light scattered from spherical targets (GMBs). This experimental apparatus was redesigned to allow the absorption measurements to be performed at the Gemini facility. Thus, we will be able to measure higher energies, and to improve our incident-beam diagnostics and collection optics. We will also be able to gather data from a larger parameter space for future target designs and for normalization of reaction-product data.

Figure V-18 shows a schematic of the new egg configuration to be used on Gemini. This design differs from the original SBS configuration in the following ways.

- In the SBS unit, the semimajor axes of the elliptical mirrors were rotated by 105°, whereas in Gemini, the axes will be rotated 180°. The angle of rotation at the SBS had to be smaller to allow the unit to fit into the target chamber. This required the use of smaller calorimeters than desired because access to the prime focal spots was limited. The 180° orientation will permit the new absorption apparatus to have an effective diameter equal to the length of the semimajor axis.
- The original optics were made of brass with a measured reflectance of 97.2% for 10.6-μm light. The new optics will be fabricated from OFHC (oxygen-free hard copper) with an expected reflectance of 99.2%.
- The original system used high-precision f/0 calorimeters, but their size was limited by the axis rotation angle and they had limited energy handling capability. In the new system, a relay optic (called a "yolk" mirror) is used to convert the f/0 output of the egg to f/1.1. This allows the use of inverse Knudsen-cell calorimeters of wide dynamic range. Because the new system maps a 4π angular space onto finite plane areas, we hope to obtain extensive angular information on scattered light with time dependence preserved.

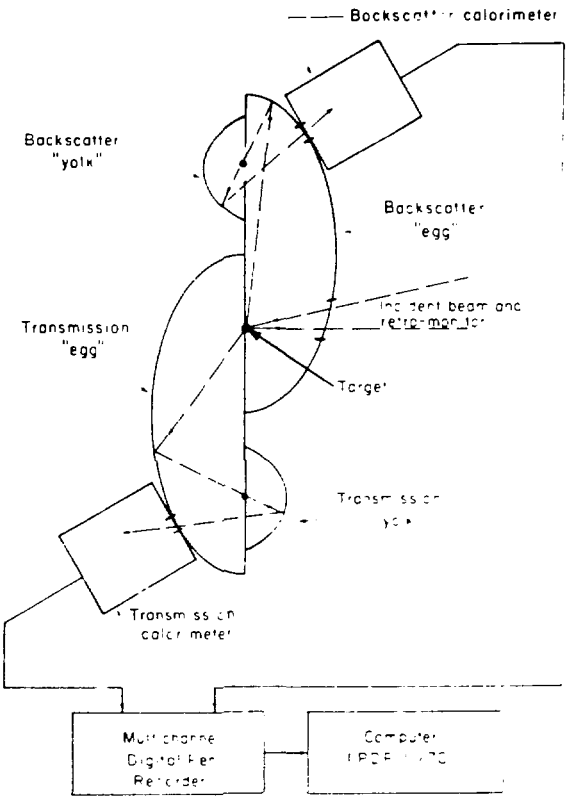

Fig. V-18.
A new 4π collection optics designed for use with Gemini.

- In the old system, the calorimeters were monitored with standard pen recorders that required manual data reduction. At Gemini, the calorimeters will be monitored with a new digital pen recorder that provides wide dynamic range and direct computer connection to allow shot-by-shot data analysis.
- The Gemini system is being retrofitted with a single-target insertion mechanism that should allow a high shot rate and a larger parameter space to be investigated in less time.

In the SBS experiments, we observed that absorption was independent of the initial GMB target radius. We also observed that out-of-focus effects were not as strong (with the GMB center on the axis of the incident laser pulse) as reported by other researchers. Our computer models show this to be due to the ~1-ns length of the incident pulse and to the expansion of the critical (absorbing?) surface during the length of the pulse. We hope to gather more information of this type with various starting radii, atomic numbers, and focal positions to provide data on absorption useful to pellet

design, as well as information on the expansion of the critical surface in the regime where ponderomotive forces are effective.

We plan to examine the importance of the absorption of thin films and the transmission of laser energy by thin films. Data from the SBS show that the transmission of 10.6 μm laser light can be quite accurately modeled. After we have collected a limited amount of absorption data, we hope that energy and light scattering balance can be measured accurately on thin films with the new Gemini absorption apparatus. These data would be of immense importance in modeling energy transport in multilayer targets, especially those employing vacuum insulation.

We also plan a series of experiments to determine with a high degree of accuracy the angular dependence of absorption for S and P polarized light. Data from the SBS indicate the existence of a resonance absorption mechanism, but these data are not of sufficient quality to allow conclusions about other mechanisms that might be operating.

Radiochemistry Collector Assembly for Helios (M. A. Yates, T. Ganley, A. Williams)

A radiochemical fusion diagnostic is being developed for the Helios system. Our problem is to design a collector assembly that maximizes the solid angle acceptance while satisfying two severe constraints: it must be small enough to be installed and removed through a reentrant port; and it must not interfere with the laser beams. The initial design consisted of two spherical segments mounted on the target insertion cart. The cups were 4.45 and 1.91 cm above and below the target, respectively, each covering ~10% of the solid angle. Various thicknesses of titanium foil from 7.6 to 46 μm were used to line the brass cups and to catch debris from the target implosions. We found that the energy density within 4.45 cm of the target caused significant damage to the surface of the titanium foil and that the maximum recovery fraction from the imploded target was ~2%.

We attempted to reduce foil damage by increasing the angle of incidence of the debris using a cylindrical upper catcher with an inverted-cone end. This catcher covered the same solid angle as before and extended 1.91 cm below to 4.45 cm above the target. However, this design was even less efficient than the cup, presumably because a rapid pressure rise within the confined space blew material away from the entrance.

A new reentrant port was constructed on top of the target chamber to allow insertion of a larger catcher assembly farther from the target (Fig. V-19). This system extends from 3.8 cm below to 14 cm above the target and covers the same solid angle as before. Experiments with this design, using the cylinder-cone and spherical cup catchers, indicate that we can trap ~12% of the target debris.

With a working catcher system tested and installed in the Helios system, we will continue development of this radiochemical diagnostic using new target designs. It is important for us to maximize the amount of debris recovered from a target. The induced radiation of interest has a half life of only ~10 min.

Short Pulse, Ultra-High-Brightness CO_2 Laser for Plasma Research (R. Carman, N. Clabo, F. Wittman)

The use of six cw CO_2 oscillators as a front end for both a research laser system and Antares has been under

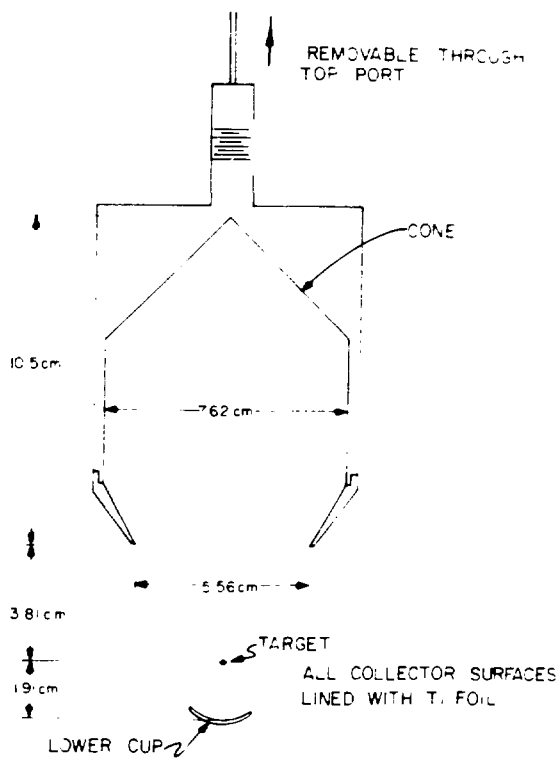

Fig. V-19.
Debris collector for radiochemistry fusion diagnostic.

development for the past 18 months. Successful beam combination of six independent beams operating on six different rotational lines about a year ago[11] cleared the way for acceptance of this system for Antares. However we encountered difficulties in using this source with a large amplifier chain. This led to minor system design changes and total modification of alignment techniques.

We found large amplitude fluctuations in the amplified output when saturable absorbers were used as isolators in a multiline system whose phases between lines were totally independent. As a result, we split our pulse selector pulse chipper system of four CdTe Pockels cells (PC), which generates our final pulse (ultimately down to 100 ps), into three separate systems with two passes of the small TEA (transversely excited atmospheric pressure) amplifier between the Pockels cell systems. The center Pockels cell system uses two cells, and the other two have just one cell. In addition, the limited use of saturable absorbers led us to raise the pressure in the small TEA amplifier from 600 torr (ambient) to 1000 torr. We expect to increase this pressure to 1500 torr shortly. Because of this pressure change, we modified the power supply capacitor bank system to provide at least 100 kV to the main sustainer bank with a total storage capacity of 550 J, rather than the original 50 kV with a total storage of 75 J. The measured gain coefficient was also increased from 2 to 3% cm at 1000 torr, with further improvements possible.

Originally, we believed that the cw oscillators used as the pulse source for the amplifier chain could also be used for aligning the entire system. However, when we allowed the cw beam to pass through only the low pressure amplifier chain [by rotating the appropriate polarizers in the GaAs Pockels cell pulse generator system (70 ns duration)], we found that the amplifiers were not centered on the pulsed laser beam and were not of the same diameter. Although the effects were small in the low pressure amplifier stages (five 1 m amplifiers of 10 torr total pressure each), they were greatly magnified after propagating over the 60 ft (20 m) path required to enter the first pass of the small high pressure TEA amplifier. A small signal gain of 3% cm was observed, but beam energy was decreasing through this first TEA amplifier pass.

Careful investigation and previous experience[12,13] with thermal lensing permitted us to identify the source of the problem. All the relevant material parameters necessary to explain and calculate the magnitude of the thermal lensing seen in each of the many elements in our laser system are listed in Table V II. From Ref. 12, the focal length f of the lens is

$$f = \frac{d^2}{\left[\frac{\alpha \ell}{2} + \frac{\left(\frac{\partial n}{\partial T}\right)_p}{\rho_0 C_p}\right] \frac{4 I_0}{\pi}} , \qquad (V\ 5)$$

where d is the laser beam diameter, α the absorption coefficient of the optical medium at 10 μm, ℓ the medium length, $\left(\frac{\partial n}{\partial T}\right)_p$ the derivative of the refractive index of the medium with temperature at constant pressure, I_0 the laser intensity, n the medium refractive index, ρ_0 the medium density, and C_p the medium specific heat at constant pressure. Note that thermal blooming, which we usually encountered, corresponds to a negative $\left(\frac{\partial n}{\partial T}\right)_p$.

Equation (V 5) applies only in the transient regime; that is, for times less than required for heat losses from the laser beams. Two mechanisms important in establishing this equilibrium are heat conduction and heat convection. The second mechanism is absent in solids but it may well dominate in gases.

For heat conduction from a cylindrically symmetric region, the time for steady state conditions to be achieved is[7]

$$t_{ss}^{cond} = \frac{\rho_0 C_p}{k} d^2 , \qquad (V\ 6)$$

where k is the medium thermal conductivity. Convective effects are much harder to model theoretically and are even more consequential as they cause beam deflections in the vertical direction due to gravity. These effects were studied extensively in previous work.*

Table V III shows the typical laser conditions encountered by several of these materials during cw alignment of our system. By combining Eqs. (V 5) and (V 6), we arrive at the approximate equation for equilibrium steady state conditions:

$$t_{steady\ state} = t_{ss} = \frac{d^2 \rho_0 C_p}{k \left(\frac{\alpha \ell}{2}\right)\left(\frac{\partial n}{\partial T}\right)_p \frac{4 I_0}{\pi}} \cdot \frac{1}{\left(1 - e^{-\alpha \ell}\right)} . \qquad (V\ 7)$$

*The complexity of convective cooling as well as a quantitative study of beam deflection effects in its pressure is reported in Ref. 12, pp. 126-143.

TABLE V II

MATERIAL PARAMETERS USED TO CALCULATE THERMAL LENSING EFFECTS OF INDIVIDUAL SYSTEM COMPONENTS

Material	$\lvert 1/n(\delta n/\delta T)_s \rvert \cdot 10^{-5}/K^{-1}$	ρC_v (J/cm^3 K)	$10^4 \kappa$(cal/cm s)K	α(cm^{-1})	n	ρ(g/cm^3)
NaCl	1.69	1.84	167 220	0.001	1.49	2.16
CdTe	-4.40	1.3	98 167	0.001	2.67	5.85
Ge	-6.70	1.65	1430	0.017	4.00	5.325
ZnSe	-1.995	0.38	400	0.003 0.005	2.405	5.267
BaF$_2$	0.645	0.40	287	0.09	1.396	4.886
GaAs	-5.64	1.42	1147	0.006	3.066	5.37

TABLE V III

TYPICAL LASER CONDITIONS THAT INFLUENCE BEHAVIOR OF VARIOUS MATERIALS DURING cw ALIGNMENT

Material	Element	$f_{ss}/l\,(1-e^{-\alpha l})$	l(cm)	I_0(W/cm^2)	$\pi\omega_{ss}^{2}/d^2$	f_{ss}(cm)
NaCl	Windows	1.93×10^{-4}	1	1	5.9	2×10^{4}
CdTe	Pockels cell	4.95×10^{-4}	5	1	6.25	1×10^{-3}
Ge	Polarizers	3.58×10^{-3}	2.5	1	0.72	8×10^{4}
ZnSe	Lens	3.37×10^{-4}	0.5	1	0.59	1.5×10^{-3}
BaF$_2$	Lens	7.45×10^{-4}	0.5	1	0.87	1.6×10^{4}
GaAs	Pockels cell	3.41×10^{-4}	4.5	10^{3}	0.77	1.26×10^{3}

where

$$\frac{\omega_{ss}^{2}}{\omega_0^2} = \frac{1}{2} \frac{P\alpha}{\pi\kappa\omega_0^2} = \frac{P(1-e^{-\alpha l})}{2\pi\kappa\omega_0^2}, \qquad (V\,8)$$

and αl has been replaced by the more precise expression in general: $(1-e^{-\alpha l})$.

The entries in Table V III correspond to minimal operating conditions in several elements frequently encountered in our laser system. Intensity levels of 20 to 30 times those listed (with element lengths increased several times because we use more than one) greatly reduce focal lengths when an entire system is analyzed.

One remaining element of our system, the CO_2 gas mix, plays an additional important role. Table V-IV lists the important parameters for CO_2, which cools by both conduction and convection. Thus, both beam diameter and beam center are modified in a cw alignment. This effect can be removed by aligning the system on a N_2:He mix, adding the CO_2 only when ready to operate the system.

At first glance, these effects may appear too small to be of consequence, but the total system length is ~46 m. Also, because we are seeking diffraction-limited performance, the beam cannot be allowed to scrape along amplifier walls or be apertured by other elements because these conditions lead to scatter and diffraction effects that increase beam divergence.

Equation (V 5) clearly shows the remedy: chop the alignment cw beam to reduce the magnitude of the effects of operating under transient conditions, while also eliminating the beam centering problems through convective cooling effects (Rayleigh Taylor instability) in the CO_2 gas. In our system, transient conditions are determined by the GaAs Pockels cells, which see a focused

TABLE V-IV

CO_2 MATERIAL PROPERTIES

$(1/n(\delta n/\delta T) \times 10^4)K$	0.1
$\rho_m C_p$ (J/cm^3 K)	4.0×10^{-4}
$\kappa \times 10^4$ cal/cm s K	1
α(cm^{-1})	0.001
ρ, mole/cm^3	4.5×10^{-6}
τ_{ss}^{cond}/d^2	0.25
$f_{ss} I_0 (1 - e^{-\alpha \ell})$	1.67×10^4
ℓ(cm)	80
I_0 W/cm^2	1
f_{ss} (cm)	2×10^{-4}

CO_2 beam of ~2 mm diameter. Table V-III shows that this corresponds to a conductive equilibrium time of ~30 ms, below which the equivalent thermal lens focal length increases inversely with chop time, provided that a very low duty cycle is used. We constructed a rotating wheel chopper to provide a 0.2 ms on time with an adjustable off time (by using a second chopper and a 1.0 s gate). Typical off times are 1 to 10 s. Using this system in connection with a Au:Ge detector (~10 ns response time at 50 Ω) and adjustable termination, we can make alignments accurate to ~ 10 μrad in direction and ~ 250 μm in diameter between the pulsed and alignment beams.

Much of our effort during the past 6 months was spent on the problems introduced by the TEA discharges of higher voltage and higher energy. We constructed an EMI noise free screen room and we are now able to see 0.5 mV signals in the ~ 1 MHz to ~2.5 GHz bandwidth range in the presence of the system when it is fired. This effort included target chamber cabling and verification that this level of noise (without the target) existed on the cables originating from within the target chamber.

Finally, we designed and built target geometry, positioning, and alignment systems. Under our most stringent operating conditions, a 25 μm diam spherical target must be placed at the center of an f/0.7 CO_2 laser-beam focus (spot size ~25 μm) to an accuracy of ± 1 μm in the transverse CO_2 directions and ±8.5 μm in the longitudinal CO_2 direction. We set up a 45-power microscope with a 7.5-cm objective lens and verified that it gives 1.5-μm resolution using the Rayleigh criterion. This implies that 1-μm centering accuracy should be achievable. Inchworm translators having 1 in. (2.54 cm) of full travel at 75 Å step are being improved and made vacuum compatible. We plan to use these translators for final target positioning.

We plan to begin checkout of the entire system by shooting plane targets with a 1 ns pulse, 1 to 6 rotational lines (selectable from ~100 lasing CO_2 lines) with ~1 J of energy in a spot of ~60 μm (f/2). We will identify the target feedback problems and then examine energy absorption as a function of laser line content, first with two lines and then with three, four, five, and six lines, at intensities ~ 10^{14} W/cm^2.

Data Acquisition and Computing (R. Peck)

Data acquisition reflected the increasing experimental activity at Helios. It is our intention to make automatic data acquisition and reduction as attractive as possible to experimenters. A scientific programmer now aids the experimenters in developing their analytic programs. Depending on the skills and interest of each person, this aid ranges from consulting to complete program writing. A data librarian was hired to collect and file films and other raw data media and to enter manually any data that are not yet acquired automatically.

Reliability and convenience of the PDP 11/70 data computer were improved by additions to its hardware. We now have a second magnetic tape drive and a high speed line printer. Memory size is now 1 Mbyte, ample to serve all the terminals in use or on order without task swapping. Two more graphics terminals were connected to serve our experimental and theoretical groups. A multiplexing serial interface adds 16 serial lines for future terminals and network links. We obtained two new types of CAMAC modules. One type, LeCroy Model 2236, is a 20 MHz transient digitizer with post triggering and internal attenuator. Attenuator setting and other switchable functions may be read along with the data. Another, built locally, contains six 500 MHz attenuators, whose settings may be read.

As anticipated, the general data acquisition program has accommodated new data types, new CAMAC modules, and minor modifications without major changes to the program. The new module types described here were added and are read along with the older modules.

Data from film sources are managed in the raw-data base in a manner similar to that from CAMAC modules. The film raw data base is less structured than that for

CAMAC data and a disk file is defined for each record of data because data will not arrive in chronological order. Subroutine GETFLM can be incorporated in analysis programs to recall film data, and program LOOK provides a quick examination of any record of film data without processing. Another extension to the data base is managed by the DETECTORS program, which contains quantitative data describing detectors and recalls detector information along with raw data, coordinated automatically by data serial number.

The latest version of the IAS operating system allows a program to remap itself during execution. This makes possible large data arrays that would otherwise cause the program to exceed the maximum address space of 32 kwords for a 16-bit computer. A set of FORTRAN callable subroutines was developed to make use of this feature easier for programmers.

Our mathematics library will now provide programmers most of the functions and subroutines that are available at the Los Alamos Central Computing Facility (CCF) under the NOS and LTSS operating systems.

Laser and target information, entered manually through programs PAGE and HPAGE, becomes the equivalent of a logging notebook. Anyone with access to a terminal can immediately read the log. The data librarian is responsible for filling in the blanks.

Figure V-20 shows the flow of data through acquisition and processing. Detectors are called "slow" if they produce signals suitable for real-time digitization by CAMAC modules, now at a 50-MHz sampling rate or slower. Faster signals must be recorded by fast oscilloscope cameras and digitized later by the Polaroid print film reader or the Tektronix graphic tablet. Some detectors produce output on film instead of by an electrical signal. These films are digitized by microdensitometers, interfaced as shown. Recent digitized data of all types reside on a dedicated computer disk; older data are stored on magnetic tape. Subroutines are provided so that analysis programs may recall raw data by data type, detector identification, and dataset number without concern for other details.

Charged Coupled Device (CCD) Based Oscilloscope Camera (V. M. Cottles, L. Sprouse)

Vidicon based oscilloscope cameras are currently available with magnetic disk and semiconductor memories that allow direct connection to computer systems. However, they have the disadvantages of spatial instabilities and large size. We developed a charged coupled device-based oscilloscope camera to provide high spatial stability in a size not much larger than a standard oscilloscope camera. These cameras should allow the quick analysis of fast pulses observed with high-speed oscilloscopes (≥ GHz bandwidth) for such

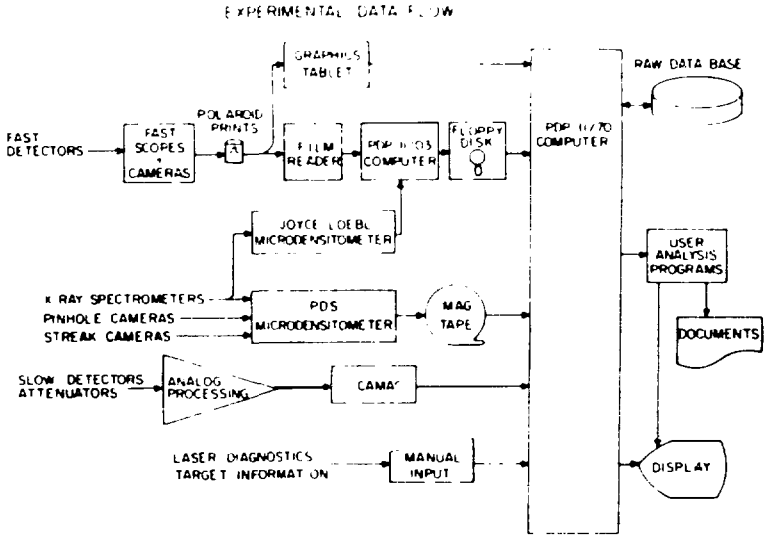

Fig. V-20.
Experimental data flow through acquisition and processing to display and storage.

applications as laser pulse temporal profile measurements and time-of-flight neutron measurements.

First, we monitored the "writing speed" of a Tektronix Model 7904 oscilloscope with a 256 element Fairchild Model 100 linear array. The arrangement used for this measurement is shown in Fig. V 21a, and Fig. V 21b shows a typical output signal. The effective writing speed of 500 ns cm corresponds to a 40-mV signal above background. Then we used a 100 × 100 Fairchild Model 202A array to detect a trace containing information. This arrangement is shown in Fig. V 22. Comparison of a Polaroid record and a digitally stored trace showed a writing speed of 200 ns cm. This setup also demonstrated the feasibility of such a system and allowed us to determine various engineering parameters (transfer functions for the optics, CCD readout speed range, CCD minimum allowable integration time).

Figure V 23 shows the configuration intended for use in the laser fusion program. It will be compatible with the high speed Los Alamos Model 76, 1776, and Tektronix Model 7104 oscilloscopes. We expect writing speeds of ~ 20 ps cm. The oscilloscope camera assemblies can be used with or without computer control and readout. The readout control system for the camera may be expanded in the future to allow readout of an array with a video dynamic range of 300. This would allow it to replace film in some diagnostic applications.

Low-Energy Pulsed Particle Acceleration (V. M. Cottles, W. Bowman)

The laser fusion program has always lacked proper calibration of simple ion monitors (that is, Faraday cups, ion charge detector) for ions of energy < 100 keV. General assumptions of detector efficiency given in the literature and in theoretical predictions are of limited use because performance is often specific for an individual detector. The method of fabrication of a charge detector can result in its secondary emission coefficient being different from a value determined from references. A facility is being developed to calibrate ion detectors for energies from 100 200 keV. It will have the following major characteristics.

- It will be pulsed, because the detectors to be calibrated are all designed to handle pulsed particle sources.
- It will provide a multitude of ion species to allow calibration as a function of atomic number and charge state.
- It will be designed to require minimum maintenance. People with limited training in accelerator technology will be able to use it.

The system will be developed in two phases. First, we will develop a source that can produce a 10 mA pulse with a FWHM duration (flat top) of 1 to 10 ms and an

Fig. V 21.
Characteristics of Tektronix 7904 oscilloscope. (a) Arrangement for monitoring writing speed of the Tektronix 7904 oscilloscope with a 256-element Fairchild 100 linear array. (b) Typical output signal from the oscilloscope.

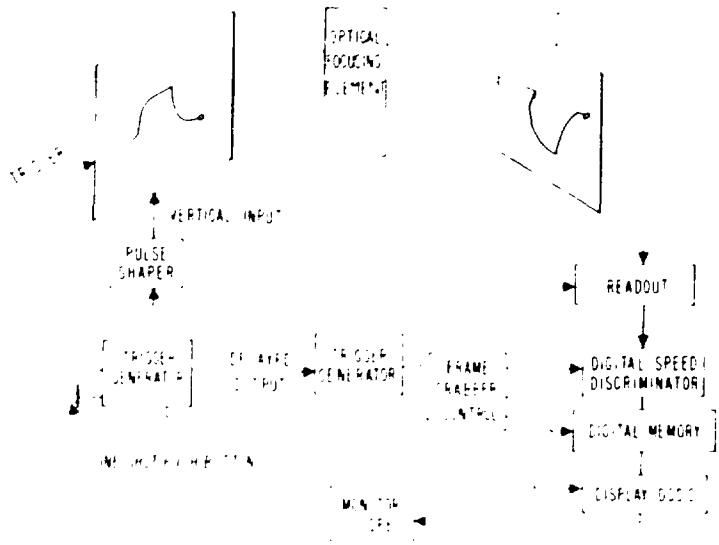

Fig. V 22.
Arrangement for observing an oscilloscope trace with a Fairchild 202A 100 by 100 array.

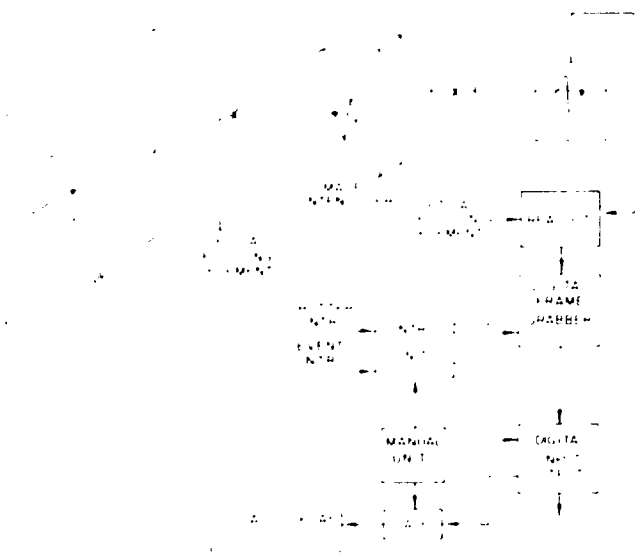

Fig. V 23.
Arrangement for digital storage and readout of data from fast oscilloscopes.

energy from $\lesssim$ 1 to 100 keV. (This energy range is that of poorest calibrations for laser fusion ion diagnostics.) Second, we will develop an ion source that can reach higher currents and potentials (that is, 1000 mA at >200 keV) to allow damage-threshold measurements even on detectors. This advanced system would be able to simulate a laser fusion pellet burn (by bunching techniques) with an ion temperature of ~6 keV and a duration of 1 ns with a yield of $>10^7$ neutrons by a D(T, He^3)n reaction. This would be invaluable for time-dependent neutron diagnostics.

The general design of such a system, shown in Fig. V 24, uses common accelerator technology. This basic system contains elements optimized for nuclear accelerators that are not designed to simulate nuclear reactions from laser fusion implosions. At present, Phase I development is centered on developing an ion source that can be pulsed from a battery supply (eliminating, for example, ion source water cooling, >200-keV isolation power transformers or plastic rod driven alternators for ion source power). Figure V 25 shows a test-stand prototype of a pulse system capable of 50 Hz to single shot reliable operation. It produces 10 mA pulses of He^+ ions. The system is being tested with line power, but indications are that it can produce 10^4 such pulses on a single battery charging with NiCd batteries. Figure V 26 is a group of tracings showing the performance of the unit. The output of the ion source is intentionally small to optimize all parameters for efficient pulse operation without dependence on the pumping speed of the vacuum system. A chopping system is being developed to allow a pulse as short as 1 ns FWHM to be chopped from the ion source output. Using main pulses of $\lesssim$2 ns duration for $\sim$1 ms pulses can give $\sim 3 \times 10^4$ pulses per battery change at 50 pps.

GWTF Target Area (R. Kristal)

The optics for directing the Gigawatt Test Facility (GWTF) were focused and aligned, and the laser was fired (at nominal energy) at surrogate targets in vacuum. Diagnostics and apparatus are being assembled to characterize the focal spot and to align targets. An in microscope with pyroelectric vidicon will be used as part of this setup.

The optics for main beam focusing were used with the old single beam laser, and they may not be optimum for the present experiment. Specifically, astigmatism, mirror figure, and pointing errors in the 3X expansion system may cancel any benefit from the expansion itself, depending on the quality of the input beam. The focal spot measurement will clarify these issues.

Grazing Incidence Spectrograph (P. Lee)

A 1.0 m long grazing incidence spectrograph, shown in Fig. V 27 was built and tested. A 10 μm horizontal slit is used at the entrance of the spectrograph to obtain a one dimensional spatial image. A bent microscope slide focuses the incident radiation through a 10 μm vertical slit and fills the whole grating. The rest of the arrangement is an ordinary Rowland mounting scheme. The angle of incidence on the grating is 2° to make use of the enhanced reflectance of short wavelength radiation at grazing incidence. The grating is a 1.0 m Bausch and Lomb concave grating with 589.23 lines/mm. The wavelength coverage is 50 to 700 Å.

The instrument was tested by using a Duoplasmatron source with neon and helium gas. Figure V 28 shows a densitometer trace of a helium spectrum. The strong HeI line at 584 Å dominates. The fine structures around the

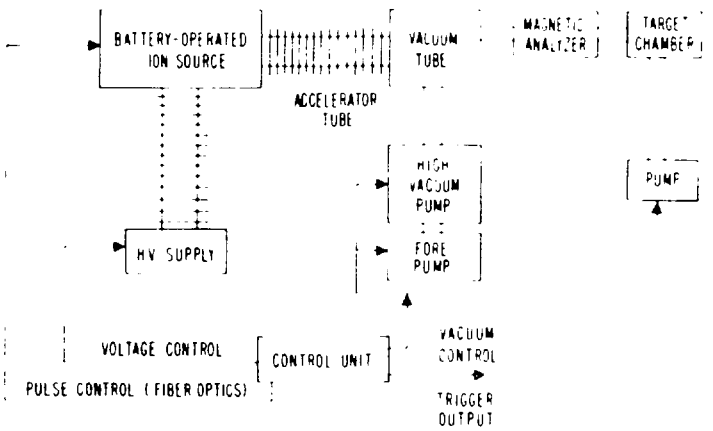

Fig. V 24.
Ion detector calibration system based on common accelerator technology.

584 Å line are grating ghosts. The HeI 1s 1s10p is clearly visible. The plate factor of the spectrograph is 4.6 Å mm. Contaminants of nitrogen and oxygen are evident in both the helium and neon spectra.

High Precision Wide Dynamic Range Calorimeters (A. Williams, V. Cottles)

Improvements are constantly being made in the performance of calorimeters for the measurement of CO laser light. Earlier we reported[14] that surface and volume calorimeters become nonlinear for power densities of $\sim 5 \times 10^{7}$ W cm^{-2} at the calorimeter element surface. An inverse Knudsen cell design was developed that remained linear for focused light at peak intensities exceeding $\sim 10^{11}$ W cm^{-2}. We built an improved version of this design that provides high linearity, large dynamic range, and superior resolution.

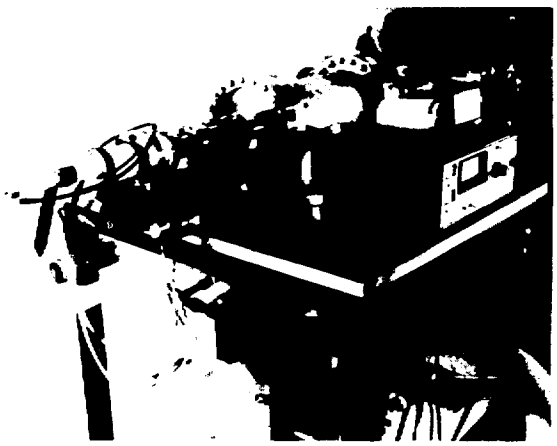

Fig. V.25.
Test stand prototype of the system shown in Fig. V.24.

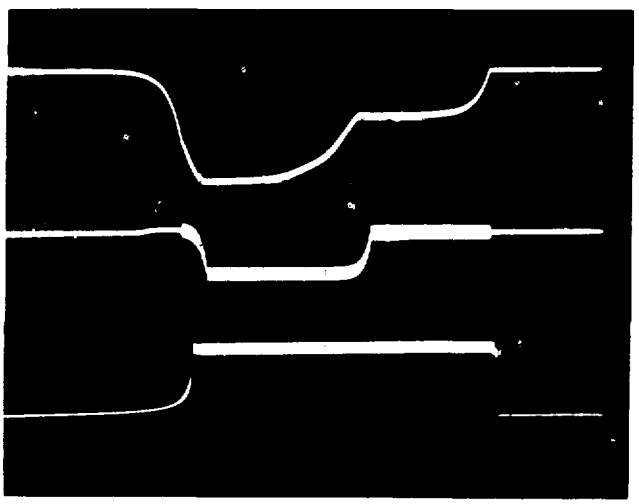

Fig. V.26.
Traces illustrating performance of the pulsed system: (top) keying signal for RF ionization oscillator; (center) ion source focusing solenoid keying signal; (bottom) ion source output current.

Figure V.29 is a diagram of a unit that is designed to accept a focused laser pulse with an f number ~1.0 and a FWHM time profile ~0.5 ns. It incorporates the following improvements over previous models.

- The new unit has 25 thermopile elements that provide a temperature averaging effect over the absorbing element, in contrast to the prototype, which uses a single element. Beryllium oxide spacers, nickel coated on both sides, are soldered to the copper calorimeter element. The thermocouple elements are connected in series and soldered to the outside faces of the BeO chips. The BeO is a good electrical isolator and such a good thermal conductor that the thermal contact of the thermocouples is within 90% of what it would be if connected directly to the copper can. This unit can accept 0 to 300 J without damage. It provides a resolution of 0.1 J and has a dynamic range of 3000 or better, depending on the mode of data analysis.
- The new unit has a high thermal-mass shield that surrounds the sensor element and acts as a reflector to return heat radiated by the element and is the cold junction for the thermopile elements. The BeO chips are also used as spacers for the cold-junction

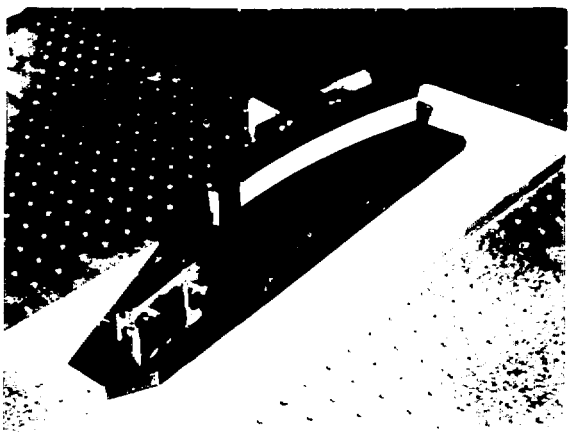

Fig. V 27
One meter grazing incidence spectrograph

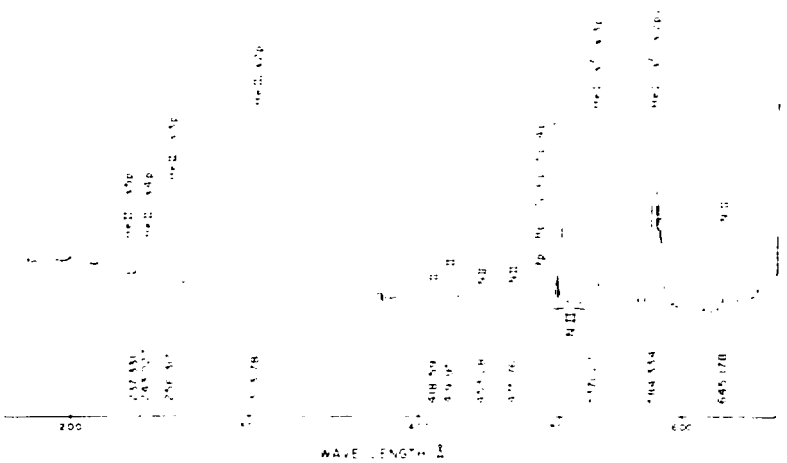

Fig. V 28
Densitometer trace of helium spectrum made with the spectrograph shown in Fig. V 27

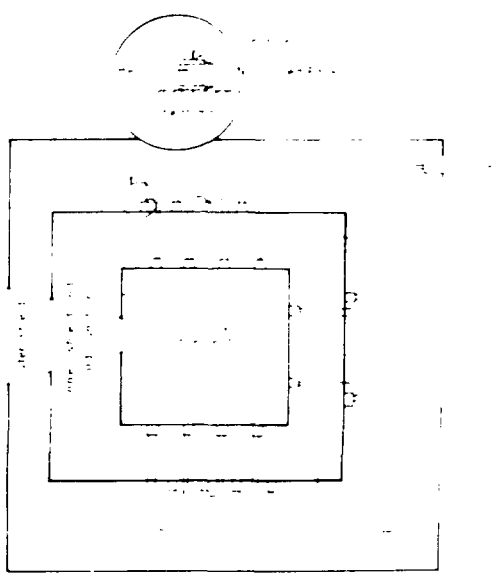

Fig. V 29.
Schematic of improved calorimeter that incorporates 25 thermopiles for temperature averaging over the absorbing element.

connections to this shield. Development of a code that models the calorimeter is not complete, but calculations indicate that the main heat loss (by a factor of 30) is caused by radiation to the shield as opposed to thermal conduction through the thermocouple wires. Because the high thermal mass [illegible] is used as the cold junction, calorimeter [illegible] is very high. When the sensing element and the shield are in thermal equilibrium, the output is a reproducible zero μVs. Also the decay curve of the system is highly reproducible. This allows the accurate extrapolation of the curve back to time zero for accurate determination of the signal voltage.

- A [illegible] shield that surrounds the whole assembly is used for mounting and electrical connections. This serves as a thermal shield to isolate the cold junction from interactions with the ambient temperature which is crucial to the stability of the [illegible].

Calibration studies have been performed to determine the response of the calorimeter element and its equilibration time using focused (~1 ns) CO$_2$ laser pulses from the Helios laser. Figure V-30a shows the placement of three thermocouples that were used to monitor individually mass elements to determine the equilibration time, which appears to be ~10 s. The element tested was not a complete unit, with outer shield. In this test we also tried to determine how much energy the unit could take before failure. Figures V-30b and c show the response of the calorimeter for an 85- and a 330-J pulse, respectively. The lower trace is a computer plotted sum of the three thermocouples and shows the enhancement created by the thermopile averaging effect. The exhibited time of 45 s reflects the lack of the shield elements. The damage threshold for the unit is greater than 330 J, but shots of higher energy using the Helios laser are expected to determine the true threshold.

The unit does not contain an electrical calibrator because it is designed to provide relative measurements of laser light in absorption experiments. These calorimeters will be used with digital pen recorders to provide precision measurements of collected scattered light in energy balance experiments. They will be calibrated in reference to the incident light monitor. Techniques of absolute calibration are being developed and the use of an electrical calibration element is not precluded by the current design.

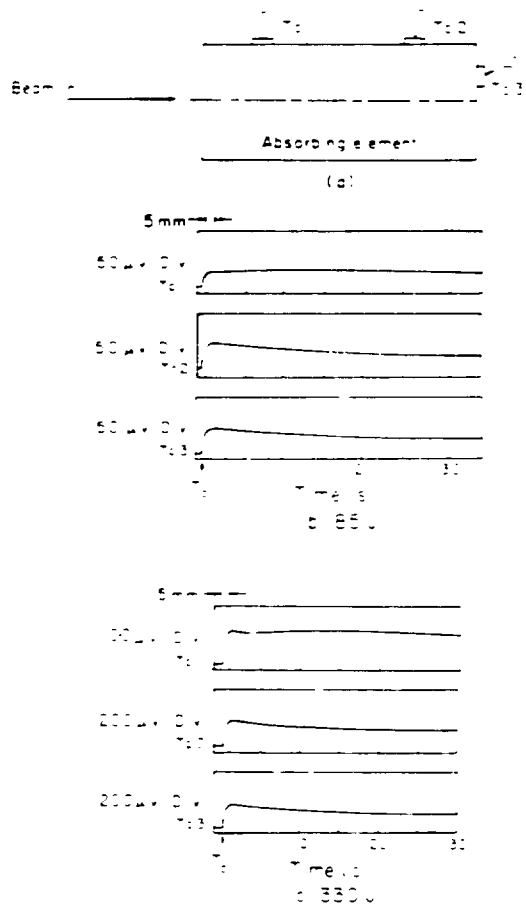

Fig. V-30.
(a) Placement of thermocouples to monitor equilibration time.
(b) Response for J pulse.
(c) A 330 J pulse focused on the calorimeter shown in Fig. V-29.

Ultrafast Detectors for Laser Fusion Diagnostics (A. Williams, T. H. Tan, L-4; P. Lyon, J-14)

General. A laser fusion target illuminated by high intensity subnanosecond laser pulses emits particles such as photons, ions, and nuclear products in a time interval comparable to the laser-pulse duration. These particles carry with them vital information concerning the mechanisms of laser energy absorption, energy transport, plasma evolution, and the subsequent hydrodynamic implosion. For example, the temporal

profile of ultrafast ions and hard x rays generated by the hot electrons produced during absorption should provide information on the time history of the laser target interactions; detection of softer x rays as a function of time could shed light on the electron energy transport; finally, by measuring the neutron emission time profile, the fusion reaction history can, in principle, be determined completely.

We developed an ultra-high speed detector assembly that can satisfy many specific needs in diagnosing laser fusion target performance. The assembly consists mainly of a quenched plastic scintillator coupled to a micro channel-plate photomultiplier (MCP PMT). Speed and sensitivity can be tailored to suit a variety of requirements by the judicious choice of quenching fraction and MCP gain level.

Quenched Scintillators. The technique of quenching fast, plastic scintillators with special dopant materials has been available for several years.[15] An increase in quench level increases the scintillator speed at the expense of a continued decline in light output. Benzophenone is the most effective quench documented for the fast commercial plastic NE111.[16] Figure V-31, plotted from data given in Ref. 16, shows the FWHM of light output from NE111 with three quench materials. For 5% levels of benzophenone, a FWHM of ~100 ps results. However, the light level for such a large quench concentration is only ~2% of NE111. Other studies have concerned spectral properties of quenched NE111,[17] excitation of quenched plastics with low-energy x rays,[18] and dose rate nonlinearity of quenched plastics.[19]

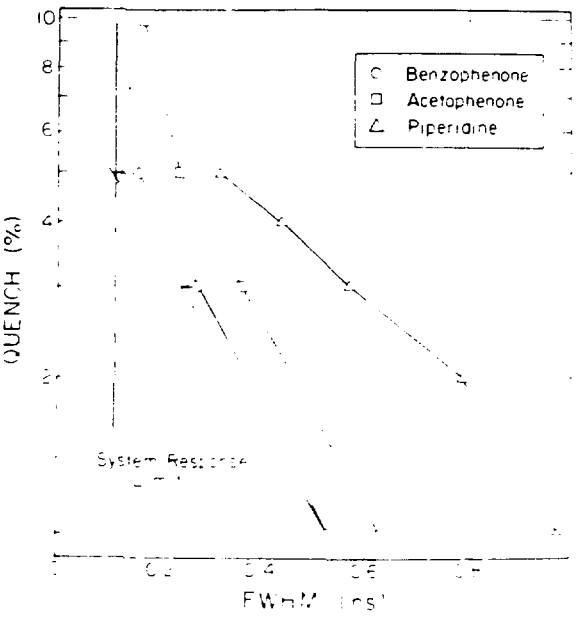

Fig. V-31.
Data points show the observed FWHM of quenched NE111 for various quenches and quench concentrations. An ITT F4014 diode with a FWHM of 120 ps was used in the measurements. The arrows reflect a corrected plastic FWHM after allowance for the diode response. Plotted from data published in Ref. 16.

Microchannel Plate Photomultipliers. A fast photodetector must view the scintillator. It must have high enough photoelectron gain to drive most fast oscilloscopes. MCP PMTs provide an ideal match to the scintillator properties.[20-22] MCP PMTs provide a subnanosecond response with high peak linear currents. A schematic of an ITT MCP PMT in a matched 50 Ω holder is shown in Fig. V-32. Response of a single-stage (one microchannel plate gain element) ITT F4126 is shown in Fig. V-33. A three-stage ITT F4129 response is shown in Fig. V-34. The multiple gain stages result in significant response degradation. Using the bias system shown in Fig. V-32, the observed performance is given in Table V-V.

MCP PMTs can deliver very large linear currents in single-pulse operation; up to 10 A have been observed.

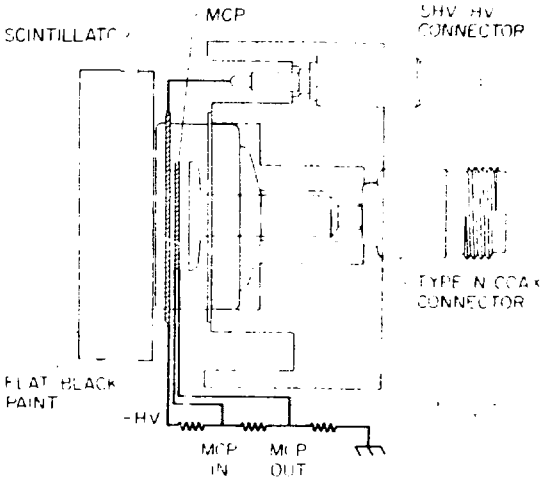

Fig. V-32.
ITT F4126 MCP PMT in a matched housing. A 5-cm diam, 1.3 cm thick scintillator is shown coupled to the PMT.

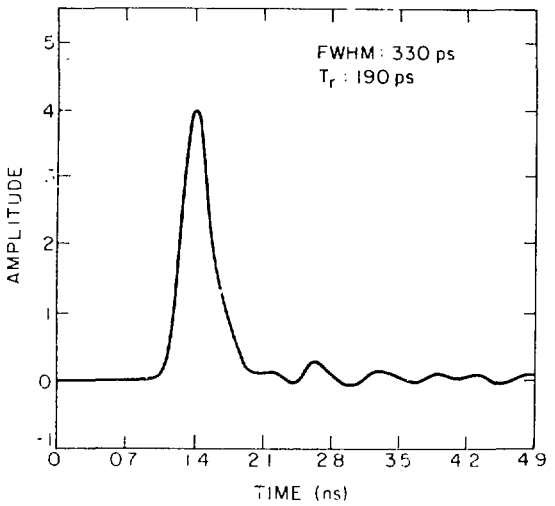

Fig. V 33.
Time response of an ITT F4126 MCP PMT with a single MCP. The MCP length: diameter (L:D) ratio was 40, gain was $\sim 10^3$.

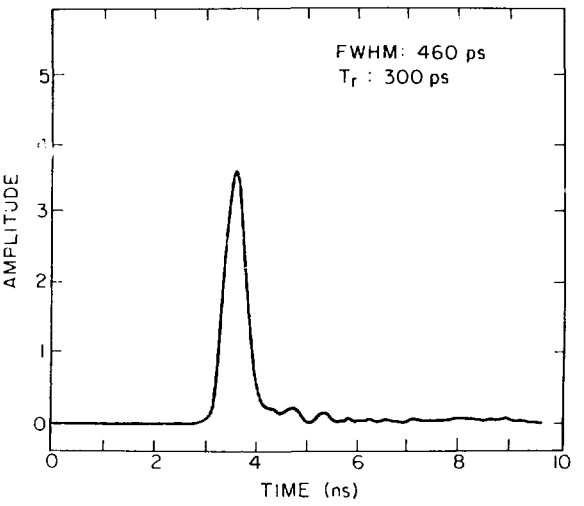

Fig. V-34.
Time response of an ITT F4129 MCP PMT with three MCPs (L:D = 40) and G $>10^6$.

TABLE V-V

SUMMARY OF MCP PMT PARAMETERS

ITT Type	Number of Plates	L:D of MCP	Gain	FWHM (ps)
F4126	1	40	$<10^3$	300
F4126	1	60	$<3 \times 10^4$	350
F4127	2[a]	60	10^7	440
F4129	3[b]	40	$>10^6$	460

[a]With drift space between the plates.
[b]No space between plates.

Figure V-35 demonstrates the 10-A output for an F4126 with L/D = 40 (L = MCP thickness, D = microchannel diameter). Figure V-35 also shows the pulse-rate limitations of an MCP PMT. The high-resistance MCP leads to long recharge times in the tens-of-milliseconds range. This long recharge time also implies a definite limit to the charge available from an MCP in a single pulse. Both the total charge and the total linear charge were documented for the F4126 in Ref. 20 to be ~20 nC and 1-3 nC, respectively. The linear-charge limit for an MCP PMT must be observed to avoid spurious data, particularly where long pulses (several nanoseconds) are being studied.

MCP PMTs also offer additional benefits in their insensitivity to magnetic fields[21] and their small size. Disadvantages include their sensitivity to hard x rays and possible long-term degradation effects.[24] In addition, as discussed in Ref. 23, an ion feedback pulse may be observed in high-gain operation. This ion pulse follows the photoelectron pulse by several nanoseconds.

Detector Performance. With MCP PMT responses in the 300- to 400-ps range, a scintillator FWHM in the

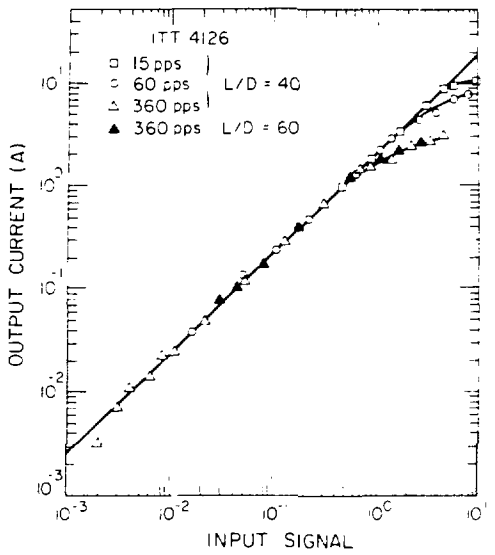

Fig. V 35.
Linearity of ITT F4126 MCP PMT, from Ref. 20.

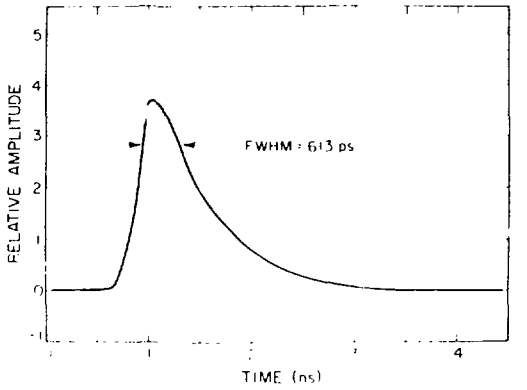

Fig. V 36.
Time response of an NE111 plastic quenched with 2% benzophenone in an ITT F4126 MCP PMT (with L:D 60).

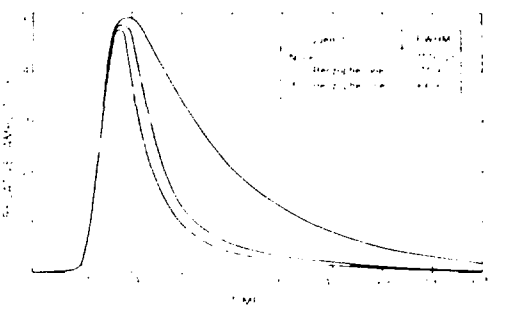

Fig. V 37
Time response of NE111 plastic with varying levels of *benzophenone quench* in an *ITT F4129 MCP PMT (L:D* 40, three MCPs). Peak values were normalized to a similar level.

same range is appropriate. For benzophenone-quenched plastics, 1-3% quench levels yield this FWHM.

Time responses of several combinations were measured on an electron linear accelerator. The linac provided 50-ps electron pulses with energy in the 2- to 20-MeV range at a repetition rate up to 360 Hz. Data were recorded with a sampling system and computed from average transients.

The plastic samples were coated with black paint on the sides and on one face to suppress internal reflections. Samples were 5 cm in diameter and 1.3 cm thick. Linac measurements were complicated by the generation of Cerenkov light in the samples and by the sensitivity of the MCP PMT to any direct electron radiation. To avoid these problems, the plastic sample was placed into the beam with the MCP PMT viewing the sample at an extreme back angle. Distance between the MCP PMT and the sample was 25 cm. In addition, a Corning glass filter (with transmission peak at 378 nm, half-transmission wavelengths of 350 nm and 394 nm) restricted the light reaching the detector to within the plastic emission band. A linac "background" was subtracted by inserting a black-painted Lucite sample of equal dimensions in place of the scintillator. This background was subtracted from the scintillator raw data. Typical linac data are shown in Figs. V-36 and -37. Time-response data are collected in Table V VI. The estimated ±40-ps uncertainty in FWHM results from noise in the data and uncertainty in the Cerenkov subtraction process.

Detector sensitivities were measured on a Co^{60} source with the detector configured as in Fig. V 32. The black-painted plastic samples were used. Sensitivities are given in terms A/rad/s. For Co^{60}, 1 R $\approx 2 \times 10^9$ γ-MeV/cm^3. Neutron sensitivities for these detectors have been qualitatively determined from the laser fusion experiments. They agree with previous measurements on other plastic scintillators, which show that division of the Co^{60} sensitivity (in A/rad/s) by $\sim 0.44 \times 10^9$ yields a detector neutron (nt) sensitivity (in A/nt/cm^2) for 14-MeV neutrons.

Relative sensitivities referenced to NE111 should be compared with Ref. 16, where 1, 2, and 3%

TABLE V VI

SENSITIVITY (A/rad/s) AND FWHM (ps)
RELATIVE TO NE111

	60/1 MCP[b]		Z-MCP[c]	
Plastic Type	S × 10 [a]	FWHM	S × 10 [a]	FWHM(ps)[d]
NE111	18	1480	770	155
NE111 + 1% Bz[a]	38	787	180	...
NE111 + 2% Bz	23	613	99	75
NE111 + 3% Bz	14	460	58	66

Bz Benzophenone quench.
[b]60/1 MCP ITT F4126 (L:D 60), G 3 × 10^4.
Z MCP ITT F4129, G 3 × 10^6.
[d]Uncertainty, ± 40 ps.

benzophenone yielded 24, 10, and 6%, respectively. While the agreement at the 1% level is good, both the 2 and 3% quench levels provide about 30% more light output than the original batch of scintillators used in Ref. 16. This suggests a variation in sample composition. From Fig. V 31, the expected FWHM for 1, 2, and 3% benzophenone quenches in NE111 is 530, 350, and 250 ps, respectively.

Measurements. Several of these high speed detectors were used at our CO_2 Helios facility to investigate high density pellet implosion. Here, we have chosen to display several examples of neutron time of flight measurements. *Neutron production time in the present generation* of laser targets is very short (< 100 ps) and can be considered a δ function for any time spectrum analysis. Hence, pertinent information such as implosion time and fuel temperature can be readily deduced.

Figure V 38 shows an oscilloscope trace of a neutron time of flight measurement from a DT filled, 20 μm plastic coated GMB target shot. A 1 GHz Tektronix 7104 oscilloscope is used as a recorder and a low loss, ultrafast coaxial cable is used for signal transmission. This system provides a neutron response time of ≤800 ps (FWHM). Gain of above 10^7 is achieved with an F4128 V plate MCP PMT. When the x-ray fiducial is delayed so that the time difference with the neutron pulse can be shortened to allow a 2 ns writing speed, time shifts < 100 ps can be measured. The implosion time is measured as a delay in excess of the expected prompt-neutron arrival time, 900 ps in this instance. The delayed time fiducial on the right records the hard x rays generated by the radiation of the suprathermal electrons produced during laser interactions. A measured pulse width of 1.35 ns (FWHM) for the x rays can be deconvolved into an intrinsic width of ≈1.1 ns, which closely tracks the 1 ns laser pulse.

Figure V 39 shows a neutron time spectrum from a similar target. Here, the apparent width of 1.28 ns can be deconvolved into an intrinsic neutron pulse width of 1 ns, which corresponds to a fuel ion temperature of 0.7 keV.

Conclusions. We have characterized the high speed particle detectors in great detail. The apparent usefulness for ultrafast pulse application in laser fusion diagnostics *is demonstrated. Thus, the capability of these detectors,* if properly exploited, should aid greatly in our quest to better understand the mechanisms of many sub nanosecond interaction phenomena.

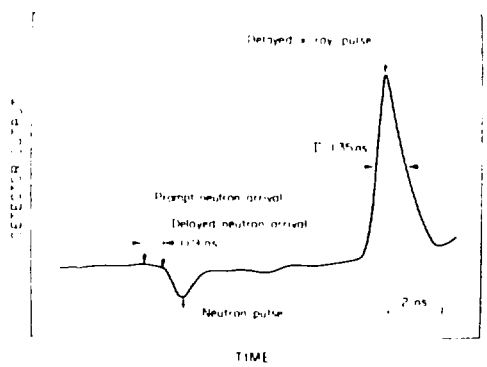

Fig. V 38.
Oscilloscope trace of a neutron time-of-flight measurement.

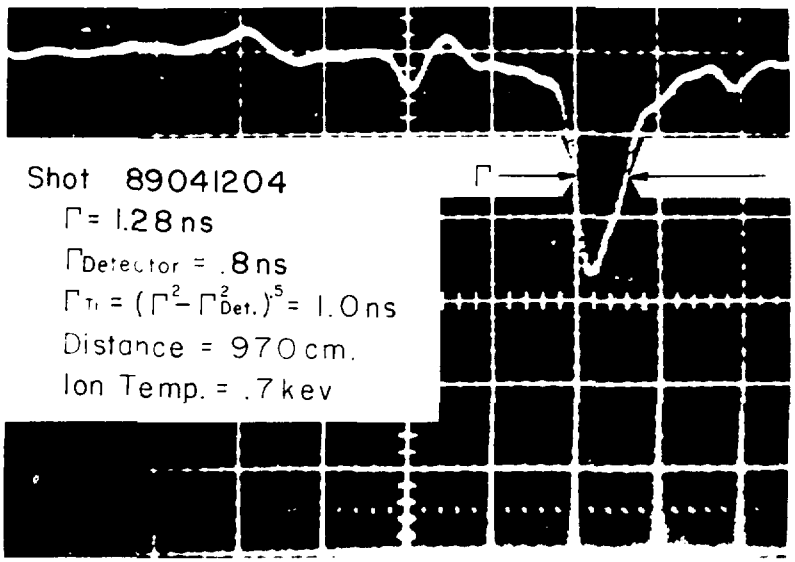

Fig. V.39.
Oscilloscope trace of a neutron time spectrum.

REFERENCES

1. B. G. Cartwright, E. K. Shirk, and P. B. Price, Nucl. Instrum. Methods 153, 457 (1978).

2. P. B. Price, PEPNEWS 4, No. 3, p. 4 (1978).

3. M. M. Mueller, "Expedient Down the Tube Calculation of Multiple Ion Scattering," Los Alamos National Laboratory L Division memorandum L-4 79) 271, April 6, 1979.

4. R. B. Perkins and the Laser Fusion Program Staff, "Inertial Fusion Program, July 1 December 31, 1978," Los Alamos National Laboratory report LA 7755 PR (October 1980).

5. C. M. Vest and D. G. Steel, "Reconstruction of Spherically-Symmetric Objects from Slit Imaged Emission: Application to Spatially Resolved Spectroscopy," Opt. Lett. 3, 54-56 (1978).

6. M. M. Mueller, "Numerical Simulations of X Ray Pinhole Images of Imploded Microballoons: Development of Narrow Aperture Methods for Determining the Size and the Emission Structure of Imploded Cores," Los Alamos National Laboratory paper LA UR 79-178 (1979).

7. G. H. McCall, *Proceedings SPIE 20th Annual Technical Symposium X Ray Imaging*, Vol. 106, 1977.

8. J. K. Silk, *Proceedings SPIE 20th Annual Technical Symposium X Ray Imaging*, Vol. 106, 1977.

9. F. Seward, J. Dent, M. Boyle, L. Koppel, T. Harper, P. Stoering, and A. Toor, Rev. Sci. Instrum. 47, 4 (1976).

10. R. Giacconi, W. P. Reidy, G. S. Vaiana, L. P. Van Speybroeck, and T. F. Zehnpfennig, Space Science Reviews 9, 3 (1969).

11. R. L. Carman, L. J. Garwin, N. Clabo, and H. Lane, "Laser Pulse Shaping," in "Laser Fusion Program at LASL, January-June 1977," Los Alamos National Laboratory report LA 6982 PR (April 1978); R. L. Carman, N. Clabo, and H. Lane, "Multiwavelength Pulse Shaped CO_2 Oscillator," in "Laser Fusion Program at LASL, July-December 1977," Los Alamos National Laboratory report LA 7328 PR (December 1978).

12. R. L. Carman, "Third Order Optical Non Linearities and the Propagation of Intense Light Beams," Ph.D. thesis, Harvard University, Cambridge, Massachusetts, September 1968, Chap. IV.

13. R. L. Carman and P. L. Kelley, "Time Dependence of Thermal Blooming," Appl. Phys. Lett. **12**, 241 (1968).

14. A. H. Williams, "Calorimetry," in "Laser Fusion Program at LASL, July-December 1977," Los Alamos National Laboratory report LA-7328-PR (December 1978).

15. P. B. Lyons, C. R. Hurlbut, L. P. Hocker, Nucl. Instrum. Method 133, 175 (1976).

16. P. B. Lyons, S. E. Caldwell, L. P. Hocker, D. G. Crandall, P. A. Zagarino, J. Cheng, G. Tirsell, and C. R. Hurlbut, IEEE Trans. Nucl. Sci. **NS-24**, 177 (1977).

17. J. G. Pronko, T. R. Fisher, and L. F. Chase, Bull. Am. Phys. Soc. **24**, 596 (1979).

18. K. G. Tirsell, G. R. Tripp, E. M. Lent, R. A. Lerche, J. C. Cheng, L. Hocker, and P. B. Lyons, IEEE Trans. Nucl. Sci. **NS-24**, 250 (1977).

19. J. G. Pronko, D. Kohler, and L. F. Chase, "Saturation Effects of Organic Scintillators to Nanosecond Pulses of Low Energy X-Rays," Bull. Am. Phys. Soc. **24**, 597 (1979).

20. L. P. Hocker, P. A. Zagarino, J. Madrid, D. Simmons, B. Davis, and P. B. Lyons, IEEE Trans. Nucl. Sci. **NS-26**, 356 (1979).

21. B. Leskovar and C. C. Lo, IEEE Trans. Nucl. Sci. **NS-25**, 363 (1978).

22. E. H. Eberhardt, "Subnanosecond Detector Developments at ITT," Los Alamos Optics 1979 Conference, May 1979, to be published by SPI as paper 190-66.

VI. LASER FUSION THEORY AND TARGET DESIGN

(D. B. Henderson)

Our theoretical support activities are closely related to our experimental efforts, with the intent of gaining a fundamental understanding of laser-target interactions, particularly of the relevant plasma physics and hydrodynamics. The relationship of theory and experiments has made it possible to eliminate theories not supported by experiment and to design more reliable targets for CO_2 laser drivers. In general, basic studies have shown that the design difficulties associated with long wavelength are less severe than believed earlier, and that breakeven target designs are attainable even in the presence of a hot electron spectrum. These results have increased our confidence that scientific breakeven can be demonstrated with CO_2 lasers.

TARGET DESIGN

Introduction

We are continuing to develop targets for Gemini, Helios, and Antares with the long term goal of attaining breakeven on Antares. Various targets are being designed to investigate the accuracy of our design codes in different performance regimes to improve target reliability at higher energies. We are reporting a theoretical survey of exploding pusher targets for the Helios laser system, which, when compared with experimental results, will allow us to verify the accuracy of our codes. Two dimensional calculations of the Sirius B targets, which have been tested on Helios, show that the symmetry of the target or of the laser illumination can be very poor before target performance is significantly degraded. This is consistent with the experimental results.

Exploding Pusher Targets for Helios (W. P. Gula)

General. We have performed numerous computer simulations for comparison with Helios target performances, along the lines of a previously published study.[1] The two main purposes are to aid in the design and interpretation of experiments on our eight beam CO_2 laser system and to update and refine the computer codes with the experimental results.

Single shell DT filled GMBs were chosen for this study because (1) they are relatively simple, with relatively few variable parameters, (2) they are easy to diagnose experimentally, and (3) the physics of these exploding pusher type targets are well understood.

The simulations were one dimensional calculations for spherical glass shells filled to an initial density of 2.4 g/cm^3 with an equimolar mixture of deuterium and tritium.

Most of the calculations were performed by using a pulse shape of the form

$$P = P_0 \exp(-\alpha t)[1-\exp(-t/\tau)]^2 \quad , \qquad \text{(VI-1)}$$

where P_0, α, and τ are adjustable parameters. We chose this pulse shape because it provides a good fit to Gemini's pulse shape. It should also provide a good fit to the Helios pulse shape, especially because the Helios amplifiers are basically improved versions of the Gemini amplifiers. In practice, the peak laser power P_0, the laser risetime $(0\text{-}100\%)\tau_R$, and the energy width $\Delta T = E/P_0$, where E is the total energy, are given and the computer then calculates α, β, and P_0.

Results. In our study, we varied the radius and the thickness of the glass shell, the DT fill pressure, the peak laser power, the laser risetime, and the percentage of neon contained in the fuel. In some instances we also varied the energy width ΔT.

The general range of the parameters considered was

Peak power (TW)	5 – 20
Risetime (ps)	100 – 300
Shell inner radius (μm)	50 – 400
Shell thickness (μm)	0.75 – 1.75
Initial fill pressure (atm)	1 – 30

The two pulse shapes used (i.e., the CO_2 pulse given in Fig. VI.1 and the triangular equivalent are shown in Fig. VI.1. Both pulses have the same 0-100% risetime [illegible] the same peak power (5 TW), and the same [illegible] kJ). Figure VI.2 shows the results of varying the pulse shape and the shell radius for a given power. As [illegible] the CO$_2$ pulse for a given peak power always [illegible] better results than the triangular pulse for the [illegible] because the CO$_2$ pulse delivers more [illegible] early for the same 0-100% risetime. Or, stated [illegible] although the 0-100% risetime of the two [illegible] different, the 0-80% risetime of the CO$_2$ pulse is [illegible] 33% shorter than that of the triangular pulse. For the cases shown in Fig. VI.2, the total energies for two pulse shapes were the same for the 5 TW (5 kJ), 10 TW (10 kJ), and 15 TW (15 kJ) runs, but were different for the 20 TW cases: the energy for the CO$_2$ pulse was 17.4 kJ, whereas that for the triangular pulse was 5 kJ.

The predicted yield as a function of target radius for different pulse widths is shown in Fig. VI.3. All the results are for the CO$_2$ laser pulse shape with a 200 ps risetime. The calculations were performed for four groups of two. Each pair had the same peak power, but the upper member of each pair had twice the energy of the lower member. In general, Fig. VI.2 shows that the peak power is more important than the total energy, that it is important for most of the energy to arrive on target early. Although in all cases an increase in total energy improves the yield, the difference is not substantial except for the larger targets, which, because of their longer run in time, are able to use the energy contained later in the pulse. Note that for targets too large for the pulse energy, we have, except for the 20 TW case, the advantage that the higher energy pulse becomes substantial. This seems to occur because the larger radius needed to take advantage of the energy delivered late in the pulse means that more fuel is available to be heated to fusion temperature and more glass mass to be exploded (all calculations were performed for a constant fill pressure of 10 atm and a constant glass shell thickness of 1 μm). The extra energy at the lower powers is insufficient to heat the extra fuel.

The importance of coupling the energy into the target early in the pulse becomes evident by comparing the curves for 10 TW, 500 ps, and 5 TW, 1 ns pulses, which each have a total energy of 5 kJ, with the curves for 20 TW, 500 ps, and 10 TW, 1 ns pulses, which each have a total energy of 10 kJ. The upper member of each pair has twice the peak power of the lower member, and from 2 to 40 times the neutron yield for the same target. However, there are some exceptions. Figure VI.4 shows the neutron yield for various targets as a function of pulse risetime. In general, the faster the risetime the better. However, for large targets and higher powers the shorter risetime evidently results in more target preheat before the shell explosion can compress the fuel effectively.

Figure VI.5 shows the neutron yield as a function of laser peak power for a given target and pulse width. These curves emphasize that the yield is highly dependent on peak power for exploding pusher targets in this regime, except for targets with a radius of ~ 100 μm

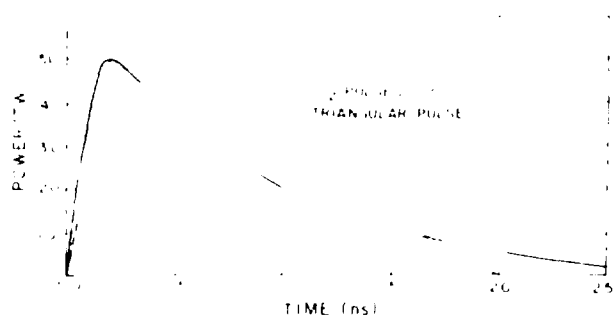

Fig. VI.1.
Temporal variation of the two laser pulses used in the evaluation of the exploding pusher target.

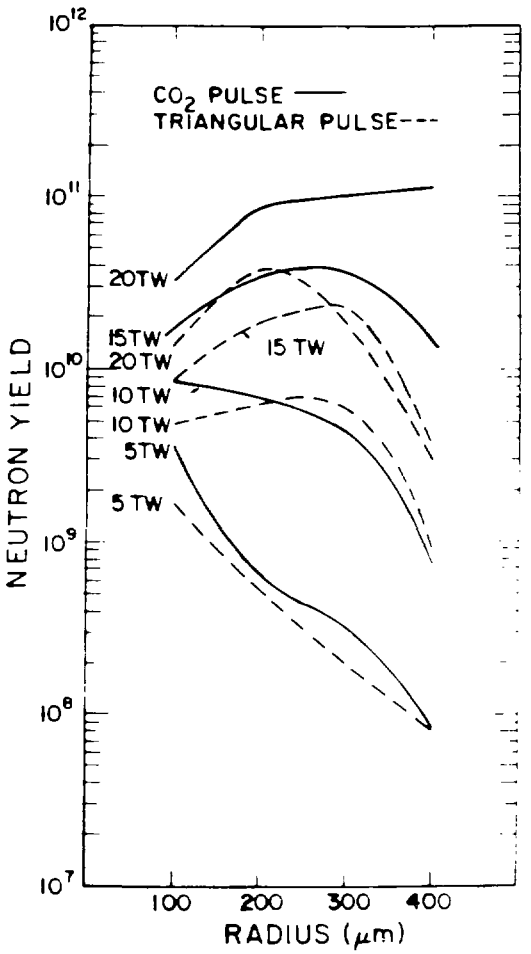

Fig. VI.2.
Neutron yield as a function of radius for laser powers in the 5 to 10 TW range for the two laser pulses shown in Fig. VI.1.

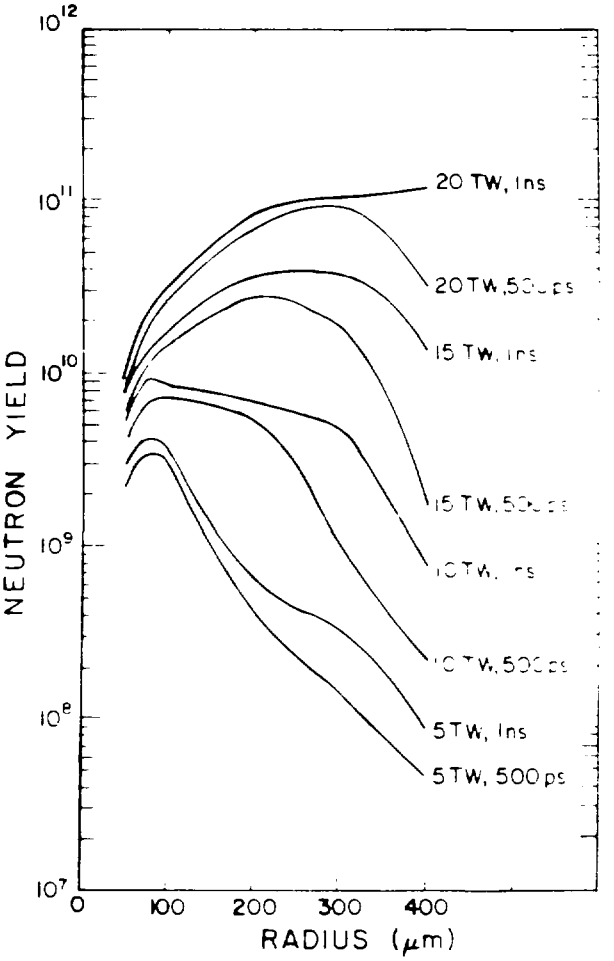

Fig. VI.3.
Neutron yield as a function of radius for laser powers in the 5 to 20 TW range for pulse lengths of 500 ps and 1 ns.

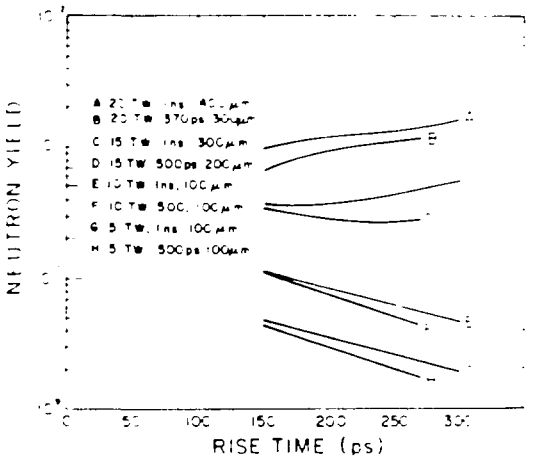

Fig. VI.4.
Neutron yield as a function of laser pulse risetime for various radii and laser pulse lengths.

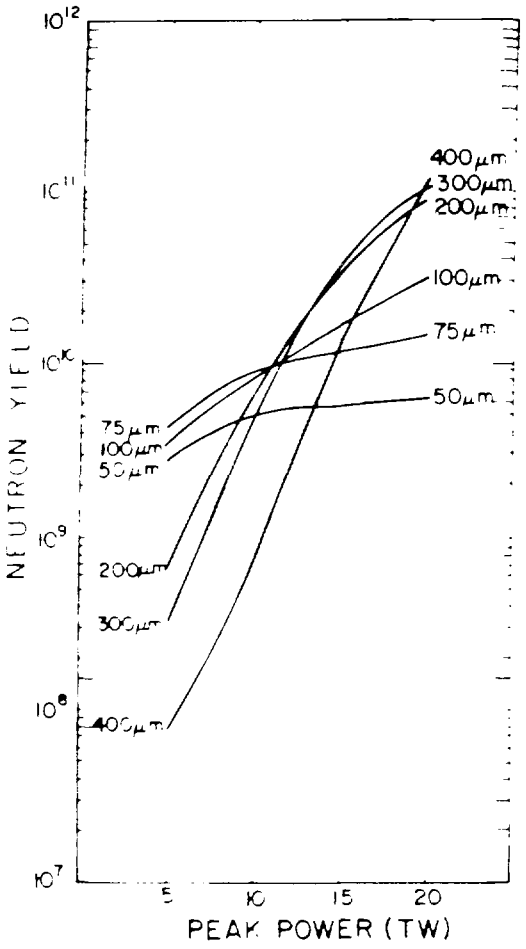

Fig. VI 5
Neutron yield as a function of peak laser power for target radii in the 50- to 400-μm range.

whose slopes are much more gradual, consistent with the result shown in Fig. II 5 of Ref. 1. These smaller targets are saturated at the power levels investigated, and any absorbed extra power (energy) cannot be converted efficiently into fuel heating.

Another variable considered was the initial fill pressure. Figure VI 6 shows how the neutron yield varied as a function of fill pressure for specific targets and laser pulses. Note that the yield at lower powers decreases as the fill pressure decreases to 1 atm. Although the yields decrease, they are still substantial enough ($>10^9$) to allow experimental verification. Neutron yield as a function of shell thickness for selected target diameters and laser pulses is shown in Fig. VI 7. The 5- and 10-TW curves show a weak dependence on shell thickness over the range considered. The 10-TW curve shows a broad maximum, but the 20-TW curves reveal that the maximum yield as a function of shell thickness also depends fairly strongly on the target radius. In fact, the most important considerations seem to be the peak power (or the total usable energy absorbed) and the mass of the shell. The 20-TW 200-μm curve indicates a maximum at a shell thickness of 1.25 μm. The corresponding maxima for the 20-TW 300-μm, and 20-TW 100-μm curves should be at 0.6 and 5.0 μm, respectively, if we accept the idea that the shell mass is the important variable. Our curves do not contradict this assumption.

The neutron yield as a function of neon content in the fuel is shown in Fig. VI 8 for four different targets and pulses. These results are of interest because neon is sometimes added to the DT fuel for diagnostic reasons. Computer simulations at lower CO_2 laser powers (< 5 TW) have predicted an increased yield due to neon addition, but experiments have shown, instead, a degradation in yield. For CO_2 laser powers of 5 to 15 TW, the addition of neon either has little effect or will degrade

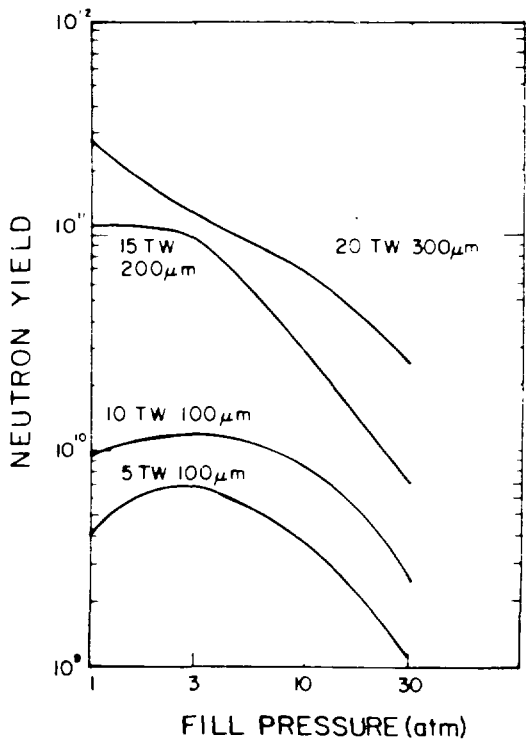

Fig. VI 6.
Neutron yield as a function of DT fill pressure for laser powers in the 5- to 20-TW range for various target radii.

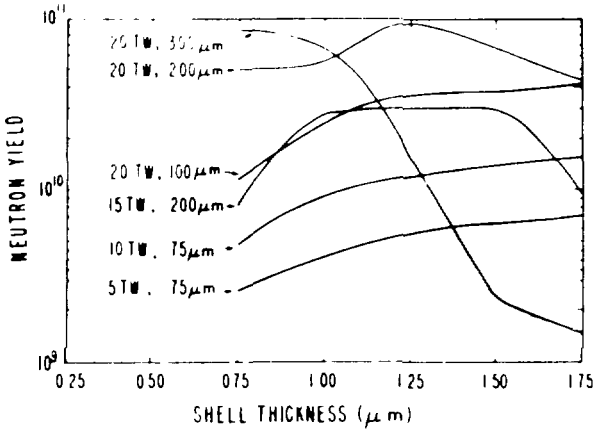

Fig. VI.7.
Neutron yield as a function of shell thickness for laser powers in the 5- to 20-TW range for various target radii.

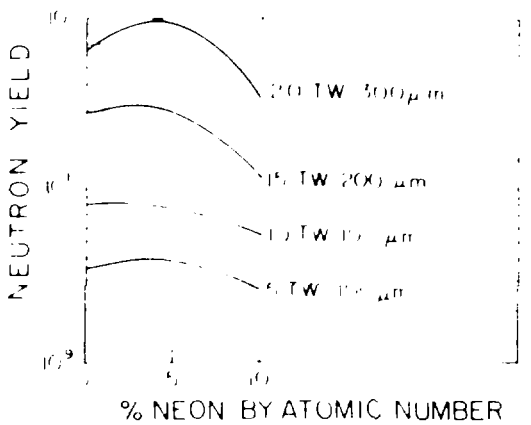

Fig. VI.8.
Neutron yield as a function of neon content in the fuel for laser powers from 5 to 20 TW for various target radii.

the yield. However, even the lower yields are above 10^7 neutrons, and the theoretical findings should be subject to experimental verification.

Conclusions. The most important result of our simulations is the indication that any reasonable exploding pusher target should produce in the Helios laser system *at least* 10^8 *neutrons. A well defined and fabricated* target should produce as many as $\sim 2 \times 10^9$ neutrons at 10 TW.

Even somewhat imperfect targets are predicted to produce measurable amounts of neutrons, and therefore, our theoretical curves plotting yield as a function of power, risetime, fill pressure, radius, and neon content in the fuel can be subject to experimental verification.

Recently, five Helios shots were analyzed for which the laser pulse was well characterized. On an average, the measured yield was 1.23 times the predicted yield. The actual yields were in the range of 1 to 3×10^8 for peak powers of 2 to 4 TW.

Two Dimensional Calculations of Sirius B Targets (R. Kopp)

Whether fuel can be compressed to a density 20 times that of liquid depends greatly on the reliability of one dimensional computer simulations of target performance (see previous reports in this series). These calculations assume perfect spherical symmetry of laser illumination and target geometry, a situation never realized completely in practice. Any departure from perfect symmetry, however small, is expected to degrade the performance. To evaluate the anticipated degree of this degradation under typical experimental conditions, quantitative two dimensional (2-D) implosion histories have been calculated for a variety of asymmetrical laser target configurations.

Many types of asymmetry are possible in a multibeam laser system such as Helios. Even in a perfectly aligned system, the finite size of the beam focal spots will ensure that the target surface will be, to some extent, nonuniformly illuminated. This nonuniformity may be further accentuated by pointing and focusing errors among the eight individual beams. In addition, the separate beams will, in general, have varying energies, and they may arrive on target at slightly different times. Finally, the target itself may acquire imperfections during fabrication, either in the form of large nonuniformities of shell thickness (noneoncentricity and or oblateness of the target) or short scale length fluctuations (e.g. surface roughness, small density inhomogeneities, support structures).

The calculations to be discussed provide only a rough guide to the effects of 2-D asymmetries on target behavior because existing computer codes do not permit modeling target implosions in geometrical laser configurations as complex as that of the eight beam Helios system. Certain simplifying approximations must be made to the actual laser geometry to permit tractable numerical modeling studies that still lead to useful

qualitative conclusions regarding the sensitivity of performance to laser target asymmetries.

Some initial 2 D calculations on the effects of laser illumination asymmetries were presented in a previous progress report (LA-7755-PR). The radiation incident on one side of the target was "hemispherically uniform," but was either temporally delayed relative to, or weaker than, the radiation striking the other side. Only small energy differences between the opposite hemispheres were treated in these early calculations.

This study has been extended to include larger energy imbalances between opposite sides of the pellet. As before, the Sirius-B targets assumed in these calculations consist of a 100 μm radius GMB filled with 100 atm of equimolar DT and coated with 100 μm of parylene. The total laser energy incident on the target was 5 kJ in all cases, of which 20% was absorbed. The illumination asymmetry is described by the ratio R = (E − E)/(E + E), where E and E are the energies incident on opposite halves of the target.

Expected neutron yields and fuel compressions are shown in Table VI I for four nonzero values of R. In all cases the burn time, defined as the interval between the beginning of the laser pulse and maximum neutron output, is 1.3 ns. Table VI I shows that the performance of this class of target begins to deteriorate noticeably only at the largest asymmetries considered. Although such large beam energy imbalances cannot be ruled out in practice, experience has shown that, for target shots with all eight beams operating on Helios, the hemispherical asymmetry index R rarely, if ever, exceeds 8%. Even if one beam fails to fire (E = 3/4 E), corresponding to R = 0.14, the degradation is still not very serious (a better treatment of this case is described below). On the other hand, if two beams misfire in the same hemisphere (R = 0.33), one can expect a substantial decline in both yield and compression due to illumination asymmetry (in addition to the degraded performance resulting from the reduced total energy on target, which was not included in these calculations). Again, experience on Helios indicates that, in the 20 times liquid density experiments, target shots with fewer than seven beams are not worth detailed analysis.

To examine the effect of *target* asymmetries, we considered two situations of interest to the current series of high compression experiments. In each case, a total CO_2 laser energy of 4 kJ, in the form of a triangular temporal pulse with 200 ps risetime and a FWHM of 600 ps, was incident uniformly over the target, which was assumed to be a GMB with 150 μm radius filled with 30 atm of DT and coated with 50 μm of parylene. (These laser target parameters represent a closer approximation to recent experimental arrangements than those of previous examples.) In the first case, the parylene "preheat shield" was intentionally made 5 μm thicker on one side than on the other, corresponding to a pessimistic assumption about current target fabrication capabilities. In the second case, the parylene thickness was uniform, but the thickness of the underlying glass pusher varied smoothly from 0.5 μm on one side to 1.5 μm on the other (again, a worst case from the fabrication standpoint).

The results of these implosion simulations are collected in Table VI II. In all cases the burn time is ~1.1 ns, and maximum fuel compression occurs about 100 ps

TABLE VI I

PERFORMANCE PREDICTIONS WITH LASER ASYMMETRY

E E E − E / E + E	Neutron Yield	Max Fuel Density (g/cm³)
0	2.9×10^{7}	6.1
0.04	2.9×10^{7}	5.9
0.08	2.9×10^{7}	5.7
0.12	2.6×10^{7}	5.3
0.24	1.1×10^{7}	4.8

TABLE VI II

PERFORMANCE PREDICTIONS WITH TARGET ASYMMETRY

Case	Neutron Yield	Max Fuel Density (g/cm³)
Spherically symmetric (1 D)	5.4×10^{8}	1.99
Asymmetrical ablator (2 D)	4.8×10^{8}	1.88
Asymmetrical pusher (2 D)	4.7×10^{8}	1.94

later. Here, too, it is comforting to observe that the *maximum* expected asymmetries in target structure have no substantially adverse effect on anticipated performance.

A third class of 2 D simulation addressed specifically the effect of a Helios beam misfire on target behavior. As mentioned above, a zero order representation of this situation may be obtained simply by diminishing the energy incident on one hemisphere of the target surface. However, because this procedure tends to underestimate *the implosion asymmetry, it assumes that the remaining* three beams in that hemisphere are spread uniformly over the surface. An opposite extreme (i.e., an overestimate of asymmetry) may be modeled in axisymmetric 2 D calculations simply by turning off the laser source in a cone of solid angle $\pi/2$ centered on the positive z axis (corresponding to one of the eight beams of Helios), while keeping the intensity unchanged elsewhere on the target surface. The laser target parameters for this case were the same as in the preceding example of shell nonuniformities, except that ~1/8 of the 4 kJ incident energy was spread uniformly over ~1/8 of the target surface.

A comparison of 1 D and 2 D performance calculations for the configuration is shown in Table VI III. The first row lists the 1 D prediction of neutron yield, fuel compression, and burn time for the full 4 kJ output of the laser; the second row gives a similar prediction for 3.5 kJ, corresponding to the energy of seven of the beams spread evenly over the pellet surface; and the last row shows the results of the 2 D calculation described above. A substantial reduction of yield (factor of 4) and compression occurs between the 1 D 4 kJ case and the 2 D 3.5 kJ case, about half of which is accounted for by the lowering of total energy incident on the ball, and half of which results from the nonuniform distribution of this reduced energy over the target surface.

TABLE VI III

SIRIUS B PERFORMANCE WITH MISSING LASER BEAM

Case	Neutron Yield	Max Fuel Density (g/cm^3)
1 D (4 kJ)	5.4×10^8	1.99
1 D (3.5 kJ)	3.0×10^8	1.75
2 D (3.5 kJ)	1.4×10^8	1.24

Figure VI 9 is a plot of the Lagrangian mesh used in the 2 D calculation near the time of peak neutron output (1.12 ns). The marked departure from spherical symmetry in this simulation is probably exaggerated because, due to some beam overlap, the misfiring of a single beam will not necessarily leave a section of the target surface totally unilluminated, as depicted here.

THEORETICAL SUPPORT

Introduction

We continued our efforts to understand the underlying physics in the areas of laser energy deposition and transport and to develop models of the various processes for use in hydrodynamics codes to improve the reliability of target calculations. Toward the goal of controlling the hot electron distribution, several different model calculations of resonance absorption have shown that the shape of the hot electron distribution function is affected by the frequency content of the electric fields in the vicinity of the critical density rather than just by the large field at the critical density. We have also discovered the mechanism by which stimulated Brillouin scattering is saturated in the case of intense 10.6 μm light; the mechanism explains the surprisingly low observed level of scattering at 10.6 μm and the surprisingly high observed level of scattering at 1.06 μm.

A more accurate set of electron transport equations have been derived and Monte Carlo calculations of electron transport have been used to compare the relative importance of transport inhibiting mechanisms. Most investigated mechanisms do not yield significant inhibition except when there are significant density troughs behind the critical density surface.

Modeling of Resonant Absorption (R. Bezzerides, D. Forslund, S. Gitomer)

Experiments have unequivocally demonstrated the presence of hot electrons generated by laser matter interaction at high laser intensities. Particle simulations have been used to study the nature of this heating. However, very little progress has been made in understanding the details of the heating mechanism. In particular, one cannot yet identify the microscopic effects

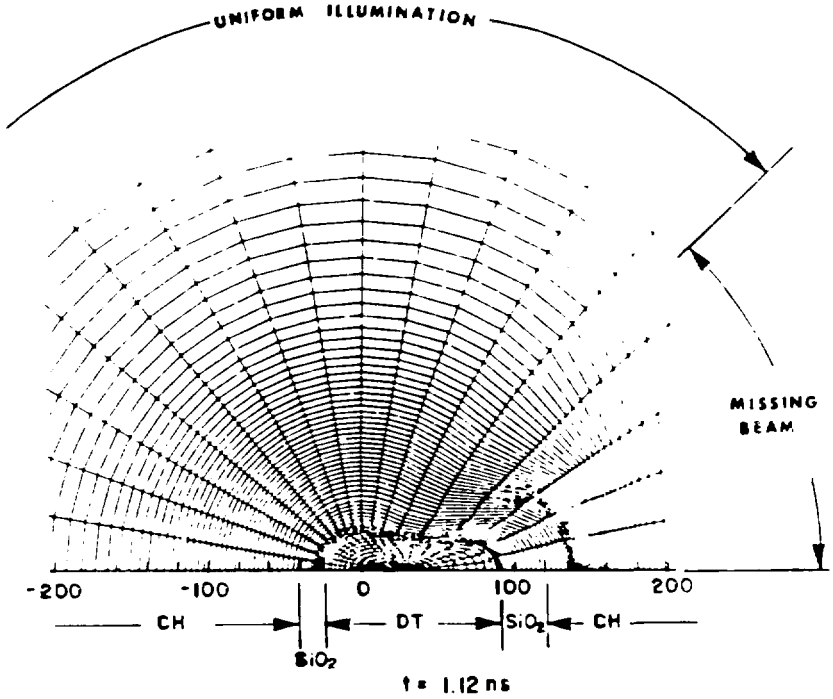

Fig. VI 9.
Lagrangian mesh plot near the time of maximum neutron yield for a Sirius B target configuration with one Helios beam missing. The z axis (axis of symmetry) is to the right, and the scale is in micrometers.

responsible for the velocity distribution of the hot electrons. If controlling features can be discovered, one may be able to profoundly affect target design efforts.

In the resonant absorption process, the incoming light wave is linearly converted to an electrostatic wave of large amplitude. We have examined the characteristics of the electrostatic wave by using both a one dimensional particle simulation (capacitor model) and a new test particle calculation scheme with the purpose of determining what features of the wave electric field are critical to obtain the observed electron heating. In our test particle calculation, particles are loaded into the computational box exactly as in a self consistent simulation. However, the particles move *independently* of one another in a *prescribed* electrostatic field. The test particle approach was subjected to a consistency check in which the electrostatic field from a self consistent simulation was used. The electron distribution function obtained in this way was identical with that obtained from the self consistent simulation.

Several calculations have been performed with prescribed electrostatic fields. We have systematically used fields derived from self consistent simulations to obtain a correct spatial field variation while providing the ability to assess variations of frequency content. In Fig. VI 10, we show the results for (a) a fully self consistent field; (b) 10 periods from a stored simulation field, replicated in time to form a full heating cycle (80 periods); and (c) a single period of a stored simulation field, replicated in time to form a full heating cycle. One conclusion drawn from these results is that purely periodic electrostatic fields cannot duplicate simulation distribution functions. Because the assumption of periodic electric fields is a fundamental feature in all earlier models of hot-electron production, this result invalidates such models.

To further characterize the frequency content of simulation electric fields, we performed a Fourier analysis in time on E(x,t) at spatial locations below, at, and above the critical-density point. Note that the simulation results are quoted for plasmas with fixed, linear-ramp density profiles. Results of the Fourier analysis are presented in Fig. VI-11, which shows that E(x,t) has frequency components (1) at the laser frequency (ω=1), (2) at harmonics of the laser frequency

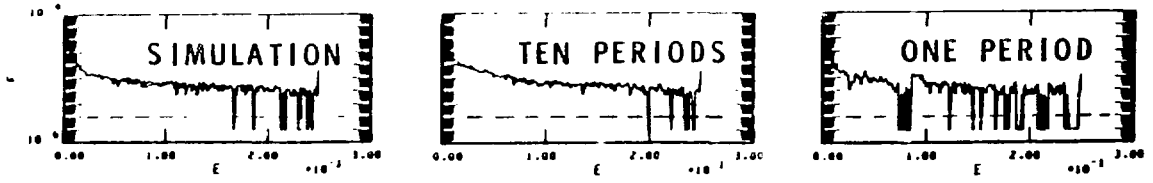

Fig. VI 10.
Distribution functions calculated by test particle method with various field models. The distribution function is plotted on a semilogarithmic plot vs energy.

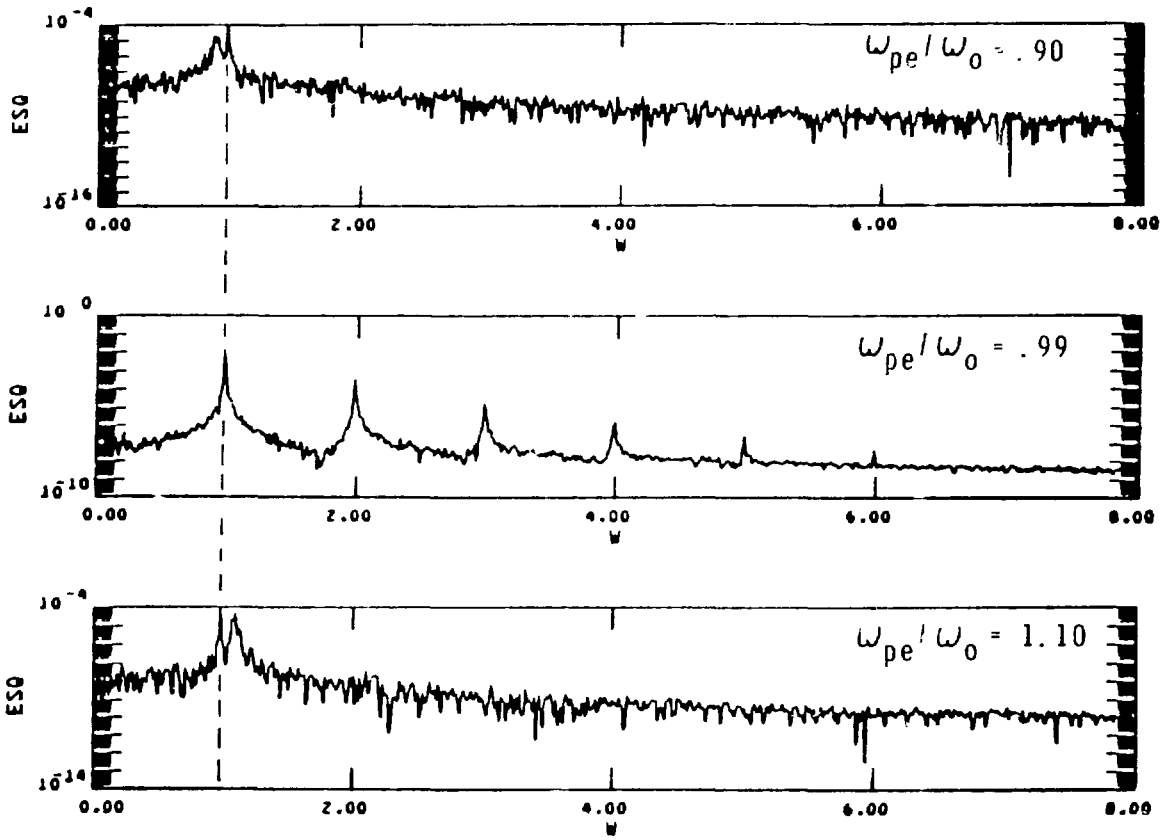

Fig. VI 11.
Fourier spectra of electric field at three spatial points. The spectral energy is plotted vs normalized frequency (ω 1).

(ω=2,3,4,5,6), and (3) at the local plasma frequency [$\omega=\omega_{pe}(x)$]. A portion of the temporal behavior of E(x,t) is shown in Fig. VI-12 for the same points at which the Fig. VI-11 spectra are computed. Subharmonic modulation of the driver is seen above and below the critical density, whereas a significant amplitude enhancement of the electric field is observed at the critical density.

To determine how important heated particles are in shaping the time character of E(x,t), we have considered a nonlinear warm fluid model in which the effect of heated particles is excluded. This model is the nonlinear extension of Ginzberg's simple thermal convectively stabilized model,[7] which is readily solved in terms of Airy functions.

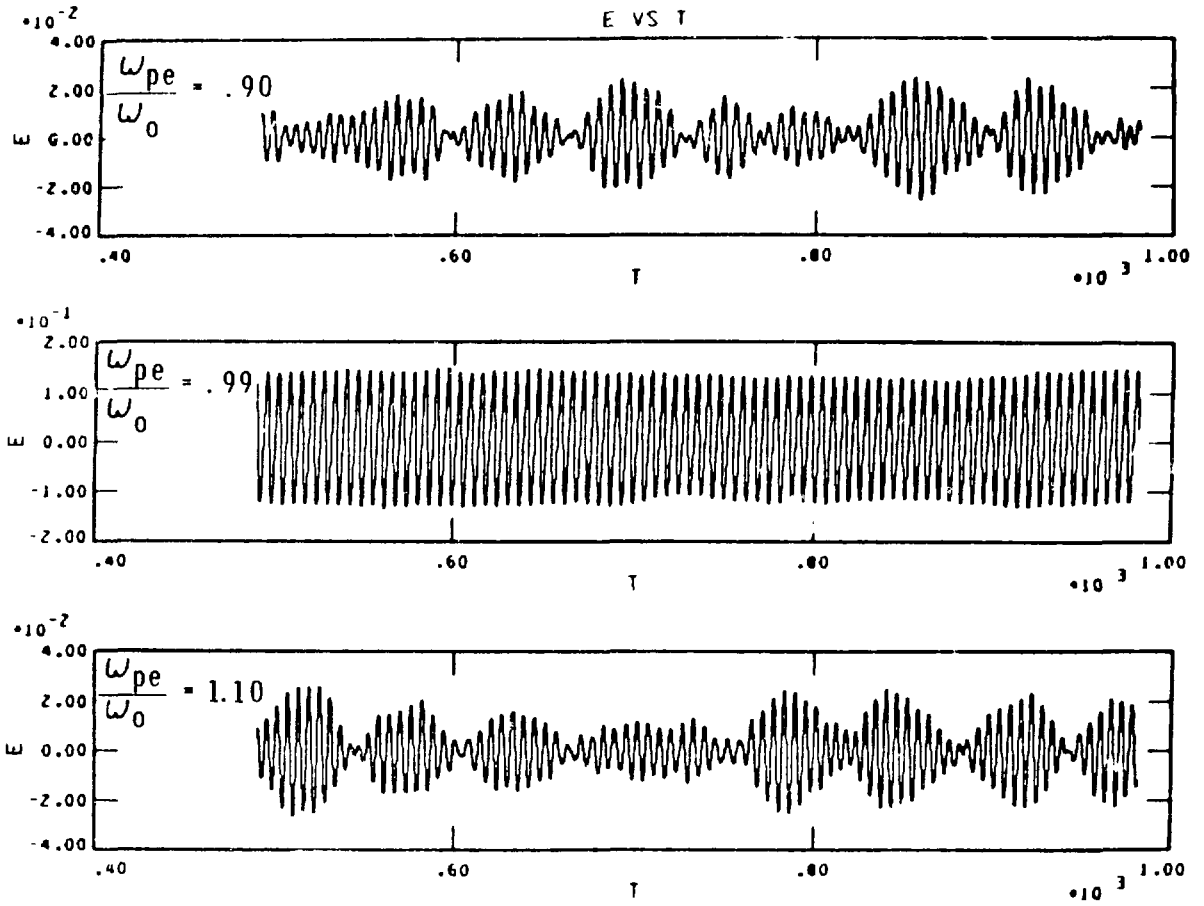

Fig. VI-12.
Field amplitude plotted vs time at three spatial points.

We start with the one-dimensional fluid equations

$$\frac{\partial v}{\partial t} + v\frac{\partial v}{\partial x} = -\frac{e}{m}E - \frac{1}{nm}\frac{\partial P}{\partial x} \quad , \tag{VI-2}$$

where v is the electron fluid velocity and P is the electron fluid pressure given by

$$\frac{\partial P}{\partial t} + v\frac{\partial P}{\partial x} + 3P\frac{\partial v}{\partial x} = -\frac{\partial Q}{\partial x} \quad . \tag{VI-3}$$

If we assume adiabatic fluid oscillations, Eq. (VI-3) leads to

$$\left(\frac{\partial}{\partial t} + v\frac{\partial}{\partial x}\right)\left(\frac{P}{n^3}\right) = 0 \tag{VI-4}$$

Equations (VI-2) and (VI-4) may be combined along with Poisson's equation to give

$$\frac{\partial^2 \delta}{\partial \tau^2} + \nu\frac{\partial \delta}{\partial \tau}\int_{x_o}^{x_o+\delta} \omega_{pe}^2(x')\,dx' + \frac{3v_{th}^2\frac{\partial^2 \delta}{\partial x_o^2}}{(1+\frac{\partial \delta}{\partial x_o})^4} + \frac{v_{th}^2\frac{1}{n}\frac{\partial n}{\partial x_o}}{(1+\frac{\partial \delta}{\partial x_o})^3} = -\frac{e}{m}E_o(\tau) \quad . \tag{VI-5}$$

Here, $\delta(x_0,\tau)$ is the Lagrangian displacement of a fluid element in terms of the variables $x_0(x = x_0 + \delta)$ and $\tau(t = \tau)$. Note that the convective speed is greatly enhanced as the wave-breaking condition is approached, that is, when $1 + \partial\delta/\partial x_0 = 0$. Thus, we may expect that the nonlinear pressure can have a profound effect on wave saturation.

This model agrees with the linear model of Albritton and Koch[3] for small field amplitudes. At high amplitudes, field saturation is observed due to the nonlinear convective term. Our model predicts field saturation levels that agree with those from particle simulations. Furthermore, as shown in Fig. VI 13, we find subharmonic field modulations as seen in Fig. VI 12 for simulations. Note, however, that the modulations in Fig. VI 13 are a transient effect, dependent upon the risetime of the driving field and the damping ν. In the simulations, this modulation feature appears to be an intrinsic characteristic of the fields.

In conclusion, we have discovered that the shape of the hot electron distribution function is significantly affected by the frequency content of the localized fields near critical density.

Stimulated Brillouin Scattering (D. Forslund)

About six or seven years ago stimulated Brillouin scattering was thought to be extremely important in determining the absorption of intense laser light by

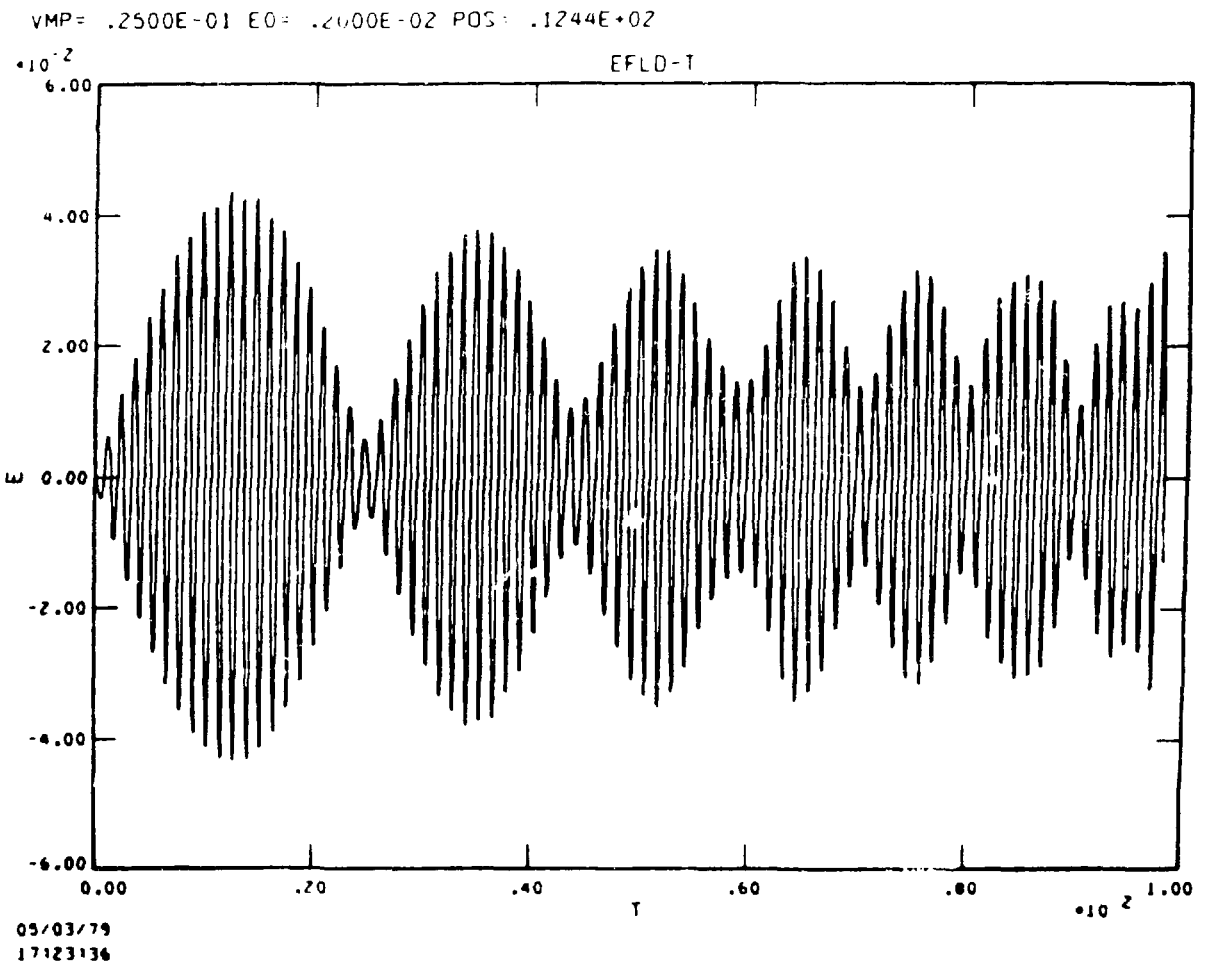

Fig. VI 13.
Results from nonlinear warm fluid model. Field amplitude plotted vs time.

plasmas. However, large scattering was not observed experimentally, and the problem was more or less set aside in the intervening years. With the advent of much more powerful lasers allowing for long intense laser pulses, stimulated Brillouin scattering has begun to reemerge as a major problem for longer pulsed reactor targets. One of the important parts of the puzzle was why CO_2 laser light with its electron oscillating velocity 10 times higher than that of Nd:glass lasers for a given intensity was not producing extremely large stimulated scattering. We have reexamined this problem and have determined the probable mechanism that limits the stimulated Brillouin scattering for CO_2 laser light to negligible levels. The basic limiting mechanism appears to be the saturation of the excited ion waves to $\delta n \lesssim 1$. In this saturated state, in fact, Brillouin scattering appears to scale inversely with the wavelength for a fixed laser intensity and pulse length.

If one neglects the nonlinearity of the excited ion waves, the well-known gain formula for stimulated Brillouin scattering is

$$g_c = \frac{\frac{1}{8}\frac{v_c^2}{v_e^2}\frac{n}{n_{cr}} k_c}{\gamma/\omega_s} , \qquad \text{(VI-6)}$$

where v_c is the oscillating velocity of electrons in the laser field, v_e^2 is the square of the electron thermal velocity, which can include ion pressure effects, n_{cr} is the critical density at which the laser frequency equals the local plasma frequency; k_c is the free space laser wave number; and γ/ω_s is the ratio of the acoustic damping rate to the acoustic frequency. This formula is valid for moderate to strong damping on the ion acoustic waves. Using the Manley Rowe relations in this same limit, one can obtain the expression for the ion wave density fluctuations,

$$\left(\frac{\delta n}{n}\right)^2 = \frac{v_c^2}{v_e^2}\frac{n_{cr}}{n} \cdot \frac{n_c}{\gamma/\omega_s} , \qquad \text{(VI-7)}$$

where n_c is the local reflectivity. If one restricts $\delta n/n$ to some level, Eqs. (VI-6) and (VI-7) give an expression for the thermal pressure v_e^2. Combining these two equations with a saturated value α of $(\delta n/n)^2$, we obtain

$$g_c = \frac{\frac{1}{8}\frac{v_c^2}{v_e^2}\frac{n}{n_{cr}} k_c}{\frac{\gamma}{\omega_s} + \frac{v_c^2}{v_e^2}\frac{n}{8\alpha} k_c v_c} . \qquad \text{(VI-8)}$$

Note that for low intensities at a fixed n/n_{cr}, g_c scales as the wavelength λ, and at high intensities, as $1/\lambda$.

For comparison, the reflectivity due to stimulated Brillouin scattering is shown as a function of intensity and wavelength in Fig. VI-14 as derived from Eq. (VI-6) and in Fig. VI-15 as derived from Eq. (VI-7). At long

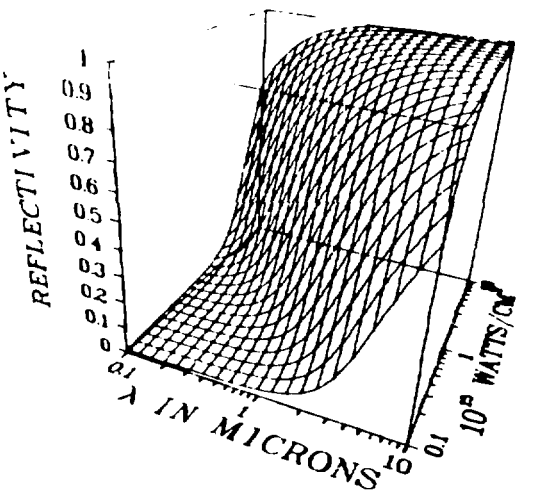

Fig. VI-14.
Stimulated Brillouin reflectivity vs intensity and wavelength using the gain formula of Eq. (VI-6). Note the extreme degree of reflectivity at long wavelengths.

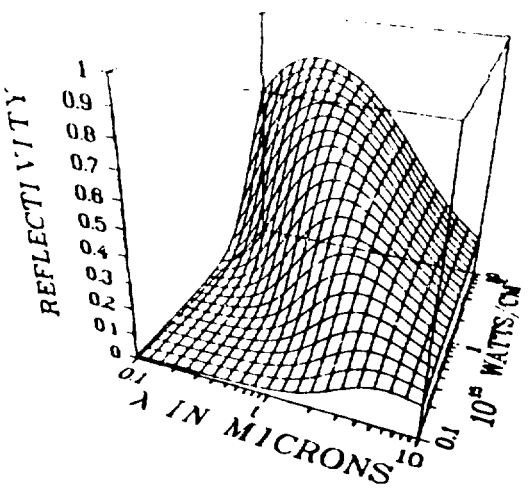

Fig. VI-15.
Stimulated Brillouin reflectivity vs intensity and wavelength using the gain formula of Eq. (VI-8). Note the large saturation effect at long wavelengths, which reduces the reflectivity to less than that at shorter wavelengths.

wavelengths, note the dramatic change arising from the onset of saturation at much lower intensities. Apparently, at a given intensity, an optimal wavelength maximizes the level of scattering and this level of scattering is higher at higher intensity. Basically, this maximum occurs when the two terms in the denominator of Eq. (VI.8) are about equal. For reflectivities near unity and $\alpha \sim 1.8$ this occurs for $\nu_e v_e^2 \sim \gamma \omega_s$. For weak ion wave damping this may occur at rather low intensities.

Intense CO_2 laser light may have only a very low gain coefficient for stimulated Brillouin scattering, which is consistent with the experimental data. This gain coefficient is so low, in fact, that stimulated Brillouin scattering is probably not a problem even in reactor targets.

Plasma Transport in the Laser Fusion Regime (H. Brysk)

Plasma transport in laser fusion hydrodynamics codes usually follows the Braginskii prescription. In this approach (based on the Chapman-Cowling development), the set of kinetic velocity moments of the Vlasov equation is truncated after the first three, yielding fluid equations for mass (continuity equation), momentum, and energy; the system is closed by modeling approximations for the evaluation of the terms involving the next higher moment and the interspecies collisions. Calculations with this scheme can produce inordinately large electronic fluxes in the laser heated corona. These are then counteracted by the imposition of an ad hoc "flux limiter," that is, by legislating an upper bound that the flux is not allowed to exceed notwithstanding the solution of the equations. This bound is classically the free streaming limit, though arguments abound for making it smaller.

The alternative we adopted is to push on to higher order in the velocity moment expansion, thus obtaining a fluid equation for the flux. Because this equation includes retardation, it cannot exceed the free streaming limit automatically. A fluid equation for the viscosity tensor is also obtained (formally of lower order). Closure still requires a model for evaluating the yet higher moments and the collision terms. In the hot underdense corona, the contributions from interspecies collisions can be viewed as weak terms. These and the other higher order terms have been accordingly calculated explicitly in the approximation of replacing the particle distribution functions by drifting Maxwellians. They have all been obtained analytically in closed form, as functions of density, temperature, and drift velocity (not depending on the flux explicitly). Use of the explicit expressions not only ensures that the weak terms remain modest in magnitude, but should also help restrain computational excursions in the solution of the fluid equations.

For a three dimensional plasma with planar symmetry, the fluid equations (apart from the continuity equation) reduce to

$$m_a n_a \left(\frac{\partial}{\partial t} + V_a \frac{\partial}{\partial x} \right) V_a + \frac{\partial}{\partial x}(n_a T_a) - e n_a E = \sum_b F_{ab} ,$$

$$\frac{3}{2} n_a \left(\frac{\partial}{\partial t} + V_a \frac{\partial}{\partial x} \right) T_a + n_a T_a \frac{\partial}{\partial x} V_a + \frac{\partial}{\partial x} q_a = \sum_b Q_{ab} ,$$

$$m_a \left(\frac{\partial}{\partial t} + V_a \frac{\partial}{\partial x} \right) q_a + \frac{16}{5} m_a q_a \frac{\partial}{\partial x} V_a + \frac{5}{2} n_a T_a \frac{\partial}{\partial x} T_a$$

$$= \sum_b S_{ab} ,$$

where the subscript a denotes the particle species for which the equations are written, whereas b denotes the other species (for example, thermal and suprathermal electrons, light and heavy ions), n_a is density, V_a drift velocity, T_a temperature, q_a flux, and E electric field. The terms on the right represent interspecies collisions and are given by

$$F_{ab} = \frac{8A_{ab}}{(z_a^2 + z_b^2)^{1/2}} \left[z_a^2 z_b^2 \right] ,$$

$$Q_{ab} = \frac{4A_{ab}}{(z_a^2 + z_b^2)^{3/2}} \left[\right] ,$$

and

$$S_{ab} = \frac{3m_a}{\alpha(z_a^2 + z_b^2)^{5/2}} \left[\right] ,$$

with the abbreviations

$$\alpha = \left(\frac{m_a}{2T_a} \right)^{1/2} , \quad \beta = \left(\frac{m_b}{2T_b} \right)^{1/2} , \quad \gamma = \frac{m_a}{m_a} V_b - V_a ,$$

$$\delta = \tau_a \left(\frac{1}{\tau_a} - \frac{1}{\tau_b} \right) ,$$

A_{ab} $\pi^{1/2} m_a^{-1} \lambda e_a^2 e_b^2 n_a n_b$ (e charge, λ collision logarithm) ,

s $\beta\gamma / 2\alpha(\alpha^2 + \beta^2)^{1/2}$,

ϕ $(\pi^{1/2}/2s)\,\mathrm{erf}(s)$,

ψ $\exp(-s^2)$.

With these approximations, then, we have obtained a set of higher order equations that remove the need for an *ad hoc* flux limiter. We hope these will allow a more accurate representation of electron transport phenomena than now exists.

Hot Electron Transport (R. Mason)

The Monte Carlo hybrid electron transport scheme described in the previous semiannual report (LA-7755-PR) has been used to study transport in new geometries. Sample results are collected in Fig. VI.16. The ions are of glass ($Z = 10$); the ion charge density $n_i \sim Zn$ rises from zero at the vacuum edge through critical (10^{21} cm^{-3}) to a plateau value of $\sim 3 \times 10^{22}$ cm^{-3} and then up to its solid density value of $\sim 5 \times 10^{23}$ cm^{-3}. Laser light (1.06 μm) impinges from the right.

It has been established[4] that return current resistive electric fields can provide transient hot electron inhibition in cold targets. Our simulations show that at plateau densities in glass targets, the inhibition sets in for *fixed* cold electron temperature (T_c) below 100 eV. The hot electrons are almost totally confined to a region near the critical surface (Fig. VI.16a-c). However, when T_c is allowed its *natural increase* from joule heating, Coulomb drag, and conduction, the inhibition from resistivity "burns out" at a rate exceeding 30 μm/ps. Comparison of Figs. VI.16a and e shows much higher hot electron density values in the burned-out case at, say, 20 μm below the critical surface; the comparative phase plots b and f also demonstrate the reduced retention of the hot electrons with burnout. In fact, hot-electron results of Figs. VI.16e-f are essentially unaltered if we entirely suppress the E-field effects on hot electrons for $x > 36$ μm. The burn-out time can be slightly longer at higher Z due to the larger classical cold collision frequency (ν_c), and considerably longer at higher density due to high specific heat. But even at $n_e \sim 5 \times 10^{23}$cm^{-3} in SiO_2, we find that the inhibition from E is, at most, only equivalent to that provided by classical hot electron scattering.

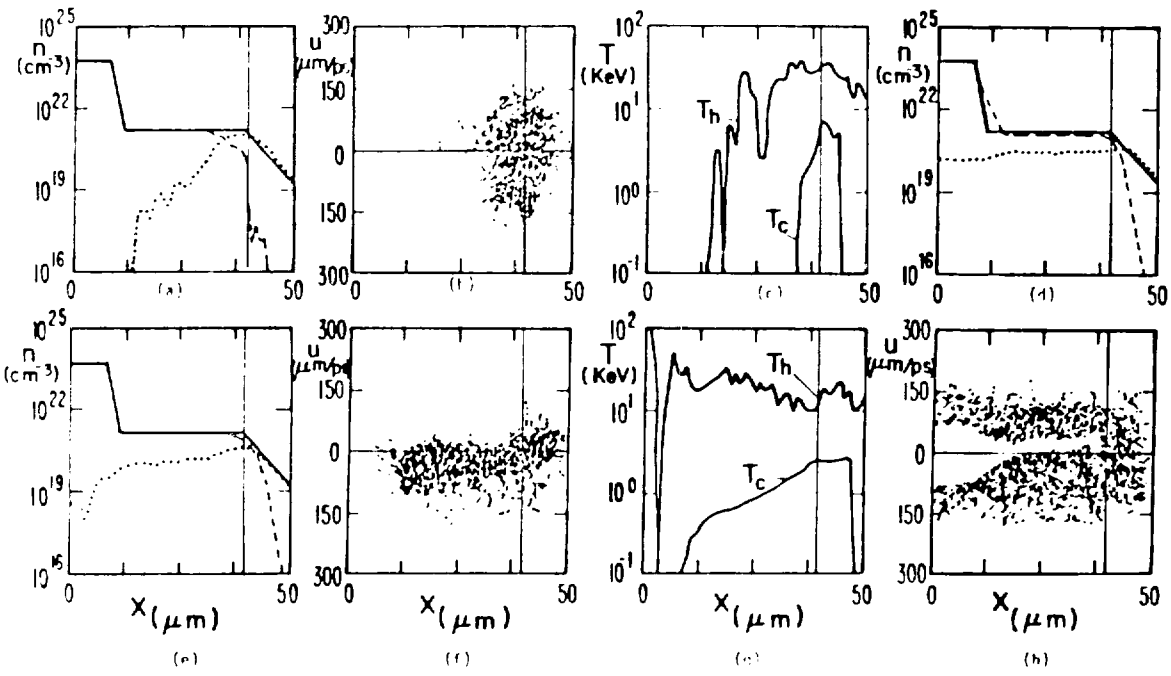

Fig. VI.16.

Return current resistive E field calculations. Results after 1.8 ps of illumination at $I = 5 \times 10^{15}$ W/cm^2 assuming 35% absorption with 5% deposition into the thermals as inverse bremsstrahlung, n_i = ——, n_h . . . . , n_c - - - - . Initially $T_c = 1$ eV. Frames a-c: T fixed for $x > 36$ μm; frames e-g: T_c may change. A vertical fiducial marks the critical surface. Frames d and h show the transport enhancing effect of the E-field containing high-density cold electrons when $T_c = 2$ keV initially; here the suprathermal scattering and drag have been suppressed.

Alternatively, the E field from cold pressure gradients at large density interfaces can overwhelm the resistive electric field for sufficiently large Γ_e, actually *enhancing* the suprathermal transport. In steady state, neglecting source and thermoelectric terms, the momentum equation for cold electrons reduces to $E \sim [\alpha(Z)\nu_{ei}/n_e] \cdot \nabla P_e$ (when ν_{ei} is classical). From critical to solid density, the potential energy change is $\Delta(e\phi) \sim T_e \log(5 \times 10^{23}/10^{21}) \approx 6.2\,T_e$. Thus, if $T_e \approx 2$ keV, a hot electron gains 12 keV on running from critical to solid density. Figure VI.16d and h exhibit the effects of this acceleration mechanism.

Ion acoustic turbulence is a suspected source of inhibition. The Lindman[4] effective ion acoustic collision frequency has been used in all our simulations. Generally, it is more than two orders of magnitude below ν_{ei} (classical). Multiplying ν_{ei} by 30 we found no effect on hot electrons, but multiplication by 10^3 provided confinement comparable to that shown in Fig. VI.16a–c.

Cold convection and thermoelectric effects, which have been overlooked, can inhibit the thermal transport. Neglecting sources and compressive PdV work, the energy equation for cold electrons reduced to

$$\frac{\partial}{\partial t}\left(\frac{3}{2}n_e T_e\right) = -\nabla \cdot (q_t + q_c + q_{te}),$$

in which q_t *is thermal diffusion and* q_{te} *is the thermoelectric heat transfer rate. The convection and thermoelectric terms move heat toward critical density so that net thermal inhibition and even* *transport reversal* can exist when

$$q_t + q_c + q_{te} < 0.$$

By quasi-neutrality $n_e u_e \sim n_i u_i$, and reversal will therefore occur in the presence of large suprathermal currents. This effect is similar to Shkarofsky's recent bi-Maxwellian results,[5] but it occurs here at high relative drift speed between the components, and even in the absence of collisions.

The conditions for reversal are straightforward under flux limitation. We have $q_t = -0.6\, n_e \nu_{ei} \nabla T_e / m_e$, and $q_{te} < 0$, so we need

$$\frac{\nabla T_e}{T_e} > \frac{\nabla n_e}{n_e}.$$

Note, for example, that for 20 keV suprathermals $u_e \approx 60$ μm ps, whereas for 4 keV thermals $v_{te} \approx 27$ μm ps. Thus, typically, reversed heat flow should occur for $u_e > 11$ μm ps or $n_i/n_e > 0.18$. The conditions are less stringent if the diffusion is unlimited, that is, $qt > F_f$. The mechanism should be stronger under Nd:glass than CO_2 illumination, assuming a constant n_e, by the ponderomotive force, because $I \sim n_e u_e T_e$, and, in general, $T_e^{CO_2} > T_e^{Nd} \sim 4$, so $n_e u_e$ is roughly four times stronger for Nd:glass yielding more inhibition by convection.

Figures VI.17a and b display the effects of the convective term. We find that, in practice, significant inhibition is difficult to achieve. First, this is true because *joule heating* tends to "mask the convective effects. Thus, going to higher Z and adding anomalous ν_{ei} to reduce q_t provides no guaranteed net increase in the inhibition. Second, in general, the necessary high n_i/n_e ratios are unlikely because, for example, at high intensities $n_i \sim I^{-1}$, while $n_e \sim I$.

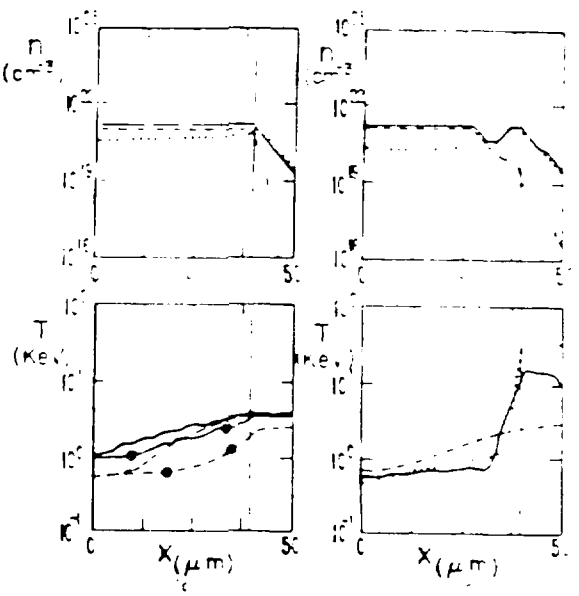

Fig. VI.17.
Convective and trough inhibition results after 4 ps of Fig. VI.16 illumination; left boundary a mirror. Frames a and b: typical density profiles with and without a trough; n_e, n_i, . . . , n_{cr}. Frame c: no trough T_e profile with joule heating "on" , and "off" ; also with the convective term in (3) "on" and "off." Frame d: T_e profiles with the trough , and without it under classical limitation , and under 1/20 classical with the convective term "off" .

As a possible resolution of these difficulties we have found that *density troughs* can markedly intensify the convection inhibition. Troughs have been calculated[10] and seen in experiment, but their depth remains uncertain. Troughs decrease the maximum q_c and increase η_{max}. Figures VI.17c and d show T_e "bottled up" behind a trough in n_e. Inhibition of the cold transport is now considerable, that with $\Gamma = 20$ the classical flux q_c/q_{cl} in the absence of a trough. With a dip to 0.1 n_{max} [illegible] insulators, even stopping the [illegible] as in Figs. VI.16a–c. Thus, strong inhibition in [illegible] experiments may be a signature for [illegible] the target density profiles.

CODE DEVELOPMENT

Introduction (K. A. Taggart)

We [illegible] the [illegible] and improved the performance [illegible] the [illegible] and its conversion to more efficient computers. We are reporting progress in converting codes to the more efficient FTN compiler on the CDC 7600 computer, and ultimately, to the CRAY 1, as well as the inclusion of a new ion beam deposition package with more accurate stopping powers and a three dimensional beam ray trace. As a result of these coding efforts, a significant improvement in design capability is anticipated in the coming months.

Ion Beam Driven Target Design Capability (G. Bohannon)

An ion beam energy deposition calculation written during this reporting period greatly increases the usefulness of our design codes for studying nonlaser driven targets. An important component of this improvement is a computer code, developed by T. Mehlhorn at Sandia National Laboratories, that gives accurate ion stopping powers for a wide range of materials and ion types. The ion beam capability includes three dimensional ion beam ray tracing as well as beam propagation along zonal grid lines.

Theoretically, several contributions affect the energy deposition, such as bound electrons, free electrons, and ions. However, the dominant contributions are from electrons, and only those contributions are considered here.

At low velocities, the stopping power of bound electrons is given by the model of Lindhard et al.,[13]

$$\left(-\frac{dE}{ds}\right)_{LSS} = 8\pi k_e a_0 Z_B^{1/6} \frac{NZ_T Z_B v}{w} ,$$

where s is the penetration depth, N is the bound electron density, Z_T and Z_B are the target and beam nuclear charges, v is the beam velocity, and a_0 is the classical electron radius. Also,

$$w = \left(Z_T^{2/3} + Z_B^{2/3}\right)^{3/2} ,$$

and k_e is a constant of order unity.

At higher velocities the Bethe[14] stopping theory is used,

$$\left(-\frac{dE}{ds}\right)_B = \frac{4\pi Z_{eff}^2 e^4}{mv^2} N Z_T \log\left[\frac{2mv^2}{I(1 - v^2/c^2)} - v^2/c^2 - C/Z_T\right] ,$$

where Z_{eff} is the effective beam charge, I is the target average ionization potential, C is the shell correction factor, and m is the electron mass.

The velocity below which the Lindhard model is used and above which the Bethe theory is applied is easily defined. In most cases that include shell correction, the Bethe stopping power increases sharply at low velocities. The Lindhard value, however, is linear in velocity and crosses the Bethe value at only one velocity. The appropriate stopping power at a particular velocity is simply the lower of the two. In the cases where the two expressions do not cross, the Bethe theory is used also at low velocity. This procedure gives excellent agreement with the phenomenological results of Northcliffe and Schilling,[15] who used a large amount of experimental data in their analysis.

The free electron contribution was given by Butler and Buckingham.[16]

$$\left(-\frac{dE}{ds}\right)_{BF} = \frac{4\pi N_f}{mv^2} \left(Z_{eff} e^2\right)^2 G(x) \log \Lambda ,$$

where N_f is the free electron density and log Λ is a Coulomb logarithm. The function G(x),

$$G(x) = erf(x) - \frac{2x}{\sqrt{\pi}} e^{-x^2} ,$$

where $x = v/(2kT/m)^{1/2}$, assumes a Maxwellian distribution of electron velocities; G approaches unity when the

beam velocity is much higher than the mean electron velocity.

Ion beam propagation in the target can be treated in two ways in our codes. The simplest is to force the beam to travel along one or more of the zonal grid lines. However, in many cases, especially for complicated target geometries, this restriction is not acceptable. In these cases, the beam can be represented by a number of rays that travel along straight lines in three dimensions through the target. This capability was achieved by modifying the existing three dimensional laser ray trace code.

As with laser beams, the ion beams can be initially focused or unfocused when the ray trace option is selected. An unfocused beam is represented by parallel rays. For example, an incident beam with a circular cross section of constant diameter can be obtained by choosing unfocused rays parallel to the z axis.

Designers who have studied laser driven targets with design codes should find it no harder to set up similar ion beam problems. Only one additional instruction is required, which specifies the beam energy, charge, and mass number. Several other parameters may be specified separately if the designer does not wish to use the default values.

FTN Conversion of Laser Fusion Simulation Codes (J. Peterson, T. Gorman, G. Bohannon)

General. One objective of the Code Development Section is to develop and maintain codes used by target designers to evaluate targets. To run more and larger problems more efficiently, our target design codes are being converted so they will run on the CRAY. The strategy is a two phase effort. In the first phase, the conversion will be from CHAT on the 7600 to FTN on the 7600. In the second phase, the effort will be to convert from the 7600 FORTRAN to the CRAY FORTRAN. At present, we are in the first phase.

The first phase comprises three major steps. First, all syntactical changes were made to replace LRLTRAN unique forms with forms acceptable to both CHAT and FTN. This step, which continued over the past 18 months, enabled us to convert codes and concurrently to enhance and maintain them. Then, the codes were frozen, and in the second step, all other conversions from LRLTRAN to FORTRAN were made. The third step is to debug the FORTRAN/7600 versions. The first two steps are complete and the third is well under way.

During phase I, step 1, the I/O was converted from NLIB76 routines to routines written using ORDERLIB routines that emulate FTNLIB routines. (FTNLIB will be available on the CRAY as well as the 7600.) Also, half word packing and unpacking, bit setting and testing, fixed point/floating point testing logic, and address determination changes were made. Changes were also made to resolve the zero pass vs one pass DO loop conventions differences of the two compilers.

During phase I, step 2, the I/O emulating routines were deleted, the overlay loading was changed to the FTN standard form, miscellaneous word packing and shifting operations were converted, and the inevitable problems with unresolved externals were solved. In addition, the compiler diagnostics produced by FTN were cleaned up. We learned about the idiosyncrasies of the codes coupled with FTN and LTSS and worked out solutions to those problems. The FTN compiler was modified to allow pointered variables, and the concomitant syntactical changes in the codes were made to be in compliance with the FTN pointer syntax. Finally, the TV80LIB graphics usage was converted to the TLIB library, which is maintained at Los Alamos.

FTN Compiler Modification. One of the most significant technical advances in the conversion effort was the modification of the Los Alamos FTN compiler to allow dynamic storage allocation, an LRLTRAN feature that is used extensively in some target design codes. Some codes are designed for optimum competition for resources in a Los Alamos Lawrence Livermore National Laboratory job mix environment. One of the most important techniques for obtaining this performance is through the allocation of Large Core Memory (LCM) at execution time, requesting only the exact amount needed for a given calculation. As competition for the limited computing resources at Los Alamos is becoming more acute, it is necessary to continue this feature in the FTN versions. Another less esoteric justification for this effort was that it would be nearly impossible to convert some large codes to FTN and still run reasonable designs without completely rewriting most of the code and logic structure.

The concept of the application program allocating storage is based on the requirements of the problem rather than on the largest problem likely to be run. This facility is especially important in a target design code because the amount of storage required by a given design varies greatly from design to design. In fact, not enough core is available on the 7600 computer to accommodate

the largest problem that could be run. Modifications to the compiler were made in such a way that no changes were needed in the usage of the data variables. Internal variables are treated exactly as described in the FORTRAN 68 standard.

The new compiler feature has been valuable in the conversion effort and will make it possible to convert other LLNL codes at Los Alamos, to maintain active communication between the Laboratories, and to reduce duplication in software development. The FTN conversion project was a cooperative effort between the Los Alamos Target Design Group and Language Group.

Graphics Conversion. The graphics routines used in the target design codes were converted to FTN, restructured to use standard Los Alamos graphics, and restructured to allow further expansion of certain graphics capabilities, which were somewhat limited in the original versions.

The graphics sections were rewritten for several reasons. First, our codes must become independent of IVSOLIB, a LLNL graphics package that had been modified to operate at Los Alamos, but used Los Alamos graphics hardware rather poorly. It would have been possible to maintain IVSOLIB at Los Alamos, but it is a waste of valuable resources to maintain several major graphics packages at one installation. Therefore, we rewrote the graphics sections in the target design codes to a standard Los Alamos supported graphics library.

Second, the basic design of the graphics sections was inflexible and did not lend itself to modern reliable, maintainable coding techniques. Also, the main graphics sections consisted of only two subroutines, one for initialization and one for graphics output. The output subroutine was at the maximum size that can be handled by the CRI FTRAN compiler supported at Los Alamos. Adding new plots of interesting parameters was virtually impossible with the earlier versions. The graphics sections were rewritten to FTN using Los Alamos graphics package TLIB. The sections were restructured by using modular programming techniques that effectively isolate the data analysis sections from the graphics production sections.

Summary. Conversion of target design codes to FTN accomplished the following objectives.

- The structures of the codes were modified to allow easier implementation of improved physics models that better represent Los Alamos targets.
- The codes now run larger problems more cost effectively on CRAY.
- FTN codes will make contributions and verification of new physics models easier.
- The replacement of system dependent features, functions, and syntax will facilitate use on other CDC installations.

The exact approach to be used during phase II to convert the 7600 to the CRAY computer will be defined during the next reporting period.

REFERENCES

1. C. W. Cranfill, "One Dimensional Computer Simulations of the Implosion of Simple Shell Targets with the Los Alamos Two Beam CO_2 Laser," Los Alamos National Laboratory report LA-6827-MS (June 1977), p. 4.

2. V. L. Ginzberg, *Propagation of Electromagnetic Waves in Plasma* (Gordon Breach, New York, 1961).

3. J. Albritton and P. Koch, Phys. Fluids **18**, 1136 (1975).

4. E. J. Valeo and I. B. Bernstein, "Fast Ion Generation in Laser Plasma Interactions," Phys. Fluids **19**, 1348 (1976).

5. E. Lindman, "Absorption and Transport in Laser Plasmas," J. de Physique **38**, C6-9 (1977).

6. I. P. Shkarofsky, "Heat Conduction and Magnetic Field Induction in the Presence of Cold and Hot electron Maxwellian Distributions," Phys. Rev. Lett. **42**, 1342 (1979).

7. K. Lee, D. W. Forslund, J. M. Kindel, and E. L. Lindman, "Theoretical Derivation of Laser Induced Plasma Profiles," Phys. Fluids **20**, 51 (1977).

8. C. E. Max and C. F. McKee, "Effects of Flow on Density Profiles in Laser Irradiated Plasmas," Phys. Rev. Lett. **39**, 1336 (1977).

9. K. A. Brueckner and R. J. Janda, "Radiation Produced Forces in Laser-heated Plasmas," Nucl. Fusion **17**, 452 (1977).

10. J. Virmont, R. Pellat, and A. Mora, "Density Profile Modification by Light Pressure in Spherical Geometry," Phys. Fluids 21, 567 (1978).

11. R. Fedosejev, M. D. J. Burgess, G. D. Enright, and M. C. Richardson, "Supercritical Density Profiles of CO_2 Laser Irradiated Microballoons," Phys. Rev. Lett. (to be published).

12. K. Lee, D. W. Forslund, J. M. Kindel, and E. L. Lindman, "Vacuum Insulation as a Way to Stop Hot Electrons," Nucl. Fusion (to be published).

13. J. Lindhard, M. Scharff, and H. E. Schiott, "Range Concepts and Heavy Ion Ranges," Kg. Danske Videnskab. Selskab. Mat. fys. Medd. 33, 1 (1963); J. Lindhard and M. Scharff, "Energy Dissipation by Ions in the keV Region," Phys. Rev. 124, 128 (1961).

14. See, for example, U. Fano, "Penetration of Protons, Alpha Particles, and Mesons," Ann. Rev. Nucl. Sci. 13, 1 (1963).

15. L. C. Northcliffe and R. F. Schilling, "Range and Stopping Power Tables for Heavy Ions," Nucl. Data Tables A7, 233 (1970).

16. S. T. Butler and M. J. Buckingham, "Energy Loss of a Fast Ion in a Plasma," Phys. Rev. 126, 1 (1962).

VII. LASER FUSION TARGET FABRICATION

(R. Jay Fries)

Our target fabrication effort, supported by extensive theoretical investigations, supplies thermonuclear fuel containing pellets for laser driven compression and heating experiments. These targets, which range from simple, deuterated, flat plastic films to complex multilayered structures containing cryogenic, solid DT fuel, are optimized for use with high power CO_2 lasers. After a target has been designed, we develop the technologies to produce the materials, shapes, and properties desired. We fill the target with thermonuclear DT fuel, assemble the necessary parts, and develop methods to measure and characterize all these properties. Finally, we insert the target in the target chamber and position it at the exact laser focal spot.

INTRODUCTION (N. R. Borch, F. H. Farnum, R. J. Fries)

Our target fabrication effort has two objectives:

(1) We supply targets of current design to satisfy the needs of the experimental program. Targets of various designs are used: thermonuclear compression targets for main sequence experiments, partial and modified compression targets for target essential experiments, a wide variety of targets for supporting physics experiments, and several types of targets for military applications experiments. All are irradiated in our laser systems.

(2) We develop techniques necessary for the fabrication of future thermonuclear compression targets envisaged in the Inertial Fusion Program Plan. Because these target designs are not fixed, we must continue to investigate all materials that have a high probability of being used in the final designs. We also develop methods to measure and characterize these materials and to assemble them into required configurations.

In addition, we provide micromachining, microassembly, and materials fabrication services to other groups.

A recent design for the Polaris multishell laser fusion target is shown in Fig. VII.1. Laser fusion targets have evolved gradually to this stage. Initial targets, called Sirius, were simply GMBs filled with DT gas at pressures of up to 30 atm. In Sirius, this single shell acts as an exploding pusher in which the preheated fuel is compressed and further heated. Although these designs cannot lead to high gains, they do produce thermonuclear reactions and neutrons. Adiabatic, or ablation driven, compression is obtained by adding a 50 μm thick layer of plastic, which is vaporized by the laser pulse causing the glass shell to implode hydrodynamically. Such a design was used in attaining our 20 times liquid density milestone. By coating the GMB with molybdenum or other high Z metal before plastic deposition we reduce preheat, and thus, more nearly approach the desired adiabatic compression.

In our Polaris target, the high Z metal coating will be added as a hot electron shield for the fuel, the ablator layer will be changed to low density plastic foam to provide a hydrodynamic cushion, and a second pusher layer will be added outside the foam.

In our high-performance targets, such as Polaris, the fuel will be frozen as a solid layer of DT ice onto the inside surface of the innermost pusher shell. Calculations show that this cryogenic modification will improve the yield substantially. We are developing techniques to freeze such layers in place within the Helios target chamber.

For these and other targets of recent design, we are developing high Z metal shells with diameter and wall-thickness uniformity deviations of not more than 1% and a surface smoothness tolerance of $\lesssim$ 1000 Å, as well as low-density, small-cell plastic foams, thick layers of plastic loaded with metals of low or high Z, and smooth metal layers of moderate or low Z. In addition, we are developing methods to prepare alternative fuels that are solid at room temperature, which contain fuel

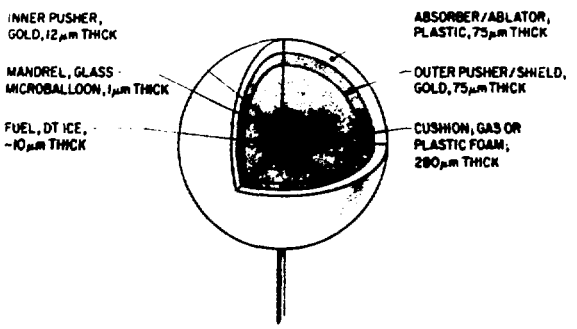

Fig. VII I.
Polaris Prime, a multilayer, multishell laser fusion target designed for Antares and Helios.

atoms at high density (for example, polyethylene, lithium hydride, or ammonia borane, in all of which the hydrogen is replaced by an equimolar mixture of deuterium and tritium). Even though the nonfuel atoms in these compounds dilute the nuclear fuel and reduce target performance, the fact that these materials are solid at room temperature may be an advantage, especially in designs that require fuel containing layers in the outer parts of the target.

Because any target must be characterized completely to understand its performance, we have devoted much of our effort to measuring and documenting all targets we deliver and to developing new, automated high resolution methods of characterizing target parts. We are developing a surface acoustic wave resonator driver to sort batches of target shells for diameter and wall uniformity using the efficiency (Q value) and frequency at which the shells bounce as an indicator of quality. We are also automating our x ray microradiographic method for observing defects and nonuniformities in opaque shells, as well as improving the capabilities of the method. Finally, we are developing techniques for nondestructively determining the composition and pressure of the fill gases inside GMBs.

TARGET FABRICATION

General

Our primary assignment is assembly, delivery, and postshot analysis of targets for our three operating laser systems. We make whatever effort is required to meet delivery requests from experimenters on these systems. In addition, we try to maintain a large and very flexible inventory of materials and techniques so that we can respond rapidly to changes in target design or specifications. As part of target assembly, we also mount and align the targets on the appropriate target-changing mechanism to eliminate any further position adjustment in the target chamber. If desired, we photograph and analyze any remnants to supplement target diagnostics.

The process of target fabrication typically includes the following steps. A GMB is chosen with the desired diameter, wall thickness, and gas permeation characteristics. High quality GMBs are now available from KMS Fusion, Inc. Suitable GMBs are optically preselected with an interference microscope and then filled with DT or DT:Ne gas mixtures by permeation through the wall at elevated temperature and pressure. The filled GMBs are cleaned in ethanol and examined carefully with an interference microscope. Targets passing optical inspection are examined and measured in three planes. Coatings of metal and or plastic are then applied and examined in three views by x ray microradiography to determine coating smoothness and uniformity, often after each successive layer has been applied. Some targets for laser fusion experiments, such as the Polaris (Fig. VII 1), require additional shells of plastic, plastic foam, or various metals. These shells are fabricated by coating suitable spherical mandrels with the desired materials, cutting the coating in half with a laser knife and then leaching out the mandrel. These shells are assembled around the coated GMB core to complete the target. We then mount the targets for use in one of our laser systems.

Fabrication Activity (S. Butler, B. Cranfill)

We supplied nearly 1000 targets to our three operating lasers and made nearly 300 other parts for diagnostic services. We supplied 230 targets for main sequence experiments, 317 for target essential and supporting physics experiments, and 439 for military applications experiments.

Gas Filling and Analysis of Laser Fusion Targets

General. To understand the performance of GMB laser targets we must be able to measure the gas fill with a high degree of accuracy. Also important are the permeation rates of deuterium and tritium through thin

layers (shells) of a variety of coating materials at various temperatures. This information will enable us to select the conditions under which a given target type should be filled. Permeation data at room temperature and below will also be important in selecting the best storage temperature for targets filled with the desired quantity of the gas.

Glow Discharge Analysis (W. L. Bongianni). Current laser fusion x-ray diagnostic experiments require the filling of GMBs with gases or gas mixtures other than D-T. Our current analytic techniques require either a radioactive gas or a destructive test to determine the composition and quantity of gases present in a GMB. A new technique, glow discharge analysis (GDA), has been developed during this period. This technique permits nondestructive determination of the composition and pressure of the gas inside a GMB for many gas fills.

Figure VII-2 shows a schematic of the experimental arrangement used in GDA analysis for gas content of laser targets. The input consists of an rf source of 20 to 200 kHz and several kilovolts peak to peak. An ultraviolet light source is used to increase the secondary electron emission from the GMB. Instrumentation required for the analysis includes an oscilloscope to monitor the voltage waveform across the GMB, a current bridge to monitor the current waveform, and an optical spectrum analyzer to monitor the characteristic spectrum of the glow discharge.

Identity of the gases, as well as impurities introduced by the blowing agent, can be identified from the spectrogram. Gas pressure is determined from the breakdown voltage as shown in Fig. VII-3, which is a plot of the breakdown voltage in neon-filled GMBs as a function of the pressure. Pressure was determined from the size of bubbles formed when the GMBs were subsequently broken under water. The theoretical (solid) curve was

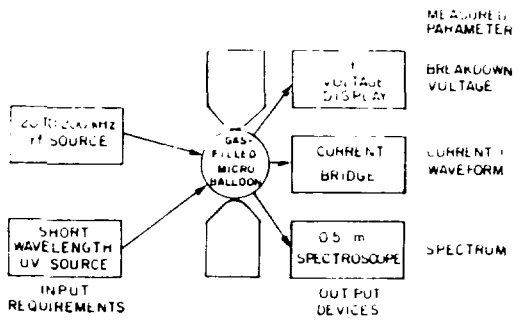

Fig. VII-2.
Experimental setup for glow discharge analysis of gases in GMBs.

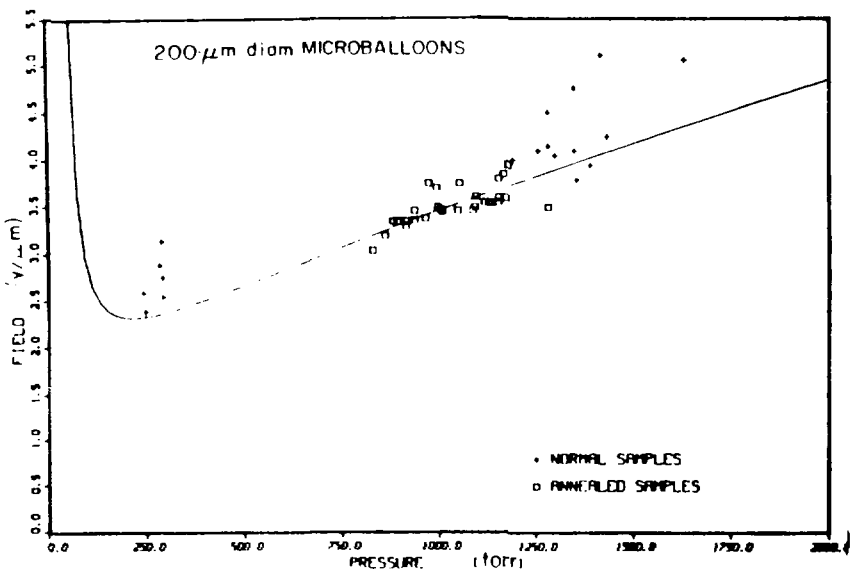

Fig. VII-3.
Calibration curve for glow-discharge analysis for neon in 200-μm-diam GMBs. Annealed samples have reduced scatter in the data due to apparent removal of impurities from residual gases in as-formed GMBs.

drawn by using the well known Townsend first ionization coefficient for neon. The 8% deviation from theoretical was well within the accuracy of the pressure measurement. The uncertainty in the breakdown measurement is estimated to be ± 1.5%. The deviation from theoretical for the unannealed samples is due to impurities associated with the glass-blowing agent, which apparently can be eliminated by annealing GMBs.

The usefulness of the GDA technique was demonstrated in a recent experimental run. Hydrogen sulfide (H_2S) was placed in targets by the drill, fill, and plug technique. Of 13 targets submitted to GDA, two were empty of H_2S, four leaked at various rates, and seven had no measurable leakage over 24-h period. Only these last targets could be shot with any confidence in their contents and pressure. The method is simple, inexpensive, and very fast; it could be easily adapted to allow a final pressure check just before insertion into the target chamber.

Quantitative Gas and Chemical Analysis via Laser Raman Spectroscopy (J. E. Barefield, II, V. Cottles). A new nondestructive, quantitative method of determining the gas content in GMBs based on laser Raman spectroscopy is being developed. This method can also be used to determine quantitatively the amount of dissolved gas in the walls of a GMB,[1] and for identification of the chemical content of surfaces (for example, glass, metal, polymer coatings).[2]

In general, a laser Raman apparatus consists of an excitation source (for example, laser, flash lamp) and a chamber designed to collect the light scattered by the sample. The underlying principle of the method is that the light scattered by a sample contains all the information necessary to quantitatively identify the chemical structure of the sample and its amount. A block diagram of the laser Raman apparatus, which has been designed and built, is shown in Fig. VII-4. The excitation source in our case is an argon ion laser. The scattering chamber comprises a set of laser focusing optics, a sample, a set of scattered-light collection optics, a spectrograph, and a photomultiplier tube (PMT) that measures the intensity of the scattered light at each frequency. The control unit generates and records the intensity vs frequency distribution (spectrum) of the scattered light.

Preliminary experiments designed to test the feasibility of this nondestructive method of gas analysis in GMBs have been completed. In this set of experiments, a Cary-82 laser Raman Spectrometer (a commercial unit) was used to record the spectrum of D_2, DT, and T_2 from single GMBs 300 μm in diameter, at 9 and 27 atm. An example of the spectrum obtained for DT appears in Fig. VII-5.

The method is based on the fact that the integrated intensity of the spectrum increases with pressure. Calibration curves of pressure as a function of integrated intensity will be developed for each size of GMB and each gas mixture of interest. Analysis for pressure will

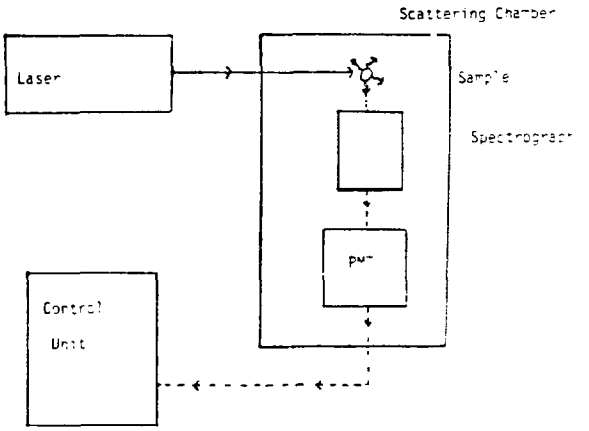

Fig. VII-4.
Laser Raman spectrometer.

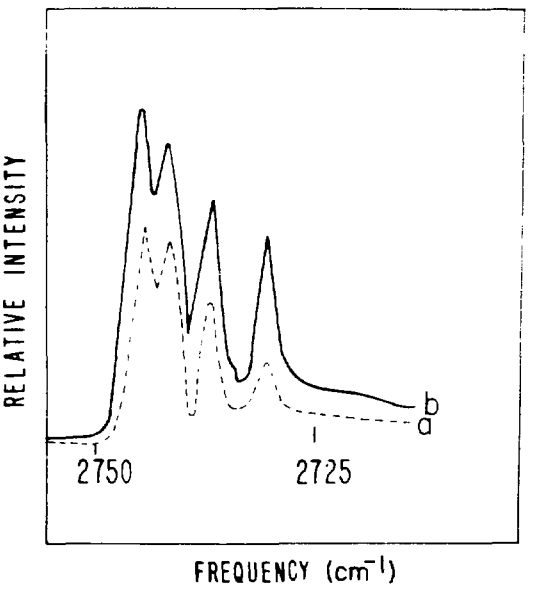

Fig. VII-5.
Raman spectrum of the Q-branch of DT at (a) 9 atm and (b) 27 atm.

then become a rather routine procedure of measuring and integrating the spectrum and comparing it to the calibration curves.

Characterization of Laser Fusion Targets

Buckling Failure of Large-Aspect-Ratio GMBs at Elevated Temperatures (J. V. Milewski). It is important to know the strength of GMBs used for targets. We need this information for quality control, to determine design limitations, and for filling requirements.

Previously we described the mechanical tensile testing and room-temperature buckling testing of GMBs.[3,4] Since then we have redesigned the apparatus for buckling testing at elevated temperatures; Fig. VII-6 shows the modified sample holder. In operation, a fully characterized microshell is placed in a small depression near the end of the 15.7-mm (0.062-in.) -diam brass rod. The brass rod is inserted into the close-fitting, thick-walled quartz tube and positioned so that the sphere is near the center of a 2.54-cm (1-in.) -long heated area of the quartz tubing. A thermocouple is placed in contact with the brass rod to record the temperature in the center of the heated zone within the quartz tubing. Once the test temperature is reached, argon gas pressure in the system is increased gradually until the sphere, observed through a binocular microscope, is seen to fail. The hexagonal data points in Fig. VII-7 and all the data in Fig. VII-8 were obtained by this procedure, which has been found to be simple, reliable, and reproducible. Note the good agreement of the crushing data obtained with argon gas at room temperature and the previously reported data obtained with mineral oil as the hydraulic fluid, as seen in Fig. VII-7.

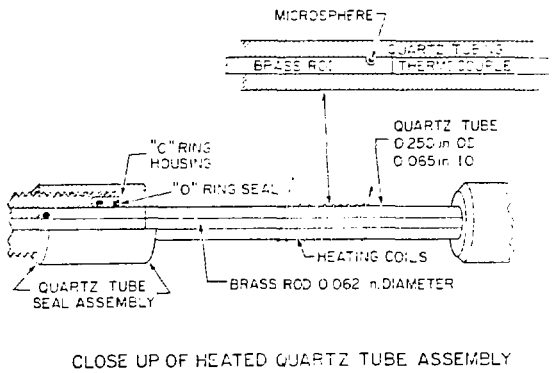

Fig. VII-6.
Modified sample holder for buckling testing of GMBs at elevated temperature.

The data recorded at elevated temperature show a much higher-than-expected strength retention (80% of room-temperature properties) at 673 K for a soda-lime glass composition. Also, in the aspect-ratio (diameter-to-thickness) range of 560 to 580, a strength retention of 30 and 15%, respectively, was recorded at 773 and 873 K for the same glass composition.

These data are significant because at 673 K, which is a normal filling temperature for this glass composition, very little strength loss is recorded. However, these tests were run in short time intervals of a few minutes, whereas the filling time generally runs from days to weeks. It is, therefore, important to also determine the long-term effects on the strength of shells under sustained pressure at elevated temperatures. The apparatus is being reworked and instrumented for this task.

Another test that we will be able to run on this apparatus will be the burst test of internally pressurized GMBs. This will be performed by filling a GMB to a calculated pressure exceeding the burst pressure and then observing the shell while the supporting background pressure is released. The tensile strength of the GMB is directly related to the difference between the internal pressure and the background pressure at failure.

It will be important to correlate the tensile strength of GMBs obtained by the above technique with earlier tensile data we obtained for GMBs by the potting and pulling technique. If a good correlation exists, the potting and pulling tensile test can be used for quality control of GMBs because this type of testing takes only minutes, whereas the internal pressurization test requires many days.

Microradiography of Laser Fusion Targets (D. Stupin). Microradiography is used to measure the wall thickness and wall-thickness nonuniformity of opaque microballoons and coatings, although this technique may also be used for transparent materials.

Whitman[5] has shown that we can detect wall-thickness variations as small as 100 Å in a 1-μm-thick GMB 120 μm in diameter if the variations are due to a Type I defect, i.e., to the nonconcentricity of spherical inner and outer surfaces. Microradiography is 2.5 times more sensitive than our previous attempts, and this increase in sensitivity is due to using a one-dimensional fast-Fourier transform in the computation

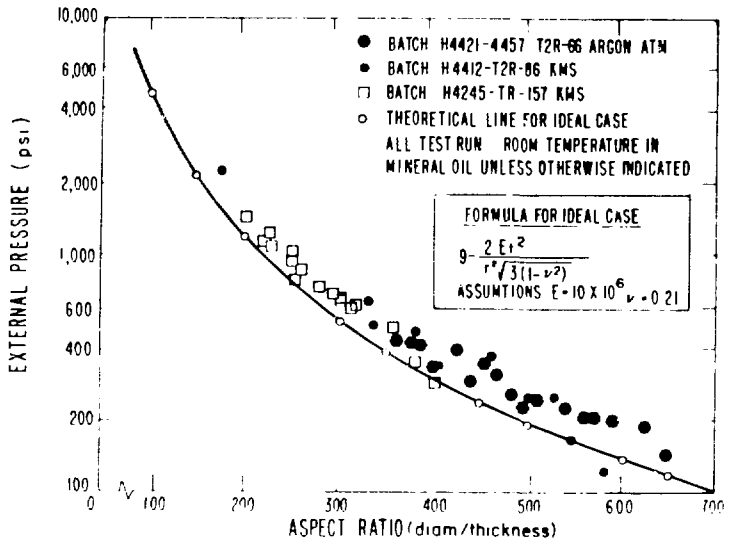

Fig. VII 7.

Buckling failure data for GMBs tested in argon and in mineral oil at room temperature. The change in testing medium has no effect on the buckling failure of GMBs.

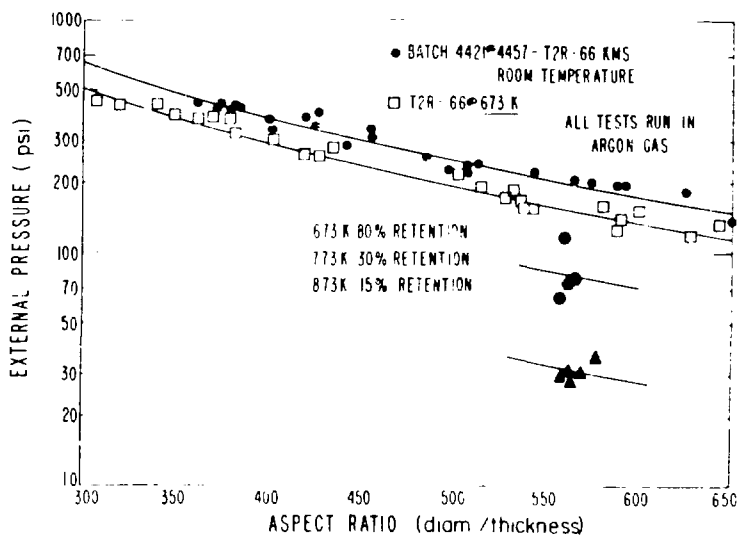

Fig. VII-8.

Buckling failure data for GMBs at various temperatures. These data are only for short times at elevated temperature.

rather than the "difference in density" method reported previously.[5]

Our ability to detect small Type III defects such as warts and dimples is also improved because we are using a bilinear interpolation algorithm to transform the data from Cartesian coordinates to polar coordinates instead of the method we used previously. We can now detect a 0.05-μm variation in the wall thickness over a 5.6- by 5.6-μm, or larger, area in a 120-μm-diam GMB with 1-μm walls. The probability for detecting this defect is 99% or greater. Figure VII-9 plots the minimum defect area that can be detected at a 99% confidence level as a

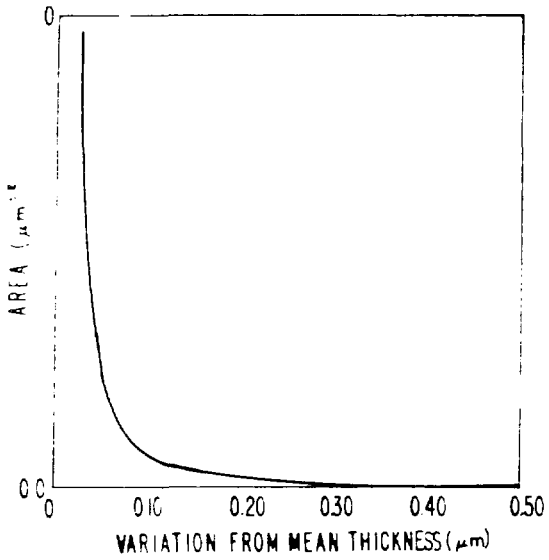

Fig. VII-9.
Defect detection boundary for small defects (such as warts and dimples) in 1 μm thick GMB walls. The curve represents the 99% confidence level to find a defect of a given area as a function of wall thickness.

function of the thickness of the defect, which is expressed as an average variation from the 1 μm GMB wall thickness.

A monochromatic x-ray source and a radiographic analysis system are being developed to increase our throughput for microradiography with the above sensitivities for Type I and Type III defects. The new x-ray source will focus 75 mA of 2 keV electrons into a 0.4 mm spot. This is nine times brighter than design specifications, and it will allow us to radiograph microballoons in 15 to 20 min, which is 10 to 20 times faster than with our older monochromatic source. Preliminary measurements show that about 90% of the x-ray photons are from the copper L_α line.

The radiographic analysis system utilizes a Data General Eclipse S230 computer. It has been interfaced to x-y stages, and the early version of the analysis code has been modified and run on this machine. Only the television camera needs to be interfaced to the computer to complete the analysis system.

Nondestructive Examination of the Inside Surfaces of GMBs (D. Stupin). To completely characterize a GMB used as a laser target, it may be necessary to examine its inside surface nondestructively. We have recently shown that high-voltage electron microscopy (HVEM) operating in the transmission mode can be used for this examination. Figure VII-10 is a photomicrograph of the inside surface of a GMB taken with a 1-MeV HVEM with the electrons passing through its walls and focused on the inside surface. We have not yet analyzed the data, but are developing a method that will facilitate a direct comparison of the same area of the inside surface of a GMB examined by HVEM in both the reflected and transmitted modes.

Laser Micromachining (E. Farnum, J. Feuerherd, K. Moore)

We have purchased and installed a pulsed dye laser for drilling holes and cutting small parts. The laser, which is capable of firing at a rate of 25 Hz is focused by a microscope onto a computer-controlled table. This table, which can be positioned within 1 μm, presently moves along two axes in a plane normal to the focus direction of the microscope. The table can be controlled with a microprocessor or with a PDP 1103 computer/microprocessor combination. A schematic of the apparatus is shown in Fig. VII-11. The laser output is a Gaussian beam with 15 mJ of energy in a pulse length of 200 ns. Because beam divergence is < 1 mrad, we should be able to achieve focal spots less than 1 μm in diameter.

Operating the laser at a wavelength of ~480 nm, we have drilled holes, scribed, and cut several types of materials. We have drilled holes less than 1.0 μm in diameter in GMBs either at the top of the GMB or, by focusing through the sphere, at the bottom. A typical hole, drilled in a 300-μm-diam GMB, is shown in Fig. VII-12. The hole size can be varied in diameter from 1 to 10 μm by varying the laser energy. In addition, we have scribed various geometric figures less than 150 μm in overall size on the surface of 500-μm-diam gold-coated microspheres for alignment experiments. Although the PDP-1103 computer is not fully operational, we have

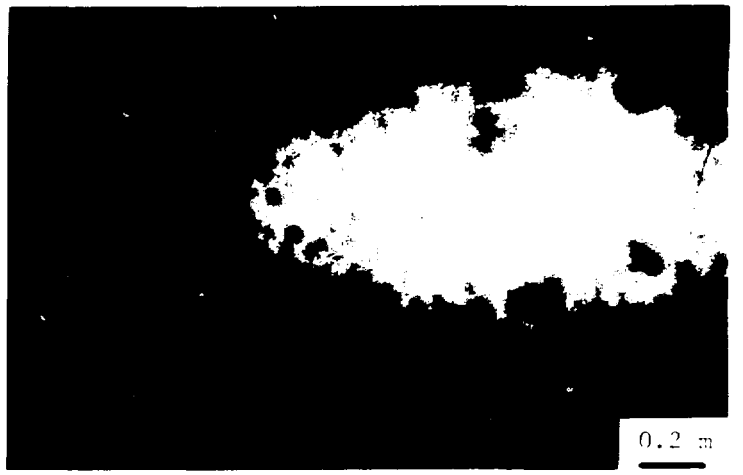

Fig. VII-10.
High voltage transmission electron micrograph of the inside surface of a GMB. Details have not yet been analyzed.

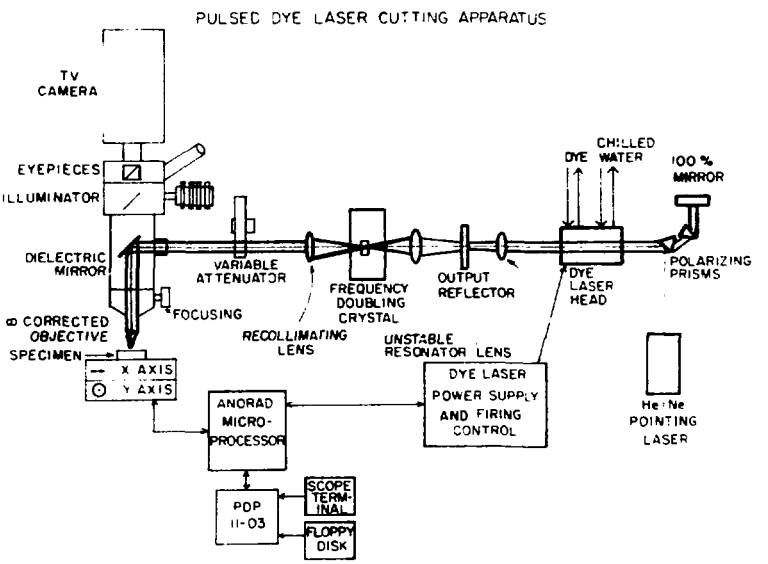

Fig. VII-11.
Pulsed dye-laser apparatus used for drilling holes in GMBs and cutting and scraping of laser targets.

Fig. VII 12.
Scanning electron micrograph of a dye laser drilled hole in a GMB. Hole is 1.25 μm diam, and was drilled from inside by focusing laser beam through opposite wall.

driven the stage in simple rectilinear directions and have simultaneously controlled laser firing with the computer. An example of this type of scribing is shown in Fig. VII 13.

X Ray Diagnostic Targets (S. Butler, B. Cranfill, M. Calcote, J. Feuerherd)

A developmental effort has been started to produce GMB targets filled with gases that do not permeate through their walls. The immediate use for these targets is as an x ray diagnostic. However, once we have the capability to produce such GMBs, we expect they will be requested also for other experiments and diagnostics.

We are working toward fabrication of several types of diagnostic targets:

(1) targets containing up to 2 atm of either pure argon or another gas containing an element with atomic number between silicon and argon;

(2) higher pressure D_2/seed-gas targets in which the seed gas is one of those used for targets of item (1), present at a few percent concentration; and

(3) DT/seed-gas targets.

The seed gases so far requested are Cl_2, PH_3, and H_2S or SO_2. Total pressures up to 60 atm are desired.

The technique we have used to make these targets is called the drill, fill, and plug (DFP) technique. We laser drill a hole in the GMB and plug the hole while the GMB is in an atmosphere of the desired gas composition and density. For experiments reported here most of the holes have been drilled with a dye laser and are ~3 μm in

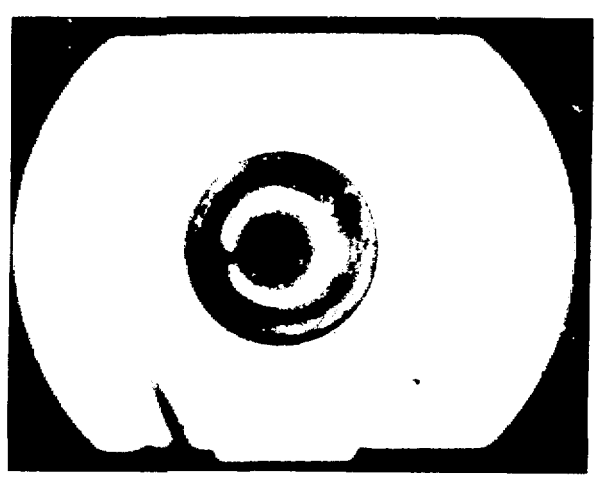

Fig. VII 13.
Laser scribed reference mark on 500 μm-diam gold-coated GMB. (30X).

diameter. Smaller holes can be drilled, but at present, larger holes are used to facilitate subsequent operations. In some cases, holes as large as ~10 μm in diameter, drilled with a ruby laser, have been used.

The first method to plug the GMBs used a "hot-melt" adhesive, either vinyl acetate or Amscomelt 340, both of which flow when heated to ~363 K. A small piece of this material is placed over the hole and the GMB is placed into a pressure vessel equipped with Lexan viewing port, heater coil, and feedthroughs for heater leads. The apparatus is evacuated and then back-filled to the desired gas density and composition. Current is applied to the heater until the adhesive begins to melt while being viewed through a microscope.

Targets with up to 1.0 atm argon and with a mixture of 20 atm D_2/0.5 atm Ar were produced by this method and delivered for laser experiments. Inspection of these targets by mass spectrometry or by breaking them under glycerin indicated that, in spite of the local heating required to melt the sealant, the GMBs were initially filled to the desired gas density. However, they had significant leak rates. Half lives for their gas fills varied widely, from a few hours to a few days.

The second method used to fabricate these targets is to plug the hole with an epoxy. We have used Epon 828 DETA filled to 35% by weight with submicron SiC whiskers. This epoxy cures in spite of the presence of reactive gases such as H_2S, and the filler gives it a workable consistency. In this case, a dab of the epoxy is applied to the hole and the GMB is loaded into a pressure vessel, which is evacuated and then back filled. The entire vessel is placed in an oven at 323 K for an overnight cure (12 to 16 h). Data on the leak rate of D_2 from two batches of GMBs plugged by this method are shown in Tables VII-I and II. Those listed in Table VII-I were treated with a silating agent (3-aminopropyl triethyoxy-silane) to prepare the surface for better bonding to the epoxy; those in Table VII-II were not treated. In both cases the nominal fill was 17 atm of D_2. The apparent wall-thickness increase after filling, as measured interferometrically, was used to measure the gas pressure inside the GMB.

The leak rate is much slower than that of the target plugged with a hot-melt adhesive, but it also varies widely among this set. No significant difference is seen between the treated and untreated GMBs; however, they were treated before the laser-drilling operation, and the perimeter of the hole may, in effect, have been untreated in both cases. The initial yield from the two runs was 84%, but several microballoons (for example GMBs 6 and 7 in Table VII-I) were underfilled. Holding the GMBs under vacuum has no effect on the gas pressure or leak rate.

With the epoxy seal we can produce targets that have a slow leak rate for D_2. Qualitative experiments indicate such targets are also quite slow for argon. We have not yet attempted to experimentally control such parameters as hole size or amount of epoxy applied. In the cases cited above, the hole was generally several microns in diameter, and the final epoxy plug was about 5 μm high by 15 μm in diameter.

Experiments using Epon 828 DETA or Epon 828/Catalyst Z to plug GMBs filled with more reactive gases (H_2S, Cl_2) indicated that a seal is formed that is highly permeable or reactive to these gases but relatively impermeable to air. These GMBs, nominally filled to 2 atm of a reactive gas, were later found to contain less than 0.5 atm of the gas.

At present, we are producing DT argon targets and seeking an organic or inorganic sealant suitable for use with more reactive gases. In addition, we are working with other projects to develop methods of nondestructive measurement of the low pressure gas content.

INORGANIC COATINGS DEVELOPMENT

General

Future targets will require shells of metals or plastic. To enhance our ability to respond to design requirements as they occur, we are developing a variety of methods for applying various metal coatings to several classes of substrates. The substrates of interest are GMBs and Solacels, and the coating techniques include electro- and electroless plating, chemical vapor deposition (CVD), physical vapor deposition (PVD), and sputter deposition. We again focused our attention on high quality coatings and on the recovery of a small number (10 to 100) of preselected GMBs specifically in support of the 20 times liquid density targets and the radiochemical diagnostic test targets.

Electroplating (A. Mayer, S. Armstrong)

In support of the 20 times liquid density target, a process has been developed for electroplating copper onto 300 μm diam Solacels using the standard apparatus for bulk electroplating of discrete microparticles. The

TABLE VII-I

RELATIVE PRESSURE LOSS IN DFP GMBs
INITIALLY FILLED TO 17 atm D_2 (TREATED GMBs)

	Time (Days)							Half-Life (Days)
GMB	0	0.3	1	4	7	11	27	
1	1.10	1.10	1.00	[a]			...	
2	1.00	1.04	1.00	0.96	0.92	0.76	0.50	26
3	0.98	0.94	0.98	0.98	0.80	0.84	0.72	49
4	0.04					...	...	
5	1.00	0.94	0.90	0.78	0.50	0.32	0.18	10
6	0.54	0.46	0.54	[b]		...	...	...
7	0.76	0.66	0.72	0.62	0.62	0.44	0.36	23
8	1.12	1.04	1.12	0.94	0.94	0.86	0.76	44
9	1.12	1.04	1.12	1.12	1.04	0.94	0.76	46
10	0.94	0.86	0.94	[c]		...	...	...

[a] No loss after 2 h 20 min in vacuum.
[b] Broken under glycerin 17.9 atm.
[c] Broken under glycerin 8.5 atm.
[d] Broken under glycerin 15.8 atm.

TABLE VII-II

RELATIVE D_2 PRESSURE LOSS IN DFP GMBs
INITIALLY FILLED TO 17 atm D_2 (UNTREATED GMBs)

	Time (Days)						Half-Life (Days)
GMB	0	0.2	1	2	7	23	
11	−0.32	...	...	...	...	...	...
12	−0.06	...	...	...	...	...	...
13	1.00	0.86	0.96	0.96	0.90	0.78	56
14	0.98	0.90	0.80	0.76	0.80	0.54	28
15	0.68	0.64	0.60	0.68	0.64	0.46	39
16	0.90	0.82	0.82	0.86	0.86	0.68	55
17	0.94	0.98	0.90	0.90	0.66	0.26	12
18	0.92	0.92	0.92	0.86	0.96	0.74	55
19	0.90	0.90	0.82	0.90	0.68	0.32	15

Solacels must first be immersion-plated with gold to protect the Solacel wall from chemical attack during the initial stages of plating. The immersion plate also enhances the adhesion between the copper and the Solacel.

Lead-plated Solacels also show promise as the pusher for the target. A standard lead fluoroborate electrolyte, again in the standard bulk-plating apparatus, produced very poor thickness uniformity and surface finishes, which were attributed to poor throwing power. A new bath, designed to produce higher throwing power, was prepared. The new bath had excellent throwing power, as shown by improved thickness uniformity. Unfortunately, the new bath was a low-metal/high-acid solution that was so corrosive to Solacels that a satisfactory plate could not be achieved. Lead-plating Solacels by the bulk plating process does not appear to be practical. It may be feasible for a stalk-mounted Solacel, and this possibility will be explored.

The first rad-chem target is to be a 300 μm-diam GMB mounted on a stalk, flashed with ~0.5 μm of copper by physical vapor deposition, and electroplated with 3 μm of copper that has been doped with ^{67}Cu. The final layer will be 30 μm of parylene. We have developed an electroplating technique that, we feel, will provide a satisfactory copper coating on the target and its stalk. A high-throwing-power copper-sulfate plating bath incorporating a proprietary brightener was prepared, and a special constant-current power supply was built for this purpose. We have found that proper rotation of the target substrate in the plating bath throughout the deposition results in uniformities of ~ ±5% (Fig. VII-14).

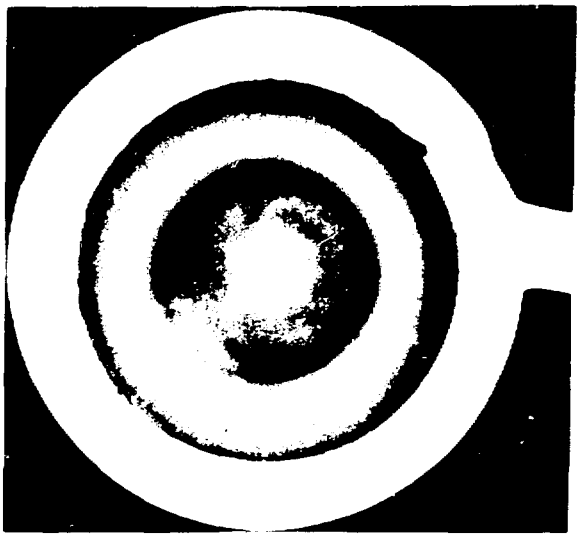

Fig. VII-14.
Stalk mounted copper electroplated GMB. Copper is 50 ± 2.5 μm thick. Note that defect in substrate leads to defect in copper coating. (175X)

Electroless-Plating (A. Mayer)

Reproducibly coating GMBs has been, in general, much more difficult than coating Solacels. The GMBs seem to be much more difficult to manipulate during the coating process. Two processes have been used to metallize and electroless-plate small quantities of preselected GMBs. The first process attempted was metallizing the GMBs with chemically vapor-deposited (CVD) nickel followed by electroless-plating. This process was not successful because the GMBs tended to crack during the plating process. The second approach involved a wet metallization process that has been quite successful.

Two other CVD metallization processes were also investigated. In the first case, 300-μm-diam KMS Fusion, Inc. GMBs were coated with 0.5 μm Mo_2C, sensitized in $SnCl_2$, activated in $PdCl_2$, and plated with 5 μm of electroless nickel. No broken parts were found, and recovery was excellent. There were some rough spots on the surface due to incomplete activation of the Mo_2C surface. The next CVD metallization process involved the CVD Mo_2C flash, but replaced the wet activation step with a flash of CVD nickel. About 50 of these CVD-treated GMBs were plated with electroless nickel. The resulting deposit was uniform and the surfaces smooth, and no breakage occurred during plating. Figure VII-15 shows the surface quality. The small bumps are a result of insufficiently clean plating baths, a circumstance, we feel, that can be corrected.

Several plating runs were made in which the GMBs were sensitized and activated in dilute solutions of $SNCl_2$ and $PdCl_2$ before plating. Figure VII-16 shows the quality of the coatings obtainable by this process.

Chemical Vapor Deposition (G. Vogt, W. McCreary, D. Carroll)

In the past, we developed procedures for CVD precision Mo_2C coatings on Solacels from molybdenum carbonyl. We are now trying to adapt the procedure to coat small numbers of preselected GMBs and have had some success. To fluidize small numbers of GMBs

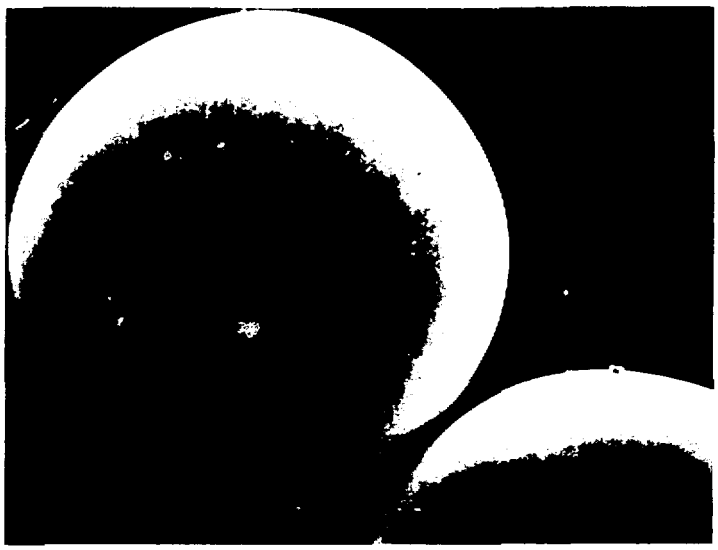

Fig. VII 15.
Electroless plated nickel on GMB, first metallized with MO-C and activated with CVD nickel. (300X).

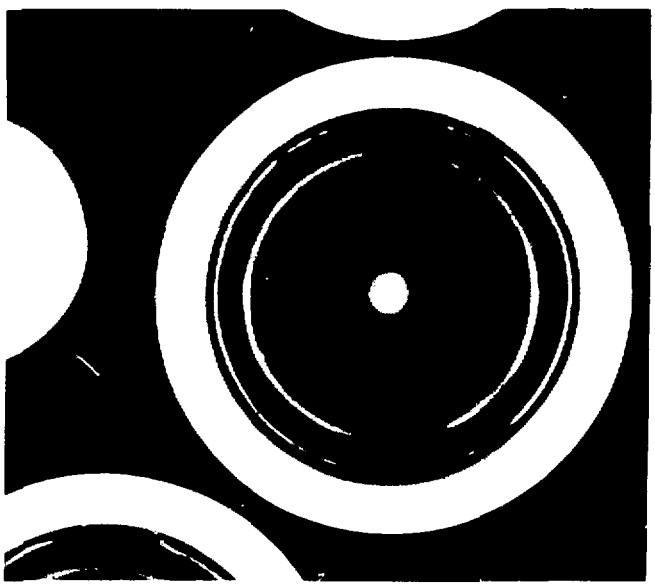

Fig. VII 16.
Electroless coated 22 μm thick nickel on GMB activated by wet chemical method. (200X).

requires the use of a carrier bed of particles consistently sized, but smaller than the particles to be coated. The carrier bed generally consists of Solacels even when GMBs are to be coated because the Solacels fluidize much better. The more buoyant GMBs ride higher in the bed, and thus are above the active coating zone. This seems to increase the number of surface nodules. Particle mixing in the bed can be improved with lower flow rates, and we intend to continue this effort.

We have been investigating CVD coatings of nickel, both to provide metallization layers onto which an electroless coating can be added and to coat to full thickness for the 20 times liquid density target. The CVD nickel coatings have been nonadherent and have had very rough surfaces, but an improved coater design has improved the process significantly. Although gas phase nucleation is still an obvious problem, we have significantly improved the coating quality. The improved coater design involves replacing the Pyrex frit diffuser plate with a plate consisting of a close packed array of tubes of uniform bore (~25 μm diam). Gas flow uniformity across the plate was increased, with the result that small batches of GMBs can be fluidized for much longer periods of time before channeling occurs. Coating parameters can now be properly controlled for longer periods of time. We will continue these experiments to further improve our CVD nickel coatings.

CVD tungsten coatings from tungsten hexafluoride have been perfected for metal substrates, such as Solacels. However, GMBs cannot be coated from the hexafluoride without first flashing them with a protective layer. Even though the CVD metal deposition from the metal carbonyl is more complicated chemically than that from the metal halide, we have begun to investigate CVD tungsten coating from the carbonyl. A thermodynamic analysis of the tungsten carbonyl system was completed to provide a first order estimate of the proper experimental conditions to obtain carbide and oxide-free tungsten coatings. We also performed several experiments to improve the thermodynamic estimates by factoring in the reaction kinetics and nonequilibrium conditions of the fluidized carrier bed.

When the conditions are adjusted to maximize the metal production, the rate of deposition is very low. Table VII III gives the coating conditions for three experiments. Although the process is too slow at present to deposit shells in a useful length of time, we have shown that we can provide a thin protective layer of tungsten from the carbonyl, which can then be over coated with tungsten from the hexafluoride at a faster rate to form the shell.

We are improving the fluidized-bed reactors to provide more precise and efficient control of the coating parameters. We are also continuing our effort to stabilize and control GMB fluidized beds.

Gas Levitation of GMBs During Sputtering (A. Lowe, C. Hosford)

Gas levitation has been a useful technique for supporting GMBs during sputtering. The technique provides a means of continuously moving a GMB during deposition without damage to the surface of the coating or the GMB and with less chance of loss of the GMB during processing. During this period, the deposition rates have been increased to 140 Å min for gold. Four GMBs are levitated simultaneously in separate dimples in a collimated hole structure, as shown in Fig. VII 17.

The apparatus for levitation sputtering has been modified to illuminate and observe the GMBs directly without mirrors. This was necessary to observe non reflective coatings such as lead. Also, the levitated GMB is now observed on a TV monitoring system.

The uniformity of gold coatings sputter deposited on gas levitated GMBs was ± 5% for a 4 μm thick coating and ± 3% for a 1 μm thick coating. The nonuniformities are determined by optical density measurements of a microradiograph. These nonuniformities are thought to be due to a preferential spin of the GMB during the coating process. To improve uniformity, the spin will either have to be controlled or eliminated.

The surface variation is no more than a few percent. However, the surface is quite granular and appears to degrade with increasing thickness. Figure VII 18 is a scanning electron micrograph of a fractured cross section of a gas levitated gold sputtered coating on a GMB. The columnar growth of the coating is clearly shown.

The surface texture of gold sputter deposited on a levitated sphere is quite different from that on a stationary sphere (Fig. VII 19). There seem to be many more nucleation sites for the levitated GMBs, which yields a finer grained deposit.

Mandrel Development (S. Butler, M. Thomas)

We are continuing our effort to produce solid microspheres suitable for use as mandrels for production of

TABLE VII-III

SUMMARY OF EXPERIMENTAL CONDITIONS FOR THREE TEST RUNS FOR $W(CO)_6$ CVD

	Experimental Runs		
	WC06-2	WC06-3	WC06-4
Bed volume (ml)[a]	~4.5	2.55 ± 0.05	2.65 ± 0.03
Bed weight (g)[a]	0.350	0.189	0.203
Vapor generator temperature (K)	314 ± 0.5	323 ± 0.5	333 ± 0.5
Vapor transport[b] rate (μg/min)	18.2	42.2	141
Max W deposited[a] (mg)	5.3	32.0	130.9
$H_2/W(CO)_6$ ratio	16 600	7100 to 17 800	1600 to 4810
$Ar/W(CO)_6$ ratio	11 500	9900	4450
Inlet pressure (torr)	150 ± 10	150 ± 10	150 ± 10
Reaction temperature (K)	595 ± 50	555 ± 40	555 ± 40
Duration of experiment (h)	9.4	24.2	29.6
Actual amount of W deposited (mg)	---	---	~102

[a]Before coating. The volume measurement was for free-fall packing.
[b]Averaged over entire run.

metal microballoons. A new droplet generator has been fabricated. New features of the apparatus include a larger volume to allow longer experiment time with each fill, better heating capacity and better insulation to allow faster heating and higher temperature capability. The apparatus is now mounted in a column exhausted to a fume hood to allow the use of a wider range of materials. The nozzle design remained unchanged: the shaker is mounted to a vertical shaft terminating with a modified Swagelok fitting that holds the orifice. The interchangeable orifices are holes electron-discharge-machined (EDM) in foils mounted on a Swagelok back ferrule.

After initial experiments with water, some drops of molten potassium thiocyanate (KSCN) were produced. This substance was chosen because it is a low-melting-point inorganic (448 to 452 K) with a small ΔV_f (<10%) and a high temperature of decomposition (773 K). However, it is too corrosive, and present plans are to continue work with $NaNO_2$ and other materials.

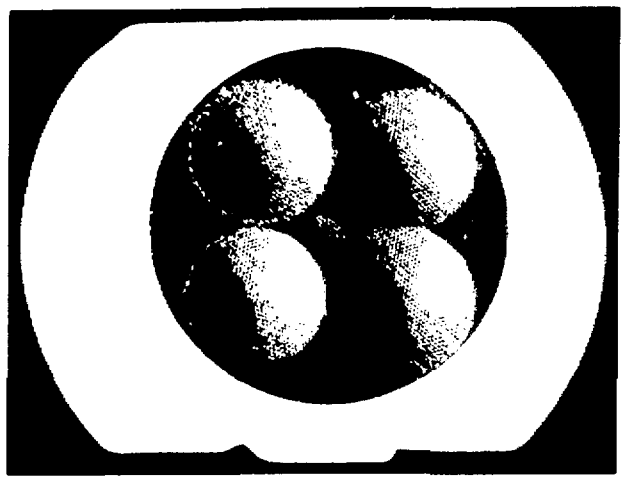

Fig. VII-17.
Collimated hole structure used to PVD coat four gas-levitated GMBs simultaneously. (8X).

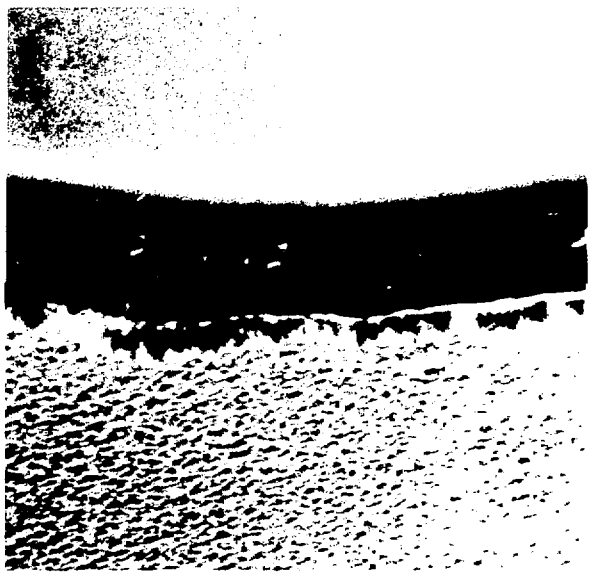

Fig. VII-18.
Scanning electron micrograph of fractured gas-levitated PVD-gold-coated GMB. Note columnar growth of gold coating. (5000X).

ORGANIC COATINGS DEVELOPMENT

General

Many of our multilayered laser fusion targets use an outer shell of low-density low-Z material as an absorber ablator layer. This layer absorbs energy from the incident laser, is heated and vaporized, and streams away from the pusher shell causing the pusher shell to implode via the rocket reaction forces. For target pellets that do not depend on the strength of this absorber/ablator to contain the fuel-gas pressure, we generally use plastic. We also provide free-standing cylindrical and spherical shells of plastic as targets and for special diagnostic measurements. These latter specimens are generally fabricated by coating appropriate mandrels, which are then dissolved in acid to leave freestanding plastic shells. We are also trying to make plastic shells by using a droplet generator. Finally, we are developing techniques for making low density small-cell-size plastic foam in the form of spherical shells that can be placed around target cores.

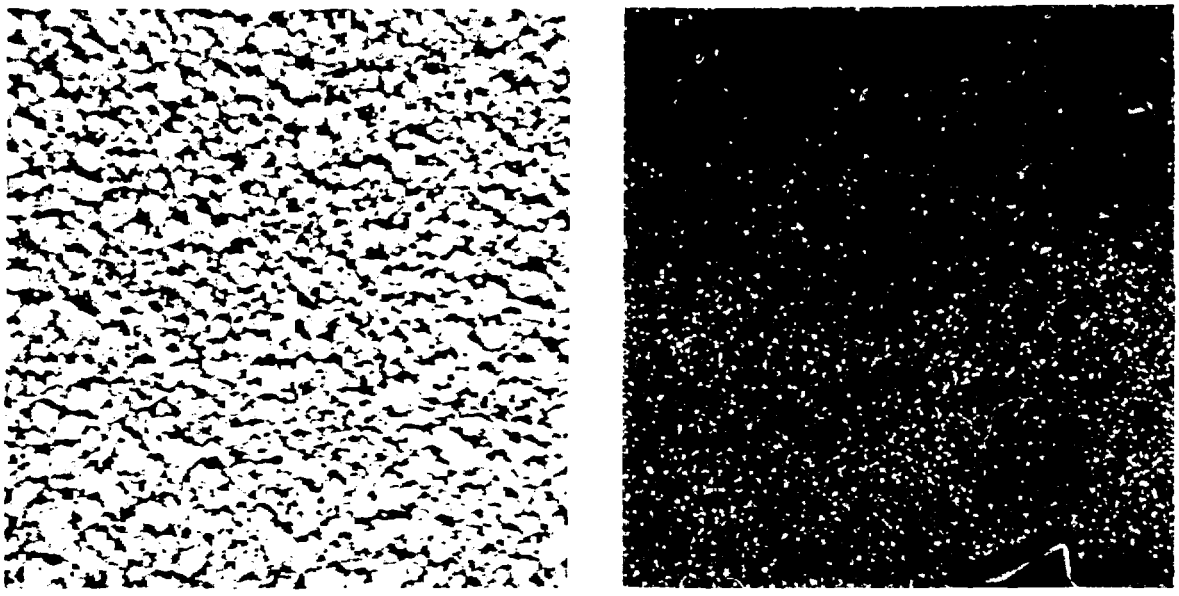

Fig. VII 19.
Scanning electron micrograph comparison of PVD gold coatings produced statically and by gas levitation on GMBs. Gas levitated PVD gold coating is much smoother. (2500X).

Gas-Phase Coatings (R. Liepins, M. Campbell, J. Clements)

General. Important requirements for coatings on laser fusion targets are sphericity and wall-thickness variations of less than 5% and surface smoothness deviations of less than ± 1 μm. We have achieved these requirements with both the low-pressure plasma (LPP) and the vapor-phase pyrolysis (VPP) processes. In addition, we can now coat a single GMB or many individually separated and characterized GMBs by LPP. We can also now deposit coatings with thicknesses exceeding 100 μm using the multiple-coatings approach. These developments represent important new capabilities. We have also made the first density determinations on the LPP poly(p-xylene) coatings and are investigating the morphology of multiple coatings.

Low Pressure Plasma Process (LPP).

Introduction. In previous work we demonstrated the ability to coat as few as eight GMBs. We have now developed techniques to coat a single GMB or many individually characterized GMBs. A study, which correlated the ionization potential of the organic species and that of the background gas with the deposition rate, was also used as basis for obtaining a multilayer coating more than 100 μm thick. We are developing a technique to provide accurate (to within 0.1 g/cm^3) density information for the plastic coatings on actual laser targets.

Coating a Single GMB and Many Individual, Characterized GMBs. The previously developed capability to coat as few as eight GMBs has been refined to allow coating either a single GMB or several individually characterized GMBs. This technique requires strict control of the thickness of the plastic precoat on the aluminum plate electrodes. We modified the bottom electrode, as shown in Fig. VII-20, to be able to keep many individually characterized GMBs separate during coating and thus to keep track of their identities.

Thick Coatings. The effects caused by the ionization potential (IP) of the background gas and the monomer, described in the last semiannual report,[4] have been investigated further and have been used to deposit thick

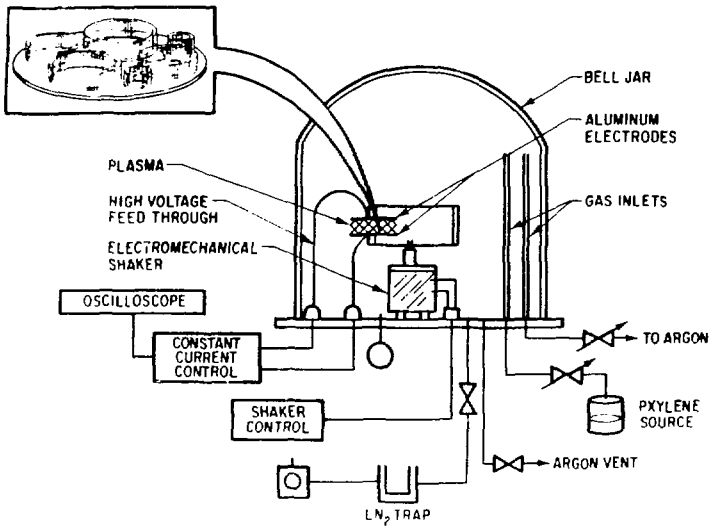

Fig. VII 20.
LPP coater with lower baseplate modified for simultaneous coating of individually characterized GMBs.

LPP coatings. For example, the effect of the back ground-gas ionization potential upon the maximum coat ing thickness obtainable in a typical run is summarized below.

Background Gas	IP(V)	Maximum Coating Thickness (m)
None	---	7
Argon	15.8	8
Krypton	13.9	10.6
Xenon	12.1	13.6

With the use of xenon as the background gas and exchange of the electrodes after each maximum coating thickness obtainable, we have deposited multiple coatings in excess of 100 μm thick.

Coating of Metallic Microballoons (MMB). Recently we have been required to coat metallic (nickel) microballoons. We found that the MMBs could not be made to bounce by themselves for any extended period of time. The solution was to mix the MMBs with GMBs and to find the appropriate shaker frequency. We can now deposit uniform 7- to 8-μm-thick coatings on MMBs.

Density of Poly(p-Xylene) Coatings. The density of a typical poly(p-xylene) coating on a GMB was determined by measuring the weight and the volume of the coating. We used eight solid glass microspheres with a glass density in the 2.19- to 2.44-g/cm^3 range for this determination. The weight was obtained on a CAHN-4700 microbalance with a 0.1-μg sensitivity, and the volume was calculated from the radiographic measurements of the uncoated and coated microspheres. The pertinent data are summarized in Table VII-IV. The densities for the eight samples ranged from 0.78 to 1.03 g/cm^3 with an average density for the eight coatings of 0.92 g/cm^3. This is a rather low density for a polymer containing aromatic units in its structure.

LPP Coating at Temperatures Above Ambient. To obtain supersmooth (< 100-Å imperfections) coating surfaces we are exploring various approaches such as coating at temperatures above ambient. Our initial work consisted of heating the lower electrode (which supports the GMBs) to 50, 75, or 110°C (323, 548, or 383 K) for about 30 min before coating. The lower electrode was then maintained at the temperature throughout the run. Deposition of the coating at 50°C showed no difference in surface smoothness from that deposited at room temperature. However, deposition at 75°C and, especially, at 110°C produced marked improvements in surface smoothness.

TABLE VII-IV

DATA ON LPP COATINGS ON SOLID GLASS MICROSPHERES

Microsphere No.	Uncoated Radius (μm)	Uncoated Weight (μg)	Coated Radius (μm)	Coated Weight (μg)	Coating Thickness (μm)	Coating Weight (μg)	Density of Coating (g/cm^3)
3	191.1	71.1	202.2	76.0	11.1	4.9	0.91
6	204.0	88.6	214.6	94.0	10.6	5.4	0.93
7	197.0	77.5	207.8	82.4	10.8	4.9	0.88
8	201.9	83.3	212.4	88.4	10.5	5.1	0.90
10	183.5	63.0	194.5	67.8	11.0	4.8	0.97
14	130.0	22.4	141.0	24.4	11.0	2.0	0.78
15	131.6	24.5	142.0	26.9	10.4	2.4	0.98
16	167.3	47.6	179.1	52.2	11.8	4.6	1.03

Morphology of Multiple-Layer Coatings. For multiple-layer coatings, in which possibilities for layer separation or delamination exist, good mechanical properties and good aging characteristics are important. To obtain better control of these properties we are investigating the morphology of the coatings and how it is affected by changes in substrate and other experimental parameters.

The coatings are fractured by compression in a micrometer at room temperature. A fracture of a 5-layer coating is illustrated in Fig. VII-21. The fracture shows that the adhesion between the first four layers was poorer than that between the fourth and the fifth layers. The work of correlating experimental parameters with adhesion characteristics between the layers is continuing.

Fracture of a multilayer coating also showed that, although all of the coating deposition parameters were nominally the same, different layers apparently had

Fig. VII-21.
Fracture of a five-layer LPP coating on a GMB exhibiting differences in adhesion between layers. (2000X).

different structures, as evidenced by differences in fracture patterns. Parameters responsible for these differences need to be investigated further because they have a direct bearing upon the mechanical strength and long-term stability of the coatings.

In the investigation of the effect of the substrate upon the surface smoothness of the coatings, major differences were observed between the LPP and VPP processes. In the LPP process, rough as well as smooth substrate surfaces give equally rough surfaces at coating thicknesses above 1 μm. Presumably, at coating thicknesses below 1 μm, the surface structure of the substrate is coated conformally. In the VPP process, rough substrates always produce coatings with rough surfaces, and smooth substrates produce coatings with smooth surfaces. Furthermore, the surface energy of the substrate appears to have no effect upon the coating surface smoothness obtainable in the LPP process. In the VPP process, high-energy surfaces (metals) lead to smooth coatings and low-energy surfaces (glass) lead to rough coatings. In addition, the coating deposition rate in the LPP process appears to have a minimal effect upon the surface smoothness obtainable. In the VPP process, high deposition rates (>1000 Å/min) produce rough surfaces, and low deposition rates (< 1000 Å/min) produce smooth surfaces.

VPP Process.

Introduction. To extend our capabilities in the preparation of thick coatings with precise control of coating thickness and surface smoothness we have developed the VPP process. In principle, the process has no coating-thickness limitation and inherently leads to a conformal coating of high surface smoothness and uniformity. The p-xylylene VPP coating possesses high mechanical strength, good thermal stability, and high resistance to most solvents and chemicals.

In previous work, we demonstrated the ability to deposit coatings on GMBs to thicknesses greater than 350 μm with surface smoothness approaching 100 nm. During this reporting period, we have concentrated on producing coatings with smooth surfaces (<10 nm) that also are transparent. We have further developed the technique of coating levitated GMBs in the VPP process and we can now levitate five GMBs at once. We have deposited coatings as thick as 19 μm on single GMBs.

Smooth, Transparent Coatings. Deposition rate has a direct effect upon the coating surface smoothness—the higher the rate the rougher the surface. By using deposition rates of less than 50 nm/min, the surface roughness decreased from ±1.0 to < ±0.05 μm, with one or two of 20 GMBs having a transparent coating. The transparent coatings always had the smoothest surfaces (< ±0.05 μm). The transparent coating formation was first noticed when we started using a small copper screen (3-cm-diam, 20-mesh) in front of the monomer exit tube to induce a more turbulent monomer flow pattern in the cold chamber. Additional experimentation with various sizes and types of screens and their locations in the chamber has revealed a way to consistently produce smooth transparent coatings in more than 90% of the GMBs coated. A typical 56 μm thick transparent coating is illustrated in Fig. VII 22. Note how clearly the glass stalk glue line to the GMB can be seen through the coated GMB.

Plastic Coatings on Levitated GMBs (with A. Lowe and C. Hosford). To coat VPP plastic on GMBs for 20-times-liquid-density targets, we must mount the GMB on an aramid fiber, apply the coating, and then machine the coated fiber off to produce a smooth, spherical target. This is a difficult, time-consuming process, which, at best, only marginally meets target specifications for sphericity and coating uniformity.

During the previous reporting period, we installed a gas levitator in our VPP cold chamber and applied a 5-μm-thick coating to a single, levitated GMB. We have extended this technique and can now gas levitate and coat five GMBs simultaneously. We have also increased the coating thickness to 19 μm and, with additional refinements in the hardware, do not foresee any problems in depositing much thicker coatings on multiple GMBs. A report detailing this technique and initial results has been written.[6]

Chemical Analysis of Plastic Films and Coatings.

Fourier Transform IR Spectroscopy of Plastic Films. Perdeuterated polyethylene (PE_D) films are used as either laser fusion diagnostic targets themselves or as components in more complex target structures. In the fabrication of PE_D films the possibility of deuterium exchange for hydrogen exists, and therefore, a quick

Fig. VII 22.
Transparent 56 μm thick p-xylylene coating on 200 μm diam GMB. Note clarity of glue line at stalk. (160X).

analytical technique for estimating the extent of deuterium exchange was of interest. We chose to develop this infrared spectroscopy technique because of its inherent simplicity and quickness. We have developed standard curves relating either CH or CD stretching vibration absorption band areas to film thickness and mole percent deuterium or hydrogen in the sample. Now, with these curves, we can run the spectrum on the unknown, measure the appropriate absorption band area and read the mole percent deuterium or hydrogen from the curves. A report has been written giving the details of this technique.

Oxygen Content of LPP Coatings. LPP coatings are extremely reactive because they have a high free radical content, and as a result, they oxidize when exposed to H_2O vapor and oxygen. Oxygen is undesirable in these coatings on laser targets. The LPP coatings are highly stressed as deposited, and the combination of stress and oxidation causes the coatings to crack and to peel off. Annealing at 50°C (323 K) was tried in an attempt to stabilize the coatings, but it only delays the cracking. An LPP coating, analyzed about one week after it was formed, had picked up 2.5 mol% oxygen from exposure to ambient air.

We reported previously[1] that extremely smooth (200 to 400 Å imperfections) LPP coatings were produced by intermittently admitting air (pulsing) to the argon background gas during coating. This technique preoxidizes the coating and may solve the cracking problem. The oxygen content of a "pulsed" coating was ~5.5 mol% after about one week exposure to ambient air.

POLYMER FOAM DEVELOPMENT

General

Low density CH foam is a highly desirable option as an implosion buffer in many target designs. This foam should have a density of ~ 0.05 g cm^3 with a very uniform small cell size (~ 1 μm).

Low Density Plastic Foams (R. Liepins)

The lower the density of the plastic the easier it should be to fabricate the low density (~0.05 g/cm^3) microfoam, regardless of the fabrication technique. The two commercially available plastics of lowest density are polyethylene (PE) and polypropylene (PP). Depending upon the crystallinity content, PE may have a density of 0.94 g cm^3, or PP, a density of 0.90 g/cm^3. Most other plastics have densities in the 1.1 to 2.3-g/cm^3 range. However, a literature survey reveals that polymers with densities below 0.90 g cm^3 have been prepared. There appears to be a direct relationship between the density of the polymer and the length and the bulk of the pendant group in the repeating unit of the polymer chain. This is

illustrated in Table VII V, which shows the crystalline densities of a series of polymers. By extrapolating this density structure relationship, we predict that the preparation of polymer structures with densities below 0.8 g cm^{-3} should not be difficult. Because of the wide applicability of this type of material in laser fusion target design, we have undertaken to synthesize such low density plastics. The initial work has involved synthesis of the monomer 5,5 dimethyl 1 hexene.

Thermally Induced Phase Separation in a Perfect Polymer Solution Approach to Foams (A. Castro, ARMAK Research Laboratory)

ARMAK has a new proprietary technique for foam generation that is based on "thermally induced phase separation" in a perfect polymer solution. They have made foams with densities as low as 0.1 g cm^{-3} and foams with average cell size as low as 1 μm. We have recently contracted with ARMAK to develop foams to our specifications.

CRYOGENIC TARGET DEVELOPMENT

General

Laser fusion targets fueled with cryogenic, liquid, or solid DT offer the advantage of high initial fuel density without the disadvantage of diluent atoms being present as they are in room temperature solids having a high hydrogen density [for example, lithium in LiD(T), carbon in $(CDT)_n$, or boron and nitrogen in NH_3BH_3]. In addition, calculations indicate that the yields from targets fueled with liquid or solid DT can be considerably higher than those from targets of the same design, but fueled with high pressure DT gas. Therefore, we are developing cryogenic targets, despite the significant experimental complications encountered in their fabrication and in their use in laser target interaction experiments. We are currently testing the prototype cryogenic processing mechanism for loading and freezing these targets in the Helios target chamber.

Helios Cryogenic Target-Producing Prototype (J. R. Miller, J. T. Murphy, C. E. Cummings, R. D. Day, J. B. Van Marter)

Further tests have been conducted on the experimental apparatus designed to produce cryogenic targets in the Helios laser system. As described previously[8] targets at room temperature will be loaded into the target chamber, processed by using the fast isothermal freezing (FIF) technique, and then uncovered through rapid retraction of the cryogenic processing shroud just before laser irradiation. We have completed tests on the cryogenic shroud retraction subsystem. We are testing a new technique for thermally isolating the target mount from room temperature, and have demonstrated that this technique also provides an adequate exchange-gas seal between the cryogenic shroud and the target mount.

The shroud retraction subsystem, designed on the basis of a suggestion from D. Musinski, KMS Fusion, Inc., relies on atmospheric pressure to rapidly collapse an evacuated, welded metal bellows. The bellows, initially magnetically latched in its extended position, collapses when the holding electromagnets are de energized. Figure VII 23 is a schematic of the test shroud retraction subsystem.

New, hydraulic shock absorbers were installed on the shroud retraction subsystem. Retractor position vs time was measured by using high speed motion pictures or multiflash stroboscopic pictures. The data are shown in Fig. VII 24. After release from the holding magnets, the retractor accelerates with ~25 g. The target begins to receive room temperature black body radiation exposure at $x = 1.5$ cm, and at $x = 4.5$ cm, the shroud is clear of the Helios laser beams and irradiation of the target can occur. Before the shroud is clear of the beams, the target is exposed to 300 K radiation for 6 to 7 ms, too short a time to perturb the uniform, solid DT layer in a typical target. The retractor velocity at contact with the shock absorber is ~6 m/s, and ~2.5 cm is available for the shock absorber to decelerate the retractor to a stop. Although the shock absorbers do not uniformly decelerate the rapidly moving shroud, this deficiency is not a problem from a mechanical fatigue or a

TABLE VII V

POLYMER STRUCTURE VS DENSITY

Structure	Density (g/cm^3)
(CH CH)	1.008
(CH CH)	
CH	0.951
CH	
(CH CH)	
CH	0.922
CH	
CH	
(CH CH)	
CH	
CH	0.908
CH	
CH	
(CH CH)	
CH	0.846
CH CH CH	
(CH CH)	
CH	0.803
CH C CH	
CH	

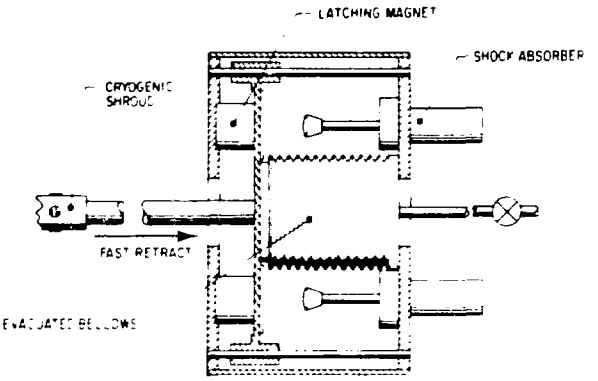

Fig. VII 23.
Cryogenic shroud retraction system.

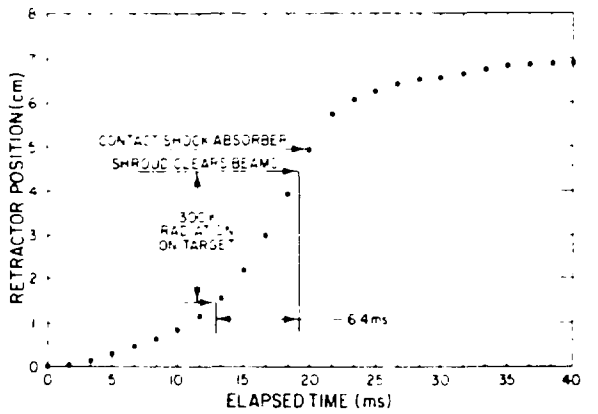

Fig. VII 24.
Cryogenic shroud retraction system performance. Cryogenic target exposed to 300 K for 6.4 ms before laser irradiation.

target chamber vibrations standpoint. Tests conducted with the retraction system attached to the Helios target chamber show that before contact with the shock absorbers is made

- the target position remains constant,
- the laser beam alignment on the target is not disturbed, and
- the laser beams reflected from the target chamber salt windows that are used for beam diagnostics are not adversely perturbed.

Minor changes in the retraction system are planned to minimize the mass and to optimize the geometry.

As currently designed, the target mount is cooled through contact with the liquid helium cooled target processing shroud. This procedure eliminates the complications introduced with independent cooling of the target mount. However, we have encountered difficulties in cooling the target mount sufficiently with this technique. In the previous configuration, the shroud could be cooled to 7 K, and the target mount to 39 K. By using three re-entrant fiber glass tubes that were drilled to produce a 50% cross sectional area reduction instead of the single fiber glass tube, the target mount could be cooled to 25 K. This 18 K temperature difference does not give the uniform temperature environment around the target needed to produce uniform solid DT layers.

Because further increases in the thermal isolation of the target mount will almost certainly lead to a corresponding decrease in the mechanical rigidity and stability of the target mount, and because no easy solution is available to reduce the thermal contact resistance between the shroud and mount, we have taken a new approach. This approach, suggested by G. Stewart of NBS, uses contact resistance for thermal isolation. In addition, this technique provides a gas seal between the cryogenic shroud and the target mount. The modified target mount, shown in Fig. VII 25, contains a stack of thin aluminized Mylar washers (super insulation) interleaved with paper. The effective thermal conductivity of such an arrangement is ~ 1 μW cm K.[1] Because the washer in contact with the shroud has a low mass and is well isolated thermally from room temperature, the shroud exchange gas should cool this washer adequately and should provide a uniform temperature around the target. We are testing this thermal isolation technique.

In addition to providing thermal standoff, this stacked-washer scheme also provides the exchange gas seal between the cryogenic shroud and the target mount. This is attained by gluing the top washer to the target mount. The shroud face, lapped to provide a smooth mating surface, is loaded against the washer stack. The exchange-gas admitted into the cryogenic shroud is contained by this sealing system. Figure VII 26 shows the seal leak rate vs exchange gas pressure for two contact forces. With a force of 0.9 N on the seal (0.2 lb) and 1000 mtorr exchange-gas pressure in the shroud, the leak rate is $\sim 10^{-6}$ atm cm^3 s. Because the imposed limit on the helium leak rate into the Helios chamber is 10^{-5} atm cm^3 s, the detachable-seal problem is solved.

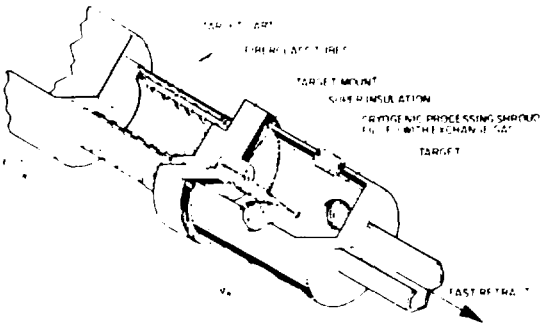

Fig. VII 25
Insulated cryogenic target mount and shroud.

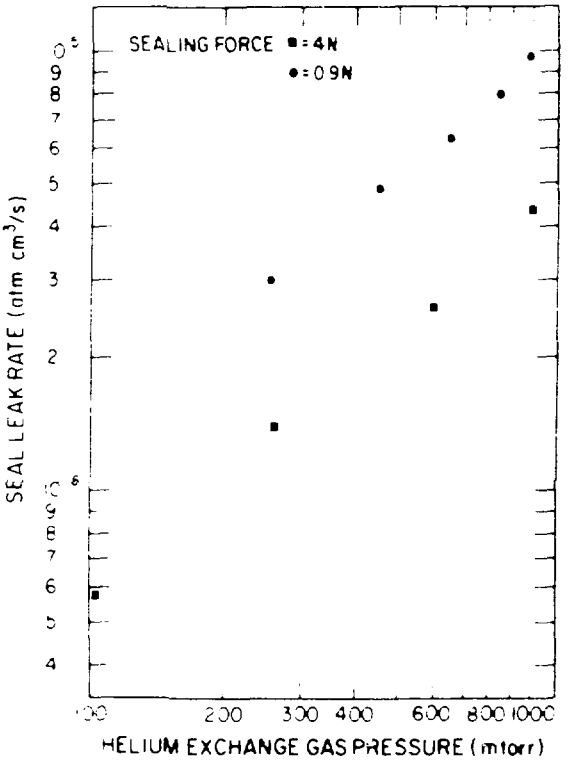

Fig. VII 26.
Performance of exchange gas seals for cryogenic target mount.

REFERENCES

1. C. M. Hartwig and J. Vitko, Phys. Rev. B 18, 3006 (1978).

2. P. Delamelleurart, E. Wallert, M. Leclecq, A. T. N'Guyen, and D. O. Londom, Anal. Chem. 51, 2 (1979).

3. E. Skoberne, Comp., "Inertial Fusion Program, January 1 June 30, 1978," Los Alamos National Laboratory report LA-7587-PR (May 1980).

4. R. B. Perkins and the Laser Fusion Program Staff, "Inertial Fusion Program, July 1 December 31, 1978," Los Alamos National Laboratory report LA-7755-PR (October 1980).

5. R. L. Whitman, R. H. Ray, R. P. Kruger, and D. M. Stupin, Appl. Opt. 18, 1266 (1979).

6. R. Liepins, A. Lowe, to be published in Journal of Applied Polymer Science.

7. R. Liepins, B. Cranfill, R. J. Fries, J. D. King, and H. Flicker, to be published in Journal of Applied Polymer Science.

8. E. Skoberne, Comp., "Laser Fusion Program, July 1 December 31, 1977," Los Alamos National Laboratory report LA-7328-PR (December 1978).

9. I. A. Black and P. E. Glaser, Adv. Cryog. Eng. 11, 26 (1966).

VIII. APPLICATIONS OF LASER FUSION—FEASIBILITY AND SYSTEMS STUDIES

(L. A. Booth)

Our feasibility and systems studies are being performed to analyze the technical feasibility and economic aspects of various commercial and military applications of lasers and laser fusion. Commercial applications include electric power generation, fissile fuel production from fusion fission hybrid reactors, and production of synthetic fuels such as hydrogen. Our studies also include assessment of advanced technologies that require development for the ultimate commercialization of laser fusion. These latter studies emphasize the CO_2 laser driver. The general objectives of these studies are the conceptualization and preliminary engineering assessment of laser fusion reactors and other energy production subsystems, the development of computer models of integrated plant systems for economic and technology tradeoff and comparison studies, and the identification of critical technology areas requiring long term development efforts.

REACTOR DESIGN STUDIES

Introduction

Our reactor design studies determine the fundamental engineering feasibility of reactor design concepts and establish scaling laws for the sizing of reactors in integrated plant designs for energy production applications. In converting pellet output energy to useful forms, two primary design considerations prevail: (1) protection of the reactor chamber structural wall from x rays and ion debris generated by the pellet, and (2) conversion of these energy forms and of the high energy neutrons to useful energy while producing the fuel constituent, tritium.

In general, these design considerations are essentially independent of each other. Because ~80% of the pellet output is in the form of high energy neutrons, this energy is most conveniently converted to thermal energy in a "blanket" surrounding the cavity and containing lithium or lithium compounds for tritium breeding; the design of this blanket is essentially not dependent upon the first wall protection scheme. Likewise, means of protecting the first wall are generally not dependent upon the blanket design. Therefore, a variety of blanket designs can be incorporated with a particular wall protection scheme and *vice versa*.

We are studying three methods of first wall protection: (1) a lithium wetted wall,[1] (2) a vacuum cavity with a low Z sacrificial liner and magnetic deflection of ion debris from the liner, and (3) a gas filled cavity with and without magnetic fields for deflection of ion debris. In the lithium wetted wall concept, the x ray output and ion debris are absorbed by the ablation of a thin film of lithium that coats the inside surface of the first wall. In the second concept, the ion debris is ducted out the ends of a cylindrical configuration where the ions are either collected on large surface areas or are slowed by MHD decelerators. The x ray energy is absorbed by ablation of small amounts of the low Z sacrificial liner. In the third concept, x ray and ion debris energies are attenuated by interaction with the background gas and, with the magnetic deflection option, ions are ducted out the ends of a cylinder, as above.

Our studies of blanket concepts include (1) a low temperature (~1000 K) liquid lithium blanket for electric power generation, (2) a high temperature (1500 to 2000 K) boiling lithium blanket for high efficiency electric power generation and as a high temperature process heat source for hydrogen production, and (3) a lithium cooled array of elements containing fertile ^{238}U and or ^{232}Th for the production of fissile fuel and electricity as a byproduct.

Reported below are results of our studies on the magnetically protected wall concept, on the high temperature boiling lithium blanket concept, and on a low power density fissile fuel production blanket (hybrid) concept.

Magnetically Protected Wall Phenomena Modeling (I. O. Bohachevsky, D. O. Dickman, J. C. Goldstein)

Our continuing studies of inertial confinement fusion (ICF) reactor cavities with magnetically protected cylindrical walls[4] and of possibilities of using high atomic number gases for protection from x rays[5] led to the formulation of a new plasma model[6] and to the development of a numerical code, LIFE B, which solves the governing differential equations and thus models cavity phenomena. In this section, we present results obtained with this code and indicate directions of current investigations.

Currently modeled in the LIFE B code are the temporal evolution of the electromagnetic field and of the state of the ionized cavity medium (continuum) propagation of fuel pellet debris ions, and the interaction of these ions with the continuum through electromagnetic and mechanical (friction) forces. Typical dependence of the frictional drag force that retards the motion of a tungsten ion through argon at a density of 10^{-6} g cm^{-3} on the ion energy (speed) is shown in Fig. VIII 1. Expressions modeling this behavior have been derived in the form of analytic approximations to experimentally determined stopping power data and have been incorporated into the code.

Figure VIII 2 shows, from the midplane of the cavity, the computed distribution of the magnetic field strength (intensity) after expansion of fuel pellet debris. Noticeable is the formation of a "bubble" in the field and the correlation between the expanding debris front and the ridge in the field intensity; this result agrees with our previous simplified computations.[4]

Figure VIII 3 illustrates the pressure increase in the background medium associated with the arrival of pellet debris viewed from the conical end of the cavity.

After we established the feasibility of using MHD decelerators in place of energy sinks to thermalize the high energy debris ions and to convert part of their kinetic energy into electricity,[7] we initiated parametric studies leading to the determination of specific cavity configurations and conditions compatible with these devices. A preliminary result is shown in Fig. VIII 4; it

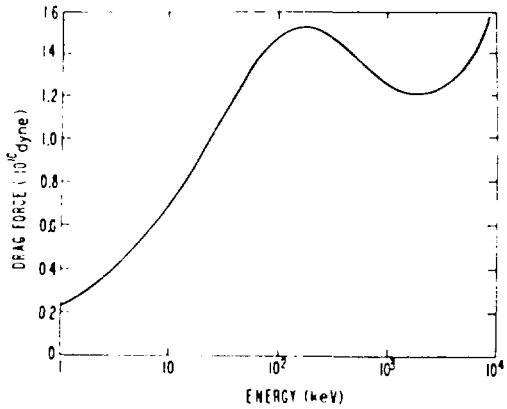

Fig. VIII 1.
Drag force regarding motion of tungsten ions through argon.

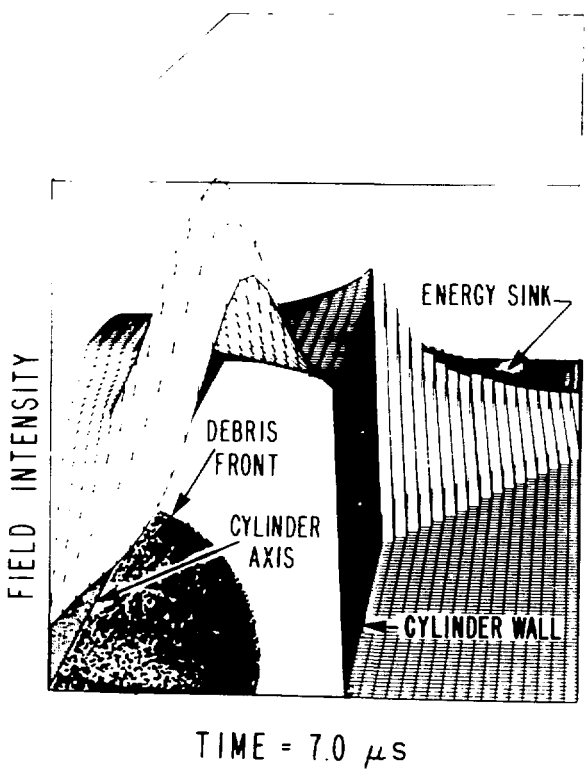

Fig. VIII 2.
Debris expansion after pellet explosion and bubble formation in the magnetic field.

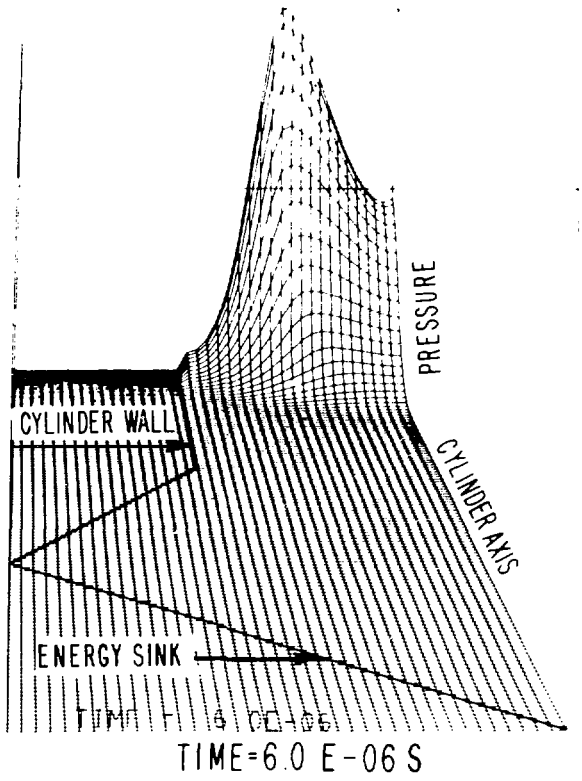

Fig. VIII 3.
Pressure wave in the reactor cavity.

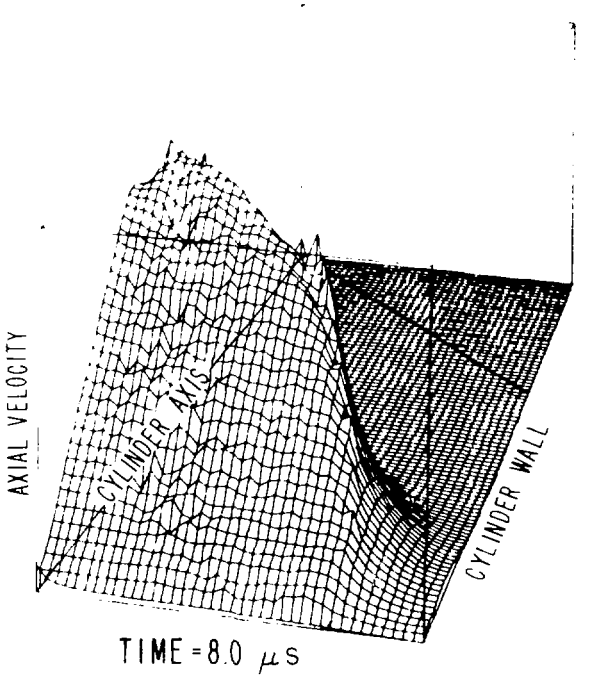

Fig. VIII 4.
Axial velocity of reactor cavity medium at an early stage of pellet expansion.

shows the axial velocity of the cavity medium at an early stage of pellet expansion. The velocity is predominantly positive, that is, out of the cavity, and concentrated along the cylinder axis, hence, suitable for driving MHD decelerators.

In addition to the parametric studies, we are investigating the effects of ion recombination on the feasibility of magnetic wall protection. We have estimated recombination rates for multiply charged ions using extrapolations of theoretically determined and experimentally verified rates for singly charged ions. Preliminary results indicate that at the anticipated operating conditions, the rates of radiative and three body processes will be comparable, and that their combined effect will reduce an ion's charge by two or three units during the ion dwell time in the cavity. We intend to continue investigating the relevant reaction rates to better model the crucially important chemical kinetics phenomena and to incorporate the appropriate expressions into the LIFE B code.

High Temperature Boiling Lithium Blanket Concept (J. H. Pendergrass)

Most studies of nonelectric applications of fusion energy, for example, as a high temperature heat source for synthetic fuel production by electrolytic or thermochemical water splitting, for steelmaking, or for nitrogen fixation, have considered only the generation of heat by neutron energy deposition in blankets that deliver heat to separate process streams. Although offering potential efficiency and capital cost advantages, direct nuclear heating of process streams is infrequently considered because of neutron-induced or plasma radioactivity contamination. If tritium breeding is restricted to lower temperature blanket regions, either in series or in parallel with high temperature process heat zones, only ~20 to 40% of total fusion reactor energy release can be delivered at high temperature if tritium breeding ratios greater than one are mandated.[8-10] However, both high fractional delivery of fusion energy at high temperature and tritium fuel cycle self-sufficiency are apparently important for economic viability of fusion reactors as process-heat sources.

The highly promising Los Alamos boiling-lithium concept[11] for simultaneous delivery of a majority of fusion reactor energy release as high-temperature heat and breeding of tritium at ratios substantially greater than one offers many advantages, for example:

- It is self-pumping with gravity return of the condensate;
- Thermal energy is delivered as latent heat and, hence, at maximum temperature;
- The concept is mechanically simple, operating pressures are low, and blanket temperatures are uniform;
- Shockwave overpressures resulting from pulsed neutron energy deposition characteristic of inertial confinement fusion are effectively damped by vapor bubbles.

However, the average vapor volume fraction, a function of volumetric energy deposition and operating pressure, can rise to over 0.5 at the tops of boiling lithium blankets, resulting in greater than usual blanket thicknesses with potential economic penalties. Also, the primary coolant loop piping sizes for similar loop thermal capacities may be modestly decreased if the primary loop involves heat transport by liquid lithium rather than by vapor.

Therefore, we have developed an alternative inertial confinement fusion reactor blanket concept that promises

- greater compactness than boiling-lithium blankets,
- delivery of similar fractions of fusion reactor energy release as high temperature heat, and
- achievement of similar tritium breeding ratios at the cost of
- some increase in mechanical complexity,
- higher operating pressures, and
- elimination of any possibility of self-pumping,

for applications in which thermal energy delivery as sensible heat over a reasonable temperature range is acceptable.

The concept, illustrated schematically in Fig. VIII-5, involves pressurization of liquid lithium tritium-breeding material and primary-coolant lithium to prevent boiling. The pressurized lithium is circulated through process-heat exchangers by electromagnetic pumps. Materials of construction and some design details were adapted from the boiling-lithium concept, and in addition, the new concept involves some design refinements that appear suitable for incorporation into the boiling-lithium concept.

For a modest neutron kinetic energy first-wall loading of 2 MW/m^2 and a liquid lithium thickness of 1 m, we calculate a tritium breeding ratio of 1.48 and a detailed total blanket thermal-power distribution of 73.5% deposited in high-temperature lithium, 10.2% appearing in

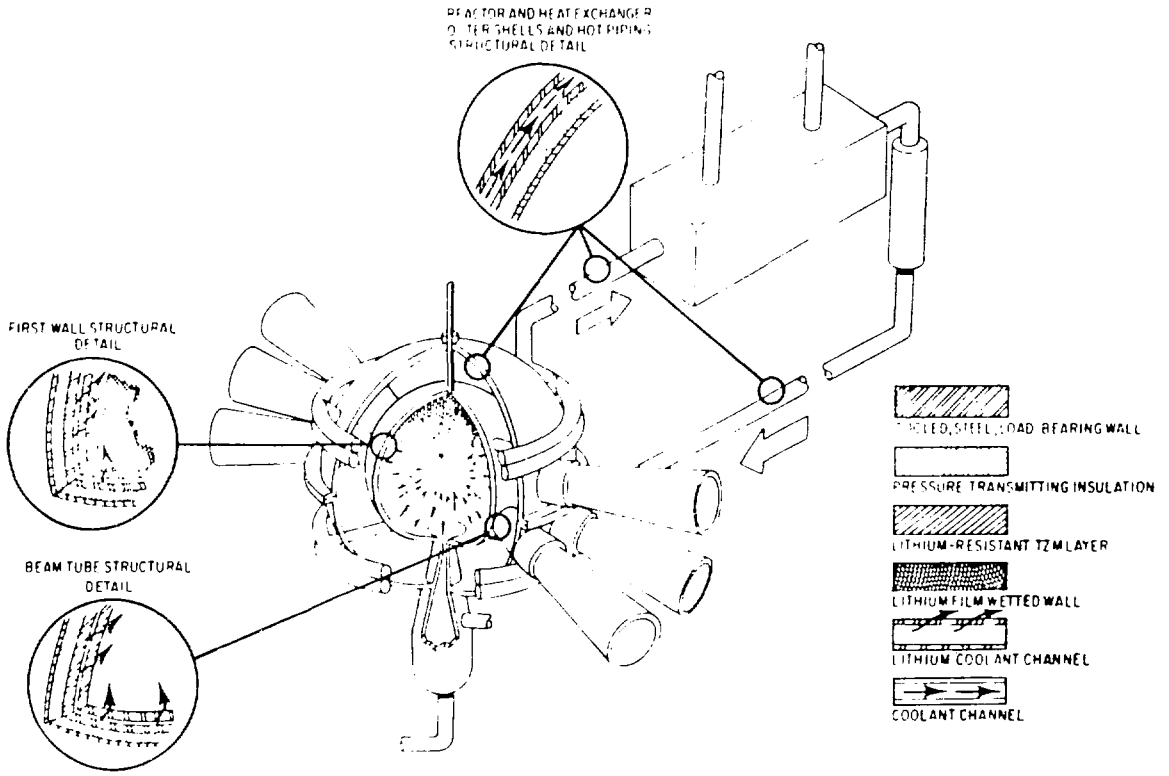

Fig. VIII.5
Pressurized high temperature liquid lithium blanket concept.

750 to 800 K lithium structural coolant, and 16.3% removed by 750 to 800 K helium used for insulation pressurization. The lower temperature heat can be converted to electric power and used either for power plant needs or sold as a product.

The pressure required to suppress boiling at 1600 K is only about 1 atm (0.1 MPa); a design value of ~30 atm (3 MPa) was selected to match blanket pressure to the Los Alamos bismuth sulfate cycle[8] process stream pressure to minimize loading on heat exchanger transfer surfaces.

Materials and design features adapted from the Los Alamos boiling-lithium concept are the use of thin (1 to 2 mm) liners of TZM for resistance to attack by hot lithium and the support of these liners by insulation capable of transmitting pressure loads to steel structures at 750 to 800 K. Experiments with TZM (0.5 wt% Ti, 0.08 wt% Zr, balance Mo), with highly purified (few ppm oxygen) refluxing lithium show no attack in 1000 h experiments at up to 1923 K.[12] Because TZM has inadequate creep resistance at the upper end of the indicated temperature range, only thin (1 to 2-mm) TZM liners are used. They are supported by insulation, for example, carbon or ceramic foams or by multilayer refractory metal foils. A new design feature provides further support for the TZM liner by pressurizing the insulation with helium to match the blanket operating pressure. The helium is circulated for tritium removal and thermal energy recovery at 750 to 800 K maximum. Recent tests of heat exchanger tubes consisting of metal liners supported by ceramics to control creep at high temperatures[13] and of molybdenum coated ceramic heat exchangers[14] lend credibility to this approach to hot lithium containment.

Roughly exponential decrease in energy deposition density in the lithium with increase in outward distance from the first wall results in a requirement of radially outwardly directed flow in the case of either spherical or cylindrical blankets or more rapid axial flow near the first wall with cylindrical blanket geometry. Internal structure is required for this purpose in the pressurized-lithium concept, but not in the boiling-lithium concept. This structure consists of ceramics or graphite encased in TZM and is cooled by the primary coolant so that

energy deposited in it is recovered at blanket temperatures.

Although the mean coefficient of thermal expansion of TZM is only about half that of steels, the temperature range over which the TZM liner is heated is more than twice that of the steel structure, and hence, allowance for differential thermal expansion is important. Such allowance is provided by designing the liner to be undersized at ambient temperature and to just fit at blanket operating temperature. Similarly, interleaved insulation panels have joints that just close at operating temperature. Accordion pleats in the liner are provided to further accommodate differential thermal expansion at critical points, for example, in piping, or at flanges. Liner integrity is ensured by seal welding liner seams protruding from flanged, bolted joints required for ready disassembly necessary for first wall replacement. Similar construction is used for primary coolant loop piping and primary heat exchangers.

The first wall insulation presents an interesting design problem. Because of substantial energy deposition within the insulation and low thermal conductivity, the maximum time averaged temperature anywhere within the reactor structure may occur in the first wall insulation. Thus, relatively thin insulation with low thermal conductivity and high maximum operating temperature limits will be required. Promising materials are carbon foams,[16] porous ceramics,[16] and multilayer refractory metal foils separated by refractory metal fibers,[17] all of which have thermal conductivities of ~0.001 W cm K. However, we have no experimental confirmation of suitable behavior under pulsed 14 MeV neutron irradiation and, therefore, have not settled on any of these alternatives.

For bred tritium recovery, (n,α) generated helium, and other impurity removal, a small sidestream of the primary coolant lithium can be flashed and distilled, as described previously in connection with the boiling lithium concept.[11] First-wall protection schemes that do not interpose massive layers of matter between the fusion neutron source and the blanket can be used with either the new blanket concept or the boiling lithium concept; neither the wetted-wall nor the magnetic deflection protection schemes significantly affect blanket performance. Therefore, we have not concentrated on this aspect of reactor design, but have selected the wetted-wall scheme for illustrative purposes.

A new heat-exchanger concept to be used with either the boiling-lithium concept or the new pressurized lithium concept for coupling to the Los Alamos bismuth sulfate thermochemical cycle has also been developed. This new concept appears to offer significant advantages regarding reliability, fabricability, and efficiency in comparison to the previously described shell-and tube heat exchanger concept. The new heat exchanger concept, illustrated in Fig. VIII 6, is a plate-type exchanger contained in a shell of cooled steel structure with helium pressurized load transmitting insulation. Plate construction permits ready assembly, reliability with low seal length to transfer area ratios, reliable scaling, and simple allowance for thermal expansion. The plates are assembled with cooled, insulated bolts. Primary loop lithium flows through TZM-lined passages separated by helium swept, pressure equalizing tritium barrier gaps from load bearing oxide-ceramic foam (for resistance to attack by the oxidizing streams) gas flow passages that are sealed with impermeable surface layers of the same ceramic. Development programs for ceramic foam heat exchangers that are capable of sustained high temperature operation with improved gas heat transfer coefficients have recently been described,[18] and our calculations indicate that such helium swept gaps make effective tritium permeation barriers. The process gas stream makes two passes and the lithium coolant channels are single pass.

The new high temperature concept and the boiling lithium concept also offer the possibility of more efficient electric power generation, provided a cost effective conversion cycle can be found that takes advantage of the high temperature capability of the concept. Gas turbines and potassium Rankine cycles or

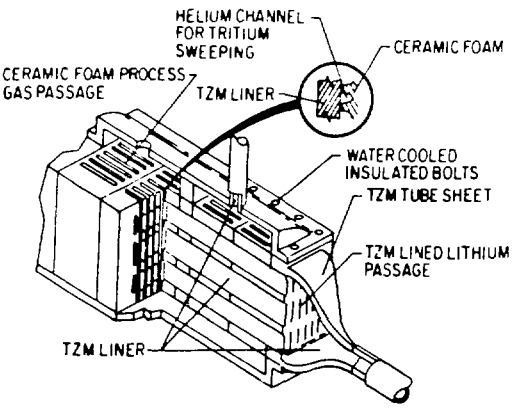

Fig. VIII 6.
Plate type heat exchanger for coupling lithium boiler blanket to Los Alamos bismuth sulfate cycle.

thermionic devices topping conventional steam cycles appear to be the most promising approaches.

Fusion-Fission Hybrid Reactor Studies (W. A. Reupke, H. S. Cullingford)

Our studies of hybrid fusion-fission applications of inertial confinement fusion have considered fission-boosted, central-station power/fissile-fuel factory blankets[19] and unboosted fissile-fuel factory blankets,[20] each using either the wetted-wall or the magnetic-wall first-wall protection scheme. Economics and systems studies are being performed to evaluate preliminary conceptual designs of each approach and to select the most promising for a complete study. We describe here our latest wetted wall, unboosted fissile-fuel factory concept.

Engineering feasibility studies were performed to conceptualize the low-power-density fissile-fuel factory. Our results have demonstrated a structurally feasible, remotely refueled and maintained, lithium-cooled, and modularized spherical cavity/blanket system.

Design objectives for the blanket system were

- a modularized approach for simplicity, reliability, ease of maintenance, and increased reactor availability;
- a spherical reaction cavity 4 m in diameter;
- the use of the wetted-wall concept for first-wall protection;
- tritium breeding in the lithium coolant;
- use of the existing fission-technology base;
- production of ^{233}U from ^{232}Th in metallic form; and
- the selection of structural materials for design simplicity, system compatibility, and economy.

Figure VIII-7 shows the cross-sectional view of a blanket module of generic design. The truncated octahedron geometry was selected as the basis of a cavity/blanket configuration in which each blanket module is independently cooled by lithium, refueled, and maintained. Each blanket module houses an array of fuel elements containing fertile ^{232}Th for ^{233}U production. Tritium self-sufficiency is achieved with breeding in the circulating liquid lithium coolant.[20] Figure VIII-8 shows the beginning-of-cycle ^{233}U production profile of a graphite-reflected blanket module.

The low-power-density hybrid concept allows the use of low-velocity (<1 m/s) lithium for cooling the blanket pin elements. This feature significantly reduces corrosion, erosion, cavitation, and flow-induced vibration problems as well as pumping power requirements (<150 kW). Table VIII-I summarizes the pertinent parameters of the blanket thermal-hydraulic analysis, including Peclet number (Pe), Reynolds number (Re), temperature rise (ΔT_f), and pressure drop (ΔP) for an unreflected blanket.

Moderate lithium temperatures (<800 K) enhance the structural life by reducing the corrosion, thermal fatigue, and creep rates. Figure VIII-9 shows the fuel-element temperature profiles for the highest power case analyzed (unreflected). Overall, the blanket design is not limited by heat-transfer and fluid-flow concerns for a 100-MJ fusion core.

Twelve promising materials were studied for structural adequacy, fabricability, lithium compatibility, tritium containment, state of technology, and availability. Austenitic stainless steels and zirconium are primary choices, but the low-alloy ferritic steels show greater promise because of better lithium compatibility. A double-wall design was selected for blanket-vessel and lithium-coolant lines. This feature is recommended for safety and maintenance, both in handling the liquid lithium and in containing the bred tritium.

Our studies have demonstrated the feasibility of a blanket system in which fissile-fuel production is maximized while tritium and electric self-sufficiency are attained. This preliminary engineering effort, supplemented by build-up and depletion calculations of blanket performance, will be used in systems and tradeoff studies of various approaches to ICF fusion fission hybrid power generation.

INTEGRATED PLANT DESIGN STUDIES

Introduction

We are studying three commercial applications of laser fusion: (1) electric power generation, (2) synthetic fuel (hydrogen) production, and (3) fissile-fuel production. Integrated plant systems for these applications are described by a computer model, TROFAN, in which plant subsystems are described analytically and important parameters may be varied for design tradeoff and optimization studies.

We previously defined preliminary electric generating plant concepts[21] based on lithium wetted-wall and magnetic deflection reactor concepts. We have essentially completed the updating of TROFAN with more definitive analytical models of reactor concepts and electric

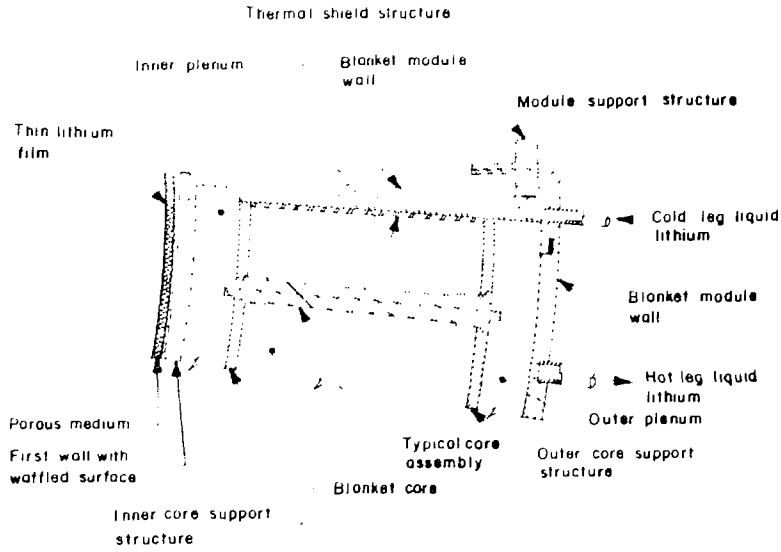

Fig. VIII 7.
Cross section of blanket module for fusion fission hybrid reactor.

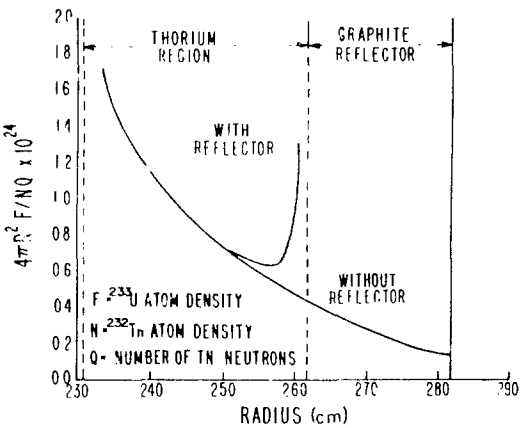

Fig. VIII 8.
^{233}U production profile of graphite-reflected fusion-fission hybrid reactor blanket module.

TABLE VIII-I

ANALYSIS OF MODULARIZED BLANKET CORE OF FUSION-FISSION HYBRID REACTORS

V (m/s)	Pe	Re	ΔT_c (K)	ΔP (Pa)
0.47	56	1210	10.0	1636
0.57	68	1468	8.0	1984
0.82	98	2100	5.7	2854
1.00	120	2575	4.7	3481
1.25	150	3219	3.8	4351

generating plant subsystems, and have incorporated a capital-cost data base developed under contract by Burns and Roe, Inc., an architect-engineering-construction firm.

Our hydrogen production studies are coordinated with a parallel study, supported by the Office of Fusion Energy, on thermochemical hydrogen production using a tandem-mirror reactor as a fusion energy source. This study is further supported at Los Alamos by the Division of Energy Storage for experimental verification of our bismuth oxide electrothermochemical cycle. Our studies include integration of the electrothermochemical process with the high-temperature lithium blanket concepts, and the production of hydrogen by high-temperature electrolysis.

Reported below are results from our studies of electric power generation and hydrogen production.

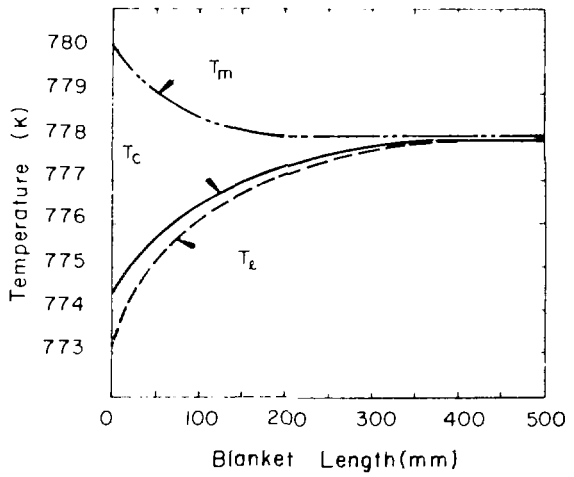

Fig. VIII 9.
Axial temperature profiles for fuel element in low power fissile fuel factory:
T_m: Fuel centerline temperature.
T_c: Cladding surface temperature.
T_ℓ: Lithium bulk temperature.

Electric Power Generation (E. M. Leonard, J. H. Pendergrass, L. A. Booth)

General. Preliminary assessments indicate that advanced-technology electric power production costs will be dominated by capital cost recovery and debt servicing so that accurate capital cost projections are essential to power production cost estimation. Advanced technology cost estimates have often been developed only for comparison of alternative concepts within a single technology, with no attempt at absolute costing. Even when such attempts were made, data bases were often inadequate with respect to accuracy, completeness, scaling laws for costs as functions of, for example, size and capacity and/or relationship to construction-code requirements. We report here a joint Los Alamos/Burns and Roe, Inc. (B&R) project to develop a capital-cost data base for capital-cost estimation for laser fusion to permit meaningful comparisons with other technologies. The primary goal is a data base that, when incorporated in our laser fusion systems code TROFAN, addresses the special requirements of tradeoff and parameter studies and the unique characteristics of laser fusion. For enhanced credibility, another data base is also provided by an independent organization that has considerable experience in costing unconventional industrial and current nuclear power-plant technology.

TROFAN. The laser fusion systems code TROFAN has been modified extensively and now allows inclusion of system scaling laws developed in part by B&R. This system studies model can indicate the sensitivity of electric power cost to numerous other system parameters in a laser fusion electricity generating station. Two laser fusion concepts incorporated are the wetted-wall and the magnetically protected wall concepts, with several point designs considered for each.

TROFAN is basically a process model, which, based on certain input parameters, calculates the system performance and the capital cost of the system. The capital cost, along with a calculation of interest during construction, is used in a levelized cost calculation that simulates the lifetime economic performance of the power plant.

A laser energy on target is specified by the user. This information, along with pellet gain curves, is used to determine pellet yield, which, in turn, specifies the size of the reactor cavity. The size of the cavity, as well as cavity material and first wall lifetimes, are all considered in the cost calculations.

The circulating-power requirements of the plant along with plant efficiency and pellet yield determine the net electrical energy generated per pulse (EOUT). The user then specifies the net power output of the generating station (PWR). The necessary laser pulse rate (PRNRC) is given by PRNRC = PWR/EOUT. Outside considerations are used to determine the allowable cavity pulse rate (PR). However, because the cavity must be evacuated between laser pulses, this procedure is the limiting consideration on the reactor pulse rate. The necessary number of reactor cavities (NRC) is determined thus:

$$NRC = \text{Integer}(PRNRC/PR) + 1.$$

Due to the physical requirement that the number of cavities be an integer, the net power output must now be recalculated. The code also has an option whereby the number of reactor cavities can be specified with the net power output allowed to float.

The size of the laser system, and thus the cost of the system, is determined by the size of the laser pulse on target (an input quantity) and by the laser pulse rate (a calculated value). At present the system is designed for a particular laser configuration. The size of the laser amplifiers can be varied to give the necessary laser pulse. Scaling laws have been devised to calculate the system cost as the laser pulse requirement varies. Another laser

system consideration is the pulse rate, which affects the cooling requirement, and thus the compressor and other associated costs.

Two steam cycles are incorporated into TROFAN as user options. One is a subcritical cycle with an inlet temperature of 516 K (450°F) and an outlet temperature and pressure of 730 K (855°F) and 2270 psia. The second is a supercritical cycle with an inlet temperature of 533 K (500°F) and an exit temperature and pressure of 810 K (1000°F) and 3500 psia. The lithium inlet and exit temperatures in the subcritical case are 755K (900°F) and 588K (600°F), respectively. In the supercritical case these temperatures are 836K (1045°F) and 669 K (745°F). The steam generators are rated at either 700 or 750 MWt and are of a special double walled design with water on the inside and lithium on the outside. Either wet or dry cooling towers may be chosen and the appropriate efficiencies have been calculated for the selected steam cycles. Appropriate turbine generator systems are also included in the overall system design.

If the size and number of cavities change, the associated piping, duct work, containment buildings, number and type of steam generators and turbines, and other associated equipment change accordingly.

The Data Base. The usefulness of the B&R data base has been ensured by adherence, where possible, to the following principles.

- Its structure is designed to facilitate incorporation into TROFAN and its format to permit ready updating with newer cost data and new concepts or plant systems. It includes relationships permitting scaling of costs with, for example, size and capacity, over reasonable ranges for several reference cases; for many plant systems it includes alternatives, and the number of parameters that must be specified for each system is reduced to a minimum consistent with accuracy and flexibility.
- The cost data are the most recent and all are valid for the same time interval, that is, mid-1978.
- Unconventional materials of construction, for example, refractory metal alloys, graphites, and ceramics, may offer significant capital, operating, and/or maintenance cost advantages for some plant systems, and the data base includes costs for some alternative materials.
- The data base is more detailed for plant systems unique to laser fusion and for interfaces of such systems with more conventional systems, and is less detailed for the more conventional systems.
- Only commercial plants for baseload operation in a mature laser fusion economy, with all R&D costs embedded in equipment or contract costs, are considered and a 40 year plant lifetime is specified.
- Costs for all components, such as wiring, controls, and piping, of each plant system are associated with that system to facilitate parametric and design tradeoff studies where possible, although arbitrary decisions as to location of system boundaries are involved and lumping together of such generic items is more typical of industrial practice.
- Redundant components required at startup to ensure acceptable plant availability and major replacement components are capitalized and their costs are associated with the appropriate systems.
- In general, only power plant equipment and structures made of conventional materials and based on established technology meet current code requirements, and due consideration was given to future regulatory requirements in developing the data base.
- Cost data for laser beam transport, and pellet fabrication, injection, and tracking systems are provided, and parallel studies concerned with such systems conducted elsewhere, for example, by Avco Everett Laboratories (AEL) and United Technologies Research Center (UTRC), whose results are incorporated into the data base, will provide additional cost data. The scope of the data base, with examples of cost scaling laws, includes
  - Los Alamos wetted-wall and magnetically protected wall reactors with respective repetition rates of 1 and 10 Hz and thermal powers of 150 to 3000 and 1400 to 5600 MWt for plants containing 1 to 20 reactors [magnetically protected wall reactor vessel (Nb-1% Zr) cost = $\$28.5 \times 10^6$ (pellet yield/150 MJ)$^{1.5}$].
  - Liquid-lithium tritium-breeding blanket and primary coolant loops with no intermediate heat exchangers, but double-wall tube and tube-sheet steam generators similar to those currently under development by Westinghouse, and tritium windows for tritium recovery [primary-coolant-loop piping cost = $\$74.4 \times 10^6$ (gross plant thermal power/5600 MWt)$^{0.8}$; steam generator cost = $\$14.0 \times 10^6$ (thermal power/750 MWt)$^{0.75}$].
  - CO_2 laser amplifiers with total pulse energies from 1 to 5 MJ with repetition rates of 1 to 40 Hz and pellet yields in the 150- to 3000-MJ range [CO^2 laser system (10 Hz) cost = $\$150.0 \times 10^6$ (total optical energy/1 MJ)$^{0.8}$].

- A 730 K (855°), 2270-psi and an 810 K (1000°F), 3500 psia steam cycle of respective overall efficiencies of 37% (42%) and 39% (44%) with dry (wet) cooling towers and with several turbine generator options [turbine generator (tandem compound up to 1600 MWe and 1000°F, 3500 psia, 25 in. Hg backpressure turbine) cost = \$49.3 × 10^6 (gross electric power output/1050 MWe)$^{0.8}$ + 1.4 × 10^6 (MWe/1050)$^{0.6}$ with additional \$6.0 × 10^6 (gross electric output/1050 MWe)$^{0.8}$ for cross compound (up to 2200 MWe); dry cooling tower cost = \$33.0 × 10^6 (*heat rejection rate 2000* MWt)$^{0.7}$].

Plant Layouts. Plant layouts, buildings, and the balance of plant systems for commercial fusion electric power plants have generally received limited attention in systems studies. Apparent reasons include a widespread perception that only present technology or its near term extrapolation is involved and that knowledge concerning the special characteristics of fusion energy sources is limited. However, for many fusion power plants, structures and the balance of plant equipment are estimated to constitute more than half the capital cost, whose recovery and debt servicing is projected to represent a majority of fusion energy production cost. In addition, the special characteristics of fusion reactors and their maintenance requirements are projected to have significant impacts on plant layouts and on the capital costs of structures and balance-of-plant equipment. Therefore, more realistic studies of plant layout, balance-of-plant systems, and plant structures are necessary for accurate estimation of unit fusion energy production costs. We concentrate herein on recent developments in our understanding of the economic impacts of balance of plant, laser and laser beam transport and on reactor equipment and structures characteristics and costs on laser fusion plant layout. Fundamental considerations in laser fusion plant layout include

- separation of plant portions that require elaborate containment and/or shielding for safety reasons from those that do not and minimization of such requirements;
- laser and beam transport systems isolation from feedback of pulsed inertial-confinement-reactor mechanical vibration, radiation fields, and parasitic optical oscillations;
- no laser beam tunnels under reactor cells, pipe chases, steam-generator cells, and turbine building;
- ready overhead crane access to all heavy equipment requiring repair, maintenance, and transport to appropriate facilities;
- minimization of primary coolant loop runs for cost and safety reasons; and
- minimization of elevation and direction changes for laser beam transport systems to minimize optical element costs.

Figure VIII-10 contains an example that illustrates the layout of a generic plant and the above principles. Other information obtained from Avco Everett Research Laboratory has identified these characteristics of CO_2 laser and beam transport systems. Some of them are illustrated in Figs. VIII-10 and -11. Figure VIII-11 illustrates some particular points in the design parameter space of CO_2 laser amplifier systems upon which the laser and beam transport system layouts in Fig. VIII-10 are based. The circular arrangement is for elimination of pressure drops due to sharp bends, and the expansion and contractions are for reduction of pressure drops in the heat exchanger sections. The minimum diameter of the laser amplifier ring can be determined by either the dimensions in Fig. VIII-11 or by the requirement of ~40 m for multipassing optical systems, necessary for achieving the assumed 10% overall laser efficiency, on either side of the laser amplifier ring plus ~10 m for the central mirror system. Thus, the minimum outer diameter of the laser amplifier complex is ~180 m. If the minimum diameter of the laser amplifier ring is smaller, there will be blank sections of CO_2 piping, and, if larger than about twice that dimension, stacked amplifier rings would be used.

Synthetic Fuel Hydrogen Production (J. H. Pendergrass)

We have developed a conceptual process design for the most promising of the Los Alamos family of bismuth sulfate hybrid thermochemical cycles for hydrogen production by water splitting. Preliminary energy balances indicate encouraging overall cycle efficiencies (percentage of primary source energy converted to stored chemical energy) of ~50% at a primary energy source temperature of 1500 K. The laser fusion reactor blanket concepts described in preceding sections and this cycle permit synthetic fuel production with no electric power export.

The chemistry of this family of cycles can be summarized as follows.

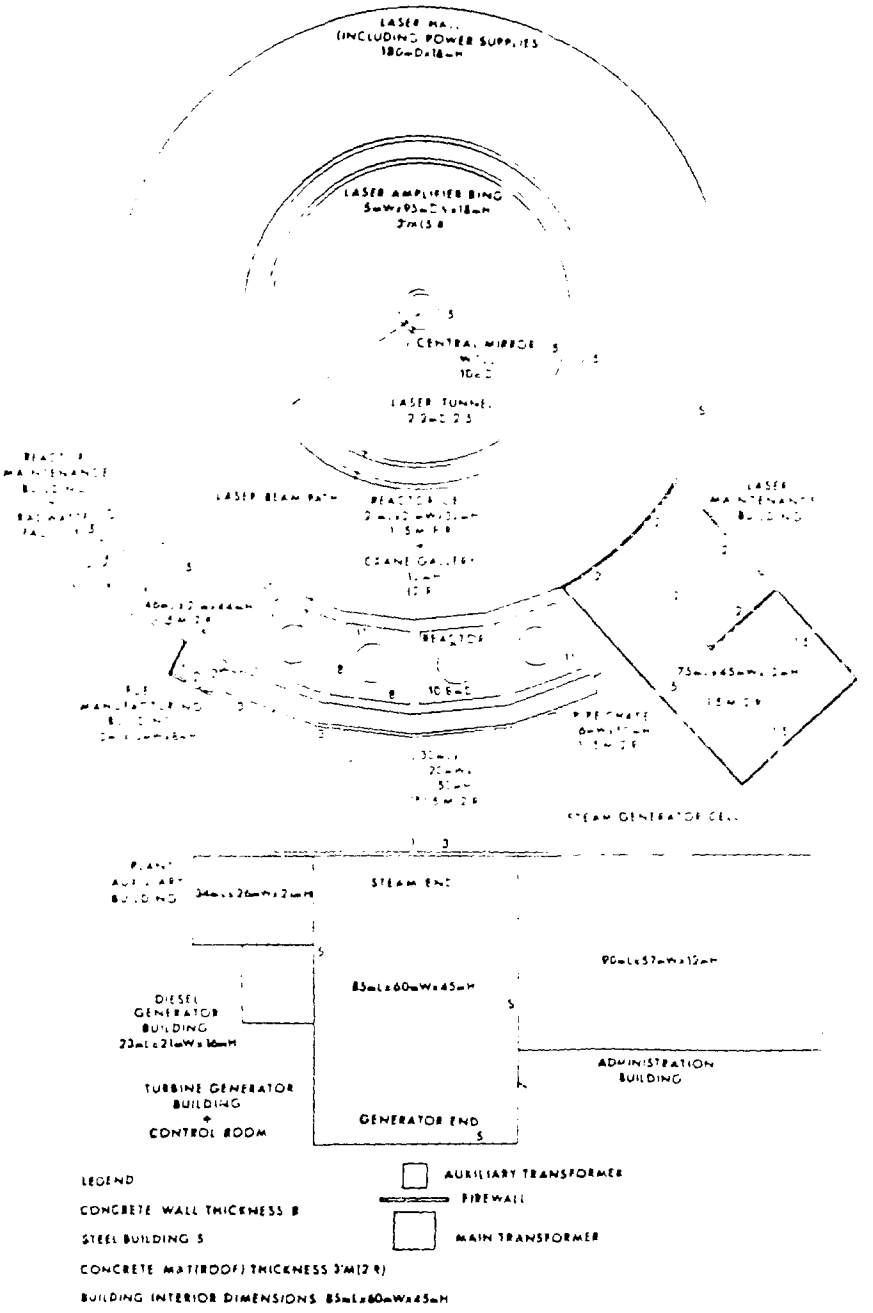

Fig. VIII-10.

Sample plant layout for 1000 MWe (net), four-reactor, 1.84-MJ (on target) CO_2 laser fusion power plant.

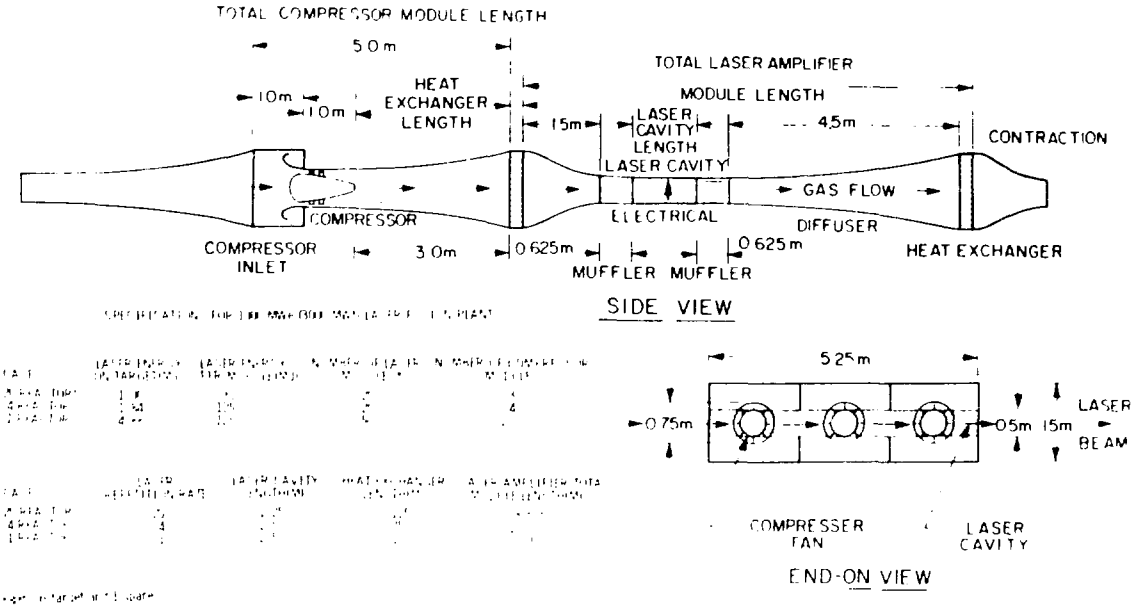

Fig. VIII 11.
Some sample CO_2 power laser amplifier design points.

(1) $SO_2(aq) + 2H_2O(\ell) \rightarrow H_2SO_4(aq) + H_2(g)$ + electrical energy — (low temperature electrolysis)

(2) $H_2SO_4(aq) + Bi_2O_3 \cdot xSO_3(s) \rightleftharpoons Bi_2O_3 \cdot ySO_3(s) + H_2O(\ell)$ — (low temperature and exothermic)

(3) $Bi_2O_3 \cdot 2SO_3(s) \rightleftharpoons Bi_2O_3(s) + SO_3(s) + SO_3(g)$ + heat — (high temperature and endothermic)

(4) $SO_3(g) \rightleftharpoons SO_2(g) + 1/2\ O_2(g)$ + heat — (high temperature and endothermic)

The chemistry of the member of this family of cycles that we have previously designated as a reference cycle is defined by respective values of 0 and 3 for x and y. The alternative cycle discussed herein is defined by respective values of 1 and 2 for x and y and was selected because the previous reference cycle

- involves the production of a molten salt with its attendant materials compatibility problems,
- requires the production of sulfuric acid at higher concentrations, and hence, higher electrolysis voltages and higher electrical energy expenditures per unit of product,
- requires a greater thermal-energy expenditure for solids decomposition per unit of hydrogen produced.

The principal disadvantage of the present alternative cycle relative to the previous reference cycle is increased materials processing per unit of hydrogen produced.

Our conceptual process design can be described briefly in terms of the principal process steps illustrated schematically in a highly simplified manner in Fig. VIII 12. Energy flows are further summarized in Table VIII II. Included in Fig. VIII 12 is a summary of the cycle energy balance for an assumed set of operating conditions (electrolysis at 0.45 V and 15 wt% acid, 5 mol water entrained mol of solids, 1250 K maximum for solids decomposition, and 1475 K maximum for sulfur trioxide decomposition). These conditions are based on parameter studies using limited thermodynamic, kinetic, and cost data and appear to be nearly optimal. The following discussion is also based on this assumed set of operating conditions. We show only the main energy flows and materials streams in Fig. VIII-12 and not all the complex thermal-energy recuperation loops, minor materials-handling work requirements, and recycle streams required by incomplete reactions and separations. In particular, a chemical heat-pipe scheme that may offer significant efficiency and capital-cost benefits (if kinetic studies confirm its practicality) is not illustrated. This scheme involves endothermic decomposition of $SO_3(g)$ to give $SO_2(g)$ and $O_2(g)$ at high tem-

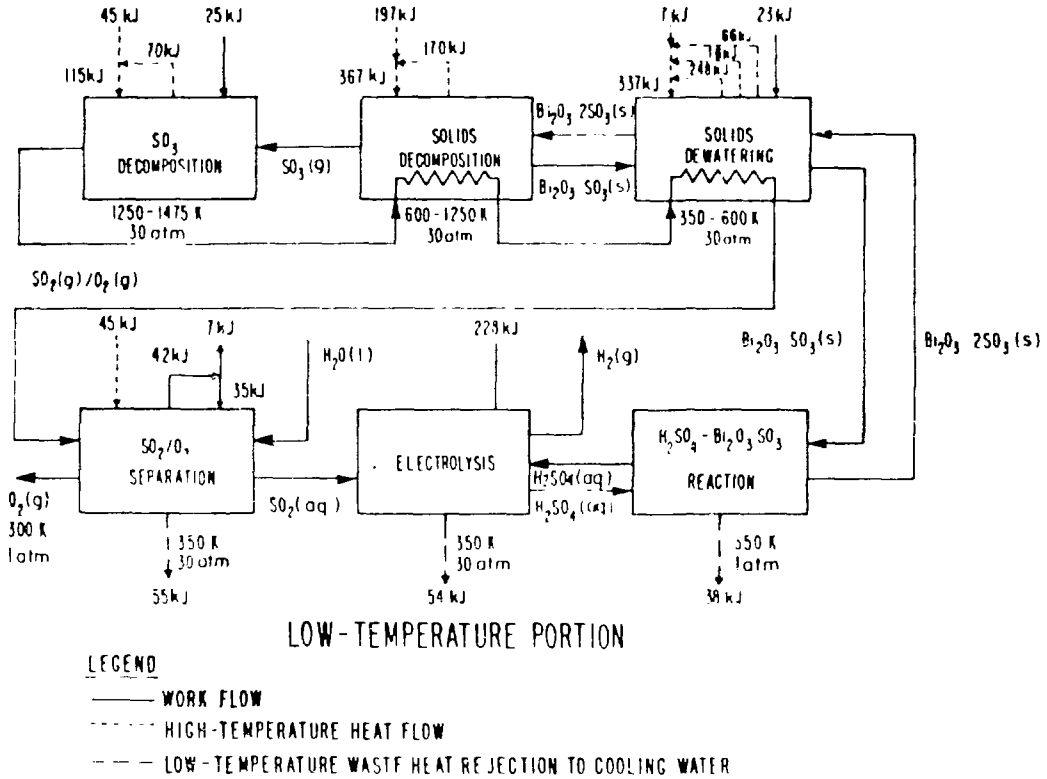

Fig. VIII 12

Schematic of most promising members of Los Alamos bismuth sulfate hybrid thermochemical cycle for hydrogen production by water splitting.

perature in excess of that required to close the thermochemical cycle, and exothermic recombination to give up heat where required elsewhere in the cycle. The use of this scheme, which is not mandatory for cycle operation, permits efficient direct-contact gas-to solids heat transfer using an efficient thermal energy carrier, that is, heat of reaction plus sensible heat rather than sensible heat alone, and a single interface between the fusion energy source and the thermochemical cycle. Thus, we show only the energy flows associated with decomposition of SO_3 required for cycle closure. Also, we do not show a direct-contact loop (using oxygen) for sensible-heat recuperation from solids. All work terms are expressed as thermal energy equivalents assuming conversion to electrical energy at an efficiency of 0.38, and the energy flows and material flows are all normalized to 1.0 mole of product.

Process Step A in the high-temperature portion of the cycle involves evaporation of water (~4.89 mol/mol H_2 produced in the example) from 15 wt% aqueous sulfuric acid solution entrained by finely divided $Bi_2O_3 \cdot 2SO_3(s)$ (~0.98 mol) and heating of the dried solid. As the concentration of sulfuric acid in the entrained solution increases, the sulfuric acid (~0.16 mol) reacts exothermally to produce ~0.16 mol of $Bi_2O_3 \cdot 3SO_3(s)$ and $H_2O(\ell)$ and to reduce the heat required for solution evaporation and solid heating to ~337 kJ. Vapor recompression from 30 to 40 atm and countercurrent condensation and cooling of the evaporated water provide 248 kJ of this heat requirement. The thermal equivalent (at 38% conversion efficiency) of the compression work is ~23 kJ. Exothermic reaction of undissociated SO_3 (~0.14 mol) with water removed from the solid provides an additional ~66 kJ/mol H_2, and ~16 kJ are provided by countercurrent cooling of the $SO_2/O_2/SO_3$ stream entering process Step D in the low-temperature portion of the cycle. Thus, the net thermal energy requirement in Step A is ~7 kJ.

TABLE VIII-II

ENERGY BALANCE SUMMARY

	Heat Required (kJ/mol H_2)	Heat Available (kJ/mol H_2)	Heat Rejected (kJ/mol H_2)	Work[a] Required (kJ/mol H_2)	Work[a] Available (kJ/mol H_2)
High Temperature Portion					
Step A—Solids Dewatering					
1. Slurry Heating, water evaporation, acid reaction with Bi_2O_3, $2SO_3$	337				
2. Vapor recompression				23	
3. Condensation, cooling		248			
4. Cooling of SO_3,O_2,SO		16			
5. SO_3 reaction of H_2SO_4		66			
NET	*7*		*(0)*	*23*	
Step B—Solids Decomposition					
1. Solids heating	171				
2. Solids decomposition	196				
3. Solids cooling		170			
NET	*197*		*(0)*		
Step C—SO_3 Decomposition					
1. SO_3 heating	16				
2. SO_3 decomposition	99				
3. SO_2,O_2,SO_3 cooling		70			
4. Gas compression (circulation)				25	
NET	*45*		*(0)*	*25*	
Low-Temperature Portion					
Step D—SO_2/O_2 Separation					
1. Acid heating	25	---	---	---	---
2. Oxygen heating	20	---	---	---	---
3. Turbine expansion	---	---	---	---	42
4. SO_2 compression	---	---	55	35	---
NET	*45*		*(55)*	*-7*	
Step E—Electrolyzer					
1. Electrolyzer	---	---	54	228	---
NET			*(54)*	*228*	
Step F—Solids/Acid Reactor					
1. Reactor	---	---	38	---	---
NET			*(38)*		
TOTALS (NET)	*294*			*269*	

[a]Heat-to-Work Conversion = 0.38.

Step B as illustrated involves heating and thermal decomposition (~367 kJ) of the mixture of $Bi_2O_3 \cdot 2SO_3$ and $Bi_2O_3 \cdot 3SO_3$ to release $SO_3(g)$ and produce $Bi_2O_3(s)$ and recuperation of sensible heat (~170 kJ) of the hot Bi_2O_3 $SO_3(s)$ for a net thermal-energy requirement of ~197 kJ. Process Step C includes heating and decomposition (~115 kJ) of the $SO_3(g)$ (~1.14 mol) released in Step B, followed by recuperation of the sensible heat (~70 kJ) of 1.0 mol of $SO_3(g)$, 0.5 mol of $O_2(g)$, and ~16 mol of undissociated $SO_3(g)$. Thus, the net thermal energy requirement for this process step is ~45 kJ. Also arbitrarily associated with this process step is ~25 kJ of work thermal equivalent used to drive the main compressor used for circulation of the gases in the chemical heat pipe scheme and in the rest of the high temperature portion of the cycle.

Step C in the low temperature portion of the cycle includes absorption of $SO_2(g)$ in incoming $H_2O(\ell)$ and dilute $H_2SO_4(aq)$ for separation from $O_2(g)$ with rejection of ~55 kJ of low temperature heat to cooling water. Also, ~20 kJ of high-temperature heat is transferred to the high-pressure $O_2(g)$ byproduct stream, which is then expanded through a turbine to produce ~42 kJ thermal equivalent of electric power. About 35 kJ (thermal equivalent of work) is needed for compression of $SO_2(g)$ flashed from the anolyte to permit use of the anolyte for $SO_3(g)$ absorption in Step D and for SO_2-free catholyte production leaving a net surplus of ~7 kJ thermal equivalent of work for this to produce 15 wt% $H_2SO_4(aq)$ and release $H_2(g)$.

Step E involves electrolytic combination of $SO_2(aq)$ and 2 $H_2O(\ell)$ at a cell potential of 0.45 V. This step requires ~228 kJ thermal equivalent of electrical energy and rejects ~54 kJ of low-temperature heat resulting from cell overvoltage to cooling water. The final process step, Step F, involves only exothermic reaction of $Bi_2O_3SO_3(s)$ and $H_2SO_4(aq)$ to give $Bi_2O_3 \cdot 2SO_3(s)$ and $H_2O(\ell)$ with rejection of ~38 kJ of waste heat to cooling water.

Summation of net thermal energy inputs and work thermal energy equivalent inputs per unit of product and division of the result into the higher heating value of 1.0 mol of $H_2(g)$, 286 kJ, leads to a cycle efficiency of ~50.8% for this example. Neglected minor energy requirements will result in decrease in cycle efficiency by 1.0% or so. Parameter studies indicate that

- moderate decreases in cycle efficiency accompany increases in aqueous sulfuric acid entrainment by $Bi_2O_3 \cdot 2SO_3$ leaving process Step F;
- variation in pressure level on the high-temperature side of the process has only small effects on cycle efficiency, but substantial effects on required process equipment capacities; and
- variations in maximum cycle temperature, in process Step C, have only small effects on cycle efficiency for temperatures above 1200 K, but substantial increases in process equipment capacities are required below ~1400 K.

REFERENCES

1. L. A. Booth, Comp., "Central Station Power Generation by Laser-Driven Fusion," Los Alamos National Laboratory report LA-4858-MS, Vol. 1 (February 1972).

2. J. J. Devaney, "Magnetically Protected First Wall for a Laser Induced Thermonuclear Reaction," Los Alamos National Laboratory report LA-5699-MS (August 1974).

3. T. G. Frank, D. Freiwald, T. Merson, and J. J. Devaney, "A Laser Fusion Reactor Concept Utilizing Magnetic Fields for Cavity Wall Protection," Proc. 1st Top. Mtg. Technology of Controlled Nuclear Fusion, Vol. 1, p. 83 (1974).

4. J. C. Goldstein, I. O. Bohachevsky, and D. O. Dickman, "Ion Motion in Laser Fusion Reactors Studies," Paper 9P7, Bull. Am. Phys. Soc. Series II 71, 1186 (October 1976).

5. R. W. Conn, "Solase, A Conceptual Laser Fusion Reactor Design," University of Wisconsin report UWFDM-220 (December 1977).

6. I. O. Bohachevsky, D. O. Dickman, and J. C. Goldstein, "A New Plasma Model for the ICF Magnetic Wall Reactor Cavity Concept," ANS Trans. **30**, 20-21 (November 1978); see also F. Skoberne, Comp., "Laser Fusion Program, July 1-December 31, 1977," Los Alamos National Laboratory report LA-7328-PR (December 1978).

7. S. Chow and I. O. Bohachevsky, "MHD Deceleration of Fusion Reaction Products," Los Alamos National Laboratory report LA-7778-MS (April 1979).

8. L. A. Booth, M. G. Bowman, G. E. Cort, K. E. Cox, D. J. Dudziak, R. A. Krakowski, J. H. Pendergrass, and A. S. Tai, "Production of Electrothermochemical Hydrogen Using a Fusion Source of High-Temperature Heat," Proc. 3rd ANS Topical Meeting on the Technology of Controlled Nuclear Fusion, Santa Fe, New Mexico, May 9-11, 1978, p. 180.

9. J. A. Fillo, Ed., "Fusion Reactors—High Temperature Electrolysis," Brookhaven National Laboratory report HCP/TOO16 (January 1978).

10. Y. Gohar, "Falling-Bed High-Temperature Fusion Blanket Design for Synthetic Fuel Production," Trans. Am. Nucl. Soc. 32, 48 (1979).

11. J. H. Pendergrass, L. A. Booth, D. R. Peterson, and S. A. W. Gerstl, "The Lithium Boiler: A 1500- to 2000-K Fusion Reactor Blanket Concept for Process Heat and/or Electric Power Generation," Proc. 14th IECEC Conference, Boston, Massachusetts, August 5-11, 1979, in press.

12. J. A. DeMastry, "Corrosion Studies of Tungsten, Molybdenum, and Rhenium in Lithium," Nucl. Appl. 3, 127 (1967).

13. P. H. Kydd, "Composite Tube Heat Exchangers," Heat Transfer Research and Applications, AICHE Symp. Ser. 74 (174), 320 (1978).

14. W. A. Ranken, "Ceramic Heat Pipe Heat Exchangers," Los Alamos National Laboratory report LA-6514-MS (October 1976).

15. Y. Amagi, Y. Nishimura, and S. Gomi, "Hollow Carbon Microspheres from Pitch Material and Their Applications," Proc. 16th National Symp. and Exhibit, Soc. Aerospace Material and Process Engineers, Anaheim, California, April 21-23, 1971, Vol. 16, p. 315.

16. E. A. Sbrabek, "High Temperature Insulations for Radioisotope Thermoelectric Generators," Proc. 13th IECEC Conf., San Diego, California, August 20-25, 1978, p. 1712.

17. P. E. Glaser, I. A. Black, R. S. Lindstrom, F. E. Puccia, and A. E. Wecher, "Thermal Insulation Systems, A Survey," National Aeronautics and Space Administration report NASA SP-5027 (1967).

18. "Heat Exchangers Made from Silicon Carbide Sponge," Chementator, Chem. Eng. 86 (7), 105 (March 26, 1979).

19. F. Skoberne, Comp., "Laser Fusion Program, July 1-December 31, 1975," Los Alamos National Laboratory report LA-6245-PR (July 1976).

20. W. A. Reupke, H. S. Cullingford, T. G. Frank, and L. A. Booth, "Wetted-Wall ICF Fissile Fuel Factory Studies," Trans. Am. Nucl. Soc. 32, 39 (June 1979).

21. L. A. Booth and T. G. Frank, "Commercial Applications of Inertial Confinement Fusion," Los Alamos National Laboratory report LA-6838-MS (May 1977).

IX. RESOURCES, FACILITIES, AND OPERATIONAL SAFETY

The design and construction of Antares facilities continued. Operational safety policies and procedures continued to be applied successfully to minimize the hazards of operating high-power lasers. The Final Safety Analysis Report (FSAR) for the Laser Fusion Laboratory was prepared for final draft approvals.

MANPOWER DISTRIBUTION

The distribution of employees assigned to the various categories of the DOE-supported Inertial Fusion Research Program is shown below.

APPROXIMATE STAFFING LEVEL
OF INERTIAL FUSION PROGRAM
June 30, 1979

Tasks	Direct Employees
CO_2 laser development	65
CO_2 laser experiments	115
Target design	32
Target fabrication	43
Diagnostics development	42
Systems and applications studies	4
Advanced technology	3
Weapons application	9
Total	313

FACILITIES

High-Energy Gas Laser Facility (HEGLF)

Construction Package I, including the laser building, the mechanical building, the office building, and a warehouse is 62% complete, with a scheduled completion date of February 1980.

Construction Package II, including the target building, the power-transmission system, and miscellaneous other construction is 66% complete with a scheduled completion date of December 1979.

In the interest of continuity, we have presented details on HEGLF Design and Construction in Sec. II.

Construction of New Laboratories

The High-Voltage and Optical-Evaluation Laboratories were completed and have been occupied for several months.

Proposed Target Fabrication Facility

A conceptual design report and Schedule 44 Construction Draft Data Sheet have been prepared for a new Target Fabrication Facility. This facility will provide target-fabrication development and assembly laboratories and office space urgently needed to support the expanded requirements of the target experimental program for Helios and in preparation for Antares.

The proposed construction consists of a new laboratory-office facility of ~53 000 square feet—30 000 square feet of target fabrication laboratory area, and 23 000 square feet of office area. Conceptual plans call for a two-story structure sited on sloping terrain immediately to the west of the Antares CO_2 laser facility. The target fabrication laboratory area will occupy the ground floor with entrance from the north, and the office area will occupy the second floor with entrance on the south at grade. The target fabrication laboratory will include a clean-room area on an isolated foundation of ~12 000 square feet. Half this area will be devoted to target assembly operations. The other half will consist of

measurement and characterization laboratories. Other laboratories will be devoted to fabrication technology development. A special laboratory for filling laser-fusion targets with D-T gas will be provided with tritium-handling dry boxes. Another special laboratory complex will be equipped for the development of cryogenic targets. The entire fabrication laboratory will be supported by a machine shop. In addition, a special laboratory will be equipped for micromachining of laser fusion target elements.

This project is being submitted for consideration as an FY-80 line item for completion in the third quarter of FY-82 with a total estimated cost of $14.0M.

OPERATIONAL SAFETY

General

The excellent lost-time injury rate continued during this period with no serious accidents reported.

Laser Fusion Facility Final Safety Analysis Report (FSAR)

The final draft of the Laser Fusion Facility (eight-beam Helios system) Final Safety Analysis Report was prepared for approval. Release of the report is anticipated in September 1979.

X. PATENTS, PUBLICATIONS, AND PRESENTATIONS

PATENTS

Serial numbers, filing dates, patent numbers, and issue dates may not be shown for several months after they are assigned. Therefore, for any given period, cases may be missing from these listings if patent activity occurred later in the reporting period.

The following applications were filed in the U. S. Patent Office.

S.N. 8,721 "Fusion Reaction Chamber Magnetic Wall Protection," Joseph J. Devaney, David A. Freiwald, Thurman G. Frank, and Thomas J. Merson, filed February 1, 1979.

S.N. 9,701 "Radiation Source," Lester E. Thode, filed February 5, 1979.

S.N. 9,702 "Device and Method for Imploding a Microsphere with a Fast Liner," Lester E. Thode, filed February 5, 1979.

S.N. 9,703 "Device and Method for Relativistic Electron Beam Heating of a High-Density Plasma to Drive Fast Liners," Lester E. Thode, filed February 5, 1979.

S.N. 37,982 "Laser Beam Alignment Apparatus and Method," Charles R. Gruhn and Robert B. Hammond, filed May 10, 1979.

PUBLICATIONS

This list of publications is prepared from a stored computer data base. This listing also includes late 1978 publications.

C. A. Anderson, J. C. Biery, L. M. Carruthers, K. E. Cox, F. T. Finch, S. H. Nelson, R. G. Palmer, J. H. Pendergrass, E. E. Stark, and J. K. Stutz, "Production of Synthetic Gas from Nuclear Energy Sources," Los Alamos National Laboratory report LA-7592-MS (1979).

R. F. Benjamin and G. T. Schappert, "Prepulse Damage to Targets and Alignment Verification," J. Appl. Phys. 50, 7 10 (1979).

R. F. Benjamin, G. H. McCall, and W. A. Ehler, "Measurement of Return Current in a Laser-Produced Plasma," Phys. Rev. Lett. 42, 890-3 (1979).

S. Chow and I. O. Bohachevsky, "MHD Deceleration of Fusion Reaction Products," Los Alamos National Laboratory report LA-7778-MS (1979).

S. J. Czuchlewski, E. J. McClellan, J. F. Figueira, E. Foley, C. E. Knapp, and J. A. Webb, "High-Power (10-GW) Short-Pulse (Less Than 1 Nanosecond) Carbon Dioxide TEA Amplifier," Lasers '78 International Conference Proc., V. J. Corcoran, Ed., Orlando, Florida (1979), pp. 498-505.

J. J. Devaney, "Existence and Lifetime of Laser Fusion Pellets Containing Tritium," Los Alamos National Laboratory report LA-7695-MS (1979).

J. J. Devaney, "Cooling of DT and T2 Cryogenic Pellets Within Very Low-Density Plastics by Helium 2," Los Alamos National Laboratory report LA-7790-MS (1979).

E. E. Fenimore, T. M. Cannon, D. B. VanHulsteyn, and P. Lee, "Uniformly Redundant Array Imaging of Laser Driven Compressions. Preliminary Results," Appl. Opt. 18, 945-7 (1979).

R. A. Fisher and B. J. Feldman, "On-Resonant Phase-Conjugate Reflection and Amplification at 10.6 Micrometers in Inverted Carbon Dioxide," Opt. Lett 4, 140-2 (1979).

D. W. Forslund, J. M. Kindel, K. Lee, and B. S. Godfrey, "Collapse of Very Large Amplitude Ion Waves," Phys. Fluids 22, 462-5 (1979).

S. J. Gitomer and D. B. Henderson, "Reexamination of Strongly Flux Limited Thermal Conduction in Laser Produced Plasmas," Phys. Fluids **22**, 364-6 (1979).

R. A. Hardekopf, R. F. Haglund, Jr., G. G. Ohlsen, and L. R. Veeser, "Polarized Triton Elastic Scattering Data," Los Alamos National Laboratory report LA-7863 (1979).

A. Hemmendinger, C. E. Ragan, and J. M. Wallace, "Tritium Production in a Sphere of (6) Lithium Deuterium Irradiated by 14-MeV Neutrons," Nucl. Sci. Eng. **70**, 274-80 (1979).

S. S. Johnson, T. Crane, and G. Eccleston, "Savannah River Plant Californium-252 Shuffler Software Manual," Los Alamos National Laboratory report LA-7717-M (1979).

A. T. Lowe and C. Hosford, "Magnetron Sputter Coating of Microspherical Substrates," J. Vac. Sci. Technol. **16**, 197-9 (1979).

R. J. Mason, "Double-Diffusion Hot-Electron Transport in Self-Consistent E and B Fields," Phys. Rev. Lett. **42**, 239-43 (1979).

R. J. Mason, R. J. Fries, and E. H. Farnum, "Conical Targets for Implosion Studies with a Carbon Dioxide Laser," Appl. Phys. Lett. **34**, 14-6 (1979).

K. B. Mitchell, D. B. VanHulsteyn, G. H. McCall, P. Lee, and H. R. Griem, "Compression Measurements of Neon-Seeded Glass Microballoons Irradiated by Carbon Dioxide-Laser Light," Phys. Rev. Lett. **42**, 232-5 (1979).

J. E. Sollid, S. J. Thomas, and C. R. Phipps, Jr., "Damage Threshold Variation with Spot Size at 10.6 Micrometers for Kalvar and Polaroid Films," Appl. Opt. **18**, 424 (1979).

G. A. Rinker, Jr., "Static and Dynamic Muonic-Atom Codes-MUON and RURP," Comput. Phys. Commun. **16**, 221-242 (1979).

D. B. VanHulsteyn, P. Lee, and K. B. Mitchell, "Two Dimensional Monochromatic X-Ray Imaging of Laser-Produced Plasmas," Opt. Lett. **4**, 126-8 (1979).

H. C. Volkin, "Calculation of Short-Pulse Propagation in a Large Carbon Dioxide-Laser Amplifier," J. Appl. Phys. **50**, 1179-88 (1979).

R. L. Whitman, R. H. Day, R. P. Kruger, and D. M. Stupin, "Microradiographs of Laser Fusion Targets. Two-Dimensional Modeling and Analysis," Appl. Opt. **18**, 1266-74 (1979).

D. C. Winburn, "Laser Safety Eyewear Update," Electro Op. Sys. Des. **10**, No. 11, 30-35 (1978).

S. J. Gitomer, "A Fast Fourier Transform Technique Applied to Subnanosecond Laser Fusion Diagnostics," IEEE Trans. Plasma Science **PS7**, 135-136 (1979).

S. J. Gitomer and W. S. Hall, "X-Ray Streak Camera Electrode Design Using a Plasma Simulation Code," Nucl. Instrum. Methods **159**, 331-335 (1979).

PRESENTATIONS

The following presentations were made at the IEEE International Conference on Plasma Science, Montreal, Canada, June 4—6, 1979.

L. A. Booth, "Inertial Confinement Fusion Reactor Technology."

R. J. Mason, "Severe Thermal Transport Inhibition Due to Suprathermal Electron Currents in Laser Produced Plasmas."

R. J. Mason, "Electron Transport Effects in Laser Produced Plasmas."

W. P. Gula, "The Effect of Nonuniform Laser Deposition on Exploding Pusher Targets."

S. J. Gitomer, E. J. Linnebur, and G. H. McCall, "Analysis of Lateral Thermal Conduction in Laser Produced Plasmas."

S. J. Gitomer, "A Fast Fourier Transform Technique Applied to Subnanosecond Laser Fusion Diagnostics."

D. W. Forslund, "Important Nonlinear Laser Fusion Plasma Problems Solved by Numerical Simulation."

H. Brysk and A. J. Scannapieco, "Absorption by a Spherical Target vs Laser Focal Shifts."

K. B. Riepe, J. Jansen, and G. Allen, "Energy Storage for the Antares 100-kJ Laser Fusion Experiment."

T. H. Tan, A. W. Williams, and G. H. McCall, "Fast Particle Measurements and Laser Fusion."

D. B. VanHulsteyn, R. A. Kopp, W. Priedhorsky, and G. H. McCall, "Pinhole Photographs from LASL Helios Experiments."

P. B. Lyons, T. H. Tan, A. Williams, L. P. Hocker, D. Simmons, and P. A. Zagarino, "High Speed Detectors for Plasma Diagnostics."

The following presentations were made at the 9th Annual Conference on Anomalous Absorption of Electromagnetic Waves, Rochester, New York, May 15-18, 1979.

R. J. Mason, "Electron Transport in Laser Produced Plasmas."

D. W. Forslund, "The Absence of Significant Stimulated Brillouin Scattering in CO_2 Laser-Produced Plasmas."

B. Bezzerides, D. W. Forslund, and S. J. Gitomer, "Resonant Absorption—Model Fields and Electron Heating."

T. H. Tan and G. H. McCall, "Fast-Ion Measurement and Hot-Electron Temperature."

The following presentations were made at the Los Alamos Scientific Conference on Optics '79, Los Alamos, New Mexico, May 23-25, 1979.

H. C. Volkin and E. E. Stark, "Multipulse Energy Extraction in CO_2 Laser Amplifiers."

R. F. Benjamin and J. Riffle, "Optical Measurements of Lateral Energy Flow and Plasma Motion in Laser-Produced Plasmas."

G. Lawrence (University of Arizona), and P. N. Wolfe, "Application of the LOTS Computer Code to Laser Fusion Systems, and Other Physical Optics Problems."

A. C. Saxman, T. Swann, W. C. Sweatt, and Q. Appert, "Antares Beam Alignment System."

C. J. Silvernail and K. C. Jones (EG&G), "Antares Power Amplifier Optical System."

T. F. Stratton, "Optical Design Considerations in CO_2 Laser Fusion Systems."

J. E. Sollid, "Single-Point Diamond-Turned Mirror Performance Before and After Polishing."

R. Williamson, "Polishing Large NaCl Windows on a Continuous Polisher."

P. N. Wolfe, A. C. Saxman, and G. Lawrence (University of Arizona), "LOTS Analysis of Optical Diffraction in Antares."

W. C. Sweatt, "Mirror Quality Required by the Antares Laser System."

J. C. Goldstein, "Calculation of Small Signal Gain Coefficients in CO_2."

The following presentations were made at the First Topical Meeting on Fusion Reactor Materials, Miami Beach, Florida, January 29-31, 1979.

J. R. Miller and W. Press, " Cryogenic Laser Fusion Target Materials."

E. H. Farnum, R. J. Fries, and James Barefield, II, "Materials Problems with Inertial Confinement Fusion Targets."

J. R. Miller, "Cryogenic Laser Fusion Target Materials."

The following presentations were made at the Third Annual Conference on Transport Process in Laser Plasmas, Traverse City, Michigan, June 18-21, 1979.

R. F. Benjamin, A. W. Ehler, and G. H. McCall, "Measurement of Return Current in a Laser Plasma."

D. Giovanielli, "Hot-Electron Transport and Energy Losses in CO_2 Heated Plasmas."

T. H. Tan, G. H. McCall, and D. Giovanielli, "Fast-Ion Measurement and Hot-Electron Temperature."

The following presentations were made at the 1979 IEEE/OSA Conference on Laser Engineering and Applications, Washington, DC, May 30-June 1, 1979.

B. J. Feldman, R. A. Fisher, I. J. Bigio, and E. E. Bergmann, "Intracavity Techniques for High-Reflectivity Phase Conjugation in Germanium and Inverted CO_2."

D. E. Watkins, C. R. Phipps, Jr., and S. J. Thomas, "Ellipse Rotation in Germanium."

J. B. Marling and I. P. Hermal (LLNL), and S. J. Thomas (Los Alamos), "Separation of Deuterium and Other Isotopes by CO_2 Laser Multiple-Photon Absorption and Subsequent Reaction."

F. Lindman, Jr., "Inertial Confinement Fusion Target Concepts and Design Considerations."

T. F. Stratton and A. C. Saxman, "Optics and Alignment in Large CO_2 Systems for Fusion Research.

H. J. Jansen, "Review and Status of Antares."

K. B. Riepe, K. J. Bickford, J. Jansen, and W. C. Turner, "300-kJ, 200-kA Marx Module for Antares."

R. D. Stine, G. F. Ross, and C. Silvernail, "The Antares Laser Power Amplifier."

W. R. Scarlett, K. Andrews, and J. Jansen, "A Large-Area Cold Cathode Grid-Controlled Electron Gun for Antares."

The following presentations were made at the ANS 1979 Annual Meeting, Atlanta, Georgia, June 3-8, 1979.

W. A. Reupke, H. S. Cullingford, T. G. Frank, and L. A. Booth, "Wetted Wall ICF Fissile Fuel Factory Studies."

I. O. Bohachevsky and S. Chow, "MHD Decelerators for ICF Reactors."

J. H. Pendergrass and S. A. W. Gerstl, "The Lithium Boiler: A High-Temperature Fusion Reactor Blanket."

In addition, the following presentations were made at various institutions.

W. A. Reupke, H. S. Cullingford, T. G. Frank, and L. A. Booth, "US/USSR Symposium on Fusion-Fission (Hybrid) Reactors, Princeton Plasma Physics Laboratory, Princeton, New Jersey, January 22—26, 1979.

The following presentations were made at IEEE, Texas Tech University, Lubbock, Texas, June 12-14, 1979.

R. Liepins, M. J. Campbell, and R. J. Fries, "Plastic Coatings for Laser Fusion Targets," Symposium on New Concepts in Coatings and Plastics, Honolulu, Hawaii, April 1-6, 1979.

P. Lee, "X-Ray Spectroscopy of CO_2 Laser Produced Plasma," Physics Seminar, University of Hawaii, Honolulu, Hawaii, May 15-19, 1979.

K. B. Mitchell, "X-Ray Spectroscopy of Laser Produced High Density Plasmas," US-Japan Seminar on Plasma Spectroscopy, Japan, May 8-11, 1979.

R. F. Benjamin, G. H. McCall, and A. W. Ehler, "Measurement of Return Current in a Laser Plasma," Conference on Transport Processes in Laser Plasmas, Sleeping Bear Dunes National Lakeshore Park, Michigan, June 18-21, 1979.

D. W. Forslund, "Important Nonlinear Laser Plasma Interaction Problems," New York University Courant Institute, May 15, 1979.

J. F. Figueira, R. K. Ahrenkiel, and D. Dunlavy, "The Nonlinear Properties of the Perrhenate Ion in KCl," The 23rd Annual Technical Symposium, San Diego, California, August 27-30, 1979.

J. F. Figueira, "Gas Lasers for Fusion Science and Engineering," Physics Seminar, Lehigh University, Bethlehem, Pennsylvania, May 1979.

R. A. Fisher, B. J. Feldman, R. G. Tercovich, I. J. Bigio, and E. E. Bergmann, "Infrared Phase Conjugation via Degenerate Four-Wave Mixing," Conference on Physics of Quantum Electronics, Snowbird, Utah, January 19, 1979.

B. J. Feldman, R. A. Fisher, I. J. Bigio, and E. E. Bergmann, "Phase Conjugation: The Wave of the Future," *Colloquium*, Massachusetts Institute of Technology, Cambridge, Massachusetts, February 15, 1979.

B. J. Feldman, R. A. Fisher, I. J. Bigio, and E. E. Bergmann, "Phase Conjugate Reflection via Light-by-Light Scattering and Four-Wave Mixing," Seminar, Lincoln Laboratory, Lexington, Massachusetts, February 16, 1979.

R. A. Fisher and B. J. Feldman, "Infrared Phase Conjugation," Seminar, Westinghouse Research Laboratory, Pittsburgh, Pennsylvania, May 16, 1979.

E. E. Stark, "The CO_2 Laser Fusion Program at Los Alamos," 16th Annual Symposium, Idaho Section of the ASME, Idaho Falls, Idaho, April 19, 1979.

J. L. Munroe, "CO_2 Fusion Optics at Los Alamos," Tutorial seminar (Laser-Optics I), University of Lowell, Lowell, Massachusetts, May 9-10, 1979.

T. F. Stratton, "Carbon Dioxide Laser for Inertial Fusion," Press Release at the American Physical Society Meeting, Chicago, Illinois, March 19-23, 1979.

W. H. Reichelt, "Antares, a 100 kJ CO_2 Laser Fusion System," American Vacuum Society Meeting, Los Angeles, California, February 20, 1979.

N. G. Wilson, "Vacuum System Design Alternative for a 25,000-Liter Laser Fusion Target Chamber," 8th Annual Symposium on Applied Vacuum Science and Technology, sponsored by the American Vacuum Society, Tampa, Florida, February 12—14, 1979.

J. L. Munroe and G. Woodfin, "An Optical Evaluation Laboratory for Laser Fusion," SPIE Los Angeles Technical Symposium, Optical Components: Manufacture and Evaluation, North Hollywood, California, January 22-23, 1979.

D. Blevins and J. L. Munroe, "Plated Copper Substrates for the LASL Antares CO_2 Laser System," SPIE Los Angeles Technical Symposium, Optical Components: Manufacture and Evaluation, North Hollywood, California, January 22-23, 1979.

W. C. Priedhorsky and K. B. Mitchell, "CO_2 Laser Generated Silicon X Ray Line Scaling," Conference on Atomic Processes in High Temperature Plasmas, Boulder, Colorado, January 17-19, 1979.

U. S. GOVERNMENT PRINTING OFFICE [illegible]